

**MECHANICAL BEHAVIORS OF BIO-INSPIRED COMPOSITE
MATERIALS WITH FUNCTIONALLY GRADED REINFORCEMENT
ORIENTATION AND ARCHITECTURAL MOTIFS**

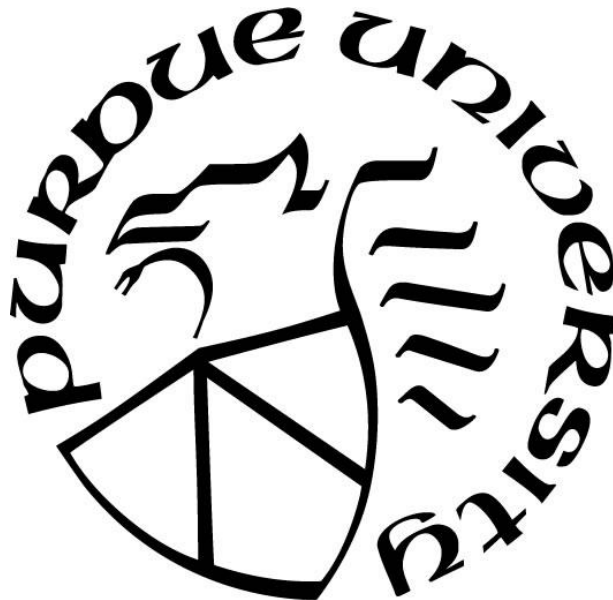
by
Di Wang

A Dissertation

Submitted to the Faculty of Purdue University

In Partial Fulfillment of the Requirements for the degree of

Doctor of Philosophy



Lyles School of Civil Engineering

West Lafayette, Indiana

May 2020

THE PURDUE UNIVERSITY GRADUATE SCHOOL
STATEMENT OF COMMITTEE APPROVAL

Dr. Pablo D. Zavattieri, Chair

Lyles School of Civil Engineering

Dr. Arun Prakash

Lyles School of Civil Engineering

Dr. Luna Lu

Lyles School of Civil Engineering

Dr. Wenbin Yu

School of Aeronautics and Astronautics

Approved by:

Dr. Dulcy Abraham

This work is dedicated

To my parents, Furen Wang and Ke Wei, whose unconditional love give me courage to chase my dream. Thank you for always being there for me

To my beloved grandparents

To the engineers and scientists in pursuit of the optimal architectural composite materials

ACKNOWLEDGMENTS

I would like to express my sincere gratitude to my advisor, Professor Pablo Zavattieri, for his support, motivation, and encouragement during my Ph.D. His support and guidance have helped me throughout my Ph.D. research and study.

Besides my advisor, I am deeply thankful to my examination committee members, Professor Wenbin Yu, Professor Arun Prakash, and Professor Luna Lu, for their precious and insightful comments and encouragement.

I wish to acknowledge financial support from the Multi-University Research Initiative (AFOSR-FA9550-15-1-0009).

Special thanks to Chan Hue Jeong, David Restrepo, Nicolás Guarín-Zapata and all my colleagues in Computational Multi-Scale Material Modeling Lab at Purdue University for their collaborations and fruitful discussions. Also, I thank my research collaborators at Micro and Nanomechanics Lab, Northwestern University and the Wolf Group, Friedrich-Alexander-University Erlangen-Nuremberg for their continuous and insightful suggestions and discussions.

Finally, I would like to thank my parents and my friends who supported me during my Ph.D. study. Without their encouragement and help, I believe that I cannot insist on pursuing my PhD degree until now.

TABLE OF CONTENTS

LIST OF TABLES	8
LIST OF FIGURES	9
ABSTRACT	18
1. INTRODUCTION	21
1.1 Biological materials	21
1.2 Motivation.....	23
1.3 Objectives and goals	26
2. FIBER REORIENTATION IN THE HYBRID BIOINSPIRED HELICOIDAL COMPOSITES WITH COMPLIANT MATRICES.....	28
2.1 Introduction.....	28
2.2 Methods.....	32
2.2.1 Geometry of 3D Printed Discontinuous Fiber Helicoids.....	32
2.2.2 FEA model.....	32
2.2.3 Analytical model.....	33
2.3 Results and discussion	34
2.3.1 Stress and strain response of hybrid helicoids.....	34
2.3.2 Moduli and strain stiffening.....	34
2.3.3 Mechanisms giving rise to strain stiffening.....	37
<i>Role of fiber reorientation</i>	39
<i>Explanation on fiber reorientation based on mechanism</i>	43
<i>Role of matrix mechanical behavior</i>	46
2.4 Conclusions.....	47
3. ON THE 3D ARCHITECTURE OF NATURALLY OCCURRING LAMELLAR STRUCTURES: A COMPARATIVE ANALYSIS	50
3.1 Introduction.....	50
3.2 Problem formulation	53
3.2.1 Three-dimensional architectures.....	53
3.2.2 Prerequisite and loading conditions.....	54
3.3 Materials and loading machine	55

3.3.1	Materials	55
3.3.2	loading machine.....	55
3.4	Results.....	56
3.5	Analytical model and FEA.....	57
3.5.1	Analytical model.....	58
3.5.2	Finite Element Analysis (FEA)	61
	<i>Materials</i>	61
	<i>Boundary condition</i>	62
3.6	Results and discussion	63
3.6.1	Elastic modulus and new dimensionless parameter.....	63
3.6.2	Critical stress and toughness.....	64
	<i>Critical stress</i>	64
	<i>Toughness</i>	66
3.7	Conclusions.....	66
4.	RESISTANCE OF CRACK INITIATION OF MATERIALS WITH FUNCTIONALLY GRADED ELASTIC MODULUS.....	68
4.1	Background.....	68
4.2	Methods and results	68
4.2.1	Dimension of model	68
4.2.2	Element and boundary condition.....	68
4.2.3	Modified J-integral	69
4.2.4	Stress distribution	70
4.2.5	Results.....	70
4.3	Conclusions.....	73
5.	INTER- AND INTRA-LAMINAR DAMAGE OF HELICOID WITH GRADIENT PITCH ANGLES.....	74
5.1	Introduction and motivations	74
5.2	Methods.....	78
5.2.1	Designs of composite laminates	80
5.2.2	Necessary information in FEA	81
5.2.3	Loading conditions	87

5.3	Dimensionless group of target parameters.....	89
5.4	Results and discussion	92
5.4.1	Three-point bending on short beam by using FEA.....	92
5.4.2	Low velocity impact on the laminated plate using FEA.....	98
5.4.3	Explanation	108
	<i>Transverse shear stresses distribution through the thickness</i>	108
a.	Analytical prediction	108
b.	FEA using solid model with two C3D20R elements per lamina.....	110
5.4.4	Justification of finite element model	116
5.5	Conclusions.....	127
6.	CONCLUSIONS	130
	APPENDIX A. SUPPLEMENTAL MATERIAL FOR CHAPTER 2	136
	APPENDIX B. SUPPLEMENTAL MATERIAL FOR CHAPTER 3	160
	APPENDIX C. SUPPLEMENTAL MATERIAL FOR CHAPTER 4	166
	APPENDIX D. SUPPLEMENTAL MATERIAL FOR CHAPTER 5	168
	REFERENCES	180
	PUBLICATIONS.....	191

LIST OF TABLES

Table 3.1. Geometrical parameters of designed samples.....	57
Table 3.2 Geometrical parameters of designed samples.....	63
Table 5.1. In-plane and interface properties of composite laminates	81
Table 5.2. Dimensionless groups of parameters in three-point bending test with constant θh	90
Table 5.3. Dimensionless groups of parameters in three-point bending test with gradient θh	90
Table 5.4. Dimensionless groups of parameters in low-velocity impact test with gradient θh	91
Table 5.5. Analytical predicted transverse shear modulus and in-plane shear modulus of helicoid composites and FGHs	120
Table A1 Components of stretch tensor polar decomposed from deformation gradient extracted from FEA	144
Table A2 E_{ini} of alternative disorder lay-up sequence predicted by CLPT with 120 N (pitches)	153

LIST OF FIGURES

Figure 2.1. Biological structures found in nature: (a) Helicoid structure of the mantis shrimp dactyl club, and (b) regular helicoid architecture. (c) Biological brick-and-mortar structure of the red abalone, and (d) regular brick-and-mortar architecture. (e) The discontinuous fiber helicoid architecture (DFH), and (f) Dimensions of the DFH architecture. (g) Undeformed single layer with misorientation θ with respect to the loading axis. (h) Schematic of fiber rotation $\Delta\theta c$ due to stretch only. Photo credits (a) S. Baron with adapted size, under CC by 2.0(left) and adapted from (Grunenfelder et al., 2014a)(right); (c) courtesy of Southwest Fisheries Science Center, NOAA Fisheries Service (left) and adapted from (Barthelat et al., 2007)(right)..... 29

Figure 2.2. (a) Experimental stress and strain curve of DFH $\theta h = 30^\circ$ with $LW = 2$ and definition of elastic modulus of three regions. (b) Initial elastic modulus, E_{ini} , normalized by the elastic modulus of the lamina with misorientation 0° with respect to the loading direction, E_{180} , as a function of pitch angle, θh . (c) Contour plot of maximum principal logarithmic strain, ϵ_{ln} , as predicted by FEA, layer by layer. (d) FEA predictions and experimental measurements (DIC) of maximum principal logarithmic strain, ϵ_{ln} , in the $\theta 30$ layer of the DFH with pitch $\theta h = 30^\circ$. (e) Γ as a function of θh calculated from FEA prediction with the hyperelastic matrix when applied strain, ϵ , is 15% , compared with Γ calculated from experimental stress and strain curves (Zaheri et al., 2018). (f) Fiber reorientation due to stretch only, denoted by $\Delta\theta c$, as a function of applied strain, ϵ , of individual laminae. 36

Figure 2.3. (a) DMB with absolute misorientation θb . Comparison of (b) Normalized FEAvand analytical results for DSLs and DMBs architectures, all with linear elastic matrix. 38

Figure 2.4. (a)-(b) Definition of direction on fibers rotation. Positive means fibers rotate toward the loading axis, whereas negative means fibers rotate away from the loading direction. The x -axis is the loading direction. $1'$ and $2'$ axes are local axes after deformation. (c)Fiber reorientation due to stretch only, $\Delta\theta c$, of individual lamina in DFH/DMB/DSL under 10% local uniaxial strain. (d) Histogram of $\Delta\theta c$ in lamina $\theta 30$ (e) Semi-analytical Γ_{iof} calculated based on $\Delta\theta c$ in DFH $\theta h = 30^\circ$ /DMB/DSL under 10% local uniaxial strain. 41

Figure 2.5. (a) $\Delta\theta c$ as a function of misaligned angle θi (b) Colormap of $\Delta\theta c$ as a function of U_{12} and U_{22} , where red dot represents for lamina $\theta 30$ in DMB $\theta b = 30^\circ$, black dot represents for lamina DSL $\theta s = 30^\circ$, and blue dot represents for lamina $\theta 30$ in DFH $\theta h = 30^\circ$ (c) Configuration of individual layer $\theta 30$ of DFH $\theta h = 30^\circ$ (d) Configuration of individual lamina $\theta 30$ of DMB $\theta b = 30^\circ$ (e) Configuration of individual layer $\theta 60$ of DFH $\theta h = 30^\circ$ (f) individual layer $\theta 30$ of DSL $\theta s = 30^\circ$, before(light grey) and after deformation(darker grey for matrix and blue for fibers)..... 43

Figure 2.6. FEA predictions on elastic modulus of laminates with linear elastic matrix deformed within 1% local true strain, ϵt , ($ELE1\%$) and at $\sim 4\%$ ϵt ($ELE4\%$). Analytical predictions are based on the CLPT model. (a) Comparison among $\theta h = 30^\circ$, $\theta b = 30^\circ$ and $\theta b = 45^\circ$ (b) Comparison between $\theta h = 30^\circ$ and the disorder architecture with lay-up sequence [30/150/60/120/0/90/30] (c) Elastic modulus as a function of local true strain, ϵt . (d) Stiffening parameter $\Gamma_{iof}(\epsilon t)$ as a function of ϵt 45

Figure 3.1 (a) SEM micrograph showing the radula teeth of Chitons and its rod-like microstructure (de Obaldia et al., 2015) (b) Basic 2D shear lag model. (c) California red abalone with pearlescent interior of nacre and the micrograph of its nacreous tablet-like microstructure (Salinas and Kisailus, 2013). (d) Biomimetic 3D rod-like and tablet-like inclusions 52

Figure 3.2. (a) Biomimetic 3D tablet-like structures. (b) General top view of the hexagon tablets. (c) model of one unit cell and its effective shear and tension area. (d) Biomimetic 3D rod-like architecture. (e) Cross-section design of 3D rod-like structures. Hexagons with grey color and with blue color represent that they are not in the same plane, which have 50% out-of-plane offset distance. (f) Unit cell of 3D rod-like architecture and its effect shear and tension area..... 54

Figure 3.3. (a) DIC of 3D architectures under uniaxial tensile loading in longitudinal direction. (b) DIC of 3D architectures under uniaxial tensile loading in transverse direction. (c) Stress and strain curves of 3D rod-like and tablet-like architectures under uniaxial tensile loading in longitudinal and transverse directions. (d) The crack surface of 3D architectures after loading in transverse direction. (e) The crack surface of 3D architectures after loading in longitudinal direction. (f) The CAD file of 3D-printed samples..... 55

Figure 3.4. (a) Radar plot of elastic modulus, strength and toughness of 3D tablet-like nacreous and rod-like chiton architectures in longitudinal direction. (b) Radar plot of elastic modulus, strength and toughness of 3D tablet-like nacreous and rod-like chiton architectures in transverse direction. 57

Figure 3.5. (a) Top view of 3D tablet-like structure including shift distance, shift area, effective shear area and the length of the unit cell. (b) Half of the 3D tablet-like structure with projected 2D geometry in blue color and their effective dimensions. (c) Projected 2D segments with effective length and boundary conditions. (d) Elastic modulus as a function of dimensionless parameter α . (e) Dimensionless parameter ξ as a function of α . (f) shear stress distribution map of interlayer matrix when $\alpha=0.5$. (g) shear stress distribution map of interlayer matrix when $\alpha=0.387$ and $\xi=0.5$ 59

Figure 3.6. Unit cell with mesh in FEA on 3D rod-like structure (a) Unit cell of 3D rod-like structure and its dimensions (b) Unit cell of 3D tablet-like structure and its dimensions 62

Figure 3.7. Elastic modulus of composites in longitudinal direction normalized by elastic modulus of fiber (E_x/E_f) as a function of dimensionless groups (V_f and A_{sl}^2/V_{cell}), all with $L/M = 15$ except two nacre structures, which are with $V_f = 0.56$ and 0.8 , shown in Table 3.2 63

Figure 3.8. (a) Critical stress σ_{yc} as a function of A_{st}/V_{cell} from experiments and analytical prediction. Black axis represents for analytical prediction and red axis represents for experimental results. (b) Toughness as a function of A_{est}/V . Dots with blue color shadow are from prediction and dots under green shadow are the results from experiments. 65

Figure 4.1. Simulation of FGMs and other types of materials. a, Nature Pinctada b, Size and boundary condition of FEA simulation model c, Functionally graded material on Young's modulus in Pinctada, layered distribution of Young's modulus based on first case, homogeneous material and inverse graded Young's modulus distribution which is the mirror of graded materials based on axis of homogeneous case. d, Normalized stress distribution of layered Young's modulus, graded Young's modulus and homogeneous materials with crack size $25\mu m$. e, Stress intensity factor of samples with different crack sizes. f, Comparison in percentage on stress intensity factor between

graded materials in nature Pinctada and homogeneous materials, inverse graded Young’s modulus and homogeneous materials, coupled with layered Young’s modulus and homogeneous materials.

..... 72

Figure 5.1. (a) Peak load under static loading condition as a function of pitch angle of thinner laminate (layer number less than 37) (Cheng et al., 2011; Liu et al., 2020, 2018a; Zhang and Zhang, 2015) (b) Peak load under static loading condition as a function of pitch angle of thicker laminate (layer number larger than 37)(Liu et al., 2020) (c) Peak load normalized by its maximum peak load of different layers and materials(Cheng et al., 2011; Liu et al., 2020, 2018a; Zhang and Zhang, 2015)..... 77

Figure 5.2. Target outputs of laminates with different numbers of layers and distinct fiber materials under dynamic-impact loading condition (a) Peak load of laminates as a function of pitch angle (b) Absorbed energy of laminates as a function of pitch angle (c) Ashby plot of absorbed energy and peak load (d)-(e) zoom in version of Ahsby plot (c) 78

Figure 5.3. (a)-(b) Designs of functionally gradient helicoids (FGHs) and (c) their pitch distance, D , as a function of height, H 81

Figure 5.4. Mesh convergence study of (a) Tc (b) P . Mesh condition of short beam under three-point bending (c) with 480 elements per layer and (d) with 2024 elements per layer..... 85

Figure 5.5. (a) P as a function of mesh number per layer with 6mm plate thickness (b) Absorbed energy per unit volume as a function of mesh number per layer with 6mm plate thickness (c) Mesh condition of LVI test with 3329 elements per layer with 6mm plate thickness (d) P as a function of mesh number per layer with 24mm plate thickness (e) Absorbed energy per unit volume as a function of mesh number per layer with 24mm plate thickness (f) Mesh condition of LVI test with 7040 elements per layer with 24mm plate thickness 86

Figure 5.6. Left figure shows the boundary and dimensions of short beam bending test and the right figure shows the boundary condition of low velocity impact test..... 88

Figure 5.7. (a) Delamination failure distribution through the thickness of short beams FGH1sym and H36sym (b) Load and displacement curves of FGH1sym(red) and H36sym(black) (c) Delamination area distribution layer by layer. Different shaded color represents for different pitches of FGH1sym 92

Figure 5.8. (a) Delamination failure distribution through the thickness of short beams FGH1sym and H45sym (b) Load and displacement curves of FGH1sym(red) and H45sym(black) (c) Delamination area distribution layer by layer. Different shaded color represents for different pitches of FGH1sym 94

Figure 5.9. (a) Delamination failure distribution through the thickness of short beams FGH1sym and H60sym (b) Load and displacement curves of FGH1sym(red) and H60sym(black) (c) Delamination area distribution layer by layer. Different shaded color represents for different pitches of FGH1sym 95

Figure 5.10. (a) P as a function of θh of helicoidal-laminated-short beam under 3-point bending (b) Tc as a function of θh of helicoidal-laminated-short beam under 3-point bending (red dots represent for FGHs with corresponding θh laid close to surface and blue dot represents for FGH1disorder) 96

Figure 5.11. Ashby plots of three-point short beam bending tests (a) Ashby plot with parameters P and Tc (b) 3D Ashby plot with parameters Tc , P and Ad (c) Ashby plot of parameters P and Ad (d) Ashby plot of parameters Tc and Ad (red dots represent for FGHs with corresponding θh laid close to surface and blue dot represents for FGH1 disorder)..... 97

Figure 5.12. (a) Force and displacement plot of H45sym under three-point bending test (b) Zoom in plot of force and displacement curve of H45sym under three-point bending test (c) First derivative on force and displacement curve of H45sym (d) Peak load before 1st drop in displacement and load curves of short beams with different pitch angles, θh , and functionally gradient helicoids (FGH1syma and FGH2sym, shown in red dots). The θh of FGH1sym and FGH2sym shown here is the first θh (close to top) of FGH laminated beam. 98

Figure 5.13. Contours of delamination process of H15sym under 40J LVI with 6mm thickness (a) The cross-section of H15sym at final state of LVI simulation (b) Zoom-in contour of delamination distribution through the thickness of H15sym at final state of LVI simulation (c)-(i) Zoom-in contours of delamination process through the thickness of H15sym (j) Zoom-in contour of delamination distribution through the thickness of H15sym at peak dent depth before rebounding 99

Figure 5.14. (a) Plot of force and displacement in LVI tests with total thickness 6mm (b) Force and time plot of LVI tests with total thickness 6mm (c) Plot of kinetic energy as a function of time with total thickness 6mm (d) Plot of force and displacement in LVI tests with total thickness 24mm (e) Force and time plot of LVI tests with total thickness 24mm (f) Plot of kinetic energy as a function of time with total thickness 24mm 100

Figure 5.15. Projected delamination area Apd of (a) H15sym, (b) H30sym, (c) H36sym, (d) H45sym, (e) H60sym and (f) H90sym with thickness 6mm 101

Figure 5.16. Projected delamination area Apd of (a) FGH1sym, (b) FGH2sym with thickness 6mm (c) Normalized projected delamination area as a function of pitch angle(normalized by the maximum value of each set of data) 101

Figure 5.17. (a) Absorbed kinetic energy (KE) as a function of pitch angle (θh) with plate thickness 6mm (b) Peak load (P) as a function of θh with plate thickness 6mm (c) Projected delamination area (Apd) as a function of θh with plate thickness 6mm (d) Delamination area in all through the thickness (Ad) as a function of θh with plate thickness 6mm..... 103

Figure 5.18. (a) Absorbed kinetic energy (KE) as a function of pitch angle (θh) with plate thickness 24mm (b) Peak load (P) as a function of θh with plate thickness 24mm (c) Projected delamination area (Apd) as a function of θh with plate thickness 24mm (d) Delamination area in all through the thickness (Ad) as a function of θh with plate thickness 24mm..... 104

Figure 5.19. (a) Energy dissipated from intralaminar failure as a function of θh featured with thickness 6mm (b) Energy dissipated from intralaminar failure as a function of θh featured with thickness 24mm 105

Figure 5.20. (a) Ashby plot of absorbed energy KE and Peak load P of models with thickness 6mm (b) Ashby plot of energy dissipated by intralaminar damage and absorbed energy KE of models with thickness 6mm (c) Ashby plot of delamination area Ad and absorbed energy KE of models with thickness 6mm 106

Figure 5.21. (a) Ashby plot of absorbed energy KE and Peak load P of models with thickness 24mm(b) Ashby plot of energy dissipated by intralaminar damage and absorbed energy KE of models with thickness 24mm (c) Ashby plot of delamination area Ad and absorbed energy KE of models with thickness 24mm.....	108
Figure 5.22. (a) Boundary conditions of quasi-static three-point bending test (b) Transverse shear stress Sxz distribution in $x - z$ plane predicted by extended CLPT (c) Sxz distribution along the thickness of the laminate H30sym when $x_1 = L$ (d) Comparison on $S13$ between H15sym and H45sym (e) Comparison on Sxz among helicoid laminates with different pitch angles separately (f) Comparison on Sxz among FGH1sym and its associated laminates (g) Comparison on Sxz among FGH2sym and its associated laminates.....	110
Figure 5.23. Transverse shear stress Sxz distribution along the thickness of the laminates with different constant pitch angles separately	111
Figure 5.24. Transverse shear stress Syz distribution along the thickness of the laminates with different constant pitch angles separately	111
Figure 5.25. (a) Maximum Sxz at free-edge (close to top indenter) of the laminated beam of helicoid laminates with symmetry lay-up to the middle plane and the laminates without symmetry lay-up to the middle plane (b) Maximum Sxz at free-edge (close to bottom rollers) of the laminated beam of helicoid laminates with symmetry lay-up to the middle plane (c) Maximum Syz at free-edge (close to top indenter) of the laminated beam of helicoid laminates with symmetry lay-up to the middle plane and the laminates without symmetry lay-up to the middle plane (d) Maximum Syz at free-edge (close to bottom rollers) of the laminated beam of helicoid laminates with symmetry lay-up to the middle plane separately	112
Figure 5.26. (a) Maximum Szz at free-edge (close to the indenter) of the laminated beam of helicoid laminates (b) Local maximum Sxz at free-edge (close to the half thickness) of the laminated beam of helicoid laminates.....	112
Figure 5.27 (a) Sxz as a function of off-axis angle, including the two cases of beam and plate (b) Transverse shear modulus as a function of off-axis angle (c) Chentsov's coefficients as a function of off-axis angle	115
Figure 5.28. (a) Sxz distribution along z -direction at free-edge of short-beam H60sym (b) Sxz distribution along z -direction at free-edge of short-beam H15sym.....	117
Figure 5.29. $LExz$ distribution along z -direction at free-edge of short-beam H15sym.....	117
Figure 5.30. (a) Sxz distribution along z -axis at free-edge of short beam H15sym and H60sym both created by solid model (b) Sxz distribution along z -axis at free-edge of short beam H15sym and H60sym both created by continuum shell model.....	118
Figure 5.31. (a) ux distribution along z -axis at free-edge of short beam H15sym and H60sym created by solid model and continuum shell models (b) dux/dz distribution along z -axis at free-edge of short beam H15sym and H60sym created by solid model and continuum shell models.....	119
Figure 5.32. Strain energy as a function of applied displacement before any damage or failure occurs in continuum shell models.....	120

Figure 5.33. (a) Transverse shear strain LE_{xz} through the thickness at free edge of solid model with two C3D20R and with eight C3D20R per lamina (b) Zoom in plot of strain distribution at interface between -60° and 60°	121
Figure 5.34. Transverse shear strain LE_{xz} through the thickness at free edge of solid model with two C3D20R and with four C3D8R per lamina.....	122
Figure 5.35. (a) Load and displacement curve of H30sym model under short beam bending with 12 laminae through the thickness. Red curve represents for continuum shell considering delamination only and black curve represents for solid model considering delamination only. (b) Delamination initiation and propagation in continuum shell model (c) Delamination initiation and propagation in solid model.....	123
Figure 5.36. (a) Load and displacement curve of H60sym model under short beam bending with 12 laminae through the thickness. Red curve represents for continuum shell considering delamination only and black curve represents for solid model considering delamination only. (b) Delamination initiation and propagation in continuum shell model (c) Delamination initiation and propagation in solid model.....	124
Figure 5.37. (a) Comparison on peak load, P , between solid and shell models in H30sym and H60sym (b) Comparison on toughness, Tc , between solid and shell models in H30sym and H60sym.....	125
Figure 5.38.(a) Delamination area distribution along the thickness of the 12 layer short beam of H30sym after first peak load occurs (b) Delamination area distribution along the thickness of the 12 layer short beam of H30sym at the last increment under 4.75mm loading displacement in z direction (c) Delamination area distribution along the thickness of the 12 layer short beam of H60sym after first peak load occurs (d) Delamination area distribution along the thickness of the 12 layer short beam of H60sym at the last increment under 4.75mm loading displacement in z direction	126
Figure A1. (a) 3D-printed sample with $LW = 2$, and (b) FEA model with $LW = 2$ (c) and (e) undeformed and deformed dog-bone samples of DSL $\theta_s = 30^\circ$ with $LW = 6$ (d) and (f) undeformed and deformed oblique tab samples of DSL $\theta_s = 30^\circ$ with $LW = 4$	136
Figure A2. Stress strain curves of (a) VeroWhite fiber material under uniaxial tensile loading, and (b) TangoPlus matrix material under uniaxial tensile loading and (c) under simple shear loading	138
Figure A3 (a) Finite element implementation of the helicoid geometry ($\theta_h = 30^\circ$), with (b) Close up showing mesh refinement across fiber and surrounding matrix (c) Illustration of free-free boundary condition (d) Illustration of free-periodic boundary condition.....	139
Figure A4. Initial elastic modulus, E_i , in FEA as a function of total number of elements	140
Figure A5 (a) Oblique tab angle, φ , as a function of laminae misorientation, θ_s , corresponding to the loading axis; (b) Theoretical deflection and rigid body rotation of dog-bone sample along longitudinal axis in uniaxial tensile; (c) Fiber reorientation of DSL with oblique tab and normal dog-bone tab. (d) $\Delta\theta_c$ measured and calculated by three different methods as a function of misorientation θ_i in DFH $\theta_h = 30^\circ$ with free-periodic boundary condition.....	142

Figure A6 (a)-(b)Fiber reorientation values due to stretch, $\Delta\theta_c$, and fiber reorientation considering in-plane warping effects, $\Delta\theta$, of DFH, DMB and DSL architectures.....	144
Figure A7. Poisson's ratio ν_{xy} and extensional-shear coupling coefficients $\eta_{xy,x}$ as a function of misorientation θ_s	145
Figure A8. Stress and strain curves in experiments ($L/W=2$) and FEA of DFHs (a) $\theta_h = 30^\circ$, (b) $\theta_h = 45^\circ$, (c) $\theta_h = 60^\circ$, (d) $\theta_h = 90^\circ$	146
Figure A9. Stress and strain curves in experiments with (a) $L/W=2$ and (b) $L/W=4$	146
Figure A10. (a)Stress and strain curves in FEA of DSL architectures with hyperelastic matrix (b-d)True stress and strain curves in FEA of DSL architectures, DFH and DMB architectures with linear elastic matrix material.....	147
Figure A11. Discontinuities in the matrix between two fibers to mimic the local failures at the beginning of region II.....	148
Figure A12. (a) $\Delta\theta_c$ of $\theta_h = 30^\circ$ with different ratios of E_{fiber}/E_{matrix} as a function of local strain. (b) Strain stiffening of $\theta_h = 30^\circ$ as a function of E_{fiber}/E_{matrix}	149
Figure A13. Maximum logarithmic strain, ϵ_{ln} distribution of $\theta_h = 30^\circ$ with different E_{fiber}/E_{matrix}	150
Figure A14. In-plane shear strain, LE_{12} , distribution at the interface of DMB $\theta_b = 30^\circ$ (left) and DFH $\theta_h = 30^\circ$ (right).....	151
Figure A15. Shear strain distribution, LE_{12} , through the thickness of different two paths of DFH $\theta_h = 30^\circ$ and DMB $\theta_b = 30^\circ$	152
Figure A16. Fiber reorientation, $\Delta\theta$, as a function of applied displacement in (a) DFH $\theta_h = 30^\circ$ and (b) DMB $\theta_h = 30^\circ$ with hyperelastic and linear elastic matrix.....	152
Figure A17. Fiber reorientation (a) after and (b) before excluding rotation tensor \mathbf{R} as a function of initial misorientation of laminae.....	153
Figure A18. (a) True stress and strain curve of DFH $\theta_h = 30^\circ$. (b) Elastic modulus as a function of local true strain.....	154
Figure A19. (b) rotation map of matrix of $\theta_s = 30^\circ$ from two different of views; (c) rotation map of matrix of θ_{30} of $\theta_h = 30^\circ$ from two different of views; (d) rotation map of matrix of θ_{30} of $\theta_b = 30^\circ$; from two different of views; (e) rotation distribution in matrix surrounding fiber and shear\ntension zone illustration; (f) Rotation values along Y direction of lamina θ_{30} in DFH $\theta_h = 30^\circ$; (g) Rotation values along Y direction of lamina θ_{30} of DMB $\theta_b = 30^\circ$; (h) Rotation values along Y direction of DSL $\theta_s = 30^\circ$	156
Figure A20. (a) Logarithmic strain in Y direction of SL30 and (b) individual lamina 30 of DFH30 with PBC. (c) Disrtibution of Logarithmic strain in Y direction along the perpendicular distance. (d) In-plane shear logarithmic strain of SL30 and (e) individual lamina 30 of DFH30. (f) Disrtibution of In-plane shear logarithmic strain along the perpendicular distance. (g) Logarithmic strain in Y direction of SL60 and (h) individual lamina 60 of DFH60 with PBC. (i) Disrtibution of Logarithmic strain in Y direction along the perpendicular distance. (j) In-plane shear logarithmic	

strain of SL60 and (k) individual lamina 60 of DFH60. (l) Disrtibution of In-plane shear logarithmic strain along the perpendicular distance.	158
Figure A21. (a) Definite value of E_{ini} of DSL and DMB (b) Definite value of E_{ini} of DFH..	159
Figure A22. Strain stiffening as a function of local true strain of numerical and analytical prediction with linear elastic matrix.....	159
Figure B1. Displacement distribution of the analytical prediction on 3D nacre model	162
Figure B2. 3D printed(vertically and horizontally) material characterization samples for simple shear (2nd row) and uniaxial tension(1st row) tests with different thickness of matrix material.	163
Figure B3. (1) Elastic modulus E and (2) maximum shear stress τ_c of matrix material with different thickness.....	163
Figure B4. 2D shear-lag model.....	165
Figure B5. (a) normalized shear stress in matrix and (b) normalized shear stress in prism 2, which is a zoom in figure.....	165
Figure C1. a. Boundary condition and mesh condition of mode I crack; b. Comparison of J-integral calculation for isotropic material and Graded, coupled with the prediction of ABAQUS; c. Comparison of J-integral calculation for isotropic material and Inverse graded, coupled with the prediction of ABAQUS.....	166
Figure C2. a. Normalized opening stress distribution close to crack tip for three different sizes of crack model b. Mesh convergence study on model with crack size $a=50\mu m$	167
Figure D1. (a) Delamination failure distribution through the thickness of short beams H30sym and H15sym (b) Load and displacement curves of H15sym(red) and H30sym(black) (c) Delamination area distribution layer by layer. Different shaded color represents for different pitch of FGH1sym	168
Figure D2. (a) Delamination failure distribution through the thickness of short beams FGH2sym and H30sym (b) Load and displacement curves of FGH2sym(red) and H30sym(black) (c) Delamination area distribution layer by layer. Different shaded color represents for different pitches of FGH2sym	169
Figure D3. (a) Delamination failure distribution through the thickness of short beams FGH2sym and H45sym (b) Load and displacement curves of FGH2sym(red) and H45sym(black) (c) Delamination area distribution layer by layer. Different shaded color represents for different pitches of FGH2sym	170
Figure D4. (a) Delamination failure distribution through the thickness of short beams FGH2sym and H90sym (b) Load and displacement curves of FGH2sym(red) and H90sym(black) (c) Delamination area distribution layer by layer. Different shaded color represents for different pitches of FGH2sym	171
Figure D5. (a) Delamination failure distribution through the thickness of short beams FGH1sym and FGH1symdisorder (b) Load and displacement curves of FGH1sym(red) and	

FGH1symdisorder(black) (c) Delamination area distribution layer by layer. Different shaded color represents for different pitches of FGH1sym.....	172
Figure D6. Force and displacement plot of H45sym under 3-point bending test(left) and stiffness as a function of displacement plot of H45sym under 3-point bending plot.....	173
Figure D7. Delamination distribution in 3D of H30sym	173
Figure D8. Projected delamination area A_{pd} of (a) H15sym, (b) H30sym, (c) H36sym, (d) H45sym, (e) H60sym and (f) H90sym with thickness 24mm	174
Figure D9. Projected delamination area A_{pd} of (a) FGH1sym, (b) FGH2sym with thickness 24mm	174
Figure D10 loading condition of short beam 3-point bending test	175
Figure D11. (a) Transverse shear strain (LE_{xz}) distribution of [-30/30/-30/30] along the thickness at free edge of mono-balanced laminate under uniaxial tensile (b) Displacement in x direction of [-30/30/-30/30] along the thickness at free edge of mono-balanced laminate under uniaxial tensile. (c) Transverse shear strain (LE_{xz}) distribution of H30sym along the thickness at free edge of mono-balanced laminate under uniaxial tensile. (d) Displacement in x direction of [-30/30/-30/30] along the thickness at free edge of mono-balanced laminate under uniaxial tensile.	178
Figure D12. (a) Transverse shear strain (LE_{xz}) distribution of [-60/60/-60/60] along the thickness at free edge of mono-balanced laminate under uniaxial tensile (b) Displacement in x direction of [-60/60/-60/60] along the thickness at free edge of mono-balanced laminate under uniaxial tensile. (c) Transverse shear stress (S_{xz}) distribution of [-60/60/-60/60] along the thickness at free edge of mono-balanced laminate under uniaxial tensile.....	179

ABSTRACT

Naturally-occurring biological materials with stiff mineralized reinforcement embedded in a ductile matrix are commonly known to achieve excellent balance between stiffness, strength and ductility. Interestingly, nature offers a broad diversity of architectural motifs, exemplify the multitude of ways in which exceptional mechanical properties can be achieved. Such diversity is the source of bio-inspiration and its translation to synthetic material systems. In particular, the helicoid and the “brick and mortar” architected materials are two key architectural motifs we are going to study and to synthesize new bio-inspired materials.

Due to geometry mismatch (misorientation) and incompatibilities of mechanical properties between fiber and matrix materials, it is acknowledged that misoriented stiff fibers would rotate in compliant matrix beneath uniaxial deformation. However, the role of fiber reorientation inside the flexible matrix of helicoid composites on their mechanical behaviors have not yet been extensively investigated. In the present project, fiber reorientation values of single misoriented laminae, mono-balanced laminates and helicoid architectures under uniaxial tensile are calculated and compared. In the present work, we introduce a Discontinuous Fiber Helicoid (DFH) composite inspired by both the helicoid microstructure in the cuticle of mantis shrimp and the nacreous architecture of the red abalone shell. We employ 3D printed specimens, analytical models and finite element models to analyze and quantify in-plane fiber reorientation in helicoid architectures with different geometrical features. We also introduce additional architectures, i.e., single unidirectional lamina and mono-balanced architectures, for comparison purposes. Compared with associated mono-balanced architectures, helicoid architectures exhibit less fiber reorientation values and lower values of strain stiffening. The explanation for this difference is addressed in terms of the measured in-plane deformation, due to uniaxial tensile of the laminae, correlated to lamina misorientation with respect to the loading direction and lay-up sequence.

In addition to fiber, rod-like, reinforced laminate, platelet reinforced composite materials, “brick and mortar” architectures, are going to be discussed as well, since it can provide in-plane isotropic behavior on elastic modulus that helicoid architecture can offer as well, but with different geometries of reinforcement. Previous “brick and mortar” models available in the literature have provided insightful information on how these structures promote certain mechanisms that lead to significant improvement in toughness without sacrificing strength. In this work, we present a

detailed comparative analysis that looks at the three-dimensional geometries of the platelet-like and rod-like structures. However, most of these previous analyses have been focused on two-dimensional representations. We 3D print and test rod-like and tablet-like architectures and analyze the results employing a computational and analytical micromechanical model under a dimensional analysis framework. In particular, we focus on the stiffness, strength and toughness of the resulting structures. It is revealed that besides volume fraction and aspect ratio of reinforcement, the effective shear and tension area in the matrix governs the mechanical behavior as well. In turns, this leads to the conclusion that rod-like microstructures exhibit better performance than tablet-like microstructures when the architecture is subjected to uniaxial load. However, rod-like microstructures tend to be much weaker and brittle in the transverse direction. On the other hand, tablet-like architectures tend to be a much better choice for situations where biaxial load is expected.

Through varying the geometry of reinforcement and changing the orientation of reinforcement, different architectural motifs can promote in-plane mechanical properties, such as strain stiffening under uniaxial tensile, strength and toughness under biaxial tensile loading. On the other hand, the various out-of-plane orientation of the reinforcement leads to functionally graded effective indentation stiffness. The external layer of nacre shell is composed of calcite prisms with graded orientation from surface to interior. This orientation gradient leads to functionally graded Young's modulus, which is confirmed to have higher fracture resistance than homogenous materials under mode I fracture loading act.

Similar as graded prism orientation in calcite layer of nacre, the helicoid architecture found in nature exhibits gradients on geometrical parameters as well. The pitch distance of helicoid architecture is found to be functionally graded through the thickness of biological materials, including the dactyl club of mantis shrimp and the fish scale of coelacanth. This can be partially explained by the long-term evolution and selection of living organisms to create high performance biological materials from limited physical, chemical and geometrical elements. This naturally "design" procedure can provide us a spectrum of design motifs on architectural materials.

In the present work, linear gradient on pitch distance of helicoid architectures, denoted by functionally graded helicoid (FGH), is chose to be the initial pathway to understand the functionality of graded pitch distance, associated with changing pitch angle. Three-point bending on short beam and low-velocity impact tests are employed in FEA to analyze the mechanical

properties of composite materials simultaneously. Both static(three-point bending) and dynamic(low-velocity impact) tests reveal that FGH with pitch angle increasing from surface to interior can provide multiple superior properties at the same time, such as peak load and toughness, while the helicoid architectures with constant pitch angle can only provide one competitive property at one time. Specifically, helicoid architectures with smaller pitch angle, such as 15° , show higher values on toughness, but less competitive peak load under static three-point bending loading condition, while helicoid architectures with middle pitch angle, larger than or equal to 22.5° and smaller than 45° , exhibit less value of toughness, but higher peak load. The explanation on this trend and the benefits of FGH is addressed by analyzing the transverse shear stresses distribution through the thickness in FEA, combined with analytical prediction. In low-velocity impact tests, the projected delamination area of helicoid architectures is observed to increase when the pitch angle is decreasing. Besides, laminates with specific pitch angles, such as 45° , classical quasi-isotropic laminate, 60° , specific angle ply, and 90° , cross-ply, are designed to compare with helicoid architectures and FGH.

1. INTRODUCTION

1.1 Biological materials

Bio-composites found in the exoskeletons of crustacean and mollusk shells combine stiff mineralized (inorganic) reinforcement with ductile biopolymers (organic) to form complex hierarchical architectures (Chen et al., 2012; Meyers et al., 2008; Zhang et al., 2010a). The superior mechanical properties of these protective architected materials, such as stiffness, strength, and fracture toughness, are of critical importance to the organism survival. This is accomplished in part through the combination of stiff and ductile materials and a hierarchical architecture over a range of length scales. Interestingly, nature offers a broad diversity of architectural motifs, exemplify the multitude of ways in which exceptional mechanical properties can be achieved. Such diversity is the source of bio-inspiration and its translation to synthetic material systems. Indeed, bio-inspired materials made by additive manufacturing technologies display similar deformation mechanisms and superior properties (de Obaldia et al., 2015; Porter et al., 2017; Studart, 2016; Suksangpanya et al., 2018; Yin et al., 2019; Zhang et al., 2016, 2015). On the other hand, metallic layered composites made by sintering exhibit enhanced damage tolerance (Hofer et al., 2020).

In part of fiber reorientation, Chapter 2, we combine two architectures: (i) the “fiber helicoid (or Bouligand)” (Bouligand, 1972; Meyers et al., 2008) and (ii) the “brick and mortar” to investigate discontinuous fiber helicoids (DFH) first introduced and investigated in (Zaheri et al., 2018). The fiber helicoid is found in the dactyl club of the Peacock mantis shrimp (*Stomatopod*) (Grunenfelder et al., 2014a; Guarín-Zapata et al., 2015; Weaver et al., 2012), the cuticle of arthropods (Cheng et al., 2011, 2008a; Grunenfelder et al., 2014a; Raabe et al., 2005; Sachs et al., 2008; Weaver et al., 2012; Yao et al., 2013; Zelazny and Neville, 1972), fish scales (Bigi et al., 2001; Bruet et al., 2008; Fang et al., 2014; Gil-Duran et al., 2016; Ikoma et al., 2003; Lin et al., 2011; Meyers et al., 2012; Murcia et al., 2017a; Torres et al., 2008; Yang et al., 2014, 2019; Zhu et al., 2012; Zimmermann et al., 2013), and plants (Chung et al., 2011; Roland et al., 1989). The “brick and mortar” is found in sea shells, e.g., the innermost layers of red abalone (*Haliotis rufescens*) (Barthelat et al., 2016; Ji and Gao, 2004; Menig et al., 2000; Salinas and Kisailus, 2013; Sun and Bhushan, 2012a).

In addition to DFH synthesized from helicoid and “brick and mortar” architectures, nacreous laminar architecture, which is original motif in nature of “brick and mortar” architecture, is studied and compared with rod-like architecture in Chapter 3. The former architecture is bio-inspired by the nacreous microstructures in the inner layer of seashells of Mother-of-pearl (nacre), staggered tablet-like architectures. Its mechanical properties are far superior to its constituents, ceramic and protein (Barthelat et al., 2007; Chintapalli et al., 2014; Pro et al., 2015; Salinas and Kisailus, 2013; Sun and Bhushan, 2012b; Yaraghi and Kisailus, 2018; Zhang et al., 2010b). The rod-like architecture is bio-inspired by the radular teeth of the gumboot Chiton, which consist of biomineralized rod-like magnetite fibers and soft organic material. Through controlling the interface strength between fibers, the possibility of catastrophic failure can be decreased and therefore the Chiton tooth is able to achieve impressive abrasion resistance (Escobar de Obaldia et al., 2016).

While the inner layer of the black-lipped pearl oyster *Pinctada margaritifera* is made of nacreous architecture as described above, the outer protective prismatic layer yields a functionally gradient material with varying Young’s modulus (David Wallis et al., in press). This gradient Young’s modulus is induced by a gradual change of the crystal lattice orientation. A common gradient on Young’s modulus in biominerals is often considered as a nonfunctional outcome, which is partially induced by incipiently deficient mineralization control (Gilbert et al., 2008; Hovden et al., 2015). Nevertheless, this functional gradient previously unrecognized in crystalline solids can provide smooth stress transition from surface to interior and promote superior fracture resistance, compared with other constitutive motifs on Young’s modulus, which is analyzed in Chapter 4.

As the gradient on Young’s modulus of *Pinctada* mentioned above, functional gradients and heterogeneities are evolved from nature material to impart high-performance biological materials. The translation of evolution confers us a spectrum of design elements associated with the variations of chemical compositions/constituents and structural characteristics involved in the arrangement, distribution, dimensions and orientations of the building units (Liu et al., 2017). One of the rich toolboxes given by nature is the porosity arrangements. The porosity of growth ring from wood stems, for instance, decreases gradually from the earlywood to the latewood (Eder et al., 2009; Gibson, 2012; Speck and Burgert, 2011) and thus this arrangement leads to opposite pattern on density and stiffness, which is beneficial to water transport and mechanical stability

during the growth period. Besides, gradients on Young's modulus and other mechanical properties also reveal unprecedented contact damage resistance that cannot be realized in conventional homogenous materials (Pender et al., 2001; Suresh, 2001). In addition to porosity arrangement, many biological materials are featured with various dimensions of their constituents to achieve specific functionality. A primary example is the sponge spicules, constituted by a central core of hydrated silica surrounded by changing layers of silica and proteinaceous material(Liu et al., 2017). The thickness of silica layers is decreasing from core to surface(Aizenberg et al., 2005; Miserez et al., 2008), which can effectively resist the depth of crack penetration from surface, since cracks tends to propagate through organic ductile layers. Like what we introduced at the beginning of the introduction chapter, many biological materials consist of anisotropic structural elements, such as fibers, tablet reinforcement and prisms. Accordingly, their properties are highly dependent on the orientation of these structural elements. Helicoid architectures, found in the fish scale and the shell of arthropods, encompass successively different lamina orientations layer by layer, such that the material is featured with close-to in-plane isotropic behavior(Yang et al., 2019) and remarkable toughening mechanisms via crack twisting(Suksangpanya et al., 2018, 2017) or reorientation, stretching and delamination of fibrils to dissipate more energy under loading(Quan et al., 2018; Yang et al., 2014; Zimmermann et al., 2013).

In nature, majority biological materials are featured with not only one element of gradient, but integration of multiple gradient elements. For instance, tooth are combined both chemical and structural gradients to achieve mastication function(Ho et al., 2009, 2007), up to 1000 N biting forces over innumerable cycled during its lifetime(Lawn et al., 2010). The dactyl club of mantis shrimp is another remarkable example of integration of multiple gradient elements. Besides helicoid architecture, consisting of successively different lamina misorientations through the thickness, found in the periodic region of dactyl club, a decreasing pitch distance is also observed in this region (Guarín-Zapata et al., 2015). In Chapter 5 we are going to design potential synthesized helicoid materials encompassing the integration of common helicoid architecture and the gradient on pitch distance found in nature.

1.2 Motivation

While the fracture resistance, toughening behavior and photonic sensory mechanism of helicoid architecture under out-of-plane impact, bending (Ginzburg et al., 2017; Grunenfelder et

al., 2014a; Mencattelli and Pinho, 2019; Suksangpanya et al., 2018, 2017; Weaver et al., 2012), and uniaxial tensile loading (Zaheri et al., 2018) (Kose et al., 2019; Shishehbor and Zavattieri, 2019) have been extensively investigated, the mechanical behavior of fiber helicoid architectures, prior to failure, have been much less studied. For instance, it has been recently proposed that helicoidal arrays of fibrils, present in *Arapaima Gigas* scales, adapt to the loading environment through laminae rotation towards the loading direction, whereas other laminae, with large off-axis angle, rotate away from the loading direction (Quan et al., 2018; Yang et al., 2014; Zimmermann et al., 2013). As reported by Zimmermann et al. (Zimmermann et al., 2013), this so-called “sympathetic” fiber reorientation has been found to contribute to enhanced ductility and toughness in fish scales (Yang et al., 2019). In the spirit of bio-mimicry, Zaheri et al. (Zaheri et al., 2018) designed a discontinuous fiber helicoidally sample to gain further insight into the phenomenon. Tensile experiments performed on such samples shown features of strain stiffening consistent with large deformation effects. However, detailed modeling accounting for fiber rotation and matrix constitutive response are needed to decouple the two effects and gain insight into the potential of discontinuous fiber helicoidally structures. Among the few models reported in the literature for related phenomenon, we can mention the work by Yang et al. (W. Yang et al., 2017), which formulated a theoretical framework to predict the rotation of two-dimensional hard particles in a soft matrix. However, such model is limited to particles with small aspect ratios and does not incorporate the anisotropic behavior typically found in composite materials. Besides, their model does not consider the rotation of particles in a multilayer laminate. Accordingly, the study of fiber reorientation in misoriented laminates requires different theoretical and computational treatments.

On the other hand, the superior mechanical properties of biological composite materials stimulate scientists and engineers to design and fabricate bio-inspired materials which can provide similar properties that biological materials have. “Brick and mortar” architecture can represent three-dimensional(3D) tablet-like and rod-like architectures by simplifying inclusions from 3D to 2D as staggered 2D brick tablets. Shear-lag analytical model is ubiquitously used to predict the mechanical properties of “brick and mortar” architecture (Sakhavand and Shahsavari, 2015; Wei et al., 2012), allowing large shear deformation in the matrix, which is sandwiched by two stiff tablets. Tension-shear chain (TSC) model (Gao, 2006; Ji and Gao, 2004) illustrates the tensile deformation resistance of “brick-and-mortar” architecture through passing normal stress in discontinuous-stiff tablets and transferring shear stress in compliant matrix. Volume fraction (V_f)

and aspect ratio of inclusions (L/M) are two key parameters to predict the mechanical properties of “brick and mortar” model.

Shear-lag and TSC models assume plane strain condition for 2D analytical model, indicating infinite thickness out of plane. However, the inclusion of biological composite material is discontinuous out of plane and it also exhibits distinct geometries, such as rod-like and tablet-like architectures from microstructures in the chiton tooth and in the seashell of nacre respectively. Seashell of nacre is the protective layer of interior-soft material, able to resist exterior multiaxial loading, impact load and penetration, while Chiton teeth is used to rasp to expose algae growing on the surface of hard rocky substrates (Escobar de Obaldia et al., 2016). Their functionalities are different and therefore the morphologies of the macro geometries and micro-structure are distinct. In the present paper, we are trying to understand why nature chooses rod-like architecture to resist longitudinal normal loading and uses tablet-like architecture to endure multiaxial loading. To accomplish this analysis, extending 2D to 3D model is necessary and not only V_f and L/M should be considered in the analysis, but also effective shear A_s and tension area A_t needs our attention.

The present work in Chapter 3 extends the 2D analytical model (shear-lag combined with tension effects from matrix) to 3D and then compare the predicted mechanical properties, stiffness, strength and toughness, under longitudinal and transverse uniaxial tensile loading with corresponding experiments and finite element analysis (FEA) in 3D. To compare two architectures at the same level, dimensionless parameters are designed, including V_f and L/M .

Last but not least, it is acknowledged that helicoidal fiber reinforced laminated structures with uniform pitch angle are provided with efficient energy dissipation through the thickness and in-plane isotropic behavior to resist materials failure. However, helicoid architectures with small pitch angles dissipate energy via in-plane delamination (Ginzburg et al., 2017; Grunenfelder et al., 2014a). Delamination failure is exhibited to have large reduction on material stiffness, strength and can even initiate failure of the whole laminate (Garg, 1988) and impair the buckling resistance when under compression load (Aslan and Şahin, 2009). However, delamination is also an effective method to dissipate energy. On the other hand, intralaminar damage, such as fiber breakage and matrix split, also plays a significant role in the damage resistance of the materials, especially stiff fibers' breakage, which can release large amount of energy, but easier to lead to catastrophic damage, unable to provide any resistance when most fibers break through the cross-section. Considering the delamination failure occurring ubiquitously in the helicoid architectures, in

Chapter 5 transverse shear stresses dominant experiments, such as three-point bending on short beam and low-velocity impact tests, are going to be adopted.

Interestingly, in nature, the pitch distance of helicoid architectures in biological materials was found not constant through the thickness of the materials, but functionally decreasing from surface to interior. It is reported that the pitch distance in dactyl club varies from 150um(or 80um), close to surface, to 10um, close to interior (Guarín-Zapata et al., 2015). Although the specific values of pitch distance in the fish scale of Coelacanth were not measured, it is also observed that the pitch distance is decreasing from surface to interior in the Coelacanth fish scale (Quan et al., 2018).

In biological helicoid architectures, the integration gradients exist as the way of gradually changing orientations of laminae and varying pitch distance through the thickness, which can be induced by different pitch angles or distinct thickness of each lamina. Due to minor pitch angles observed in dactyl club, it needs extensively studies to determine the gradient pitch distance from surface to interior is dependent on lamina thickness or different pitch angles Nevertheless, (Quan et al., 2018) reported that the pitch angle in the double Bouligand structures of Coelacanth fish scale is increasing from surface to interior. Accordingly, it is necessary to investigate the specific function of varying pitch angles first along the thickness of the materials. Moreover, the contribution of the gradient of the pitch angle in helicoid architectures to the overall mechanical behaviors and fracture resistance behaviors has not yet been studied. This presents an opportunity to study and understand the specific function of the gradient of the pitch distance associated with varying pitch angles through the thickness of the materials. Thus, in the present study we are going to study the contribution of gradient pitch distance, associated with varying pitch angles, to the mechanical behaviors under static and dynamic loading conditions in Chapter 5.

1.3 Objectives and goals

The goal of this work is to understand the fundamental mechanical behaviors of bio-inspired composite materials featured with functionally graded lamina orientations and different geometries of architectural reinforcements in terms of deformation and failure mechanics. Specifically, the deformation resistance before failure and damage propagation, incorporated with fracture mechanism, are going to be studied on these bio-inspired composite materials. In order to achieve this goal, I propose the following objectives,

1. To study the effect of fiber reorientation on strain stiffening, and the reason inducing fiber reorientation of helicoidal architectures.
2. To conduct mechanical behavior analysis in three-dimension by using effective shear and tension deformation in the matrix of architectures featured with tablet-like(nacre) and rod-like(chiton) reinforcements.
3. To investigate the contribution of gradients associated with structural characteristics of helicoid architectures and nacreous architectures to fracture tolerance.

2. FIBER REORIENTATION IN THE HYBRID BIOINSPIRED HELICOIDAL COMPOSITES WITH COMPLIANT MATRICES

Chapter 2 is part of the publication “Fiber Reorientation in Hybrid Helicoidal Composites”, *Journal of the Mechanical Behavior of Biomedical materials* (2020), Status: submitted and revisions being processed

2.1 Introduction

Bio-composites found in the exoskeletons of crustacean and mollusk shells combine stiff mineralized (inorganic) reinforcement with ductile biopolymers (organic) to form complex hierarchical architectures (Chen et al., 2012; Meyers et al., 2008; Zhang et al., 2010a). The superior mechanical properties of these protective architected materials, such as stiffness, strength, and fracture toughness, are of critical importance to the organism survival. This is accomplished in part through the combination of stiff and ductile materials and a hierarchical architecture over a range of length scales. Interestingly, nature offers a broad diversity of architectural motifs, exemplify the multitude of ways in which exceptional mechanical properties can be achieved. Such diversity is the source of bio-inspiration and its translation to synthetic material systems. Indeed, bio-inspired materials made by additive manufacturing technologies display similar deformation mechanisms and superior properties (de Obaldia et al., 2015; Porter et al., 2017; Studart, 2016; Suksangpanya et al., 2018; Yin et al., 2019; Zhang et al., 2016, 2015). On the other hand, metallic layered composites made by sintering exhibit enhanced damage tolerance (Hofer et al., 2020). In this work we combine two architectures: (i) the “fiber helicoid (or Bouligand)” (Bouligand, 1972; Meyers et al., 2008) and (ii) the “brick and mortar” to investigate discontinuous fiber helicoids (DFH), which was first introduced and investigated in (Zaheri et al., 2018).

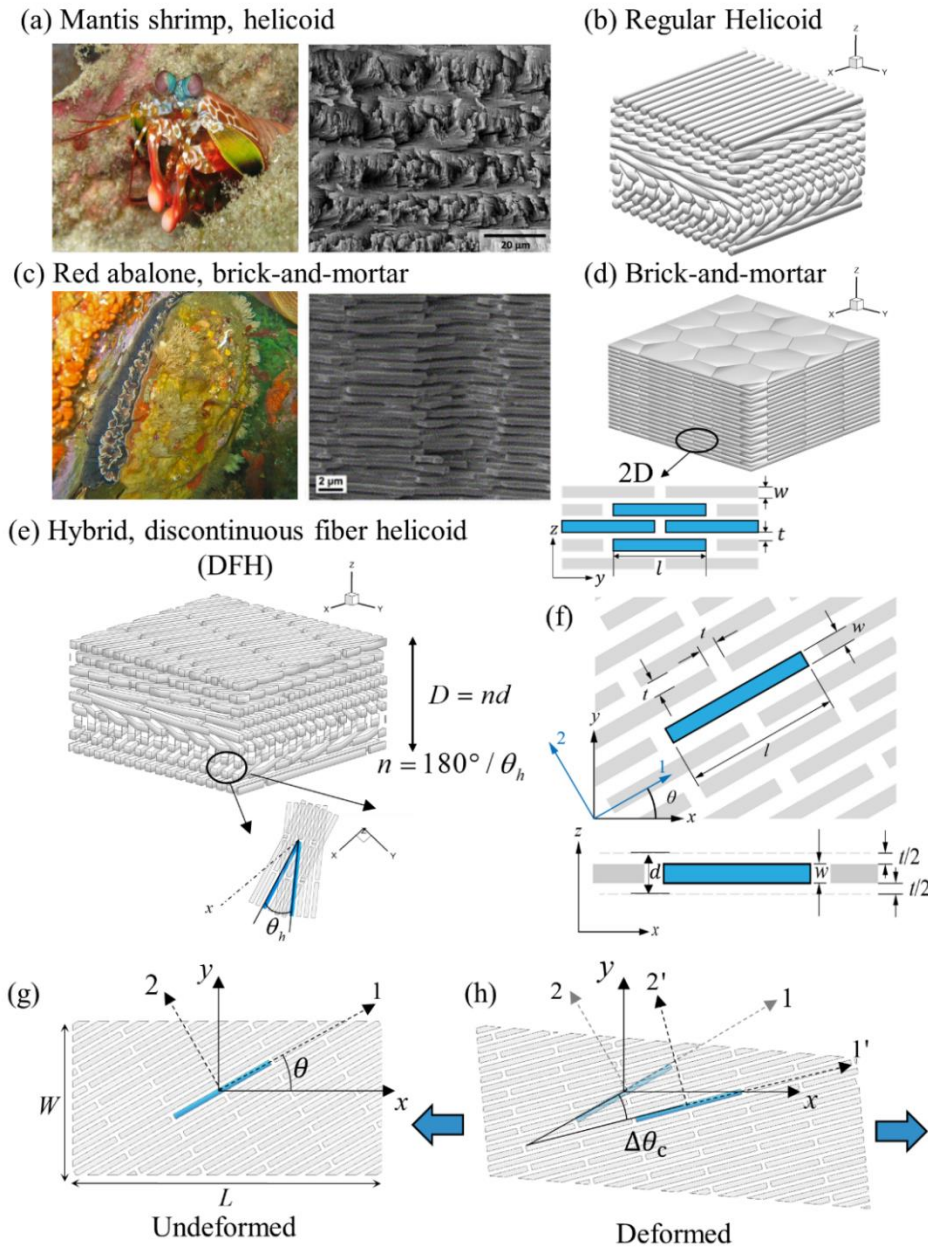


Figure 2.1. Biological structures found in nature: (a) Helicoid structure of the mantis shrimp dactyl club, and (b) regular helicoid architecture. (c) Biological brick-and-mortar structure of the red abalone, and (d) regular brick-and-mortar architecture. (e) The discontinuous fiber helicoid architecture (DFH), and (f) Dimensions of the DFH architecture. (g) Undeformed single layer with misorientation θ with respect to the loading axis. (h) Schematic of fiber rotation $\Delta\theta_c$ due to stretch only. Photo credits (a) S. Baron with adapted size, under CC by 2.0(left) and adapted from (Grunenfelder et al., 2014a)(right); (c) courtesy of Southwest Fisheries Science Center, NOAA Fisheries Service (left) and adapted from (Barthelat et al., 2007)(right).

As a complement to this previous work, the current paper focuses on the fiber reorientation and its contribution to strain stiffening behavior before failure occurs, which is analyzed via nonlinear micromechanical finite elements. The fiber helicoid is found in the dactyl club of the Peacock mantis shrimp (*Stomatopod*) (Figure 2.1(a) and (b))(Grunenfelder et al., 2014a; Guarín-Zapata et al., 2015; Weaver et al., 2012), the cuticle of arthropods (Cheng et al., 2011, 2008a; Grunenfelder et al., 2014a; Raabe et al., 2005; Sachs et al., 2008; Weaver et al., 2012; Yao et al., 2013; Zelazny and Neville, 1972), fish scales (Bigi et al., 2001; Bruet et al., 2008; Fang et al., 2014; Gil-Duran et al., 2016; Ikoma et al., 2003; Lin et al., 2011; Meyers et al., 2012; Murcia et al., 2017a; Torres et al., 2008; Yang et al., 2014, 2019; Zhu et al., 2012; Zimmermann et al., 2013), and plants (Chung et al., 2011; Roland et al., 1989). The brick and mortar is found in sea shells, e.g., the innermost layers of red abalone (*Haliotis rufescens*) (Barthelat et al., 2016; Ji and Gao, 2004; Menig et al., 2000; Salinas and Kisailus, 2013; Sun and Bhushan, 2012a) (Figure 2.1(c) and (d)).

While the fracture resistance, toughening behavior and photonic sensory mechanism of helicoid architecture under out-of-plane impact, bending (Ginzburg et al., 2017; Grunenfelder et al., 2014a; Mencattelli and Pinho, 2019; Suksangpanya et al., 2018, 2017; Weaver et al., 2012), and uniaxial tensile loading (Zaheri et al., 2018) (Kose et al., 2019; Shishehbor and Zavattieri, 2019) have been extensively investigated, the mechanical behavior of fiber helicoid architectures, prior to failure, have been much less studied. For instance, it has been recently proposed that helicoidal arrays of fibrils, present in *Arapaima Gigas* scales, adapt to the loading environment through laminae rotation towards the loading direction, whereas other laminae, with large off-axis angle, rotate away from the loading direction (Quan et al., 2018; Yang et al., 2014; Zimmermann et al., 2013). As reported by Zimmerman et al. (Zimmermann et al., 2013), this so-called “sympathetic” fiber reorientation has been found to contribute to enhanced ductility and toughness in fish scales (Yang et al., 2019). In the spirit of bio-mimicry, Zaheri et al. (Zaheri et al., 2018) designed a discontinuous fiber helicoidally sample to gain further insight into the phenomenon. Tensile experiments performed on such samples showed features of strain stiffening consistent with large deformation effects. However, detailed modeling accounting for fiber rotation and matrix constitutive response are needed to decouple the two effects and gain insight into the potential of discontinuous fiber helicoidally structures. Among the few models reported in the literature for related phenomenon, we can mention the work by Yang et al. (W. Yang et al., 2017),

which formulated a theoretical framework to predict the rotation of two-dimensional hard particles in a soft matrix. However, such model is limited to particles with small aspect ratios and does not incorporate the anisotropic behavior typically found in composite materials. Besides, their model does not consider the rotation of particles in a multilayer laminate. Accordingly, the study of fiber reorientation in laminates with distinct misaligned angle requires different theoretical and computational treatments.

As illustrated in Figure 2.1(e), the DFH architecture consists of aligned and staggered fibers (in the x - y plane), in which each lamina presents a fiber rotation by a constant pitch angle, θ_h , from the preceding lamina (along the z -axis). For example, for $\theta_h = 30^\circ$ the lay-up sequence is [0/30/60/90/120/150], where the angle is defined between the fiber and the x -axis. Once the lamina achieves 180° rotation, with respect to laminae with misorientation 0° , a full period in the helicoid architecture is achieved. The number of laminae needed to complete a 180° rotation is $n = D/d = 180/\theta_h$, where D is the period of the DFH architecture, also called pitch distance (Guarín-Zapata et al., 2015), Figure 2.1(e). d is the height of one lamina, composed of fiber height, w , and the separation between two fibers, t , such as $d = w + t$, as shown in Figure 2.1(f). Employing this geometry and Finite Element Analysis (FEA), we investigate the fiber rotation and matrix response, for several matrix constitutive laws, to elucidate the origin of strain stiffening in the DFH architecture as a function of imposed deformation (Zaheri et al., 2018). Both nonlinear constitutive response and finite deformations are investigated. To decouple the effects of fiber rotation, Figure 2.1(g) and (h), and matrix constitutive response on strain stiffening, linear elastic, hyper-elastic, and elasto-plastic matrix constitutive responses are considered. To decouple the composite lay-up effects on fiber rotation upon uniaxial tensile, we introduce two ancillary architectures: discontinuous single lamina (DSL) and discontinuous mono-balanced (DMB). We expect this analysis to provide information on interlaminar constrains in terms of strain and stress, a key characteristic in composites. The computational study will provide information on strain stiffening measured in the DFH architecture, and insights for the design of bio-inspired composites, with the DFH architecture, exhibiting strain stiffening.

2.2 Methods

2.2.1 Geometry of 3D Printed Discontinuous Fiber Helicoids

The discontinuous fiber helicoid (DFH) composites are 3D printed with two materials. A stiff polymer (VeroWhite (Stratasys Ltd., 2018)) for the fibers and soft polymer, rubber like (nearly incompressible), materials (TangoPlus (Stratasys Ltd., 2019)) for the matrix, see *section A1* of the supplemental material (SI), following Zaheri et al., (2018). VeroWhite material is more than 3 order of magnitude stiffer than the TangoPlus. On the other hand, TangoPlus is brittle under tension and shear deformation and it shows anisotropic behavior, due to the printing process. The fibers are printed with a square cross-section area to maximize resolution of the 3D printer. The stiff fibers have a length, l , and a square cross-section with width, w (Figure 2.1(f)). We choose a fiber aspect ratio $l/w = 20$ for all the cases and a sample gauge length to fiber length $L/l = 2.8$ for $L/W = 2$, which is the aspect ratio of the gauge, see Figure 2.1(g). The soft matrix separates the fibers in all three dimensions by a thickness t , as illustrated in Figure 2.1(f). The ratio of matrix thickness over the fiber width is also kept constant $t/w = 0.8$ for all the cases. As such, the fiber volume fraction is 29.7%. Further analysis indicates that materials with this fiber volume fraction are sufficient to be considered as a homogeneous anisotropic behavior in each lamina. Within the plane of a single lamina, the fiber and matrix form a brick and mortar structure, where fibers are off-set from neighboring rows by a distance $(l + t)/2$ to provide optimum staggering for shear transfer, Figure 2.1(f). This results in maximum in-plane stiffness in the longitudinal direction (Sakhavand and Shahsavari, 2015; Wei et al., 2012; Zhang et al., 2015, 2010a). Each lamina is defined by its misorientation, θ_i , with respect to the loading direction (x -direction). Here, the subscript “ i ” refers to the misorientation in a given lamina, Figure 2.1(g). For example, θ_{30} represents the lamina with a misorientation of 30° with respect to the loading direction. Any fiber reorientation upon deformation is labeled as $\Delta\theta_c$, as shown in Figure 2.1(h). Further details of specimens and testing are given in (Zaheri et al., 2018).

2.2.2 FEA model

The FEA model of 3D printed dog-bone samples is depicted in Figure A1. Geometries are meshed using first order tetrahedral elements (C3D4). The mesh size is selected such that there is mesh convergence (See *section A2*). Finite deformation is included in all simulations. The fiber

material is modeled as linear elastic with a Young's modulus $E = 1.108$ GPa and Poisson's ratio $\nu = 0.3$. The matrix is modeled as a hyperelastic material with a 2nd order polynomial model (Rivlin and Saunders, 1951). The model parameters are obtained by fitting matrix stress-strain experimental results in tensile and shear deformation, see *section A1*. In a subset of simulations, the matrix is also considered to be linear elastic with a Young's modulus $E = 0.337$ MPa and elasto-plastic with a bilinear law with a hardening modulus of 0.03 MPa and a yielding stress of 0.014MPa.

Most of the numerical simulations are conducted on specimens with finite size and free-edge boundary conditions on the faces with normal vectors in the y - and z -directions to replicate the conditions during the experiments, Figure A1 and Figure A3(c). However, to assess the applicability of these results to architectures with a large number of laminae in the z -direction (number of pitches, $N \rightarrow \infty$), a set of simulations is carried out with periodic boundary conditions on the planes perpendicular to the z -axis. Faces with vector normal in the direction of the y -axis remain free. Hence, we denote this configuration as free-periodic boundary condition, see Figure A3(d). A uniform displacement is prescribed in the x -direction, on the loading faces of the specimen, while the faces of the tabs normal to y - and z -axes are fixed in the y - and z -directions, Figure A3(c-d), for both free-free and free-periodic boundary conditions.

Fiber reorientation in each individual lamina is directly extracted from the FEA by computing the average rigid body rotation in each fiber. The simulations reveal that fiber rotation induced by stretch only, $\Delta\theta_c$, is hindered by the rotation of the gauge section, see *section A3*. Thus, in addition to the rotation that arises through stretching, rotation of the gauge section of the specimen (warping effect) also contributes to the apparent rotation, Figure A5(b). The latter contribution is removed since this is a geometric effect related to the fiber initial orientation, dimensions of the specimen, boundary condition, and the number of periodic layers. In the calculations, the warping effect is removed by polar decomposition of the deformation gradient. Details of the calculation process are provided in *Section A4*.

2.2.3 Analytical model

While limited to small strains, analytic methods can be used to obtain homogenized properties for both single oriented lamina and laminate composed of multiple laminae. Here, we employ the Halpin-Tsai equation (Halpin, 1969; Tucker and Liang, 1999) to predict the elastic

modulus of each layer with staggered-discontinuous fibers. Since Halpin-Tsai requires scalar quantities for the moduli, inputs are obtained through linearization of the matrix material under uniaxial tensile. The Halpin-Tsai equation for moduli is give as:

$$\frac{P}{P_m} = \frac{1+\xi\eta v_f}{1-\eta v_f} \text{ with } \eta = \frac{(P_f/P_m)-1}{(P_f/P_m)+\xi}, \quad (2.1)$$

where, P represents one of the homogenized composite moduli, such as E_{11} , E_{22} and G_{12} . P_f and P_m are the fiber and matrix moduli, respectively. ξ is an empirically derived factor that depends on the boundary conditions. For the quantities E_{11} , E_{22} and G_{12} , the factor ξ takes the values: $2(l/w)$, 2 and 1, respectively. Classical Laminate Plate Theory (CLPT) (Isaac M Daniel and Ori Ishai, 1994; Ramirez, 1999) is used for predicting the in-plane stiffness of a complete laminate.

2.3 Results and discussion

2.3.1 Stress and strain response of hybrid helicoids

The experimental stress-strain response of the 3D printed DFH architecture with various pitch angles θ_h shows a complex behavior as it can be observed in a typical stress-strain response in Figure 2.2(a) (Case $\theta_h = 30^\circ$). The complete set of experimental data and FEA data for θ_h in the range 15° - 180° is given in section A5. The stress-strain response for all DFH architectures can be divided into 3 distinct regions, Figure 2.2(a). Region I is defined by an initial elastic response with modulus E_{ini} . Region II shows a drop in the tangent modulus associated with fiber-matrix debonding at the fiber ends, followed by a hardening response. In this region a minimum and maximum tangent modulus can be defined, E_{min} and E_{max} , respectively, details described in *section A6*. Likewise, we can define a stiffening parameter defined as the ratio of $\Gamma = E_{max}/E_{min}$. Region III describes the material response as it accumulates further damage followed by final failure (Zaheri et al., 2018).

2.3.2 Moduli and strain stiffening

In our FEA, Regions I and II are independently considered to study the behavior of laminates without and with local discontinuity in the matrix between fiber ends, see *section A7*. The purpose of the first set of simulations is designed to capture the initial modulus E_{ini} (*Region*

I with intact matrix), while the second set of simulations includes discontinuities at the ends of the fibers (*debonded fiber-matrix interface*) to capture the stress-strain behavior in Region II. The second set of models is also employed to compute the stiffening parameter Γ . Specifically, in the FEA with discontinuous matrix (Region II), the elastic modulus after accumulated deformation is defined as E_{max} and the elastic modulus at the beginning of the stress and strain curve is defined as E_i . Hence, $\Gamma_{iof} = E_{max}/E_i$ defines the stiffness ratio, which is a measure of strain stiffening. Further details on these parameters can be found in *section A6* with the difference between Γ_{iof} and Γ depicted in Figure A8(a). The longitudinal elastic modulus of lamina with misorientation 0° , θ_0 or θ_{180} , denoted by E_{180} , are obtained following the Halpin-Tsai equation. Then using the CLPT model, the laminate properties are estimated as depicted in Figure 2.2(b). The employed constituent properties for the fiber are $E = 1108$ MPa, $\nu = 0.3$ and for the matrix $E = 0.337$ MPa, $\nu = 0.48$. The model predicted a lamina longitudinal elastic modulus of 6.07 MPa and a transverse modulus of 0.76 MPa.

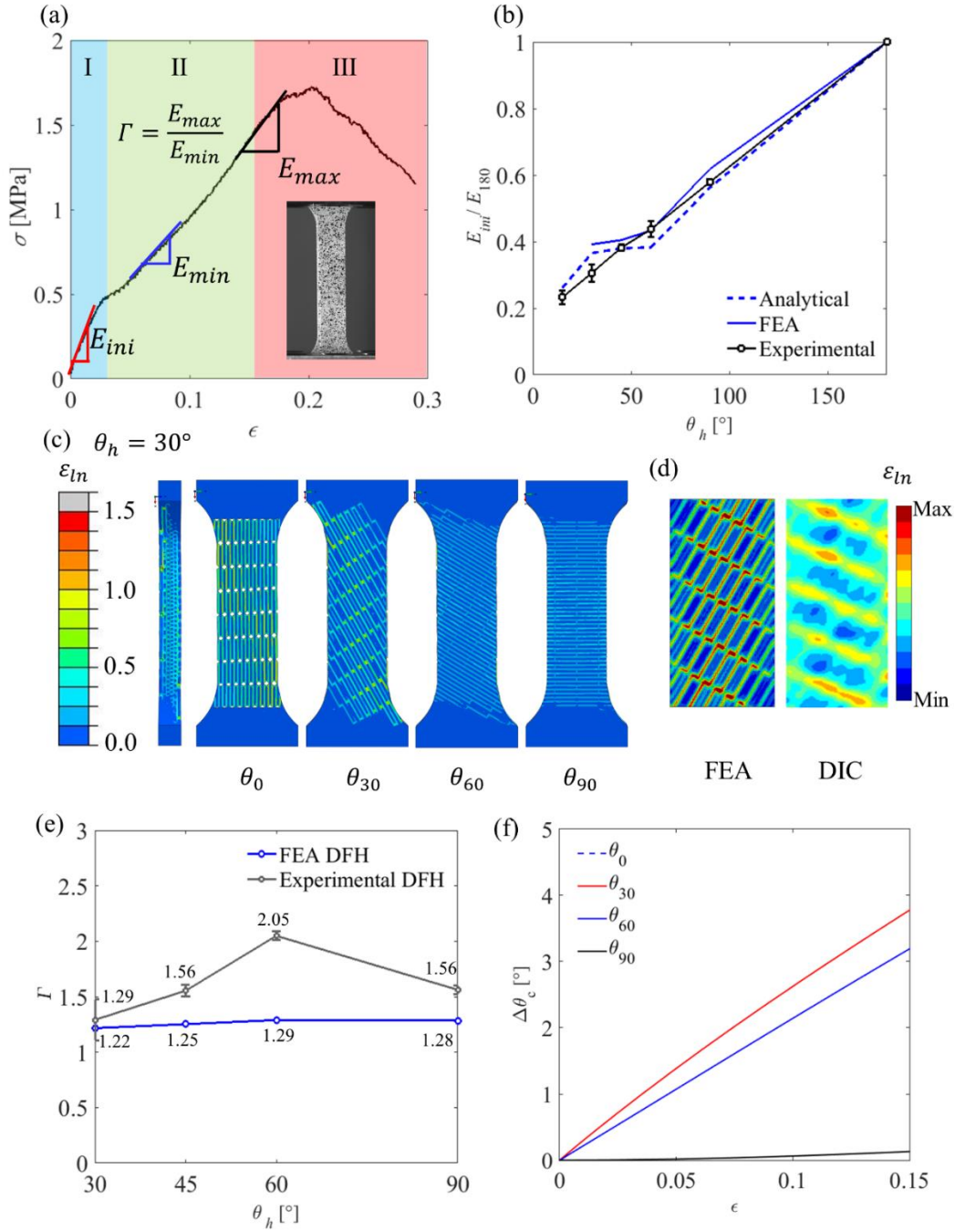


Figure 2.2. (a) Experimental stress and strain curve of DFH $\theta_h = 30^\circ$ with $L/W = 2$ and definition of elastic modulus of three regions. (b) Initial elastic modulus, E_{ini} , normalized by the elastic modulus of the lamina with misorientation 0° with respect to the loading direction, E_{180} , as a function of pitch angle, θ_h .

(c) Contour plot of maximum principal logarithmic strain, ϵ_{ln} , as predicted by FEA, layer by layer. (d) FEA predictions and experimental measurements (DIC) of maximum principal logarithmic strain, ϵ_{ln} , in the θ_{30} layer of the DFH with $\theta_h = 30^\circ$. (e) Γ as a function of θ_h calculated from FEA prediction with the hyperelastic matrix when applied strain, ϵ , is 15%, compared with Γ calculated from experimental stress and strain curves (Zaheri et al., 2018). (f) Fiber reorientation due to stretch only, denoted by $\Delta\theta_c$, as a function of applied strain, ϵ , of individual laminae.

The analytical, experimental, and FEA predictions of E_{ini} are in close agreement, as it can be observed in Figure 2.2(b). Since the FEA analysis uses a hyperelastic model for the matrix, while the analytical predictions are based on linear elasticity, the agreement is consistent with the isotropic constitutive model. Unlike $\theta_h = 0^\circ$, the DFH architectures with different pitch angles θ_h provide more compliant in-plane behavior. Note that some differences between theory/FEA and experimental measurements are apparent when θ_h is smaller than 45° . This may be partially induced by the distinct components of extensional-bending coupling in the tested asymmetric laminate.

The maximum logarithmic strain distributions for the DFH with $\theta_h = 30^\circ$ obtained from the FEA are plotted lamina-by-lamina in Figure 2.2(c). We can observe that the logarithmic strain is distributed evenly in the matrix along the gauge section, which implies finite sample size effects can be neglected. According to the strain distribution at the top surface of the DFH $\theta_h = 30^\circ$, both FEA and experimental results display large strains in the region between fiber ends (red color), Figure 2.2(d). Less prominent matrix strains between parallel fibers are also observed (blue color), up to 25% lower than the matrix strains between fiber ends.

2.3.3 Mechanisms giving rise to strain stiffening

As discussed before, region II of the stress-strain curve is characterized by a strain stiffening behavior, i.e., $\Gamma > 1$. A comparison between experiments and FEA predictions is shown in Figure 2.2(e). We note that the FEA results exhibit a similar trend as that measured in experiments, both achieving a peak value when $\theta_h = 60^\circ$, although the strain stiffening is less prominent in FEA since the 3D printed matrix material employed in experiment exhibits a slightly different behavior at large strains. We surmise that the difference between FEA and experiment in terms of absolute values of Γ is due to the 3D printed material for matrix. While our model assumes isotropic behavior, the 3D printed material is anisotropic. The detailed explanation and comparison between experiment and FEA is addressed in *section S1* (See. Fig. S2 for example). Besides, the reason why $\theta_h = 60^\circ$ shows the largest difference on Γ can be explained by the fact that the individual layer $\theta = 60^\circ$ in $\theta_h = 60^\circ$ undergoes significant global transverse contraction than the individual layer $\theta = 60^\circ$ in $\theta_h = 30^\circ$ for instance, and therefore, there is more local shear deformation between fibers in the matrix leading to a larger strain stiffening. On the other hand, a likely source for such stiffening is fiber reorientation towards the loading direction, as

hypothesized by Zimmermann et al., (2013). Hence, we quantify fiber reorientation caused by stretching, $\Delta\theta_c$, in the DFH with $\theta_h = 30^\circ$, by tracking the coordinate of the individual fibers, in each lamina, in their undeformed and deformed configurations. The averaged fiber reorientation values as a function of strain and fiber orientation in each lamina, are plotted in Figure 2.2(f), where positive value indicating that fibers rotating toward the loading direction. It is observed that $\Delta\theta_c$ of laminae with small misorientation, such as θ_{30} and $\theta_{150} = \theta_{-30}$, show higher values than the laminae with larger misorientation, such as θ_{60} and $\theta_{120} = \theta_{-60}$. Moreover, the $\Delta\theta_c$ for fibers along θ_0 and θ_{90} is close to 0 as expected. Indeed, the motion of fibers along θ_0 and θ_{90} , is translation in the loading direction, despite the significant mismatch of mechanical properties between fiber and matrix. Plots of $\Delta\theta_c$ as a function of applied strain for the DFH architecture with various fiber to matrix moduli ratios, in the range of 0.01 to 3000, are given in *section A8*. Clearly, softer matrices result in a more prominent reorientation of the fibers towards the loading direction.

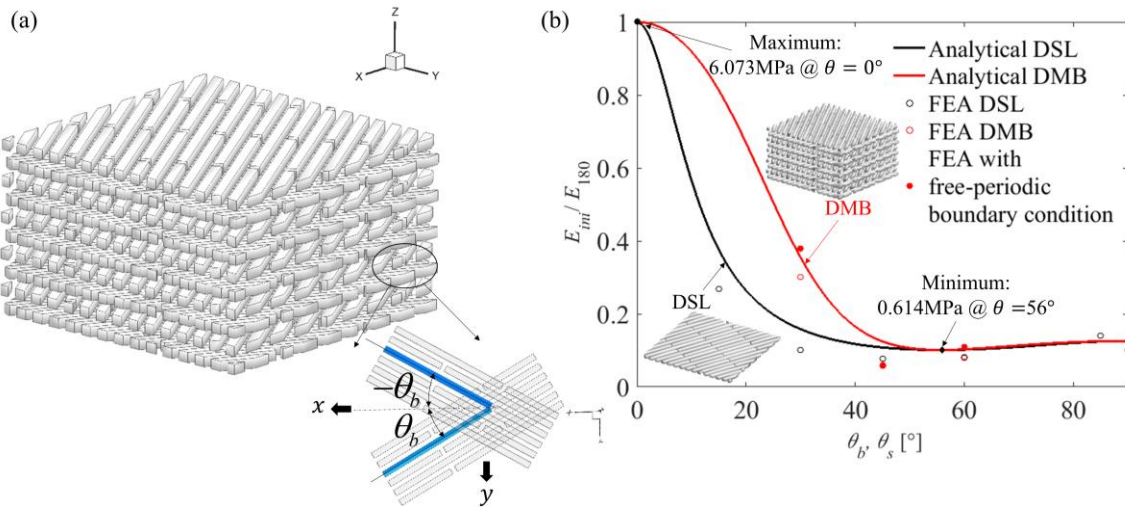


Figure 2.3. (a) DMB with absolute misorientation θ_b . Comparison of (b) Normalized FEAvand analytical results for DSLs and DMBs architectures, all with linear elastic matrix.

While our FEA shows the presence of fiber reorientation in each lamina of the DFH architecture, the effects of the composite lay-up sequence, the occurrence order of lamina misorientation from bottom to top in one laminate, and matrix constitutive response needs to be fully understood to ascertain its impact. For example, a hyperelastic matrix response may also lead to strain hardening. Likewise, it is useful to compare the DFH architecture with other architectures such as discontinuous single lamina (DSL) and discontinuous mono-balanced laminate (DMB).

The DSL architecture simply comprises one lamina with one misorientation with respect to the loading axis, and the DMB architecture consists of balanced pairs of laminae, where every positive orientation is adjacent to its negative counterpart, shown in Figure 2.3(a). In a sense, the DSL architecture configuration avoids interlaminar incompatibilities in terms of deformation. Conversely, the DMB architecture exhibits a simplified lay-up sequence, with one absolute misorientation (see Figure 2.3(a)). By contrast, the DFH architecture presents a mixture of different misorientations. Simply stated, the DSL architecture provides an example of unconstrained rotational behavior, while the DMB architecture exhibits a symmetrically constrained configuration, which can be compared to rotations observed in the DFH architecture. To some extent, this allows us to extract information about the fiber reorientation effect as a function of lay-up sequence.

Role of fiber reorientation

We start by comparing analytic predictions of E_{ini} for the DSL and DMB architectures. As depicted in Figure 2.3(b), both architectures exhibit the same E_{ini} when $\theta_i = 0^\circ$ and for a range of θ_i between 56° and 90° . The DMB architecture exhibits a greater stiffness than the DSL architecture with misorientations between 0° and 56° . This is due to the reduced contribution of the shear deformation due to the restriction imposed by the adjacent laminae misorientation in the DMB architecture.

Another interesting observation, which could influence the contribution of fiber reorientation to strain stiffening, is that the relation between lamina misorientation, θ_s , and E_{ini} is not linear, as shown in Figure 2.3(b). For instance, even if fibers in $\theta_s = 60^\circ$ rotate 20° toward the loading direction, reoriented at 40° , the stiffening effect would be much less than the stiffening effect of $\theta_s = 30^\circ$ rotating 10° toward the loading direction. FEA are included in Figure 2.3(b) for comparison purposes. As it can be observed, the FEA predictions are in good agreement with the analytical results. For the DMB case, the free-periodic boundary condition makes only a small difference on E_{ini} with respect to DMB architecture with free-free boundary.

We next analyze fiber reorientation and define fibers rotating toward the loading direction as positive and away as negative, as illustrated in Figure 2.4(a) and (b). Figure 2.4(c) shows the stretching-induced rotation, $\Delta\theta_c$, in the DFH architecture alongside rotation in the DMB and DSL

architectures. Each point in the figure represents the mean value of $\Delta\theta_c$, in the corresponding lamina, and the error bar is defined by the standard deviation among fibers in each lamina. It is observed that the $\Delta\theta_c$ values of each lamina in the DFH architecture are smaller than the ones obtained with the DSLs, up to 29.5% difference. Thus, the fibers in one lamina without constraint from other laminae have more freedom to rotate under uniaxial tensile. The DMB architecture with $\theta_b = 30^\circ$, $\theta_b = 45^\circ$, and $\theta_b = 60^\circ$ shows generally higher $\Delta\theta_c$ values than those in the DFH architecture with $\theta_h = 30^\circ$, $\theta_h = 45^\circ$, and $\theta_h = 60^\circ$. The maximum difference in $\Delta\theta_c$ between the DMB and the DFH architectures is observed between the individual layer θ_{45} in $\theta_b = 45^\circ$ and $\theta_h = 45^\circ$, which is 28.6%.

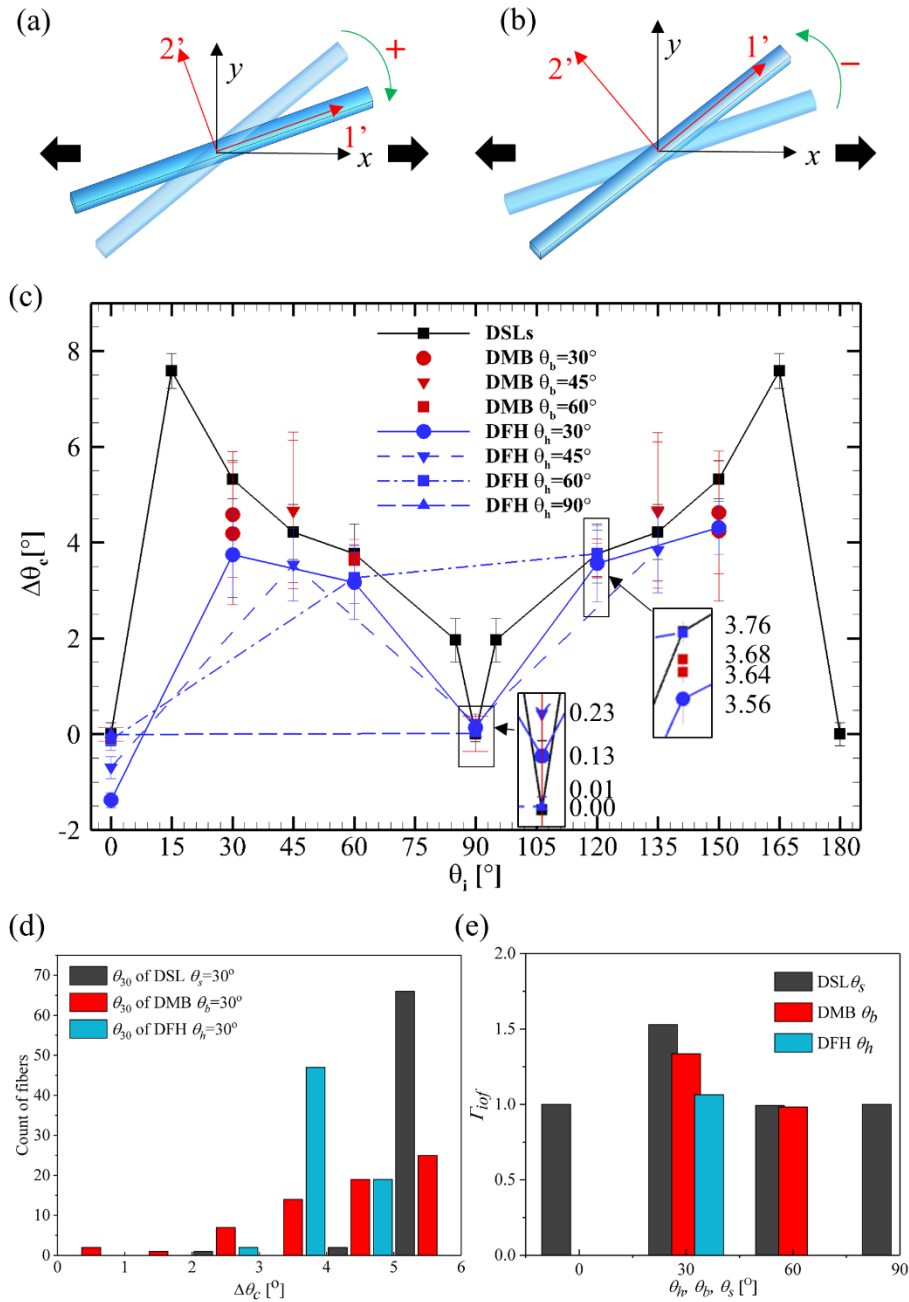


Figure 2.4. (a)-(b) Definition of direction on fibers rotation. Positive means fibers rotate toward the loading axis, whereas negative means fibers rotate away from the loading direction. The x -axis is the loading direction. 1' and 2' axes are local axes after deformation. (c) Fiber reorientation due to stretch only, $\Delta\theta_c$, of individual lamina in DFH/DMB/DSL under 10% local uniaxial strain. (d) Histogram of $\Delta\theta_c$ in lamina θ_{30} (e) Semi-analytical Γ_{iof} calculated based on $\Delta\theta_c$ in DFH $\theta_h = 30^\circ$ /DMB/DSL under 10% local uniaxial strain.

Different lay-up sequences promote distinct in-plane mechanical properties, such as Poisson's ratio and coupling coefficients, which in turn influences deformation of each lamina and

reorientation of fibers embedded in the matrix. Here we discuss the histogram of $\Delta\theta_c$ in different architectures, see Figure 2.4(d), which depicts the difference of distribution of fiber reorientation among distinct laminates. It is observed that the distribution of $\Delta\theta_c$ in $\theta_s = 30^\circ$ is concentrated between 5° and 6° , while fibers along θ_{30} of the DFH architecture with $\theta_h = 30^\circ$ shows its $\Delta\theta_c$ values between 3° and 5° . However, $\Delta\theta_c$ in the DMB architecture with $\theta_b = 30^\circ$ exhibits increasing fiber amounts with growing $\Delta\theta_c$, which could be partially explained by the specific contraction that DMB architecture undergoes.

The direct correlation between fiber reorientation and stiffness variation is obtained by using a semi-analytical method. E_i can be obtained by considering the lay-up sequence, before deformation, in the CLPT model, and then calculated as $1/h\overline{S_{11}}$, where h is the height of the laminate and $\overline{S_{11}}$ is the in-plane component of compliance matrix in the first row and first column. An averaged fiber reorientation can be obtained by computing the angle between fiber orientations before and after deformation from the FEA. Next, the new deformed lay-up sequence is calculated by using the initial fiber orientation to subtract the averaged fiber reorientation values, when the initial fiber orientation is less than or equal to 90° . When the initial fiber orientation is larger than 90° , we consider sum of the initial fiber orientation and fiber reorientation values as new deformed fiber orientation. E_{max} can then be computed by the new deformed lay-up sequence combined with CLPT. The calculation procedure is the same as the one used for E_i . Finally, the values of Γ_{iof} for $\theta_b = 30^\circ, 60^\circ$ and $\theta_s = 0^\circ, 30^\circ, 60^\circ, 90^\circ$ (associated laminae of the DFH $\theta_h = 30^\circ$) are shown in Figure 2.4(e) in comparison with DFH architecture with $\theta_h = 30^\circ$.

The bar chart shows that DMB $\theta_b = 30^\circ$ and DSL $\theta_s = 30^\circ$ stiffen more than the DFH architecture with $\theta_h = 30^\circ$, up to 30.4%, under the same uniaxial tensile stretch. Other laminates, $\theta_s = 0^\circ, 60^\circ, 90^\circ$ and $\theta_b = 60^\circ$, show negligible stiffening, compared with $\theta_s = 30^\circ$ and $\theta_b = 30^\circ$. This could be explained by the trends shown in Figure 2.3(b), in which no strain stiffening is expected once θ_s is larger than 56° , unless very large $\Delta\theta_c$ occur. Thus, based on these observation, it is possible to conclude that the reason why the DFH architecture with $\theta_h = 30^\circ$ exhibits lower stiffening (Γ_{iof}) is because it shows smaller values of $\Delta\theta_c$ in each lamina, when compared to corresponding lamina misorientation in DSL ($\theta_s = 30^\circ$ and $\theta_s = 60^\circ$) and DMB ($\theta_b = 30^\circ$ and $\theta_b = 60^\circ$) architectures.

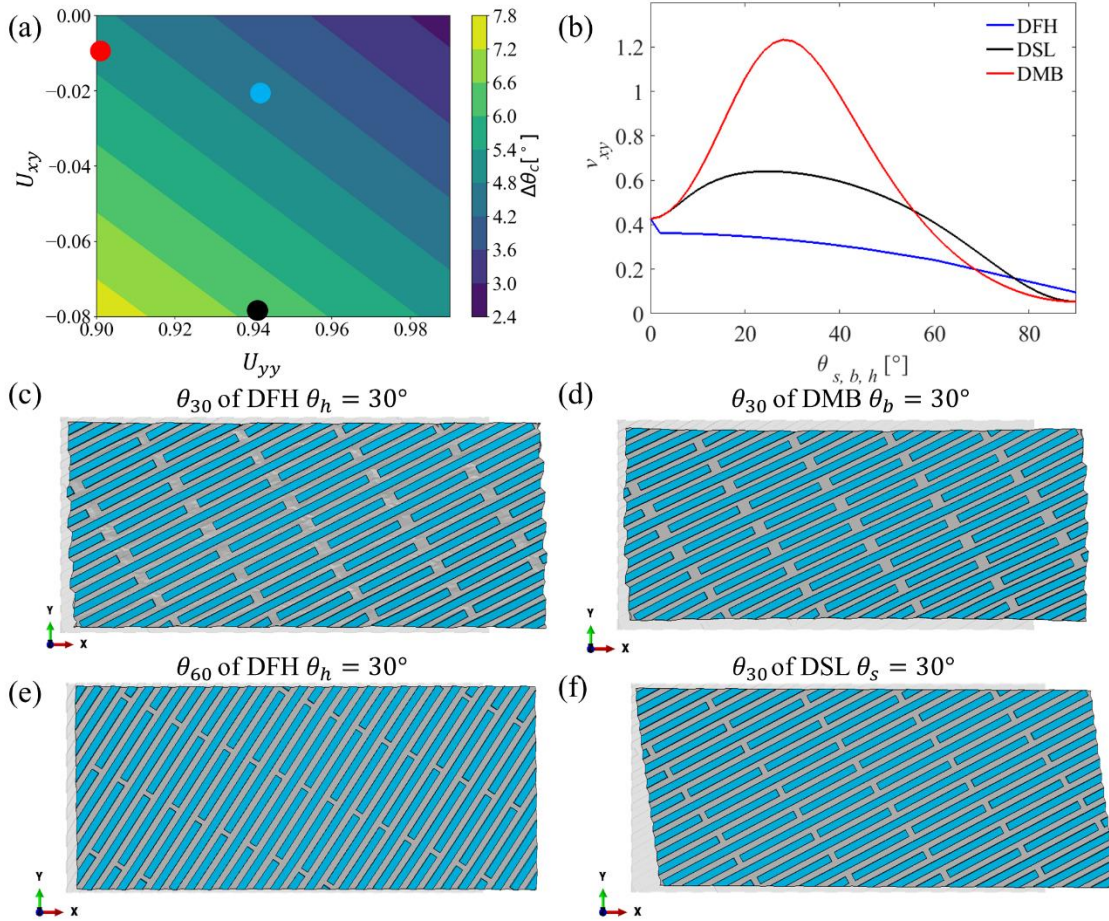


Figure 2.5. (a) $\Delta\theta_c$ as a function of misaligned angle θ_i (b) Colormap of $\Delta\theta_c$ as a function of U_{12} and U_{22} , where red dot represents for lamina θ_{30} in DMB $\theta_b = 30^\circ$, black dot represents for lamina DSL $\theta_s = 30^\circ$, and blue dot represents for lamina θ_{30} in DFH $\theta_h = 30^\circ$ (c) Configuration of individual layer θ_{30} of DFH $\theta_h = 30^\circ$ (d) Configuration of individual lamina θ_{30} of DMB $\theta_b = 30^\circ$ (e) Configuration of individual layer θ_{60} of DFH $\theta_h = 30^\circ$ (f) individual layer θ_{30} of DSL $\theta_s = 30^\circ$, before(light grey) and after deformation(darker grey for matrix and blue for fibers)

Explanation on fiber reorientation based on mechanism

We now look into potential mechanistic explanations on fiber reorientation and its contribution to strain stiffening based on the anisotropic behavior of the different laminae and their individual in-plane shear and transverse contraction deformation induced by the uniaxial load. Using the polar decomposition method, an analytical expression for $\Delta\theta_c$ as a function of in-plane components of the stretch tensor, \mathbf{U} , can be derived. Consider a unit vector describing fibers in the undeformed configuration with orientation, θ , namely, $\bar{v}_0 = (\cos\theta, \sin\theta)$. If \bar{v} is the vector in the

deformed configuration, \bar{v} and \bar{v}_0 are related by $\bar{v} = \mathbf{U} \cdot \bar{v}_0$ (Reddy, 2013) with the angle between them given by $\cos\Delta\theta_c = \frac{\bar{v} \cdot \bar{v}_0}{|\bar{v}| |\bar{v}_0|}$, or

$$\Delta\theta_c = \arccos \left\{ \frac{[\cos^2\theta U_{xx} + \sin^2\theta U_{yy} + 2\sin\theta \cos\theta U_{xy}]}{\sqrt{(U_{xx}\cos\theta + U_{xy}\sin\theta)^2 + (U_{xy}\cos\theta + U_{yy}\sin\theta)^2}} \right\} \quad (2.2)$$

where U_{xx} , U_{yy} , and U_{xy} are the in-plane components of the \mathbf{U} . A close examination of Figure A5(d) reveals that the theoretical prediction of $\Delta\theta_c$ is in close agreement with the results obtained by FEA and those calculated from whole laminate deformations. A color map of $\Delta\theta_c$, as a function of the individual stretch tensor components can be constructed using equation (2.2), as shown in Figure 2.5(a). Moreover, the $\Delta\theta_c$ of each individual lamina for various architectures can be analyzed based on the components of the stretch tensor obtained from simulations. For example, the $\Delta\theta_c$ of the individual lamina θ_{30} in the DMB $\theta_b = 30^\circ$ (shown as a red dot in left-top corner of the color map in Figure 2.5(a)) implies that transverse contraction, rather than in-plane shear deformation, U_{xy} , is the one promoting fiber reorientation in the architecture. This result is consistent with the prediction of the CLPT model for balanced architecture, in which the extensional-shear coupling components are zero, i.e., no in-plane shear deformation due to uniaxial tension (Carlsson et al., 2014). By contrast, the $\Delta\theta_c$ of the DSL with $\theta_s = 30^\circ$ (shown as a black dot in Figure 2.5(a)) primarily results from U_{xy} , 8.15 times higher than the U_{xy} value of θ_{30} in DMB $\theta_b = 30^\circ$, and moderately results from transverse contraction, U_{yy} , 42.2% lower than the one of DMB architecture. Interestingly, when comparing the DMB architecture to the DSL $\theta_s = 30^\circ$, the former exhibits a 93.4% higher value of the effective Poisson's ratio, ν_{xy} , see Figure 2.5(b). The DFH architecture exhibits a behavior in which both in-plane shear deformation and transverse contraction are smaller, blue dot in Figure 2.5(a). Less shear deformation than corresponding DSL architectures is because in the DFH architecture, for each lamina with misorientation θ , there is always a lamina with misorientation $-\theta$. Accordingly, at the laminate level, the DFH architecture also satisfies the balanced laminate condition, which means no in-plane shear deformation due to uniaxial tension. On the other hand, unlike the DMB architecture composed of multiple laminae with one absolute value of misorientation, indicating compatible properties lamina by lamina, the DFH architecture is composed of multiple laminae with different absolute values of misorientation, which means incompatible properties lamina by lamina. Therefore, the DFH architecture cannot reach as high transverse contraction as the DMB

architecture, and then the individual lamina with different θ in the DFH architecture will rotate less than the corresponding DSL and DMB architectures, see Figure 2.5(b) and Figure A7. The global deformation of the DFH, DMB, and DSL architectures is illustrated in Figure 2.5(c-f) and the deformation magnitudes of the different architectures, under the same uniaxial tensile strain, are tabulated in Table A1.

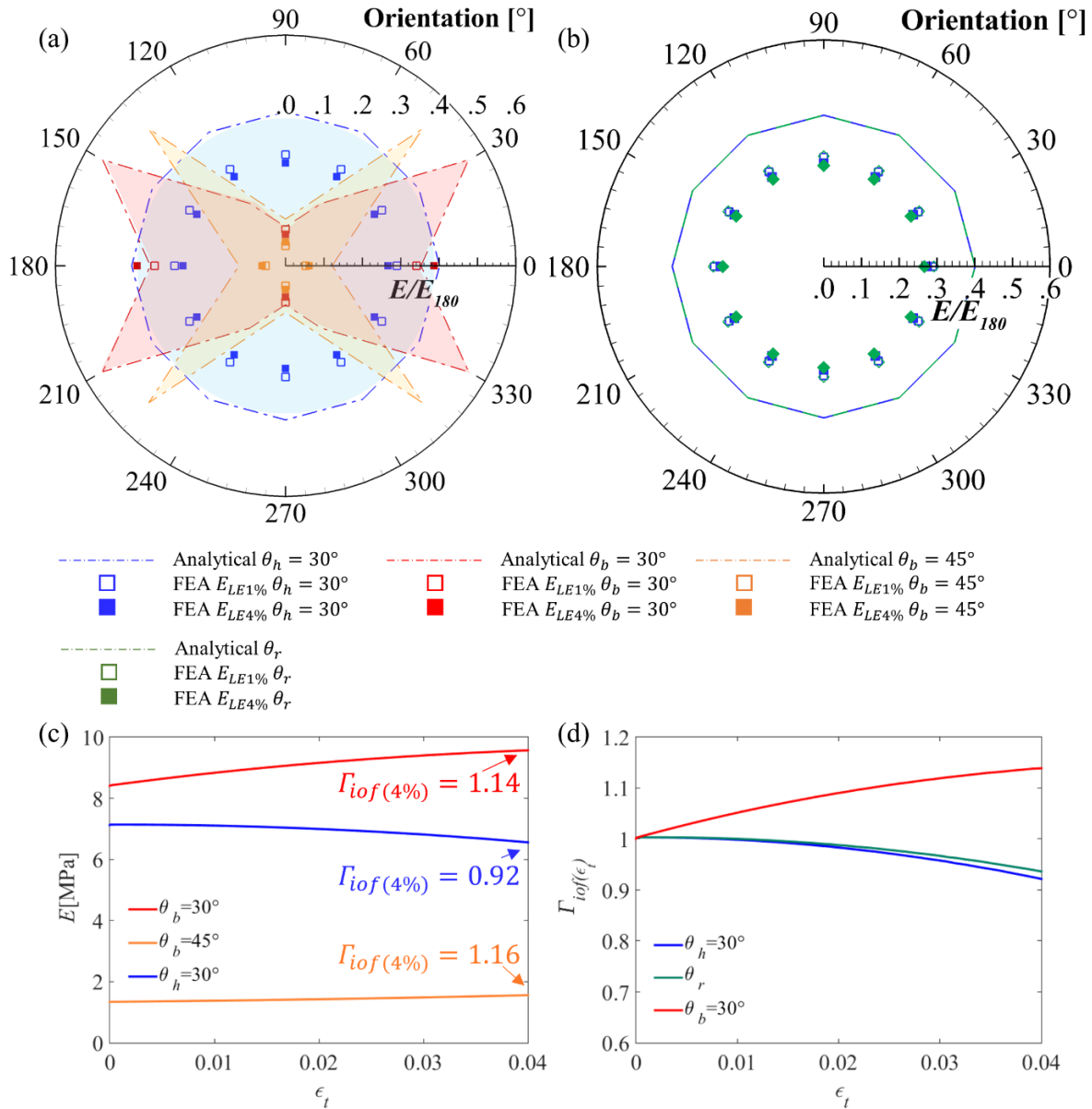


Figure 2.6. FEA predictions on elastic modulus of laminates with linear elastic matrix deformed within 1% local true strain, ϵ_t , ($E_{LE1\%}$) and at ~4% ϵ_t ($E_{LE4\%}$). Analytical predictions are based on the CLPT model. (a) Comparison among $\theta_h = 30^\circ$, $\theta_b = 30^\circ$ and $\theta_b = 45^\circ$ (b) Comparison between $\theta_h = 30^\circ$ and the disorder architecture with lay-up sequence [30/150/60/120/0/90/30] (c) Elastic modulus as a function of local true strain, ϵ_t . (d) Stiffening parameter $\Gamma_{iof}(\epsilon_t)$ as a function of ϵ_t .

Role of matrix mechanical behavior

In the previous section, we studied the correlation between $\Delta\theta_c$ and strain stiffening, Γ_{iof} , by using a semi-analytical method and examining the $\Delta\theta_c$ distribution computed for different architectures. In this section, we investigate the effect of matrix constitutive behavior on strain stiffening. We begin by analyzing a linear elastic matrix and conclude with the analysis of an elasto-plastic matrix.

In analyzing the effect of a linear elastic matrix, a maximum local true strain $\epsilon_t = 4\%$ is used for comparing various laminates. The local strain is based on the deformation at two ends of the gauge region, u_{gauge}/L_{gauge} whereas the global(applied) strain, ϵ , is calculated by the applied deformation at the end of dog-bone sample, $u_{applied}/L_{gauge}$. A free-periodic boundary condition is applied to all FEA in this section. Moreover, it is important to note that the fiber reorientation values for the DFH and the DMB architectures with linear elastic matrix are the same as the fiber reorientation values computed for the DFH and the DMB architectures with hyperelastic matrix, see *section A10*.

The normalized elastic modulus, along various orientations, for the $\theta_h = 30^\circ$ and $\theta_b = 30^\circ$ architectures, at $\epsilon_t = 1\%$ ($E_{LE1\%}$), and at 4% ($E_{LE4\%}$), are plotted in Figure 2.6(a). By contrast, FEA and analytical predictions are in close agreement for the DMB architectures, 3.95% difference for $\theta_b = 30^\circ$ in both longitudinal and transverse directions. The normalized elastic modulus for the DFH architecture with $\theta_h = 30^\circ$, for both $E_{LE1\%}/E_{180}$ and $E_{LE4\%}/E_{180}$ are smaller than the analytical prediction. This is the case, because in the FEA, the DFH architecture is modeled by discontinuous fibers, resulting in localized failure (fiber end-matrix debonding). As expected, the DFH architecture presents close to in-plane isotropic behavior on elastic modulus, whereas the $E_{LE1\%}$ of $\theta_b = 30^\circ$ is relatively large only in the direction close to the initial lamina misorientation 30° . The $E_{LE1\%}$ of the $\theta_b = 30^\circ$ along the longitudinal direction is three times and a half over the $E_{LE1\%}$ in transverse direction.

We next examine $\Gamma_{iof(4\%)}$, where $\Gamma_{iof(4\%)}$ is defined as the strain stiffening of architecture finally deformed under 4% of ϵ_t in uniaxial direction (subscript “4%” means 4% of ϵ_t), and $\Gamma_{iof(\epsilon_t)} = E_{max}(\epsilon_t)/E_i$, value E_{max} as a function of ϵ_t over E_i . In Figure 2.6(c), although $\theta_b = 45^\circ$ shows the maximum $\Delta\theta_c$ and strain stiffening $\Gamma_{iof(4\%)} = 1.16$, compared with $\theta_b = 30^\circ$ and $\theta_h = 30^\circ$, the $E_{LE1\%}$ of $\theta_b = 45^\circ$ is only 18.8% of the value of $\theta_h = 30^\circ$ both in the longitudinal

and transverse directions. Although a small stress softening value ($\Gamma_{iof(4\%)} = 0.92$) is exhibited by the DFH architecture, isotropic stiffness is achieved.

It is important to understand if the specific lay-up sequence of the DFH architecture can influence $\Delta\theta_c$ and strain stiffening and thus, we consider a disorder laminate $\theta_r = [30/150/60/120/0/90/30]$, which contains the same associated laminae but different lay-up sequence from $\theta_h = 30^\circ$. θ_r is representative of other alternative laminates with different lay-up sequences, since E_i calculated by CLPT is independent on the lay-up sequence, shown in *section A11*. In Figure 2.6(b), the elastic modulus of disorder laminate θ_r before and after deformation, compared with $\theta_h = 30^\circ$ is shown. It is observed that the values of E_i of θ_r and $\theta_h = 30^\circ$ show close agreement on both analytical prediction and FEA. However, the $\Gamma_{iof(4\%)}$ of θ_r due to difference on fiber reorientation, see Figure A18 of *section A11*, is 1.44% higher than the value of $\theta_h = 30^\circ$, as depicted in Figure 2.6(d). This means that different lay-up sequence does influence the stiffness variation caused by fiber reorientation. However, compared with the strain stiffening $\Gamma_{iof(\epsilon_t)}$ of the DMB $\theta_b = 30^\circ$, Figure 2.6(d), the difference between θ_r and DFH $\theta_h = 30^\circ$ is negligible.

The above results show that the strain stiffening of the DFH architecture in the experimental system is mostly the result of the hyperelastic properties of the matrix, since in this section we show that fiber reorientation in the DFH architecture is constrained by the specific lay-up sequence and therefore strain stiffening was not predicted, which is consistent with the explanation in section of “Explanation on fiber reorientation based on mechanism” and the analytical prediction in Figure 2.4(e).. Moreover, we investigated the effect of an elasto-plastic matrix to replace the linear elastic matrix for the DFH architecture with $\theta_h = 30^\circ$, large strains, and found no strain stiffening either, see *section A12*.

2.4 Conclusions

This work examines the mechanical properties of a hybrid architecture, the Discontinuous Fiber Helicoid (DFH), which takes inspiration from a regular helicoid composite and a ‘brick and mortar’ architecture. The combination of these two motifs gives rise to some unique composite mechanics. Like the regular helicoid, each unidirectional lamina is highly anisotropic due to the

alignment of the fibers. However, the elastic behavior of whole helicoidal laminate is transversely isotropic.

The properties of DFH architecture are a function of the geometry and the property of its constituents. Among the dominant geometrical features, we can mention pitch angle, θ_h . Constitutive properties, such as the fiber to matrix stiffness ratio, as well as the matrix nonlinear behavior, are relevant as they relate to strain stiffening and overall failure. To deconvolve the various effects, we examined various architectures, namely DFH/DMB/DSL, to gain insights into the contribution of deformation to fiber reorientation, $\Delta\theta_c$, as it relates to lamina misorientation with respect to the loading direction and lay-up sequence.

- We found that the DFH architecture exhibits less in-plane shear deformation and less transverse contraction leading to smaller values of fiber reorientation, $\Delta\theta_c$, compared with the DMB and DSL architectures. We compared and quantified $\Delta\theta_c$ in individual laminae from different architectures. For instance, we found that the individual lamina θ_{30} of the DFH $\theta_h = 30^\circ$ exhibits up to 29.5% lower $\Delta\theta_c$ than found in the DSL $\theta_s = 30^\circ$ upon 15% ϵ . On the other hand, the θ_{45} lamina in the DMB architecture exhibits 28.6% higher value of $\Delta\theta_c$ than the θ_{45} lamina in the DFH with $\theta_h = 45^\circ$. In fact, the DFH architecture, due to its overall balanced lay-up sequence, exhibits smaller in-plane shear deformation than the DSL architecture and less contraction in the transverse direction than the DMB architecture. The DMB $\theta_b = 30^\circ$ exhibits a 93.4% higher v_{xy} than the DSL architecture with $\theta_s = 30^\circ$. This is due to its compatible mechanical properties among balanced laminae.
- The analysis reported in this study revealed that the DFH architecture, with a linear elastic or elasto-plastic matrix with small plastic hardening, shows negligible strain stiffening, compared with the DMB architecture, under uniaxial tensile loading, whereas the DMB architecture, show superior strain stiffening compared with DFH architecture (up to 16% under 4% local ϵ_t and 33.6% under 10% local ϵ_t). Furthermore, evidence that no strain stiffening shown in the FEA with linear elastic matrix and very small values obtained from the plate theory indicates that the strain stiffening observed in 3D printed samples is primarily due to the hyperelastic constitutive response of the matrix.
- Although the DFH architecture and the disorder laminates show the same elastic modulus before deformation, their fiber reorientation and strain stiffening values are slightly different after the same tensile strain (4% local ϵ_t). This observation confirms that lay-up

sequence influences the deformation in each lamina through the thickness and thus, has an impact on the fiber reorientation behavior.

In closing, we have provided a rigorous analytical, experimental, and computational analysis of deformation and strain stiffening for a variety of discontinuous fiber architectures, which should be valuable for the design of composite materials in which tailoring of constitutive behavior, following some inspiration from these natural materials, can lead to better mechanical performance. The DFH architecture exhibits some interesting mechanical behavior, which can be employed in some specific applications. For example, helicoidal composites with compliant matrix and stiffer fibers can find applications where isotropic elastic properties are required under general and relatively low loads, but higher strength and toughness, along the loading direction, under higher loads.

3. ON THE 3D ARCHITECTURE OF NATURALLY OCCURRING LAMELLAR STRUCTURES: A COMPARATIVE ANALYSIS

Chapter 3 is part of the publication “On the 3D Architecture of Naturally-occurring Lamellar Structures. A Comparative Analysis”, (2020), Status: In progress

In addition to the fiber reinforced laminate materials, nacreous lattice structure, shown in Figure 3.1(c), can endure high toughness without sacrificing strength. In Chapter 3, we plan to compare tablet-like architecture found in the nacreous layer of the abalone shells and the rod-like microstructure of the radula teeth of Chiton, Figure 3.1(a), through different dimensionless parameters. Previous studies have provided insightful information on how these structures promote certain mechanisms. However, few of them focus on three-dimensional representations. In this work, we present a detailed comparative analysis that looks at the three-dimensional geometries of the rod-like and tablet-like structures. We 3D print and test rod-like and tablet-like architectures and analyze the results employing a computational and analytical micromechanical model under a dimensional analysis framework. In particular, we focus on the stiffness, strength and toughness of the resulting structures. Our preliminary results show that besides volume fraction and aspect ratio of the building blocks, the specific shear area governs the mechanical behavior of these microstructures. In turns, this leads to the conclusion that rod-like microstructures exhibit better performance than tablet-like microstructures when the architecture is subjected to uniaxial load. However, rod-like microstructures tend to be much weaker and brittle in the transverse direction. On the other hand, tablet-like architectures tend to be a much better choice for situations where biaxial load is expected.

3.1 Introduction

Biological composite materials, combination of stiff mineralized inclusions and compliant biopolymers, are ubiquitous in nature. Living organisms ingeniously evolve these architectural materials to perform remarkably under specific circumstances for survival. One of the examples is the nacreous microstructures in the inner layer of seashells of Mother-of-pearl (nacre), staggered tablet-like architectures, shown in Figure 3.1(c). Its mechanical properties are far superior to its constituents, ceramic and protein (Barthelat et al., 2007; Chintapalli et al., 2014; Pro et al., 2015;

Salinas and Kisailus, 2013; Sun and Bhushan, 2012b; Yaraghi and Kisailus, 2018; Zhang et al., 2010b). Another example is the radular teeth of the gumboot Chiton, shown in Figure 3.1(a), which consist of biomineralized rod-like magnetite fibers and soft organic material. Through controlling the interface strength between fibers, the possibility of catastrophic failure can be decreased and therefore the Chiton tooth is able to achieve impressive abrasion resistance (Escobar de Obaldia et al., 2016). Studies on the microstructures of Stomatopod dactyl club (Grunenfelder et al., 2014b; Weaver et al., 2012), crab shell (Cheng et al., 2008b; Yao et al., 2013), fish scale (Murcia et al., 2017b; Zimmermann et al., 2013) and cuticles of beetles (Vargas et al., 2016; R. Yang et al., 2017) reveal that they are composed of biomineralized fibers reinforced laminates. Each lamina rotates a specific angle through the thickness to accomplish 180° rotation. This architecture, denoted helicoid architecture, displays high-energy dissipation during impact and crack propagation by amplifying the surface area per unit crack length (Weaver et al., 2012).

These superior mechanical properties of biological composite materials stimulate scientists and engineers to design and fabricate bio-inspired materials which can provide similar properties that biological materials have. “Brick and mortar” architecture can represent three-dimensional(3D) tablet-like and rod-like architectures by simplifying inclusions from 3D to 2D as staggered 2D brick tablets, shown in Figure 3.1(b). Shear-lag analytical model is ubiquitously used to predict the mechanical properties of “brick and mortar” architecture (Sakhavand and Shahsavari, 2015; Wei et al., 2012), allowing large shear deformation in the matrix, which is sandwiched by two stiff tablets. Tension-shear chain (TSC) model (Gao, 2006; Ji and Gao, 2004) illustrates the tensile deformation resistance of “brick-and-mortar” architecture through passing normal stress in discontinuous-stiff tablets and transferring shear stress in compliant matrix. Volume fraction (V_f) and aspect ratio of inclusions (L/M) are two key parameters to predict the mechanical properties of “brick and mortar” model.

Shear-lag and TSC models assume plane strain condition for 2D analytical model, indicating infinite thickness out of plane. However, the inclusion of biological composite material is discontinuous out of plane and it also exhibits distinct geometries, such as rod-like and tablet-like architectures from microstructures in the chiton tooth and in the seashell of nacre respectively, shown in Figure 3.1(d). Seashell of nacre is the protective layer of interior-soft material, able to resist exterior multiaxial loading, impact load and penetration, while Chiton teeth is used to rasp to expose algae growing on the surface of hard rocky substrates (Escobar de Obaldia et al., 2016).

Their functionalities are different and therefore the morphologies of the macro geometries and micro-structure are distinct. In the present paper, we are trying to understand why nature chooses rod-like architecture to resist longitudinal normal loading and uses tablet-like architecture to endure multiaxial loading. To accomplish this analysis, extending 2D to 3D model is necessary and not only V_f and L/M should be considered in the analysis, but also effective shear A_s and tension area A_t needs our attention.

The present paper extends the 2D analytical model (shear-lag combined with tension effects from matrix) to 3D and then compare the predicted mechanical properties, stiffness, strength and toughness, under longitudinal and transverse uniaxial tensile loading with corresponding experiments and finite element analysis (FEA) in 3D. To compare two architectures at the same level, dimensionless parameters are designed, including V_f and L/M .

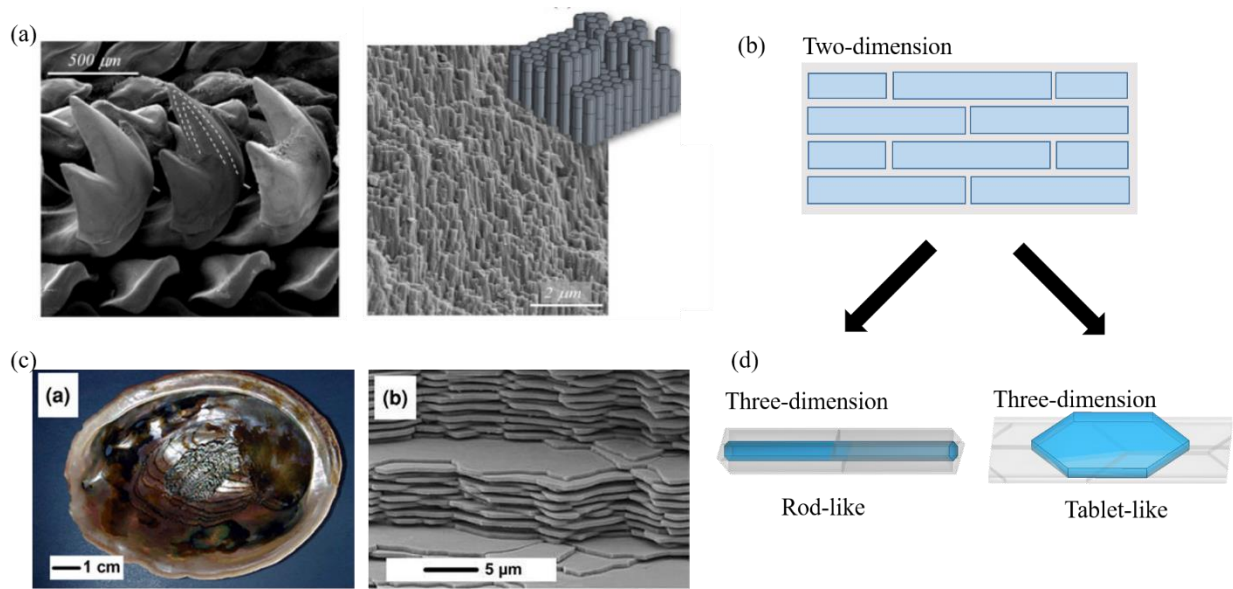


Figure 3.1 (a) SEM micrograph showing the radula teeth of Chitons and its rod-like microstructure (de Obaldia et al., 2015) (b) Basic 2D shear lag model. (c) California red abalone with pearlescent interior of nacre and the micrograph of its nacreous tablet-like microstructure (Salinas and Kisailus, 2013). (d) Biomimetic 3D rod-like and tablet-like inclusions

3.2 Problem formulation

3.2.1 Three-dimensional architectures

We designed two 3D architectures based on the microstructures of biological materials, inner layer of nacre and radular teeth of Chitons. Tablet-like 3D architecture, bio-inspired by the microstructure of nacre, is composed of in-plane hexagon tablets, exhibiting staggered pattern through the thickness, shown in Figure 3.2(a) and (b). We are going to apply uniaxial tensile in the longitudinal direction (along x -axis) and in transverse direction (along y -axis) to study the stiffness, strength and toughness behavior of this bio-inspired tablet-like architectures. Different from 2D shear-lag model, architectures in 3D are featured with effective shear area and tension area, dependent on 3D geometry and arrangement of the reinforcement, to resist the uniaxial deformation in longitudinal direction. As shown in Figure 3.2(c), matrix above and below hexagon tablets (blue) are under shear deformation and the matrix between two tablets in-plane (yellow) is under tension deformation when the whole architecture is under uniaxial tensile. Because of periodicity of the representative volume element (RVE), we extract one hexagon tablet and three tablets from adjacent top and bottom layers separately, see Figure 3.2(c). In further step, due to geometrical symmetry in z direction of this unit cell, only half of the thickness is considered in our analytical analysis, shown as the region enveloped in red curve in Figure 3.2 (c). The volume of the unit cell is V_{cell} , including tablets and surrounded matrix. The other architecture is rod-like structure bio-inspired by the microstructure of Chitons teeth, shown in Figure 3.2(d) and (e). Similar as the arrangement pattern of tablet-like architectures, we staggered adjacent columns of fibers by 50% of the length of one RVE, which including one fiber and surrounded matrix. The unit cell of rod-like architecture is half length of the RVE in the longitudinal direction due to symmetry geometry, shown in Figure 3.2(f). In rod-like architecture, effective shear zone (blue) are the matrix between two fibers with 50% off-set in their longitudinal direction, whereas the tension zone (yellow) are the matrix between two aligned fibers, shown in Figure 3.2(f). The detailed calculation of effective shear (A_s) and tension area (A_t) are described in appendix B.

We introduce the length in longitudinal direction of both tablet and rod reinforcements as L , the thickness of hexagon tablet as M while the M of the rod-like architecture is the distance between two parallel edges of hexagon cross-section, shown in Figure 3.2(c) and (f). The matrix gap between reinforcements is t . We denote w_n and w_c as the edge length of hexagon of tablet-

like and rod-like architectures separately. The dimensions of each sample we tested are tabulated in Table 3.1.

Besides aspect ratio (L/M) and volume fraction (V_f), two key parameters for 2D theoretical model, we assume that A_s and A_t are another two critical parameters necessary to be considered in 3D when we consider the effective mechanical property of rod-like and tablet-like architectures.

3.2.2 Prerequisite and loading conditions

When 3D tablet-like nacreous architecture is in comparison with rod-like chiton architecture, both two architectures are with the same V_f and L/M , which are the key parameters of 2D shear-lag model. We designed two sets of experiments under uniaxial tensile loading condition in longitudinal and transverse directions respectively to investigate the mechanical properties of tablet-like and rod-like architectures, shown in Figure 3.2 (a) and (d).

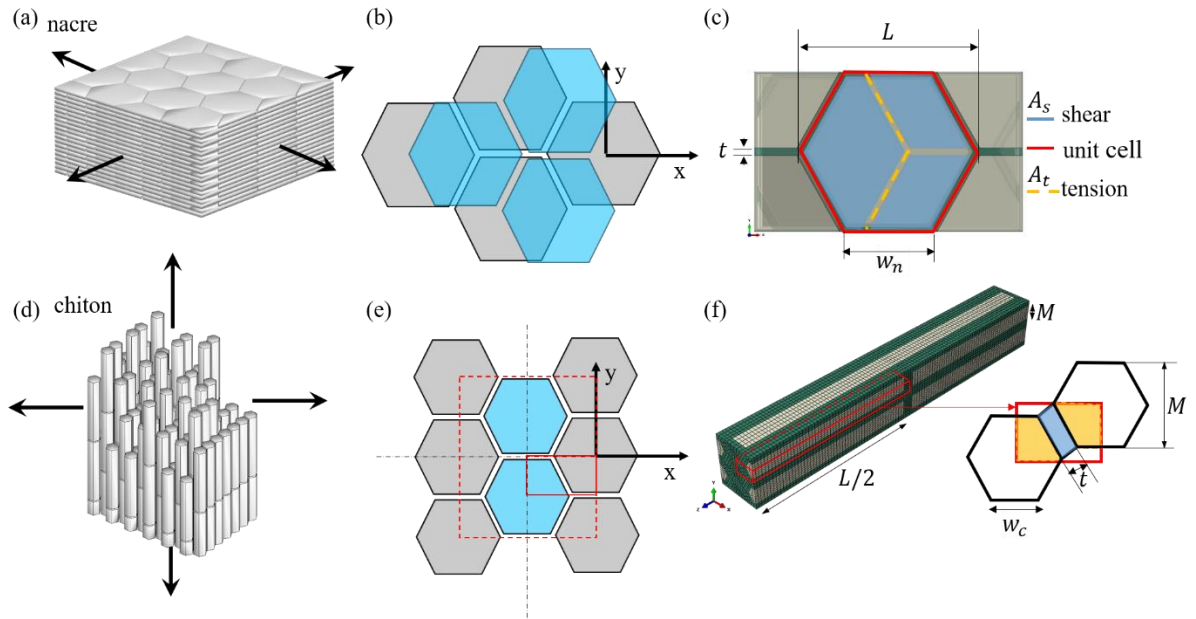


Figure 3.2. (a) Biomimetic 3D tablet-like structures. (b) General top view of the hexagon tablets. (c) model of one unit cell and its effective shear and tension area. (d) Biomimetic 3D rod-like architecture. (e) Cross-section design of 3D rod-like structures. Hexagons with grey color and with blue color represent that they are not in the same plane, which have 50% out-of-plane offset distance. (f) Unit cell of 3D rod-like architecture and its effect shear and tension area.

We expect there is difference between tablet-like and rod-like architectures even when they are featured with the same V_f and L/M , since their A_s and A_t are different. On the other hand, rod-

like architectures can provide less deformation resistance in transverse direction compared with its resistance in longitudinal direction, while tablet-like structures, due to its in-plane geometry, can offer close to consistent deformation resistance in both loading directions.

3.3 Materials and loading machine

3.3.1 Materials

Multi-material 3D printer (fused deposition modeling) is used to print our bio-inspired tablet-like and rod-like architectures. Stiff polymer is applied as the materials of reinforcement (fibers and tablets) and tabs, while soft elastomer is employed for matrix materials.

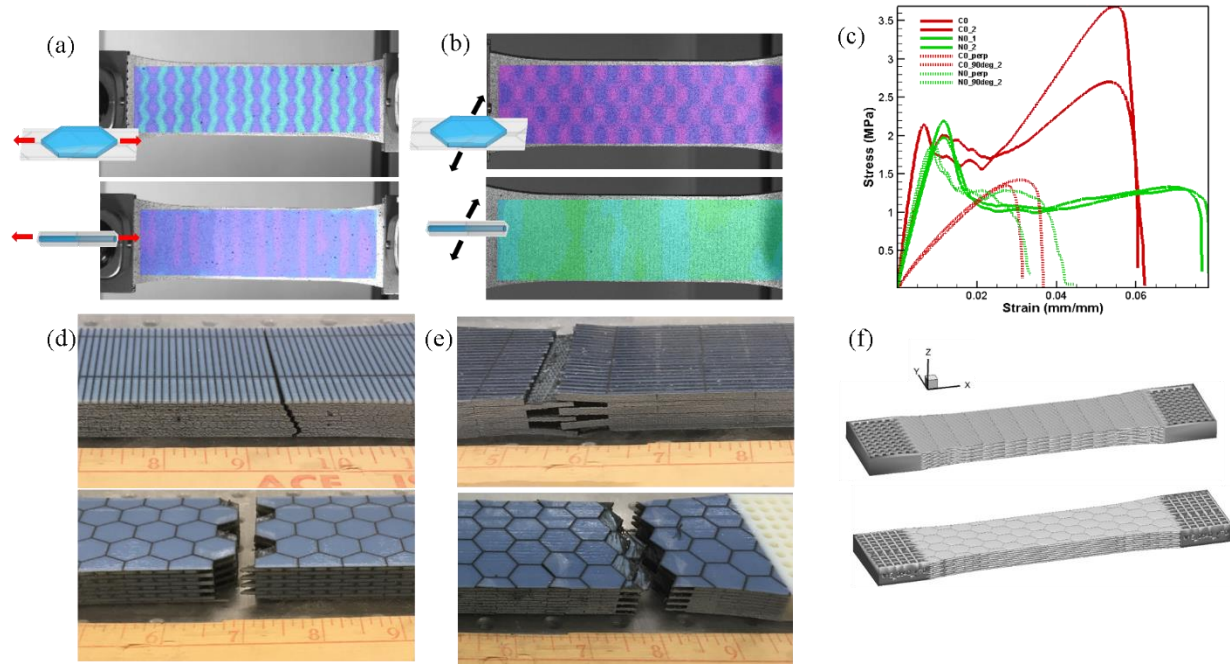


Figure 3.3. (a) DIC of 3D architectures under uniaxial tensile loading in longitudinal direction. (b) DIC of 3D architectures under uniaxial tensile loading in transverse direction. (c) Stress and strain curves of 3D rod-like and tablet-like architectures under uniaxial tensile loading in longitudinal and transverse directions. (d) The crack surface of 3D architectures after loading in transverse direction. (e) The crack surface of 3D architectures after loading in longitudinal direction. (f) The CAD file of 3D-printed samples

3.3.2 loading machine

Uniaxial tensile test is conducted with the assistance of MTS machine equipped with two mechanical grips. The loading rate is 0.2 mm/min. Digital image correlation (DIC) is in

conjunction with the uniaxial tensile loading to measure the strain distribution map, shown in Figure 3.3(a) and (b).

3.4 Results

The stress and strain curves of uniaxial tensile tests both in transverse and longitudinal directions are illustrated in Figure 3.3(c). We consider the initial slope of the stress and strain curve as stiffness E , first peak load as strength σ_y and the area enveloped under stress and strain curve as toughness T_c . The strength σ_y of 3D tablet-like architecture in transverse direction is 88.7% of its σ_y in longitudinal direction. However, σ_y of 3D rod-like architecture in transverse direction is only 30.75% of its σ_y value in longitudinal direction. The toughness of rod-like architecture in transverse direction can reach 23.08% of the toughness of rod-like architecture in longitudinal direction. Meanwhile, the toughness of tablet-like architecture in transverse direction can provide 40% of the toughness of tablet-like architecture in longitudinal direction. Both two results are under our expectation in the previous stage.

The area of fracture interface can visually explain how much energy dissipated by the materials. Both architectures under tensile exhibit similar fracture mechanism. The crack propagates through the ductile interlayer between tablets or rods through the thickness, performing crack interface like a zig-zag shape, shown in Figure 3.3(d) and (e). The samples before printing are shown in Figure 3.3(f).

It is observed that rod-like architecture behaves more beneficial in longitudinal direction than its transverse direction, which is under our expectation. The stiffness, strength (1st peak stress) and toughness of tablet-like and rod-like structures in both loading directions are summarized in Figure 3.4(a) and (b) separately. In longitudinal direction, Figure 3.4(a) shows that rod-like architecture with the same $V_f = 70\%$ and $L/M = 15$ of tablet-like architecture performs with higher stiffness and toughness, up to 43.3% and 39.2% respectively, in the longitudinal direction than the values of tablet-like architecture, though they can provide close value of strength, only 0.5% difference. This difference on stiffness and toughness is induced by distinct effective shear and tension area A_s and A_t , tabulated in Table 3.1. On the other hand, the behavior in transverse direction of tablet-like architecture exhibits robust benefit over rod-like architecture in stiffness, strength and toughness.

Based on these results, in order to confirm the influence of A_s and A_t on mechanical behaviors, we need to compare the two 3D architectures analytically by dimensionless group parameters.

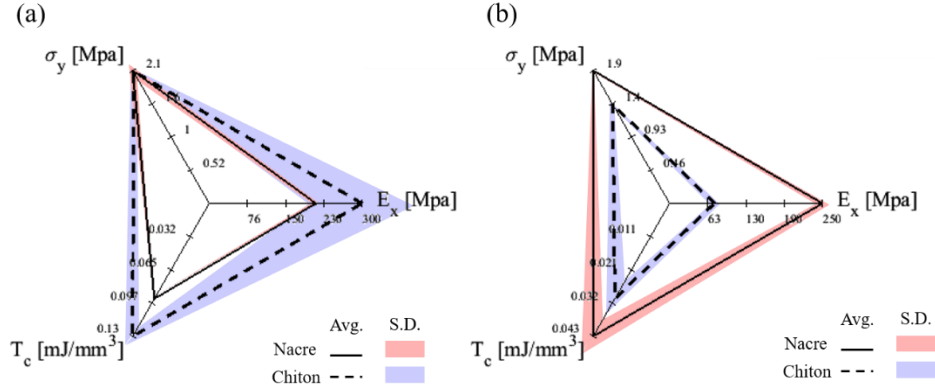


Figure 3.4. (a) Radar plot of elastic modulus, strength and toughness of 3D tablet-like nacreous and rod-like chiton architectures in longitudinal direction. (b) Radar plot of elastic modulus, strength and toughness of 3D tablet-like nacreous and rod-like chiton architectures in transverse direction.

Table 3.1. Geometrical parameters of designed samples

Name	$L(\text{mm})$	$t(\text{mm})$	$M(\text{mm})$	L/M	V_f	$\frac{A_s}{V_{cell}}(\text{mm})$	$\frac{A_t}{V_{cell}}(\text{mm})$
Nacre0	16.8	0.4	1.12	15	0.698	0.59	0.076
Chiton0	31	0.4	2.078	14.915	0.694	0.44	0.083

3.5 Analytical model and FEA

As previous study of (Zhang et al., 2015), shear-lag model was extended from 2D to 3D with hexagon cross-section, considering tension effect between fiber ends for rod-like architectures. This 3D analytical model is applied for elastic modulus prediction on our rod-like architectures bio-inspired by chiton.

$$\frac{1}{E} = \frac{1}{E_f V_f} + \frac{1}{c_m \frac{l_s}{t} + E_f V_f \frac{k}{4} \tanh\left(\frac{k}{4}\right)} \quad (3.1)$$

where $k = \sqrt{\frac{2G_m w_c l_s^2}{E_m A t}}$, $c_m = \frac{E_m(1-\nu_m)}{(1+\nu_m)(1-2\nu_m)}$, $A = \frac{1}{4} \frac{3\sqrt{3}}{2} w_c^2$

In the present paper, we can provide the analytical model of 3D tablet-like architecture based on the shear-lag model, considering the effects of tension between two aligned tablets.

3.5.1 Analytical model

One hexagon tablet and its three tablets from adjacent top and bottom layers respectively, combined with the interlayer matrix, are extracted as RVE of our analytical 3D model, shown in Figure 3.5(a). Because of its symmetry to $x_1 - x_2$ and $x_1 - x_3$ planes, the unit cell can be cut by half both in x_2 and in x_3 directions, illustrated in Figure 3.5(b). Based on the unit cell, the cross-section at the midline of the trapezoid (black dashed line in Figure 3.5(b)) is employed to represent the 3D tablet-like architecture in 2D($x_1 - x_2$ plane). The effective length of the top hexagon tablet, $l_s = \frac{3}{2} w_n - \frac{2}{\sqrt{3}} t$, of the unit cell excludes the longitudinal distance of matrix gap in between two adjacent tablets. The effective length, l_w , of the bottom tablet in the unit cell projected in $x_1 - x_2$ plan is determined by the effective shear area of the hexagon tablets.

$$l_w = \frac{A_{shift}}{A_s} l_s \quad (3.2)$$

where A_{shift} is the area enveloped by red dashed line in Figure 3.5(a), which is the overlap area of two tablets stacked along x_2 direction.

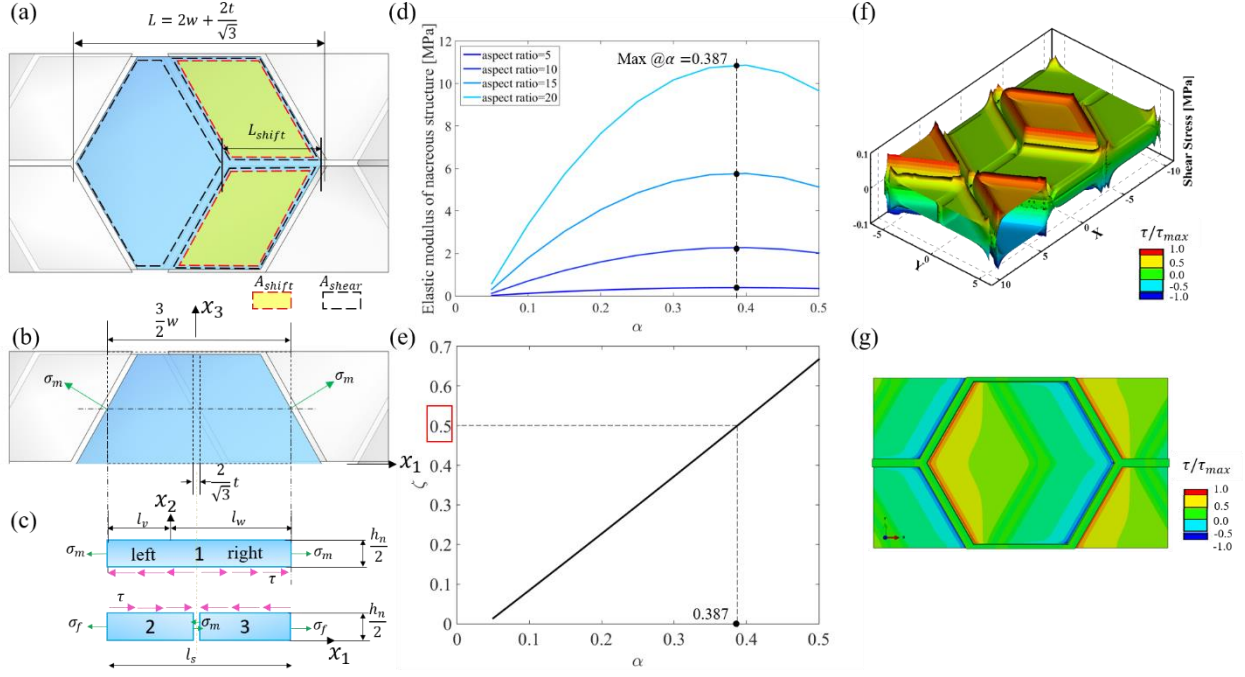


Figure 3.5. (a) Top view of 3D tablet-like structure including shift distance, shift area, effective shear area and the length of the unit cell. (b) Half of the 3D tablet-like structure with projected 2D geometry in blue color and their effective dimensions. (c) Projected 2D segments with effective length and boundary conditions. (d) Elastic modulus as a function of dimensionless parameter α . (e) Dimensionless parameter ξ as a function of α . (f) shear stress distribution map of interlayer matrix when $\alpha=0.5$. (g) shear stress distribution map of interlayer matrix when $\alpha=0.387$ and $\xi=0.5$.

Stress in tension from matrix (σ_m) and normal stress of tablets (σ_f) are applied as boundary condition of the unit cell, shown in Figure 3.5(c). Based on the analysis of free body diagram, we have

$$\int_V \frac{\partial \sigma_f(x_1)}{\partial x_1} dV = \int_A \tau(x_1) dA \quad (3.3)$$

Transfer to differential equation,

$$\frac{\partial \sigma_f(x_1)}{\partial x_1} dx_{1f} dx_{2f} dx_{3f} = \tau(x_1) dx_{1m} dx_{3m} \quad (3.4)$$

Put $dx_1 dx_3 = dA_s$,

$$\frac{\partial \sigma_f(x_1)}{\partial x_1} dx_{2f} dA_s = \tau(x_1) dA_s \quad (3.5)$$

Integrate through thickness on one tablet,

$$\frac{\partial \sigma_f(x_1)}{\partial x_1} \frac{h_n}{2} = \tau(x_1) \quad (3.6)$$

Finally, for each tablet, we set up equilibrium equations as,

Right part of tablet 1:
$$\frac{\partial^2 u_r(x_1)}{\partial x_1^2} = \frac{k^2}{w_n^2} (u_r(x_1) - w(x_1)) \quad (3.7)$$

Left part of tablet 1:
$$\frac{\partial^2 u_l(x_1)}{\partial x_1^2} = \frac{k^2}{w_n^2} (u_l(x_1) - v(x_1)) \quad (3.8)$$

Tablet 2:
$$\frac{\partial^2 u_r(x_1)}{\partial x_1^2} = \frac{k^2}{w_n^2} (v(x_1) - u_l(x_1)) \quad (3.9)$$

Tablet 3:
$$\frac{\partial^2 u_r(x_1)}{\partial x_1^2} = \frac{k^2}{w_n^2} (w(x_1) - u_r(x_1)) \quad (3.10)$$

Where $k = \sqrt{\frac{2w_n^2 G_m}{E_f h_n t}}$, $u_r(x_1)$, $u_l(x_1)$, $v(x_1)$ and $w(x_1)$ are the displacement functions of tablet 1 on right, tablet 1 on left, tablet 2 and tablet 3 separately.

The boundary conditions of these three tablets are shown below, where $M_{cof} = c_m w_n / E_f t$.

$$u_r(0) = 0 \quad (3.11)$$

$$u_r'(l_w) = \frac{M_{cof}}{r} (-(v(-l_v) - u_l(-l_v)) + w(l_w) - u_r(l_w)) \quad (3.12)$$

$$u_l'(-l_v) = \frac{M_{cof}}{r} (-(v(-l_v) - u_l(-l_v)) + w(l_w) - u_r(l_w)) \quad (3.13)$$

$$u_l(0) = 0 \quad (3.14)$$

$$v'(-l_v) = P \quad (3.15)$$

$$v'(0) = \frac{M_{cof}}{r} (-(v(-l_v) - u_l(-l_v)) + w(l_w) - u_r(l_w)) \quad (3.16)$$

$$w'(0) = \frac{M_{cof}}{r} (-(v(-l_v) - u_l(-l_v)) + w(l_w) - u_r(l_w)) \quad (3.17)$$

$$w'(l_w) = P \quad (3.18)$$

Based on the boundary conditions and equilibrium equations, the displacement functions $u_r(x_1)$, $u_l(x_1)$, $v(x_1)$ and $w(x_1)$ are able to be solved in closed form. Besides, numerical solution is employed as well to confirm the results and the displacement plots are shown in appendix B.

The average strain is defined as,

$$\bar{\varepsilon} = \frac{|w(l_w) - u_r(l_w)| + |v(-l_v) - u_l(-l_v)|}{l_w + l_v} \quad (3.19)$$

The average stress is

$$\bar{\sigma} = (\sigma_m + \sigma_f) V_f \quad (3.20)$$

Now the elastic modulus is

$$E_{nacre} = \frac{\bar{\sigma}}{\bar{\varepsilon}} \quad (3.21)$$

The details of the equation of E_{nacre} are described in appendix B.

However, 3D tablet-like architecture with 50% off-set distance in longitudinal direction is not featured with the optimum deformation resistance, because the shear stress distribution in the matrix is not uniform, shown in Figure 3.5(f). Thus, in the next step, the off-set distance is defined as a variable of $L_{shift} \in (0, w + \frac{t}{\sqrt{3}}]$, illustrated in Figure 3.5(a), to investigate the maximum elastic modulus the unit cell can provide and its corresponding geometry.

Instead of directly using L_{shift} , $\alpha = \frac{L_{shift}}{L} \in (0, 0.5]$ is introduced to do the optimization analysis. Specifically, to set up the connection between 3D geometry to 2D analytical model, dimensionless parameter $\xi = \frac{A_{shift}(\alpha, t, w)}{A_{shear}(\alpha, t, w)} = \frac{l_w}{l_s}$ is introduced. The elastic modulus as a function of α and the relationship between α and ξ are illustrated in Figure 3.5(d) and (e) respectively. It is revealed that when $\xi = 0.5$, which represents the off-set area occupies 50% area of the whole effective shear area, the 3D tablet-like model is provided with the optimum in-plane elastic modulus in the longitudinal direction. However, the dimensionless length parameter α is 0.387, not 0.5, when the 3D tablet-like model achieves the maximum elastic modulus. Featured with optimum arrangement, $\xi = 0.5$ and $\alpha = 0.387$, 3D tablet-like architecture exhibits uniform shear stress distribution in the matrix interlayer, shown in Figure 3.5(g).

The finite element models and 3D printed samples discussed in this work are all based on this optimum geometry.

3.5.2 Finite Element Analysis (FEA)

The FEA unit cells of rod-like and tablet-like architectures are shown in Figure 3.6(a) and (b). At least 4 elements are assigned in the matrix between two fibers in all chiton models. Reduced integration 2nd order brick element (C3D8R) is used for analysis. The analysis is under linear static solver, since the elastic modulus is the required output.

Materials

Matrix material are represented by elastic linear model, featured with elastic modulus equal to 0.437MPa and Poisson's ratio equal to 0.41, which are characterized from uniaxial tensile test on compliant elastomer material. At the same time, fiber is defined as elastic linear model as well,

with elastic modulus equal to 2500MPa and Poisson's ratio equal to 0.3. The stress and strain curves of the material characterization tests are described in the appendix B.

Boundary condition

Periodic boundary condition is applied to the unit cells of tablet-like and rod-like architectures to represent the infinite boundary in nature and exclude the size effect. Nodes at top and bottom surfaces perpendicular to the y and z axes satisfy the following equations

$$u_i^{top} - u_i^{bottom} = 0, \text{ where } i = y \text{ and } z \tag{3.22}$$

The displacement at nodes of paired surfaces perpendicular to the x axis is correlated to the displacement of dummy node, which is located away from the model (Al Kassem and Weichert, 2009).

$$u_x^{top} - u_x^{bottom} = u_x^{dummy} \tag{3.23}$$

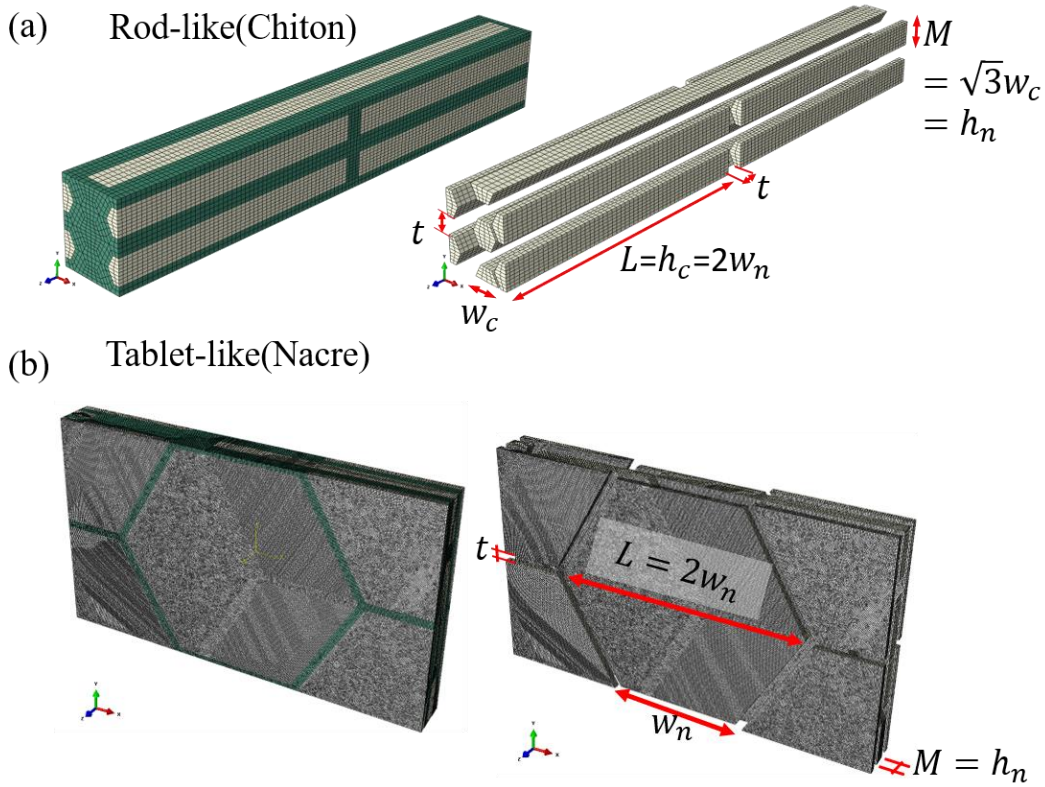


Figure 3.6. Unit cell with mesh in FEA on 3D rod-like structure (a) Unit cell of 3D rod-like structure and its dimensions (b) Unit cell of 3D tablet-like structure and its dimensions

Table 3.2 Geometrical parameters of designed samples

Name-Direction	Nacre1-x	Nacre2-x	Chiton1-x	Chiton2-x	Chiton3-x
$L(\text{mm})$	14	5.06	18.6	16.8	50
$t(\text{mm})$	0.4	0.4	0.4	0.4	0.4
$M(\text{mm})$	2.4	0.79	1.25	1.12	3.3
L/M	5.833	6.405	14.9	15	15.033
V_f	0.803	0.557	0.557	0.530	0.790
$A_s/V_{cell}(\text{mm})$	0.315	0.591	0.591	0.616	0.314
$A_t/V_{cell}(\text{mm})$	0.091	0.231	0.153	0.169	0.048

3.6 Results and discussion

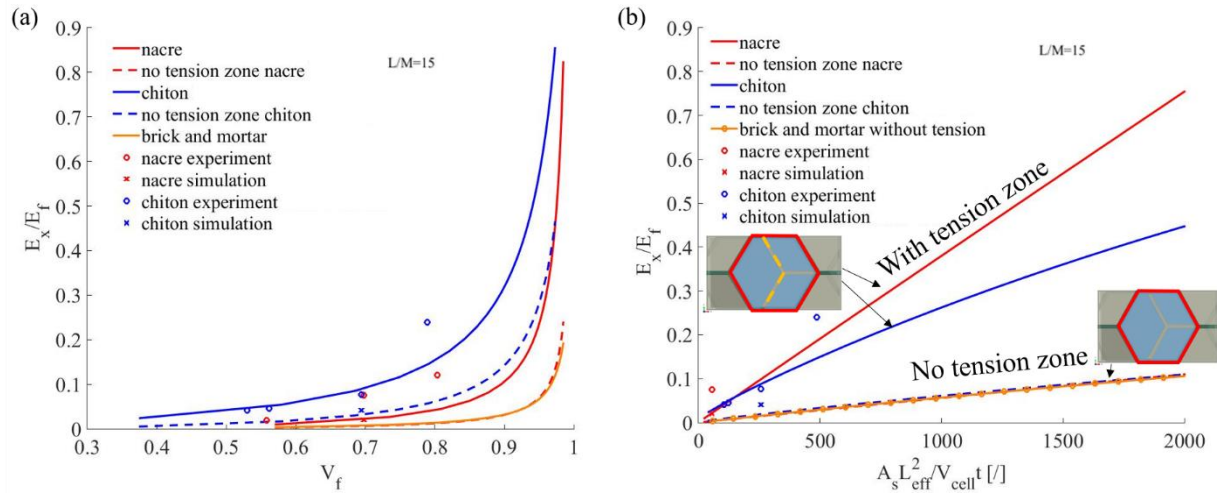


Figure 3.7. Elastic modulus of composites in longitudinal direction normalized by elastic modulus of fiber (E_x/E_f) as a function of dimensionless groups (V_f and $A_s L_s^2 / V_{cell} t$), all with $L/M = 15$ except two nacre structures, which are with $V_f = 0.56$ and 0.8 , shown in Table 3.2

3.6.1 Elastic modulus and new dimensionless parameter

To compare the tablet-like nacre architectures and rod-like chiton architectures in the same level, five dimensionless groups of parameters are introduced. They are $\pi_1 = E_x/E_f$, $\pi_2 = E_f/E_m$, $\pi_3 = V_f$, $\pi_4 = L/M$ and $\pi_5 = \nu_m$, where E_x is the elastic modulus in longitudinal direction, E_f and E_m are the elastic modulus of fibers and matrix respectively, V_f is the volume fraction of fibers, L and M are the length and width of the unit cells separately and ν_m is the Poisson's ratio of matrix

material. Alternatively, V_f can be replaced by $\pi_3 = A_s l_s^2 / V_{cell} t$, where A_s is the effective shear area. This dimensionless term is determined by the extreme case that fibers are infinite stiff compared with the stiffness of matrix. The detailed description is explained in appendix B.

In addition to the samples illustrated in Figure 3.4, alternative experimental samples of tablet-like and rod-like architectures with different L/W and V_f are introduced and compared, which is tabulated in Table 3.2. As what is observed in Figure 3.4(a), even tablet-like nacre and rod-like chiton architectures are featured with the same volume fraction and aspect ratio, their elastic modulus is different in FEA and analytical prediction, shown in Figure 3.7(a). The rod-like architecture, for instance, due to 4.7 larger value of $A_s l_s^2 / V_{cell} t$ over the tablet architecture, can provide stiffer behavior in longitudinal direction, up to 2.75 times. Alternatively, the considerable amount of effective tension area A_t could be another reason to explain the stiffer behavior of chiton architecture.

$A_s l_s^2 / V_{cell} t$ can provide accurate deformation resistance when the 3D model is under uniaxial tensile loading, since Figure 3.7(b) shows that once the model ignores the contribution of tension effects, the analytical predictions on elastic modulus of 3D tablet-like and rod-like architectures closely align with each other when $A_s l_s^2 / V_{cell} t$ are the same. On the other hand, see Figure 3.7(b), the difference between the elastic modulus with tension effects and the one without tension effects indicates that the tension mechanism in our 3D models cannot be ignored.

3.6.2 Critical stress and toughness

Critical stress

To examine the strength and toughness of the 3D biomimetic architectures, we introduce another two dimensionless groups σ_{ys} / τ_c and T_c / τ_c , where σ_{ys} is the critical (maximum) stress of 3D architectures, τ_c is the critical shear stress of the matrix material, and T_c is the toughness of architectures.

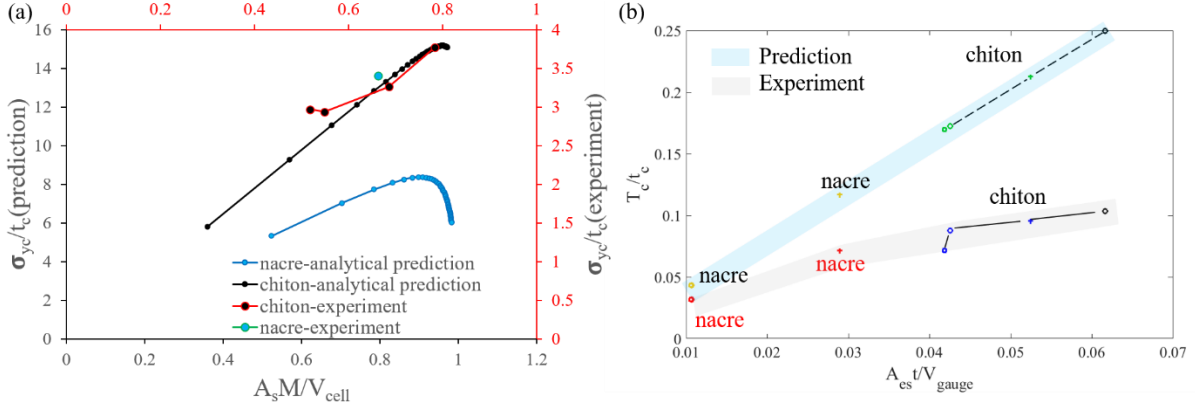


Figure 3.8. (a) Critical stress σ_{y_c} as a function of $A_s t/V_{cell}$ from experiments and analytical prediction. Black axis represents for analytical prediction and red axis represents for experimental results. (b) Toughness as a function of $A_{es} t/V$. Dots with blue color shadow are from prediction and dots under green shadow are the results from experiments.

According to the known displacements $u_r(x_1)$, $u_l(x_1)$, $v(x_1)$ and $w(x_1)$ of three tablets in the unit cell, solved in the previous equivalent equations, the shear stress distributed in the matrix interlayer is able to be calculated. The shear stress of right and left segments of the tablets is defined as the function of displacements of the tablets,

$$\tau_{right} = \frac{u_r - w}{t} G_m \quad (3.24)$$

$$\tau_{left} = \frac{u_l - v}{t} G_m \quad (3.25)$$

The shear stress distribution along the longitudinal direction is illustrated in appendix B. From Figure B5, the shear stress reaches the maximum value at both ends of the tablets, while minimum value, τ_{max} , locates at the middle of the tablets. Accordingly, when $x = 0$ or $x = -l_v$, shear stress in the matrix shows maximum value and then the corresponding critical normal stress is achieved by $\sigma_c = \tau_{max} A_s \frac{M}{2} / V_{cell}$, which is described in appendix B.

Same algorithm of calculating critical stress is applied for 3D rod-like architectures, and then the critical load of 3D rod-like architecture is,

$$\sigma_c = \frac{\tau_c E_m t}{G_m} \left(\frac{2c_m}{E_m t V_f} + \frac{k}{l_s \tanh(k/4)} \right) A_s \frac{M}{2} / V_{cell} \quad (3.26)$$

It is revealed that results from analytical prediction and experiments are summarized in Figure 3.8(a). It is interesting to show that as $A_s M/V_{cell}$ is increasing, the value of critical stress of both 3D models is increasing, while the value of σ_{y_s}/τ_c in experimental 3D rod-like architecture exhibits increasing inclination as well. However, the value of analytical prediction is 4 times higher

than the experimental results, which can be explained by that the critical stress, σ_{ys} , is induced by tension failure between rods end in the experiments, rather than the maximum shear stress as predicted by analytical model.

Toughness

Instead of using the shear area A_s of unit cell and volume of unit cell V_{cell} , for experimental results, the effective shear area is measured based on the crack surface of failure samples A_{es} and the volume is the whole gauge part of the samples V_{gauge} . If we assume the crack would propagate through the interlayer of matrix of each unit cell in the experimental sample, the prediction would be highly overestimated. We assume that once the shear stress of matrix from the interlayer equals to critical shear stress τ_c along the longitudinal axis, the matrix material starts to fail and then the whole structure fails. Thereby, the analytical prediction of the 3D tablet-like and rod-like architectures is based on following equation. V_{shear} is $A_{es}t$.

$$T_c = \frac{V_{shear}}{V_{gauge}} \frac{t_c^2}{2G_m} \quad (3.27)$$

Normalized toughness T_c/τ_c as a function of V_{shear}/V_{gauge} is illustrated in Figure 3.8(b). It reveals that with the increase of V_{shear}/V_{gauge} , both experimental results and analytical prediction exhibit that normalized toughness is amplifying, which is under our expectation.

3.7 Conclusions

In the present paper, we set up the comparison between 3D tablet-like nacre architectures and rod-like chiton architectures based on dimensionless groups of mechanical properties and geometry parameters. Rigorous analytical, experimental and numerical analyses are exploited to compare and analyze the properties of two architectures from different associated factors.

Compared to 3D tablet-like nacre architectures, rod-like chiton architectures are more efficient on mechanical properties in longitudinal direction when both featured with the same volume fraction V_f and aspect ratios L/M . However, 3D rod-like nacre architectures are more beneficial in biaxial loading. This also answers our initial question that why nature chooses rod-like chiton structures to endure axial loading in their longitudinal direction and chooses tablet-like structures to be the structured components of the shell of nacre. This phenomenon can be explained

by the different effective shear and tension area of the architectures, which are the hidden confounder for general geometry parameters, V_f and L/M , and mechanical properties, such as stiffness, strength and toughness. Accordingly, in three-dimension, in addition to V_f and L/M , the effective shear and tension area are another two key parameters needed to be considered to calculate mechanical properties, encompassing elastic modulus, critical load and toughness.

In closing, the comparative analysis of two architectures can provide valuable design insights to study architectures inspired by different building units.

4. RESISTANCE OF CRACK INITIATION OF MATERIALS WITH FUNCTIONALLY GRADED ELASTIC MODULUS

Chapter 4 is part of the publication “Functional gradients by crystallographic gradation toughens calcareous bivalves”. (2020), Status: In progress

4.1 Background

We introduced nacreous structure, inner layer of nacre, in Chapter 3. Here we are going to investigate the calcite layer, exterior layer of *Pinctada margaritifera*, which is composed of space-filling prismatic pillar. Nacre is composed of calcite external layer and nacreous inner layer. The orientation of longitudinal direction of crystallite prisms varies from exterior to interior. As a result of changing prisms orientation, the Young’s modulus varies graded functionally through the thickness of *Pinctada*, shown as red in Figure 4.1(c). We are interested in exploring why nature chooses this specific graded pattern and what the relation is between gradient and fracture tolerance.

4.2 Methods and results

4.2.1 Dimension of model

Based on the graded Young’s modulus as shown in Figure 4.1(c), we set up classical tension test on one strip with half crack (Mode I) and its size is a , as shown in Figure 4.1(b). The length (L) and width (W) of the strip is 4.8mm and 0.6mm separately. Additionally, layered sample has been divided into 6 constant values on Young’s modulus by using trapezoidal rule and the width is w_0 (0.1mm). And the values are 79.4GPa, 91.0GPa, 92.8GPa, 88.3GPa, 86.5GPa and 86.4GPa. Besides, we perform finite element analysis (FEA) with seven crack sizes, $a=1\ \mu m$, $12\ \mu m$, $25\ \mu m$, $38\ \mu m$, $50\ \mu m$, $75\ \mu m$, $100\ \mu m$, $125\ \mu m$ and $150\ \mu m$ combined with above four patterns of Young’s modulus so as to calculate the J-integral.

4.2.2 Element and boundary condition

The element type is CPE4R, which is the plane strain two-dimensional brick element. The singular element close to the crack tip is collapsed by 4 nodes. The basic mesh condition is shown in Figure C1(a). The mesh size around the crack tip was determined by a preliminary convergence

study on the values of the J-integral values with three different mesh sizes, shown in Figure C2. Thereby, the element size near the crack tip was determined to be small enough to provide an accurate stress field. The ratio of mesh size close to crack tip over crack size, **a**, keeps the same through all of samples we are going to test here. Uniform displacement is applied at the top of the strip and we extract half of the sample as shown in Figure 4.1(b) to analyze because it is symmetry.

4.2.3 Modified J-integral

The fracture resistance for each case is measured in terms of the predicted stress intensity factor (K_I) as a function of the initial crack length. For comparison purposes we also considered layered, inverse graded, and homogeneous materials as shown in Figure 4.1(c).

Since the Young's modulus is not constant through the growing thickness, the calculation of domain J-integral is modified as equation (4-1). According to this modified calculation, the J-integral is independent on contours. The plot of comparison between modified J-integral and classic domain integral method is illustrated in Figure C1(b) for "Graded" material and in Figure C1(c) for "Inverse graded" material. It is exhibited that the values of modified J integral of "Graded" and "Inverse graded" material through different contours close to crack tip are constant, while the calculation of domain integral for "Graded" and "Inverse graded" materials is various over distinct contours. Besides, the domain integral predicted by Abaqus is the same as what we calculate.

$$\bar{J} = \sum_A \sum_{p=1}^N \left\{ \left[\sigma_{ij} u_{i,1} q_{1,j} - W q_{1,1} - W_{,1} q_1 \right] \det \frac{\partial x_k}{\partial \zeta_l} \right\} w_p \quad (4.1)$$

Where, w_p is the weights of integration. $\det()$ is the determinant of Jacobian matrix. W is the strain energy density. $u_{i,1}$ is the derivative on x of displacements. q_1 is a continuous function and has value zero on the outer contour and has value one on the contour close to crack tip (Anlas et al., 2000; Gu et al., 1999; Li et al., 1985; Raju and Shivakumar, 1990). N is the number of integration points. A is the area of integration contour. σ_{ij} is the components of Cauchy stress tensor.

And $W_{,1} = \frac{dW}{dx} = \frac{dW}{dE(x)} \cdot \frac{dE(x)}{dx}$. E is a function of x and $W = 0.5(\varepsilon_{11}\sigma_{11} + \varepsilon_{22}\sigma_{22} + \gamma_{12}\sigma_{12})$. Based on the constitutive law of plane strain, we could derive the equation of $\frac{dW}{dE(x)}$. Because of chain rule, we have

$$q_{1,i} = \begin{Bmatrix} \frac{\partial q_1}{\partial x} \\ \frac{\partial q_1}{\partial y} \end{Bmatrix} = \begin{bmatrix} \frac{\partial x}{\partial \xi} & \frac{\partial y}{\partial \xi} \\ \frac{\partial x}{\partial \eta} & \frac{\partial y}{\partial \eta} \end{bmatrix}^{-1} \begin{Bmatrix} \frac{\partial q_1}{\partial \xi} \\ \frac{\partial q_1}{\partial \eta} \end{Bmatrix} \quad (4.2)$$

Where ξ and η are orthogonal axes of standard quadrilateral element. $q_1 = N_m Q_m$. N is the shape function of element and Q is the scalar value 1 or 0. And then, use equation (4-3) to calculate intensity factor K_I .

$$K_I = \sqrt{\frac{\bar{J} \cdot E_{tip}}{1 - \nu^2}} \quad (4.3)$$

4.2.4 Stress distribution

According to the normalized stress distribution, shown in Figure 4.1(d), it is exhibited that there is high values of stress concentration around the crack tip of homogeneous case, compared with other two cases. Though the values of stress distribution of graded material away from crack tip (region from $1.0\sigma_{yy}/\sigma_\infty$ to $1.1\sigma_{yy}/\sigma_\infty$ in Figure 4.1(d) is higher than the values of same position of homogeneous material, the graded material releases the stress concentration close to crack tip. Material with graded Young's modulus has smoothly graded stress transition. In the same time, material with layered Young's modulus possesses sharp stress transition at the discretion boundary. Detailed normal stress distribution along the growing thickness is illustrated in Figure C2(a). We could see the opening stress close to crack tip of graded material for all of crack sizes is modest among other cases. Additionally, like what we described for Figure 4.1(d), in Figure C2(a) the stress transition along the crack growth direction of graded material is smooth without "jump".

4.2.5 Results

Stress intensity factors (K_I) calculated by equation (4-1) and (4-3) of samples with four designs of Young's modulus distribution are illustrated in Figure 4.1(e) with the development of

crack sizes a . The graded Young's modulus material has less values of K_I , compared with the trend of layered, homogeneous and inverse graded Young's modulus distribution. Graded material has maximum 20% higher fracture resistance than homogeneous material. However, inverse graded material has lower fracture resistance, compared with homogeneous material. As shown in Figure 4.1(f), the trend of normalized difference between stress intensity factor of homogeneous material (K_{Ih}) and of graded material (K_{Ig}), and the trend of normalized difference between K_{Ih} and inverse graded materials (K_{Ii}) are closely symmetry to the x-axis (difference of two absolute values equals to 0). Though layered material possesses more benefits on fracture resistance compared with inverse graded material, it does not have as good fracture resistance behavior as graded material does. Especially when we compare the stress transition between graded material and layered material. Thus, the materials increasing Young's modulus smoothly from exterior to interior are equipped with more fracture resistance in mode I.

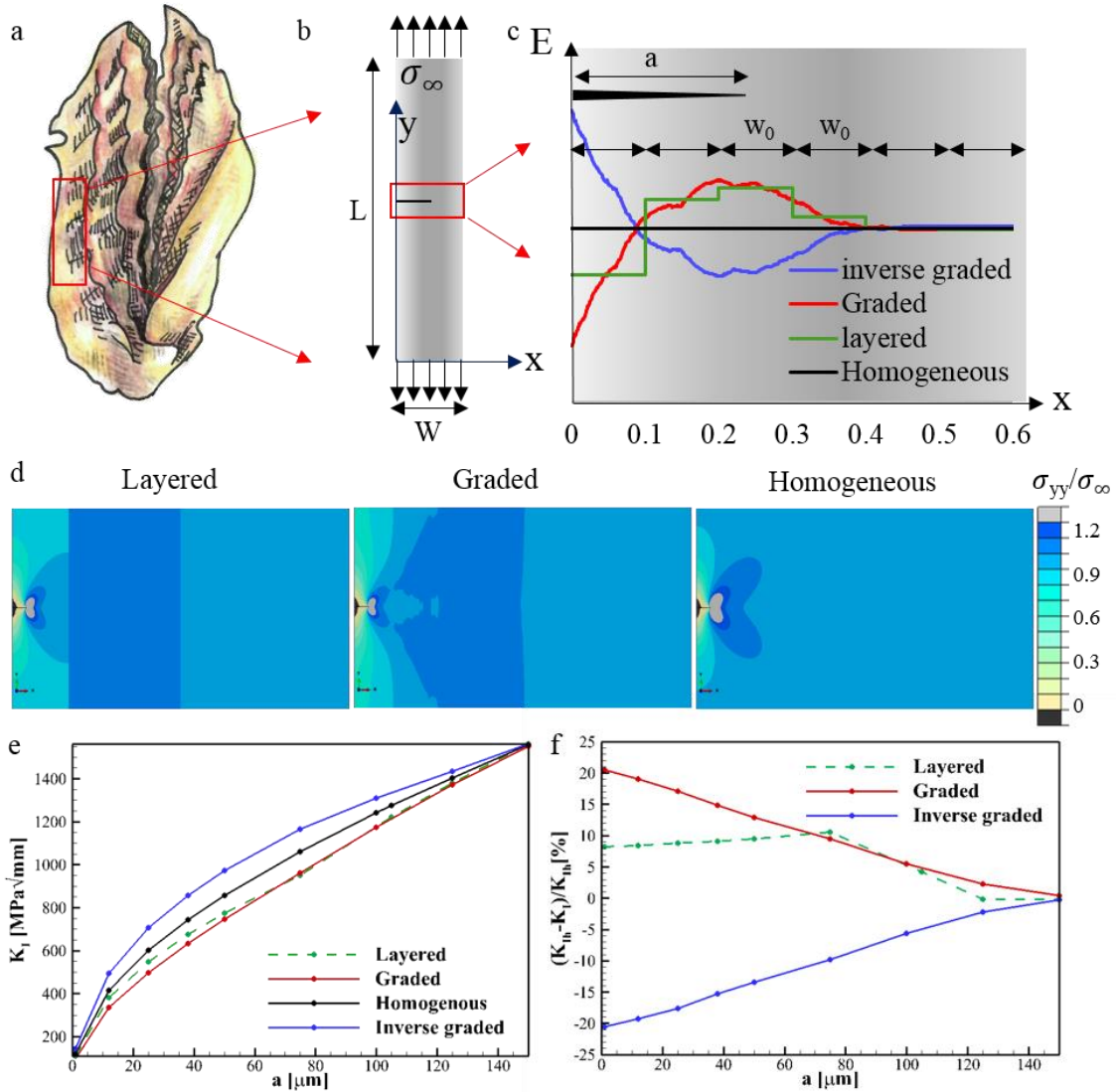


Figure 4.1. Simulation of FGMs and other types of materials. (a) Nature Pinctada (b) Size and boundary condition of FEA simulation model (c) Functionally graded material on Young's modulus in Pinctada, layered distribution of Young's modulus based on first case, homogeneous material and inverse graded Young's modulus distribution which is the mirror of graded materials based on axis of homogeneous case. (d) Normalized stress distribution of layered Young's modulus, graded Young's modulus and homogeneous materials with crack size 25um. (e) Stress intensity factor of samples with different crack sizes. (f) Comparison in percentage on stress intensity factor between graded materials in nature Pinctada and homogeneous materials, inverse graded Young's modulus and homogeneous materials, coupled with layered Young's modulus and homogeneous materials.

4.3 Conclusions

Although the layered material possesses more benefits on fracture resistance compared with inverse graded material, it does not have as good fracture resistance as the graded case. Besides, the stress transition of graded material is smooth, not like the discrete transition of layered material, shown in Figure 4.1(d). Thus, the materials increasing Young's modulus smoothly from exterior to interior are equipped with more outstanding fracture resistance in mode I.

The function of specific gradients of prism orientation in calcite layer of nacre is analyzed. At the same time, as mentioned in Chapter 1, the gradients of pitch distance D in helicoid laminate is possibly favorable to delamination resistance, which will be discussed in the next chapter, Chapter 5.

5. INTER- AND INTRA-LAMINAR DAMAGE OF HELICOID WITH GRADIENT PITCH ANGLES

5.1 Introduction and motivations

In nature, the pitch distance of helicoid architectures in biological materials was found not constant through the thickness of the materials, but functionally decreasing from surface to interior. The pitch distance is defined as the thickness to accomplish 180-degree rotation in helicoid architecture, which is the same as the definition in Chapter 2. It is reported that the pitch distance in dactyl club varies from 150um(or 80um), close to surface, to 10um, close to interior (Guarín-Zapata et al., 2015). Although the specific values of pitch distance in the fish scale of Coelacanth were not measured, it is also observed that the pitch distance is decreasing from surface to interior of Coelacanth fish scale (Quan et al., 2018).

Functional gradients and heterogeneities have been evolved to create high-performance biological materials in living organisms (Kokkinis et al., 2018; Liu et al., 2017). In the map of biological materials design, the gradients are functionally related to the changes in two major sorts of elements, chemical compositions/constituents, and structural characteristics, involving the arrangement, distribution, dimensions and orientations of structural building units (Liu et al., 2017). In biological helicoid architectures, the gradients of pitch distance can exist as the way of orientations of fibers in each laminate or the thickness of each laminate. Due to the minor pitch angles observed in dactyl club, whether the gradient of pitch distance from surface to interior is dependent on laminate thickness or different pitch angles needs extensively studies. Nevertheless, (Quan et al., 2018) reported that the pitch angle in the double Bouligand structures of Coelacanth fish scale is increasing from surface to interior. Thus, it is necessary to investigate the function of varying pitch angle first in helicoid architectures. Moreover, the contribution of the gradient of the pitch angle in helicoid architectures to the overall mechanical behaviors and fracture resistance behaviors has not yet been studied. This presents an opportunity to study and understand the specific function of the gradient of the pitch distance associated with varying pitch angles through the thickness of the materials. Thus, in the present study we are going to study the contribution of gradient pitch distance, associated with varying pitch angles, to the mechanical behaviors under static and dynamic loading conditions. Although the possibility that varying pitch distance is

induced by changing lamina thickness cannot be excluded, it will not be discussed in the present work, which can be the potential future work for other colleagues in the lab.

Functional gradients and heterogeneities are evolved from nature material to impart high-performance biological materials. The translation of evolution confers us a spectrum of design elements associated with the variations of chemical compositions/constituents and structural characteristics involved in the arrangement, distribution, dimensions and orientations of the building units (Liu et al., 2017). One of the rich toolboxes given by nature is the porosity arrangements. The porosity of growth ring from wood stems, for instance, decreases gradually from the earlywood to the latewood (Eder et al., 2009; Gibson, 2012; Speck and Burgert, 2011) and thus this arrangement leads to opposite pattern on density and stiffness, which is beneficial to water transport and mechanical stability during the growth period. Besides, gradients on Young's modulus and other mechanical properties also reveal unprecedented contact damage resistance that cannot be realized in conventional homogenous materials (Pender et al., 2001; Suresh, 2001). Except for porosity arrangement, many biological materials are featured with various dimensions of their constituents to achieve specific functionality. A primary example is the sponge spicules, constituted by a central core of hydrated silica surrounded by changing layers of silica and proteinaceous material(Liu et al., 2017). The thickness of silica layers is decreasing from core to surface(Aizenberg et al., 2005; Miserez et al., 2008), which can effectively resist the depth of crack penetration from surface, since cracks tends to propagate through organic ductile layers. Like what we introduced at the beginning of the introduction chapter, many biological materials consist of anisotropic structural elements, such as fibers, tablet reinforcement and prisms. Accordingly, their properties are highly dependent on the orientation of these structural elements. Helicoid architectures, found in the fish scale and the shell of arthropods, encompass successively different lamina orientations layer by layer, such that the material is featured with close-to in-plane isotropic behavior(Yang et al., 2019) and remarkable toughening mechanisms via crack twisting(Suksangpanya et al., 2018, 2017) or reorientation, stretching and delamination of fibrils to dissipate more energy under loading(Quan et al., 2018; Yang et al., 2014; Zimmermann et al., 2013).

It is known that helicoidal fiber reinforced laminated architectures with uniform pitch angle can provide efficient energy dissipation through the thickness and in-plane isotropic behavior to resist materials failure. However, helicoid architectures with small pitch angles dissipate energy

via in-plane delamination (Ginzburg et al., 2017; Grunenfelder et al., 2014). Delamination failure can lead to large reduction on material stiffness, strength and can even initiate failure of the whole laminate (Garg, 1988) and impair the buckling resistance when under compression load (Aslan and Şahin, 2009). However, delamination is also an effective method to dissipate energy, which is also discussed in (Ginzburg et al., 2017). On the other hand, intralaminar damage, such as fiber breakage and matrix split, also plays a significant role in the damage resistance of the materials, especially stiff fibers' breakage, which can release large amount of energy, but easier to lead to catastrophic damage, unable to provide any resistance when most fibers break through the cross-section. Accordingly, considering the delamination failure occurring ubiquitously in the helicoid architectures, in this chapter transverse shear stresses dominant experiments, such as three-point bending on short beam and low-velocity impact tests, are going to be adopted.

Three-point bending tests can provide overall stiffness, strength (peak load) and toughness, which can be indicators of damage resistance of one beam structure. On the other hand, peak load or maximum deflection and energy absorbed after impact are significant outputs that need to be considered when we do the low-velocity impact tests.

The peak load and toughness under static plate bending as a function of pitch angle is illustrated and summarized in Figure 5.1.(a) and (b), combined with their normalized results shown in Figure 5.1(c), based on the reports of (Cheng et al., 2011; Liu et al., 2018a, 2020; Zhang and Zhang, 2015). It is shown that when the pitch angle of laminates is decreasing, the laminate can provide increasing peak load under static plate bending when the layer number is less than 37. However, when layer number increases to 74, it seems that there is an optimum pitch angle for the maximum peak load, which is also dependent on fiber material. Accordingly, there is no consistent results on peak load of helicoid architectures under plate bending and the framework is not consistent either for comparison purpose. Furthermore, the toughness under static plate bending is not discussed in these references. So far, the peak load and toughness values of laminate with different pitch angles starting from 0° to 90° under bending needs extensively study under a consistent framework, since there is no consistent results and conclusions on these helicoidal laminates with different pitch angles. Besides, the influence of different thickness on delamination resistance and in-plane damage resistance is not the objective in the present study, which can be a potential future work for others.

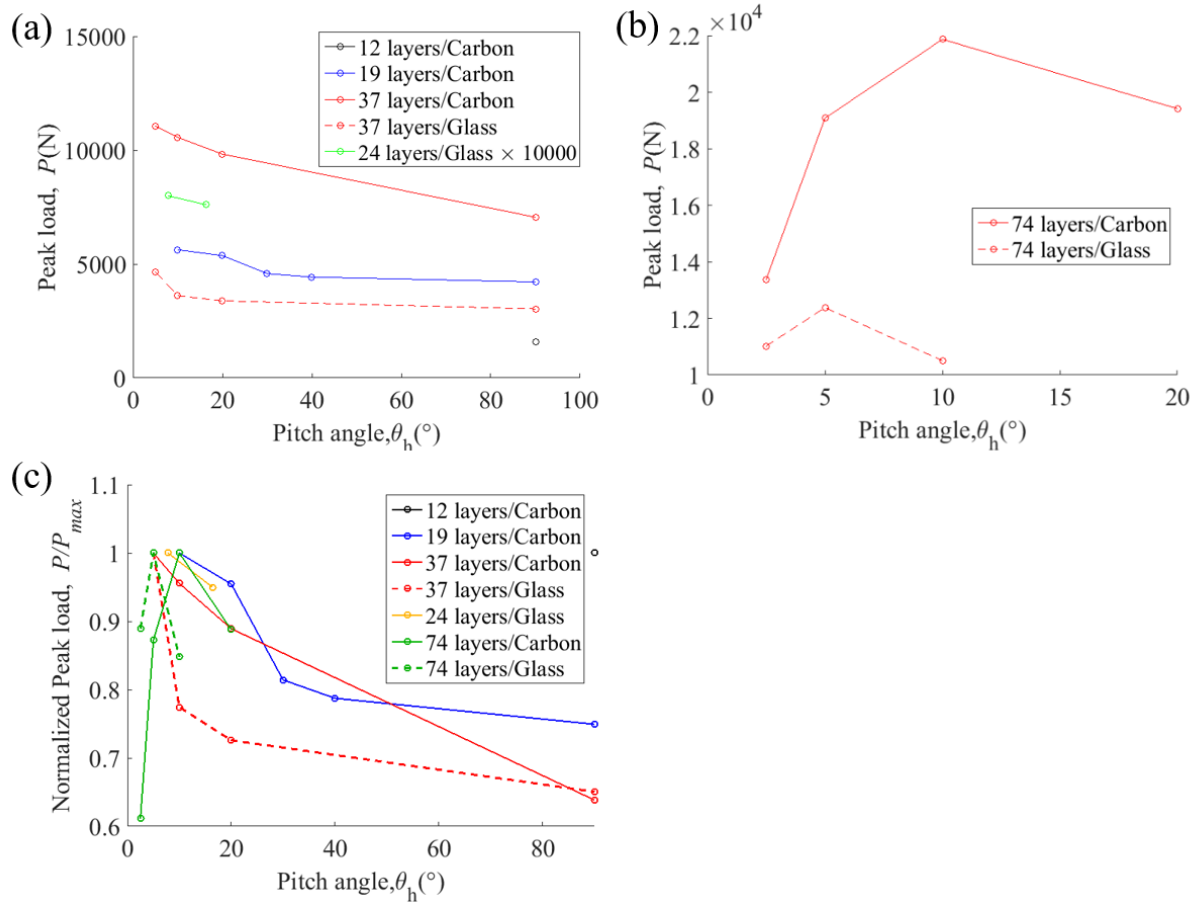


Figure 5.1. (a) Peak load under static loading condition as a function of pitch angle of thinner laminate (layer number less than 37) (Cheng et al., 2011; Liu et al., 2020, 2018a; Zhang and Zhang, 2015) (b) Peak load under static loading condition as a function of pitch angle of thicker laminate (layer number larger than 37)(Liu et al., 2020) (c) Peak load normalized by its maximum peak load of different layers and materials(Cheng et al., 2011; Liu et al., 2020, 2018a; Zhang and Zhang, 2015)

It is observed that less pitch angle leads to higher peak load under low-velocity impact tests (LVI), shown in Figure 5.2.(a), while there is no clear trend in energy absorbed with the development of pitch angles under LVI tests, shown in Figure 5.2.(b). The Ashby plots of peak load and absorbed energy from low-velocity impact tests are also summarized in Figure 5.2.(c)-(e). Results from (Ginzburg et al., 2017) with 32 carbon fiber layers show little difference on absorbed energy among different pitch angles, whereas (Mencattelli and Pinho, 2019) reported carbon fiber laminates with 146 layers exhibit that larger pitch angle laminates can provide higher absorbed energy but lower values of peak load.

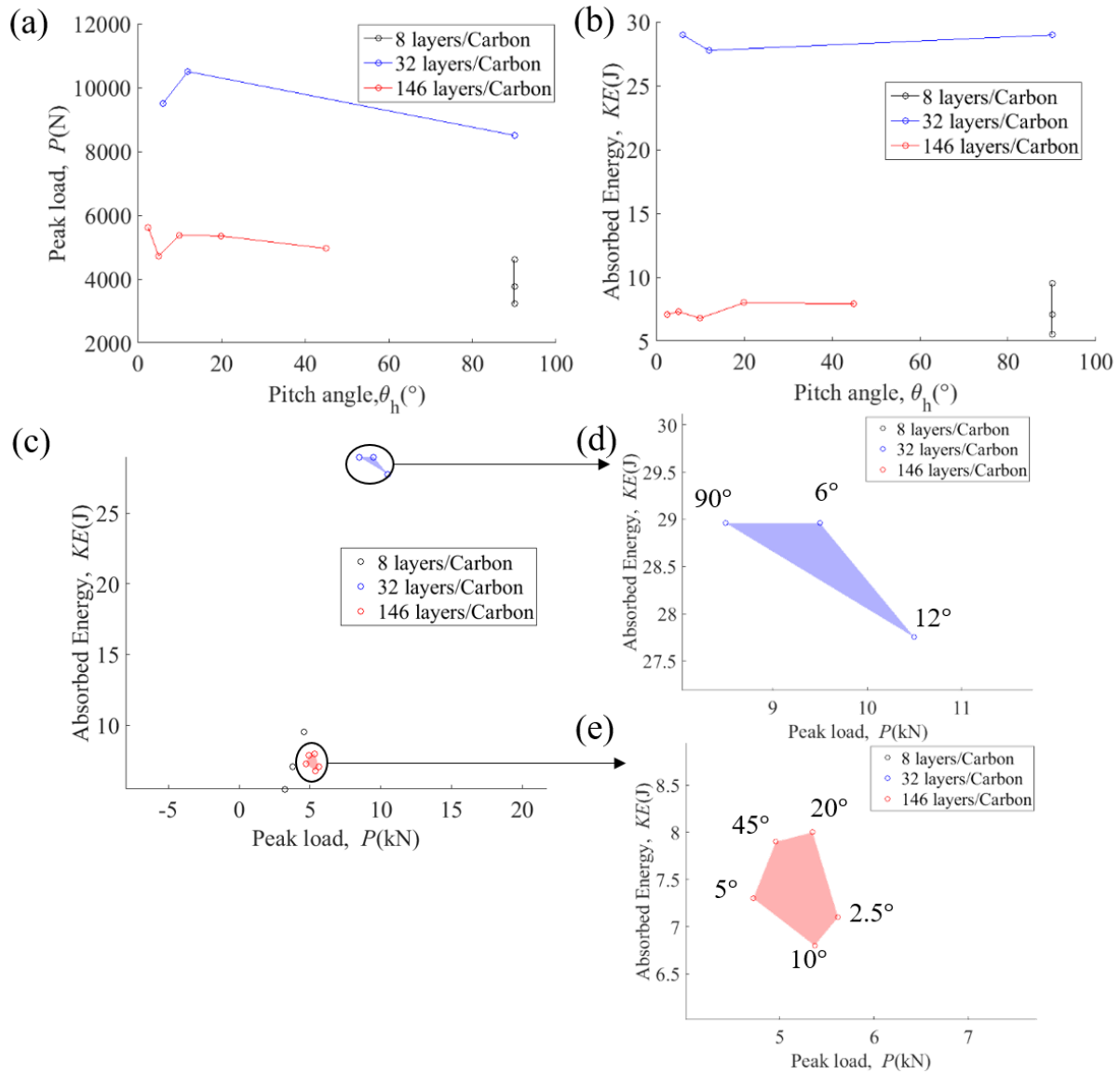


Figure 5.2. Target outputs of laminates with different numbers of layers and distinct fiber materials under dynamic-impact loading condition (a) Peak load of laminates as a function of pitch angle (b) Absorbed energy of laminates as a function of pitch angle (c) Ashby plot of absorbed energy and peak load (d)-(e) zoom in version of Ashby plot (c)

In addition to the observation on different pitch angles summarized in the last paragraph, it has been observed that laminate with smaller pitch angles exhibit less penetration damage, but larger in-plane delamination after low velocity impact tests while larger pitch angle shows less delamination area but larger amount of intralaminar damage through the thickness (Ginzburg et al., 2017; Grunfelder et al., 2014). Besides, laminates with larger pitch angle exhibit longer crack path under low-velocity impact and quasi-static plate bending (Jiang et al., 2019; Liu et al., 2020,

2018b; Suksangpanya et al., 2017) and thus it can absorb less energy and maintain higher values of toughness. However, the distribution of interlaminar stresses is discrete through limited thickness of the materials with larger pitch angle, representing that maximum interlaminar stresses occur very often through the thickness. Inversely, helicoids with smaller pitch angle is with smooth distribution of interlaminar stresses through the thickness (Liu et al., 2018a; Mencattelli and Pinho, 2019), indicating limited occurrence of maximum interlaminar stresses when the thickness of the material is fixed. Accordingly, the number of delamination interfaces through the thickness is highly inclined to be larger in the laminate with larger pitch angle, compared with smaller one. However how this number of delamination interfaces can influence the delamination area and the projected delamination area needs to be extensively investigated, since the larger number of the delamination interfaces does not mean larger delamination area in all.

We suppose that gradient pitch angles of helicoidal architectures can provide multiple competitive mechanical properties to create a high-performance material, since the synthesized functionally graded pitch angles integrate the benefits and functions of different pitch angles. This integration can offer the global architectures multiple competitive mechanical properties simultaneously, such as achieving higher toughness and peak load simultaneously, due to the combination of factors including 1) laminates with distinct pitch angles can provide different values of maximum transverse stresses at free-edge and discrepancy on transverse stresses distribution through the thickness, 2) delamination initiation and evolution are based on strength and energy release rate and the energy release rate is supposed to show local discrepancy in distinct off-axis angles, which are related to different pitch angles and 3) the number of laminae with misorientation close to ($< 5^\circ$) or equal to 0° can influence the in-plane damage evolution of the whole laminate when the total thickness, T , is fixed. For instance, helicoid with constant pitch angle $\theta_h = 30^\circ$ can behave as a coating material, delaying delamination induced by concentration stress close to bottom and top surfaces, and then can provide higher peak load, but less toughness among pitch angles in the range of 15° and 60° , while $\theta_h = 45^\circ$ can offer superior toughness over other helicoids dropped in the range of 15° and 60° . FGH with $\theta_h = 30^\circ$ arranged close to top and bottom surfaces and $\theta_h = 45^\circ$ arranged in the middle of the laminate along the thickness can provide higher peak load and superior toughness at the same time under bending.

The importance of continuous gradient on pitch angle/distance is to provide the whole material a smooth stress transition along the thickness direction, instead of discrete stress transition

with a lot of “jumps”, similar as what we discussed in Chapter 4. In Chapter 4, specifically graded elastic modulus can lead to smooth stress transition from crack tip to interior and then it can provide benefits on fracture resistance over the case with discrete stress distribution. However, this is still a developing claim, which needs further study in analytical prediction and numerical calculations to explain in the future.

In the present work, quasi-static three-point bending tests on short beam and low velocity impact tests are conducted on helicoid architectures with different constant pitch angles and linearly varying pitch angles. Both experiments consider interlaminar (delamination) and intralaminar damage simultaneously.

5.2 Methods

5.2.1 Designs of composite laminates

In the present work, the whole thickness of the laminate (T) is fixed for both short beam bending and low-velocity tests separately. The thickness of each layer in the laminate (t) is constant through the thickness as well. Accordingly, the number of layers for each laminate is $n = T/t$ and n is 24 for both tests. In short-beam bending tests, the length and width of the laminates are denoted by L and W separately, and the aspect ratio L/W is fixed as 3.125 for all the short-beam bending tests. In the low-velocity impact tests, instead of using rectangular shape for the laminates, in-plane circular shape was used to represent the isotropy property of helicoid architectures. The radius of the plate is denoted by R .

Pitch angle θ_h was introduced in Chapter 2 and in this Chapter, the θ_h is 15° , 22.5° , 30° , 36° , 45° , 60° , and 90° , including the associated θ_h s in functionally graded helicoids. Like what we introduced in Chapter 2, when the fiber reinforced laminae accomplish $(180^\circ - \theta_h)$ rotation, we call it one pitch and the thickness to accomplish the rotation is one pitch distance D . The number of pitches in one laminate, N , is determined by $n/(180^\circ/\theta_h)$ in the laminate with constant pitch angle. However, when we need to define functionally gradient helicoids, T and N need to be defined first and then determine the gradient of the pitch angles through the thickness. In the present work, the gradient of pitch angle, k , is defined by the first and last pitch angles along the thickness of one laminate, which is linear and the pitch angles are monotonically decreasing from surface to interior, bio-inspired by biological materials(Guarín-Zapata et al., 2015; Quan et al.,

2018). It is deserved to be noticed that all the laminates are symmetric to its middle plane, since unsymmetrical laminates can lead to extension-bending coupling behavior, indicating that $[B] \neq 0$ in classical laminate plate theory. The detailed definition of pitch-angle gradient is shown in the following equation.

$$k = \frac{\theta_{h1} - \theta_{hN}}{H_1 - H_N} \quad (5.1)$$

Where $H_i = \sum_{i=1}^{i-1} D_i + \frac{D_N}{2}$, $D_i = \frac{\pi}{\theta_{hi}} t$, $T = \sum_{i=1}^N D_i$. H_i is the height of the i th pitch, representing the distance from surface to the middle point of one pitch laminate, as shown in Figure 5.3. The designs of FGH1sym and FGH2sym are illustrated in Figure 5.3(a) and (b). Besides, their pitch distance, D , as a function of the height, H , of each pitch is shown in Figure 5.3(c) as well. FGH1symdisorder, including $\theta_h = 45^\circ$, $\theta_h = 36^\circ$ and $\theta_h = 60^\circ$ from surface to interior, is designed for validating the contribution of decreasing pitch distance to delamination and in-plane damage under short beam bending, see Figure 5.3(c).

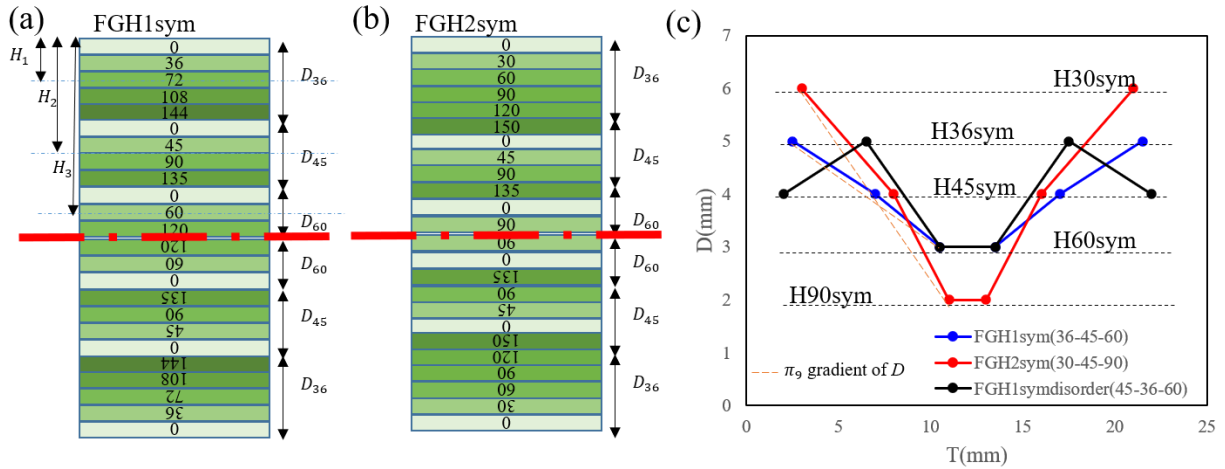


Figure 5.3. (a)-(b) Designs of functionally gradient helicoids (FGHs) and (c) their pitch distance, D , as a function of height, H .

5.2.2 Necessary information in FEA

The intralaminar and interlaminar properties of E glass/Epoxy composite materials for FEA are tabulated in Table 5.1. Due to transversely isotropic properties of aligned fiber reinforced laminates, the transverse shear strength and fracture energy in two different directions are the same.

Table 5.1. In-plane and interface properties of composite laminates

In-plane properties	
Elastic (GPa)	$E_1 = 30.5, E_2 = E_3 = 4.02, \nu_{12} = \nu_{13} = 0.29, \nu_{23} = 0.39, G_{12} = G_{13} = 2.08, G_{23} = 1.44$
Strength (MPa)	$X_t = 686, X_c = 270, Y_t = 35, Y_c = 88, S_{12} = 52, S_{23} = 27$
Fracture Energy (N/m)	$G_{1t} = 62000, G_{1c} = 47000, G_{2t} = 250, G_{2c} = 920$
Interface properties	
Strength (MPa)	$\sigma_n^c = 35, \sigma_s^c = \sigma_t^c = 52$
Fracture energy (N/m)	$G_I^c = 280, G_{II}^c = G_{III}^c = 440$

Laminae in FEA were modeled by 3D continuum shell elements (SC8R), which are based on Mindlin-Reissner plate theory, considering transverse shear stresses, σ_{13} and σ_{23} , through the thickness. The accuracy of plate theory under bending is confirmed by (Pagano, 1970) and SC8R elements are confirmed by conducting corresponding experiments as well (Jiang et al., 2019; Liu et al., 2018b; Long et al., 2015; Shang et al., 2016). Specifically, the justification of this continuum shell combined with cohesive interaction is discussed in section 5.4.4. The intra-laminar damage criterion is represented by Hashin damage model (Camanho and Davila, 2002; Hashin, 1980; Hashin and Rotem, 1973; Matzenmiller et al., 1995), including fiber tension, fiber compression, matrix tension and matrix compression, four categories of damage modes. The damage criterion is shown in the following equations.

Fiber tension ($\sigma_{11} \geq 0$):

$$F_f^t = \left(\frac{\sigma_{11}}{X_t}\right)^2 + \alpha \left(\frac{\sigma_{12}}{S_{12}}\right)^2 \quad (5.2)$$

Fiber compression ($\sigma_{11} \leq 0$):

$$F_f^c = \left(\frac{\sigma_{11}}{X_c}\right)^2 \quad (5.3)$$

Matrix tension ($\sigma_{22} \geq 0$):

$$F_m^t = \left(\frac{\sigma_{22}}{Y_t}\right)^2 + \left(\frac{\sigma_{12}}{S_{12}}\right)^2 \quad (5.4)$$

Matrix compression ($\sigma_{22} \leq 0$):

$$F_m^c = \left(\frac{\sigma_{22}}{2S_{23}}\right)^2 + \left(\left(\frac{Y_c}{2S_{23}}\right)^2 - 1\right) \left(\frac{\sigma_{22}}{Y_c}\right) + \left(\frac{\sigma_{12}}{S_{12}}\right) \quad (5.5)$$

Delamination was simulated by zero-thickness surface-based cohesive contact model. In the contact normal direction, when the stress components $\sigma_{33} < 0$ (compression), the two surfaces are governed by pressure-overclosure relationship. When the stress components $\sigma_{33} > 0$ (tensile)

or there are transverse shear stresses at interface, the bilinear traction and separation law will take charge of the case (Hibbit et al., 2012; Zhang and Zhang, 2015). If the surface does not begin to damage, then only traction and separation law contributes to interlaminar stresses. Once the cohesive stiffness starts degrading, the friction model with coefficient 0.3 activates and contributes to shear stresses. To avoid penetration between two surfaces, penalty contact behavior was added in the normal direction.

The contact stiffness in normal and transverse directions satisfy the requirements raised by (Turon et al., 2007, 2006), which is that the contact stiffness in normal direction needs to be larger than $50 E_2/t$, so as to without numerical singularity problems, where t is the thickness of adjacent laminae and E_2 is the elastic modulus in the transverse direction. The contact stiffness in transverse direction needs to be larger than $50G_{12}/t$, where G_{12} is the in-plane shear modulus of aligned fibers reinforced lamina. Besides, the mesh size at interface satisfies the requirement that it should be less than or equal to the cohesive zone length. All laminates are designed to be symmetric to their middle plane, and thus the cohesive traction in the normal direction, t_n , is decoupled from the cohesive separation in the transverse shear directions, δ_s and δ_t , as shown in the following equation.

$$\begin{bmatrix} t_n \\ t_s \\ t_t \end{bmatrix} = \begin{bmatrix} k_{nn} & 0 & 0 \\ 0 & k_{ss} & 0 \\ 0 & 0 & k_{tt} \end{bmatrix} \begin{bmatrix} \delta_n \\ \delta_s \\ \delta_t \end{bmatrix} \quad (5.6)$$

Delamination damage initiates, indicating the cohesive stiffness starts degrading, when the traction stresses in normal, t_n , and transverse directions, t_s and t_t , satisfy the following equation, which is quadratic stress criterion.

$$\left\{ \frac{t_n}{\sigma_n^c} \right\}^2 + \left\{ \frac{t_s}{\sigma_s^c} \right\}^2 + \left\{ \frac{t_t}{\sigma_t^c} \right\}^2 \geq 1 \quad (5.7)$$

The overall degrading scalar D was employed to capture the overall delamination failure propagation and its relationship with separation is shown in the equation (5.8).

$$D = \frac{\delta_m^f(\delta_m^{max} - \delta_m^o)}{\delta_m^{max}(\delta_m^f - \delta_m^o)} \quad (5.8)$$

Where δ_m^{max} is the effective separation when surfaces are totally fail under mixed-mode. δ_m^o represents for the separation of delamination onset. δ_m^f is the effective separation during failure propagation. The relationship between effective separation and separation in normal and shear direction is shown in the equation(5.9) (Camanho and Davila, 2002).

$$\delta_m = \sqrt{\langle \delta_n \rangle^2 + \delta_s^2 + \delta_t^2} \quad (5.9)$$

The interface failure propagation satisfies Benzeggagh-Kenane (B-K) fracture criterion (Benzeggagh and Kenane, 1996; Camanho and Davila, 2002; Hibbit et al., 2012), shown in the equation (5.10), which is suitable for transversely isotropic laminae ($G_{II}^c = G_{III}^c$).

$$G_I^c + (G_{II}^c - G_I^c) \left\{ \frac{G_S}{G_T} \right\}^\eta = G_m^c \quad (5.10)$$

Where $G_S = G_{II} + G_{III}$, $G_T = G_I + G_{II} + G_{III}$, G_m^c is the critical fracture energy release rate under mixed-mode and $\eta = 1.45$ is the cohesive property parameter.

In the present work, three-point bending, and low-velocity impact tests are going to be employed to analyze the damage of helicoid composites, and thus surface-based cohesive contact model was used, instead of cohesive elements. Cohesive elements are based on traction and separation law and only when cohesive elements totally fail, the penalty contact can contribute to the normal stresses (Hibbit et al., 2012). Cohesive elements work very well if the two surfaces through the thickness of the laminates are under tension or shear. However, if the dominant loading condition is compression, then cohesive elements are not accurate for predicting stresses and failure (Li et al., 2008; Zhang and Zhang, 2015).

Mesh convergence study is conducted by three or four sets of simulations both for short beam bending and low-velocity impact tests. In the short beam three-point bending, the first set is with 2024 SC8R (3 integration points per layer) elements per lamina and 480, 360 for second and third sets separately. The mesh convergence status of maximum peak load (P) and toughness (T_c) is shown in Figure 5.4(a) and (b), indicating that both P and T_c show the converged value with mesh size 2024 per layer.

In the low-velocity impact (LVI) tests on plate with 6mm thickness, 2013, 2422 and 3329 SC8R elements are created per layer for the laminates. Mesh convergence study on P and absorbed energy per unit volume is plotted in Figure 5.5(a)-(c). The converged inclination is clearly observed in Figure 5.5 (a) and Fig. (b) and thus models with 3329 elements per layer are employed for all LVI tests. On the other hand, for the plate with 24mm thickness, 2592, 3416, 4736 and 7040 SC8R elements are created per layer for the plate. Results of P and absorbed energy per unit volume are shown to be converged when the element number is 7040 per layer, see Figure 5.5(d)-(f).

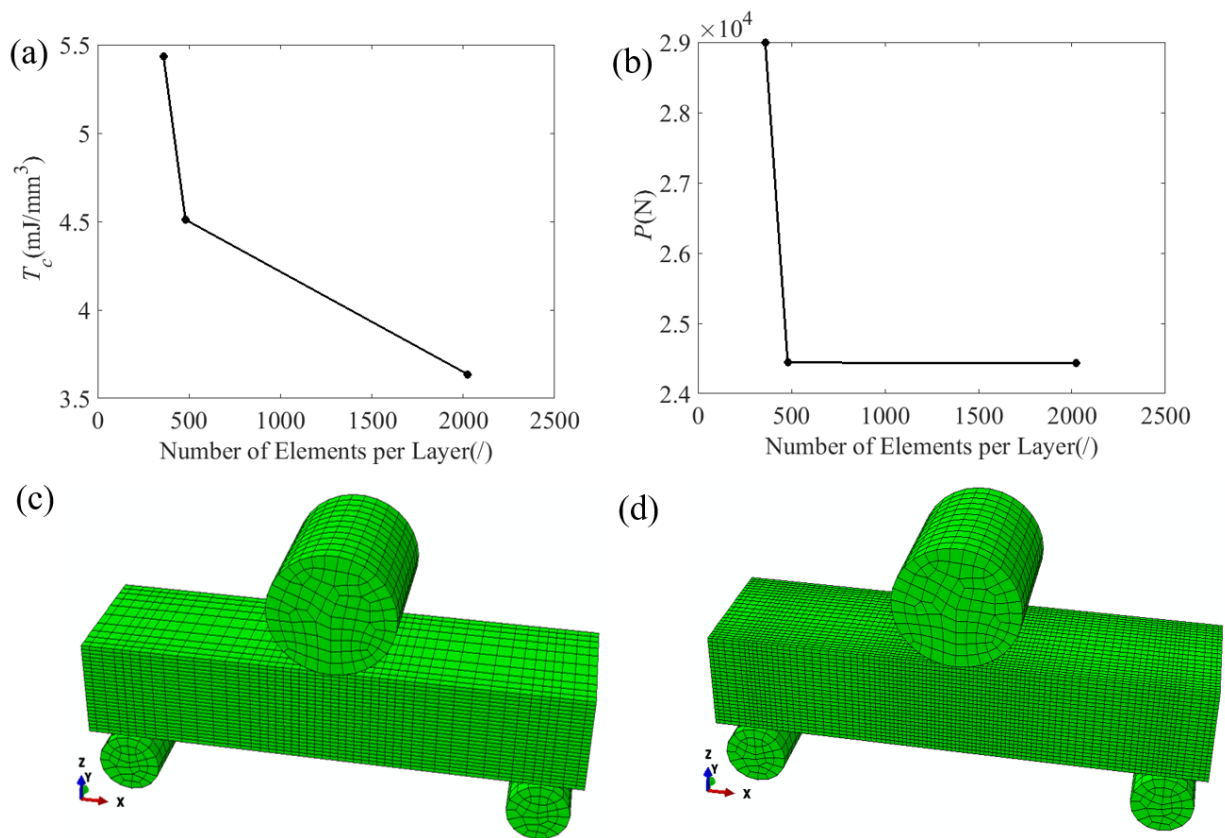


Figure 5.4. Mesh convergence study of (a) T_c (b) P . Mesh condition of short beam under three-point bending (c) with 480 elements per layer and (d) with 2024 elements per layer.

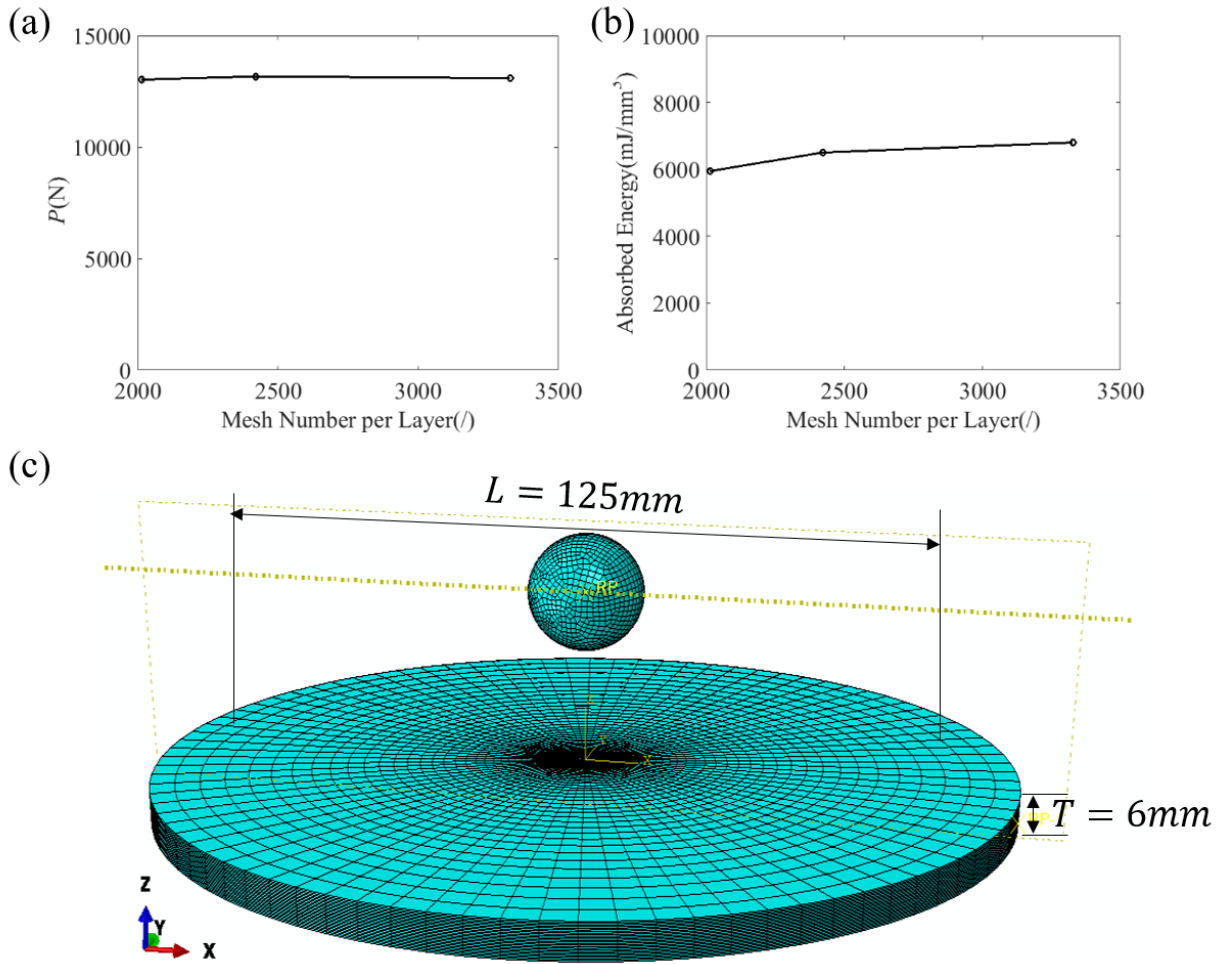
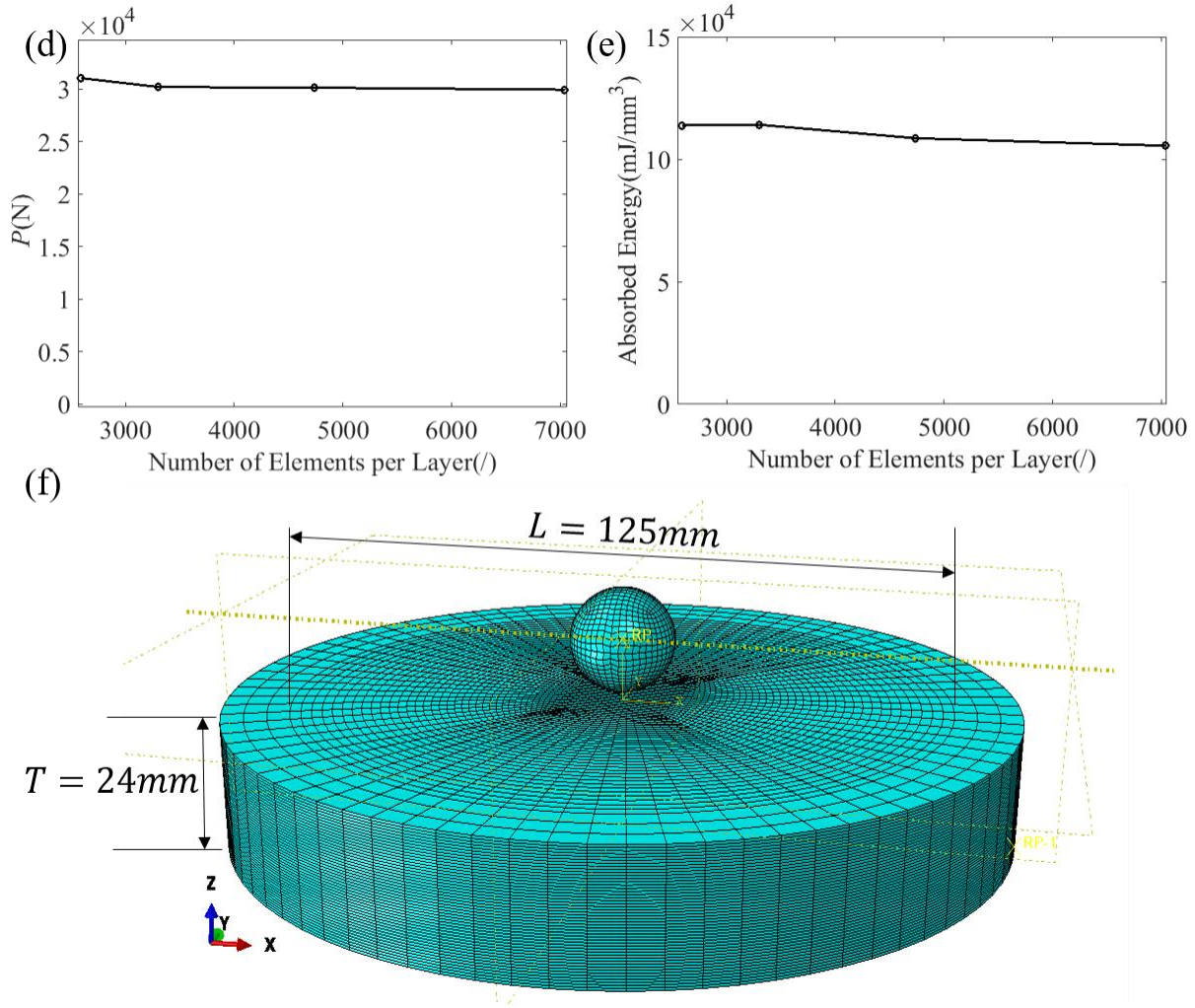


Figure 5.5. (a) P as a function of mesh number per layer with 6mm plate thickness (b) Absorbed energy per unit volume as a function of mesh number per layer with 6mm plate thickness (c) Mesh condition of LVI test with 3329 elements per layer with 6mm plate thickness (d) P as a function of mesh number per layer with 24mm plate thickness (e) Absorbed energy per unit volume as a function of mesh number per layer with 24mm plate thickness (f) Mesh condition of LVI test with 7040 elements per layer with 24mm plate thickness

Figure 5.5 continued



5.2.3 Loading conditions

Three-point bending on short beam and low velocity impact tests are chosen for validating the function of pitch angle gradient in helicoid architectures. The disadvantages of delamination are described in section 5.1, and our motivation is to understand if FGHs can provide balanced material properties derived from different θ_h s, such as balanced delamination failure and internal fiber/matrix damage to achieve higher toughness and higher peak load. Bending, compression and impact are three major loading conditions for validating delamination resistance, since delamination is sensitive to these loading conditions (Garg, 1988). In the present work, instead of long beam bending tests, we employ short beam bending, since short beam bending is transverse-

shear-stress dominant, rather than flexure failure which often occurs in long beam bending. Thus, the maximum peak load, P , represents for the maximum load to resist catastrophic delamination failure. Low velocity impact tests are conducted because no plastic deformation is observed in real experiments with low impact velocity (Ginzburg et al., 2017) and thus we can adopt linear elastic fracture mechanics and its sub-branch, cohesive model. Besides, low velocity impact, due to long time contact between impactor and the surface of plates, can produce global structure deformation, such as bending and transverse shear deformation, while ballistic impact can provide short time contact and the damage is highly localized.

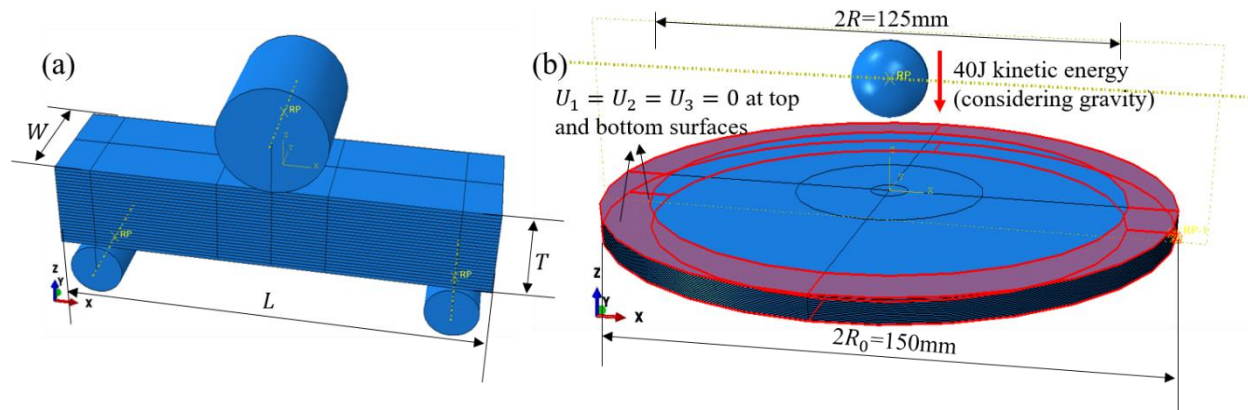


Figure 5.6. (a) the boundary and dimensions of short beam bending test and (b) the boundary condition of low velocity impact test

In FEA of three-point bending tests, the dimensions of short beam and indenter satisfy the requirements of ASTM D2344, as shown in Figure 5.6(a). The aspect ratios $L/T = 4$ and $W/T = 4/3$ keep constant through all the bending analyses. Loading cell is assigned 5mm/sec velocity downward (negative z direction) in ABAQUS/Explicit solver. General contact is employed for the whole model and cohesive contact behavior is specified at each interface of the laminated short beam.

In FEA of LVI tests, circular in-plane shape is with diameter 150mm and the clamped top and bottom surfaces ($U_x = U_y = U_z = 0$) constrain the plate with effective internal diameter as 125mm, shown in Figure 5.6(b). The impactor is assigned 40J energy for 6mm thick plate and 150J energy for 24mm thick plate (considering initial velocity and velocity due to drop height) before touch the surface of the laminate. General contact combined with specific cohesive contact behavior is employed in ABAQUS/Explicit solver, which is the same as the short beam bending

analysis. The dimensions of LVI tests reference ASTM D7136/D7136M – 15, except the shape of the laminates. Cylinder shape with suggested 6mm or 24mm thickness is used to avoid directional size effect of the damage and fracture that can be associated with the aspect ratio (Ginzburg et al., 2017), instead of rectangular shape as mentioned in the standard. Plates with 24mm thickness are created to keep lamina thickness consistent as the model of short beam bending test.

5.3 Dimensionless group of target parameters

There are substantial amounts of geometric and mechanical parameters involved in our study, and thus we need to do dimensionless group study to compare properties at the same level. For the case that helicoid architectures with constant θ_h , the known and unknown parameters are listed in the Table 5.2 and their potential dimensionless groups are included as well. The in-plane properties are also involved in the dimensionless groups study, including modulus of laminate ($\theta_h = 0^\circ$), E_1 , E_2 , ν_{12} , ν_{23} , G_{12} , G_{23} , and its tension and compression strength both in longitudinal(X_t, X_c) and transverse directions(Y_t, Y_c). In-plane shear strength (S_{12}) and transverse shear strength (S_{23}) are also included. Besides, energies dissipated during fiber tension(G_{1t}), fiber compression(G_{1c}), matrix tension(G_{2t}) and matrix compression(G_{2c}) failure modes are introduced to represent the linear softening of the laminate. Detailed values are tabulated in Table 5.2. Since we consider cohesive interaction at each interface, cohesive zone length ($l_{IIc} = \sqrt{\frac{E_2 G_{II}^c}{S_{12}^2} t}$) for mode II is included as well. Through using Buckingham π theorem, three sets of 25 dimensionless groups of parameters are all linearly independent to each other.

Table 5.2. Dimensionless groups of parameters in three-point bending test with constant θ_h

Known	$T, L, W, t, l_{IIc}, \theta_h, \sigma_n^c, \sigma_s^c, G_I^c, G_{II}^c, E_1, E_2, \nu_{12}, \nu_{23}, G_{12}, G_{23}, X_c, X_t, Y_c, Y_t, S_{12}, S_{23}, G_{1t}, G_{1c}, G_{2t}, G_{2c}$		
Unknown	P, A_d, T_c	No. of physical variables	27
Units	[F][L]	Necessary dimensionless groups	25
Input dimensionless group	$\pi_1 = \frac{T}{L}, \pi_2 = \frac{t}{T}, \pi_3 = \frac{\pi}{\theta_h}, \pi_4 = \frac{Y_c}{S_{23}}, \pi_5 = \frac{\sigma_n^c}{\sigma_s^c}, \pi_6 = \frac{G_I^c}{G_{II}^c}, \pi_7 = \nu_{12}, \pi_9 = \nu_{23}, \pi_{10} = \frac{X_t}{E_1}, \pi_{11} = \frac{X_c}{E_1}, \pi_{12} = \frac{Y_t}{E_2}, \pi_{13} = \frac{Y_c}{E_2}, \pi_{14} = \frac{S_{12}}{G_{12}}, \pi_{15} = \frac{S_{23}}{G_{23}}, \pi_{16} = \frac{G_{1t}}{G_{2t}}, \pi_{17} = \frac{G_{1c}}{G_{2c}}, \pi_{18} = \frac{\sigma_n^c}{Y_t}, \pi_{19} = \frac{\sigma_s^c}{S_{12}}, \pi_{20} = \frac{G_I^c}{G_{2t}}, \pi_{21} = \frac{G_{II}^c}{S_{23}}, \pi_{22} = \frac{X_t}{Y_c}, \pi_{23} = \frac{G_{2c}}{G_{1t}}, \pi_{24} = \frac{l_{IIc}}{T}, \pi_{25} = \frac{W}{L}$		
Output dimensionless group	$\pi_8 = \frac{P/LW}{\sigma_s^c}, \pi_8 = \frac{A_d}{LW}, \pi_8 = \frac{T_c \cdot W}{G_{II}^c}$		

Same for the case that helicoid with gradient θ_h through the thickness of the laminate, which is tabulated in Table 5.3. k is the linear slope of θ_h as a function of height H , $k = \frac{\theta_{h1} - \theta_{hN}}{H_1 - H_N}$, where θ_{h1} is the first pitch angle close to surface(top), θ_{hN} is the last pitch angle close to middle plane, which is shown in Figure 5.3, and $H_i = \sum_{i=1}^{i-1} D_i + \frac{D_N}{2}$, $D_i = \frac{\pi}{\theta_{hi}} t$, $T = \sum_{i=1}^N D_i$. All 26 dimensionless parameters are linearly independent to each other.

Table 5.3. Dimensionless groups of parameters in three-point bending test with gradient θ_h

Known	$T, L, W, t, l_{IIc}, k, N, \sigma_n^c, \sigma_s^c, G_I^c, G_{II}^c, E_1, E_2, \nu_{12}, \nu_{23}, G_{12}, G_{23}, X_c, X_t, Y_c, Y_t, S_{12}, S_{23}, G_{1t}, G_{1c}, G_{2t}, G_{2c}$		
Unknown	P, A_d, T_c	No. of physical variables	28
Units	[F][L]	Necessary dimensionless groups	26
Input dimensionless group	$\pi_1 = \frac{T}{L}, \pi_2 = \frac{t}{T}, \pi_3 = \frac{kt}{\pi}, \pi_4 = N, \pi_5 = \frac{Y_c}{S_{23}}, \pi_6 = \frac{\sigma_n^c}{\sigma_s^c}, \pi_7 = \frac{G_I^c}{G_{II}^c}, \pi_9 = \nu_{12}, \pi_{10} = \nu_{23}, \pi_{11} = \frac{X_t}{E_1}, \pi_{12} = \frac{X_c}{E_1}, \pi_{13} = \frac{Y_t}{E_2}, \pi_{14} = \frac{Y_c}{E_2}, \pi_{15} = \frac{S_{12}}{G_{12}}, \pi_{16} = \frac{S_{23}}{G_{23}}, \pi_{17} = \frac{G_{1t}}{G_{2t}}, \pi_{18} = \frac{G_{1c}}{G_{2c}}, \pi_{19} = \frac{\sigma_n^c}{Y_t}, \pi_{20} = \frac{\sigma_s^c}{S_{12}}, \pi_{21} = \frac{G_I^c}{G_{2t}}, \pi_{22} = \frac{G_{II}^c}{S_{23}}, \pi_{23} = \frac{X_t}{Y_c}, \pi_{24} = \frac{G_{2c}}{G_{1t}}, \pi_{25} = \frac{l_{IIc}}{T}, \pi_{26} = \frac{W}{L}$		
Output dimensionless group	$\pi_8 = \frac{P/LW}{\sigma_s^c}, \pi_8 = \frac{A_d}{LW}, \pi_8 = \frac{T_c \cdot W}{G_{II}^c}$		

For low-velocity impact tests. Instead of using rectangular shape in-plane, circular shape with radius, R , is employed. The dimensionless groups with functionally gradient θ_h under low-velocity impact are shown in Table 5.4. Buckingham theory is used to calculate the linear dependency of all 25 dimensionless groups of parameters and the all of them are linearly independent to each other.

Table 5.4. Dimensionless groups of parameters in low-velocity impact test with gradient θ_h

Known	$T, R, t, l_{IIc}, k, N, \sigma_n^c, \sigma_s^c, G_I^c, G_{II}^c, E_1, E_2, v_{12}, v_{23}, G_{12}, G_{23}, X_c, X_t, Y_c, Y_t, S_{12}, S_{23}, G_{1t}, G_{1c}, G_{2t}, G_{2c}$		
Unknown	$P, A_{dp} KE$	No. of physical variables	27
Units	[F][L]	Necessary dimensionless groups	25
Input dimensionless group	$\pi_1 = \frac{T}{R}, \pi_2 = \frac{t}{T}, \pi_3 = \frac{kt}{\pi}, \pi_4 = N, \pi_5 = \frac{Y_c}{S_{23}}, \pi_6 = \frac{\sigma_n^c}{\sigma_s^c}, \pi_7 = \frac{G_I^c}{G_{II}^c}, \pi_9 = v_{12}, \pi_{10} = v_{23}, \pi_{11} = \frac{X_t}{E_1}, \pi_{12} = \frac{X_c}{E_1}, \pi_{13} = \frac{Y_t}{E_2}, \pi_{14} = \frac{Y_c}{E_2}, \pi_{15} = \frac{S_{12}}{G_{12}}, \pi_{16} = \frac{S_{23}}{G_{23}}, \pi_{17} = \frac{G_{1t}}{G_{2t}}, \pi_{18} = \frac{G_{1c}}{G_{2c}}, \pi_{19} = \frac{\sigma_n^c}{Y_t}, \pi_{20} = \frac{\sigma_s^c}{S_{12}}, \pi_{21} = \frac{G_I^c}{G_{2t}}, \pi_{22} = \frac{G_{II}^c}{S_{23}}, \pi_{23} = \frac{X_t}{Y_c}, \pi_{24} = \frac{G_{2c}}{G_{1t}}, \pi_{25} = \frac{l_{IIc}}{T}$		
Output dimensionless group	$\pi_8 = \frac{P/\pi R^2}{\sigma_s^c}, \pi_8 = \frac{A_{dp}}{\pi R^2}, \pi_8 = \frac{KE \cdot R}{G_{II}^c}$		

5.4 Results and discussion

5.4.1 Three-point bending on short beam by using FEA

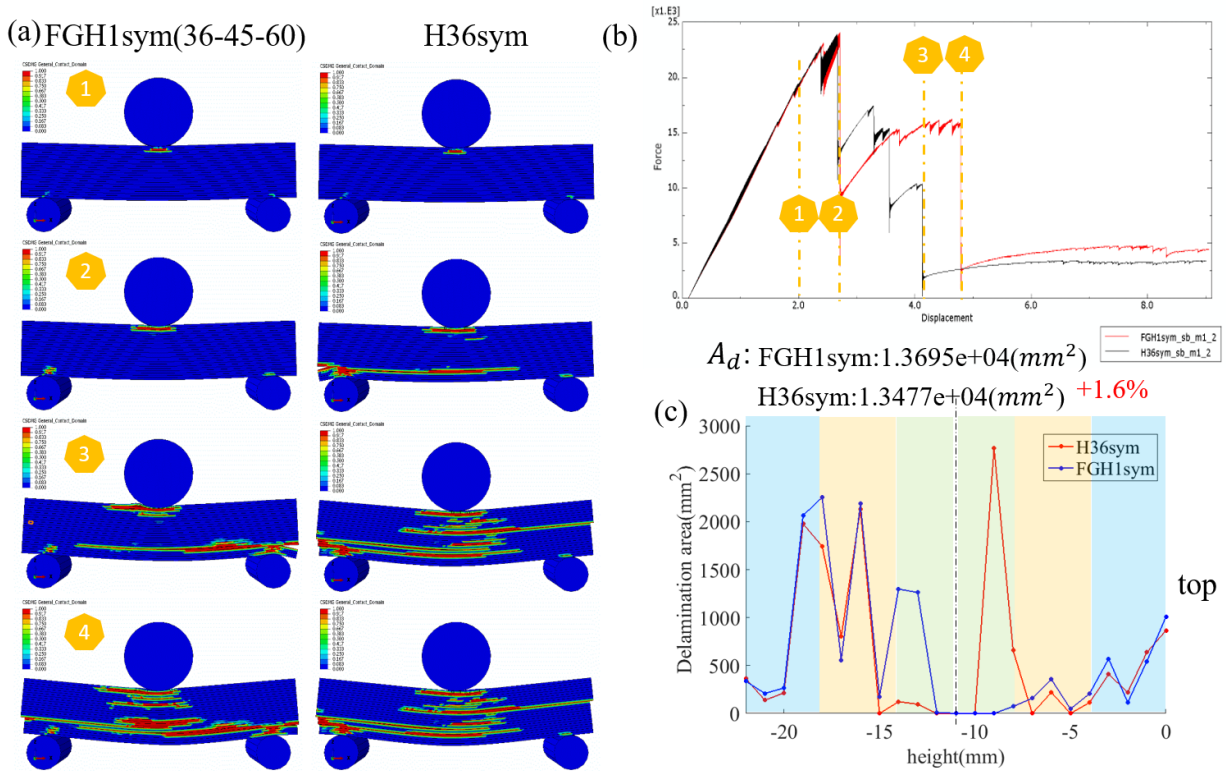


Figure 5.7. (a) Delamination failure distribution through the thickness of short beams FGH1sym and H36sym (b) Load and displacement curves of FGH1sym (red) and H36sym (black) (c) Delamination area distribution layer by layer. Different shaded color represents for different pitches of FGH1sym

In this section, the results of FGH1sym and FGH2sym, combined with their associated helicoid architectures, H30sym($\theta_h = 30^\circ$), H36sym($\theta_h = 36^\circ$), H45sym($\theta_h = 45^\circ$), H60sym($\theta_h = 60^\circ$) and H90sym($\theta_h = 90^\circ$) are introduced and discussed. In order to investigate the trend of different pitch angle, H15sym($\theta_h = 15^\circ$), H22.5sym($\theta_h = 22.5^\circ$) are also adopted to compare the mechanical properties. Our target outputs, as introduced in section 5.3, are maximum peak load, P , toughness, T_c , and whole delamination area through the thickness, A_d , of the laminated beam.

Figure 5.7(a) shows the schemes of delamination failure at proceeding applied displacement points shown in Figure 5.7 (b). At point 1, local delamination failure occurs in the laminates close to rigid indenter due to concentrated contact force. However, this local delamination failure cannot lead to catastrophic failure for the whole laminate, which means huge

drop in the force and displacement curve. This local delamination failure only brings minor drop in the load and displacement curve, and the degradation of stiffness before and after drop can be ignored, see Figure 5.12(a)-(c). The maximum peak load before 1st drop, P_{1std} , occurring in the force and displacement curve is illustrated as a function of pitch angle, θ_h , shown in Figure 5.12(d). Except H90sym, helicoids with increasing values of θ_h exhibit higher P_{1std} . The FGHs do not show any benefits over their associated laminates with same θ_h . However, P_{1std} is unable to present the general property of the whole laminated beam, and thus this parameter is not our target output.

It is observed that H36sym shows catastrophic delamination failure earlier than FGH1sym at point 2 of applied displacement, indicating that maximum peak load, P , of FGH1sym is higher than the P of H36sym under 3-point bending. From point 2 to point 4, it is clear to see the propagation of delamination failure through the thickness of two laminated beams. As shown in Figure 5.7 (b), after P occurs, FGH1sym stores more energy than H36sym before total failure happens and FGH1sym can provide more deformation than H36sym. The delamination area layer by layer of FGH1sym and H36sym is illustrated in Figure 5.7 (c). Although maximum delamination area occurs in the middle layer of H36sym, the sum of the delamination area through the thickness, A_d , of FGH1sym is 1.6% larger than the A_d of H36sym. Compared with H36sym, FGH1sym also shows 1.1% higher value of P and up to 23.8% benefits on T_c . The comparison on A_d , P and T_c between FGH1sym and its other associated laminated helicoidal beam is summarized in Figure 5.8 and Figure 5.9. Besides, the comparison on delamination propagation between FGH1sym and FGH1symdisorder is shown in Figure D5.

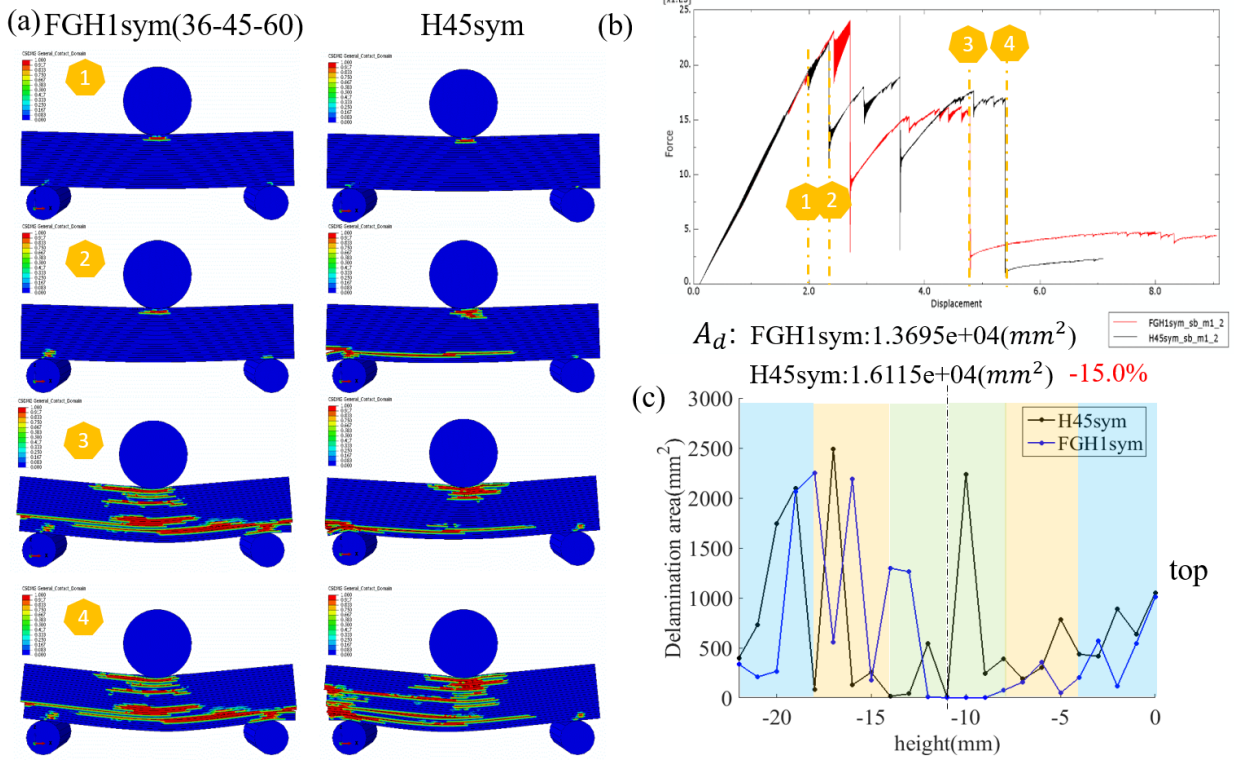


Figure 5.8. (a) Delamination failure distribution through the thickness of short beams FGH1sym and H45sym (b) Load and displacement curves of FGH1sym (red) and H45sym (black) (c) Delamination area distribution layer by layer. Different shaded color represents for different pitches of FGH1sym

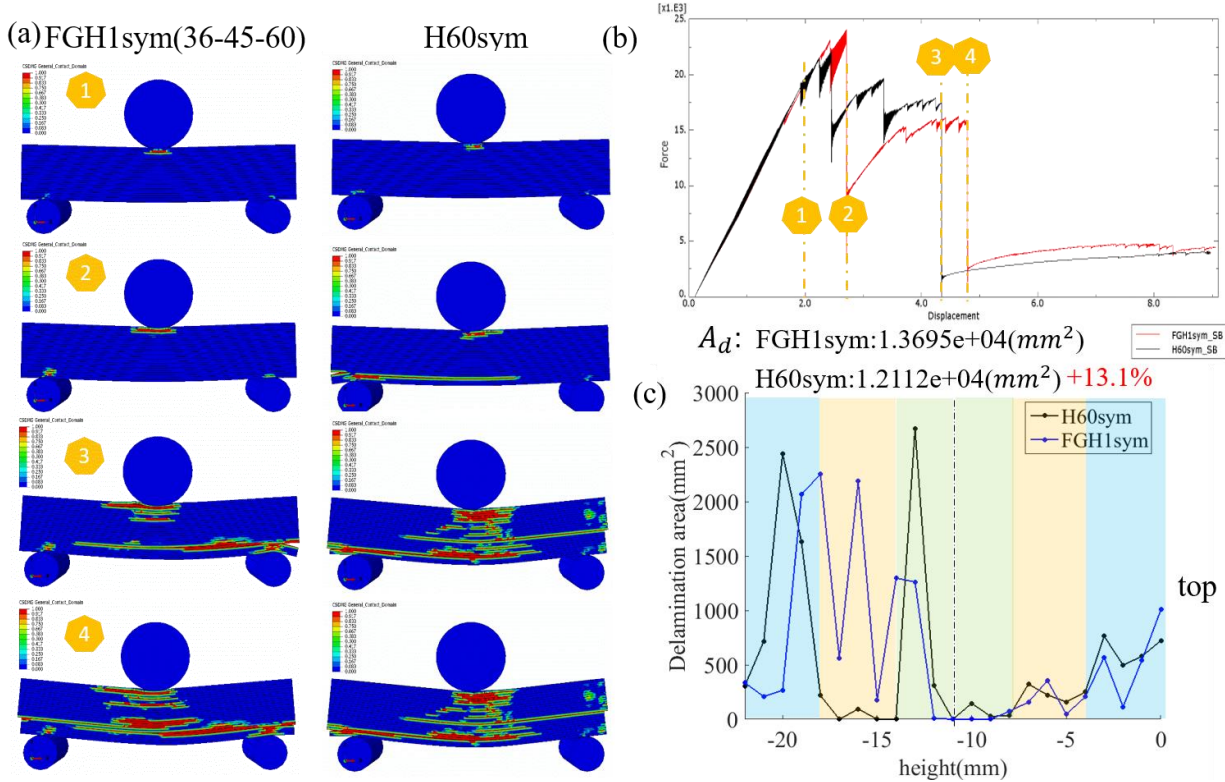


Figure 5.9. (a) Delamination failure distribution through the thickness of short beams FGH1sym and H60sym (b) Load and displacement curves of FGH1sym (red) and H60sym (black) (c) Delamination area distribution layer by layer. Different shaded color represents for different pitches of FGH1sym

As shown in Figure 5.8 and Figure 5.9, FGH1sym is featured with 8.2% and 10.6% higher P compared with H45sym and H60sym separately, which represents that FGH1sym can endure more load before catastrophic delamination failure occurs. Although, FGH1sym does not show benefits on T_c over H45sym, 8.5% lower T_c than H45sym, it provides generally higher P and up to 23.8% higher T_c than H36sym. The comparison between FGH2sym and its associated laminates is illustrated in Appendix D1.

The comparison on P and T_c among FGHs and helicoids with constant θ_h under 3-point bending are illustrated in Figure 5.10. P values of helicoids show decreasing values when θ_h is increasing from 30° to 90° , whereas helicoids with $\theta_h = 15^\circ$ and $\theta_h = 22.5^\circ$ exhibit lower value of P . T_c of H45sym is maximum among other helicoids, whereas H15sym also exhibits competitive value of T_c . It is worthy to be noted that H90sym does not totally fail until the applied displacement point that we calculate the T_c , which is 6mm in z direction. FGH1disorder exhibits

lower peak load value than its associate laminates, while it can provide the same toughness of H36sym, but lower value than H45sym and H60sym.

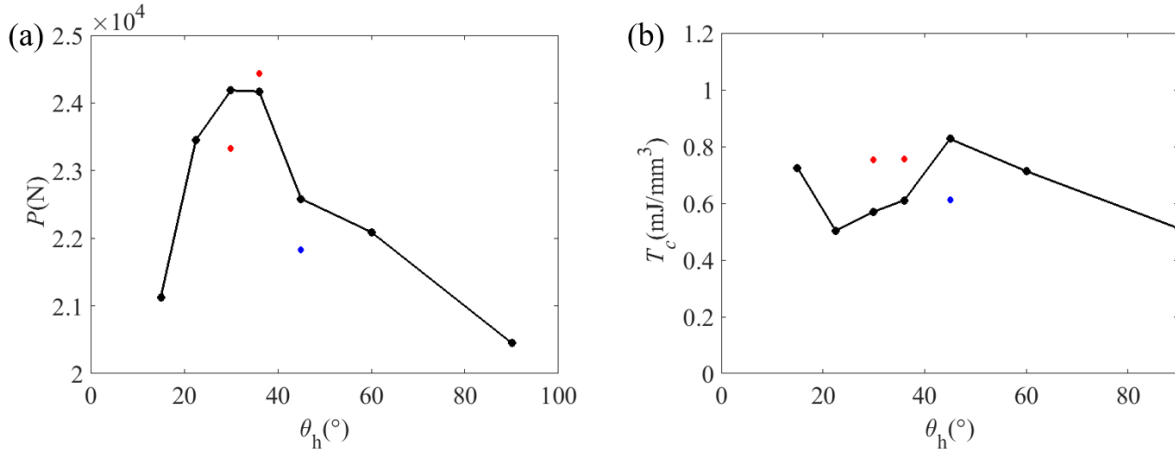


Figure 5.10. (a) P as a function of θ_h of helicoidal-laminated-short beam under 3-point bending (b) T_c as a function of θ_h of helicoidal-laminated-short beam under 3-point bending (red dots represent for FGHS with corresponding θ_h laid close to surface and blue dot represents for FGHS1 disorder)

To compare overall properties of FGHS and their associated helicoid laminates simultaneously, Ashby plot with target outputs, P and T_c , is designed and illustrated in Figure 5.11(a). Helicoids with constant θ_h either show higher P but lower T_c , or larger T_c but lower P , while FGHS can provide higher T_c and P at the same time. As shown in Figure 5.11(a), only FGHS and H45sym locate at the optimum area of the Ashby plot. FGHS1symdisorder exhibits lower values of peak load and toughness. Helicoids with middle θ_h , such as $\theta_h = 22.5^\circ$, $\theta_h = 30^\circ$ and $\theta_h = 36^\circ$, provide substantial P , whereas helicoids with smaller θ_h , such as $\theta_h = 15^\circ$, stores more energy and then can provide more deformation before catastrophic failure occurs. Larger pitch angle laminates, such as H90sym, H60sym and H45sym laminates, which are closer to conventional cross-ply, angle-ply, and quasi-isotropic laminates respectively, can provide less peak load, but higher toughness under three-point short beam bending.

In three-point short beam bending tests, transverse shear stresses are dominant for failure, and thus P and T_c are dependent on delamination initiation and evolution. It is necessary to investigate the relationship among delamination area, A_d , P and T_c , which is shown in Figure 5.11(b)-(c). Delamination failure releases the stress concentration through the thickness of laminated short beams and thus the initiation of intralaminar damage, especially fiber breakage, can be delayed, which can store more energy before catastrophic failure occurs, since stiffness of

fibers contributes majority stiffness to the overall laminated beams. Matrix split through the thickness is another important failure mechanism needs our attention. In Figure 5.11(c), FGHs, H15sym, H60sym and H45sym locate at the optimum area, which means that they can provide higher T_c and higher A_d simultaneously. However, in Figure 5.11(d), only FGHs and H45sym still drop in the optimum area of Ashby plot with parameters P and A_d .

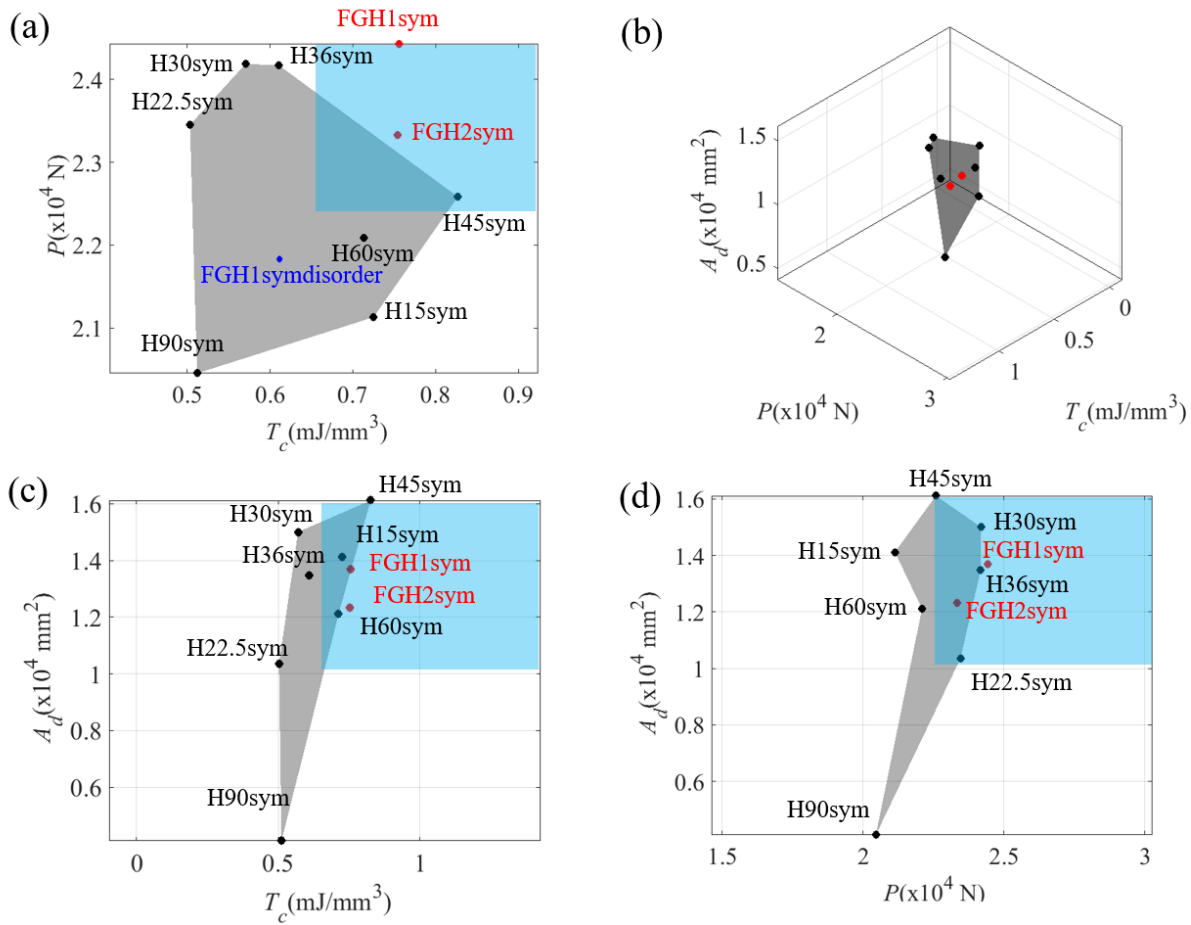


Figure 5.11. Ashby plots of three-point short beam bending tests (a) Ashby plot with parameters P and T_c (b) 3D Ashby plot with parameters T_c , P and A_d (c) Ashby plot of parameters P and A_d (d) Ashby plot of parameters T_c and A_d (red dots represent for FGHs with corresponding θ_h laid close to surface and blue dot represents for FGH1disorder)

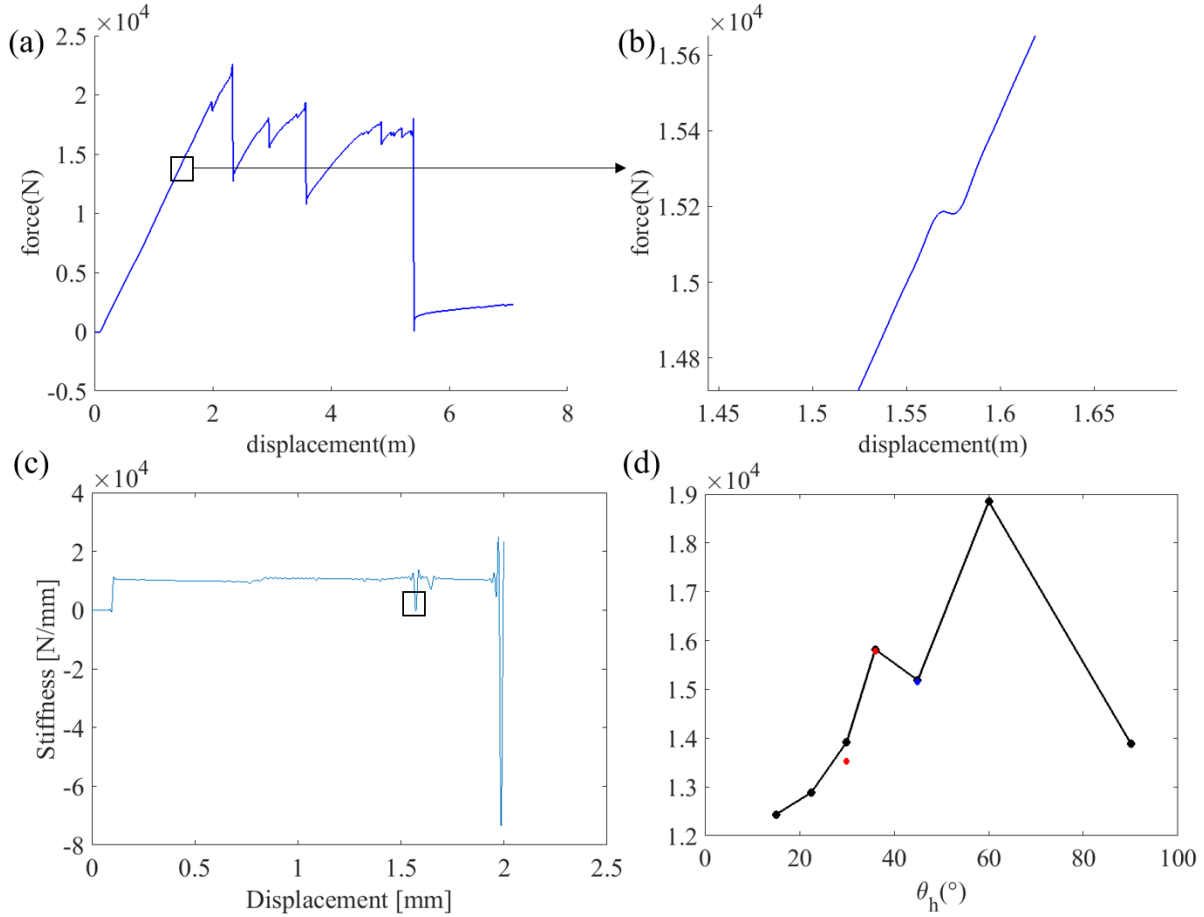


Figure 5.12. (a) Force and displacement plot of H45sym under three-point bending test (b) Zoom in plot of force and displacement curve of H45sym under three-point bending test (c) First derivative on force and displacement curve of H45sym (d) Peak load before 1st drop in displacement and load curves of short beams with different pitch angles, θ_h , and functionally gradient helicoids (FGH1syma and FGH2sym, shown in red dots). The θ_h of FGH1sym and FGH2sym shown here is the first θ_h (close to top) of FGH laminated beam.

5.4.2 Low velocity impact on the laminated plate using FEA

In addition to quasi-static analysis, dynamic analysis is also conducted in the present work, since impact loading condition is one of the major loading acts for biological materials. Two sets of models are prepared, one with 6mm thickness under 40J impact and one with 24 mm thickness under 150J impact. The latter model is with the same thickness as short beam bending models. Thinner plate with 6mm thickness is dominant by global flexure deformation, while thicker plate with 24mm thickness is dominant by transverse shear stresses. Both sets of models are under the impact of shear wave and tension stress wave, whereas compression stress wave does not influence delamination.

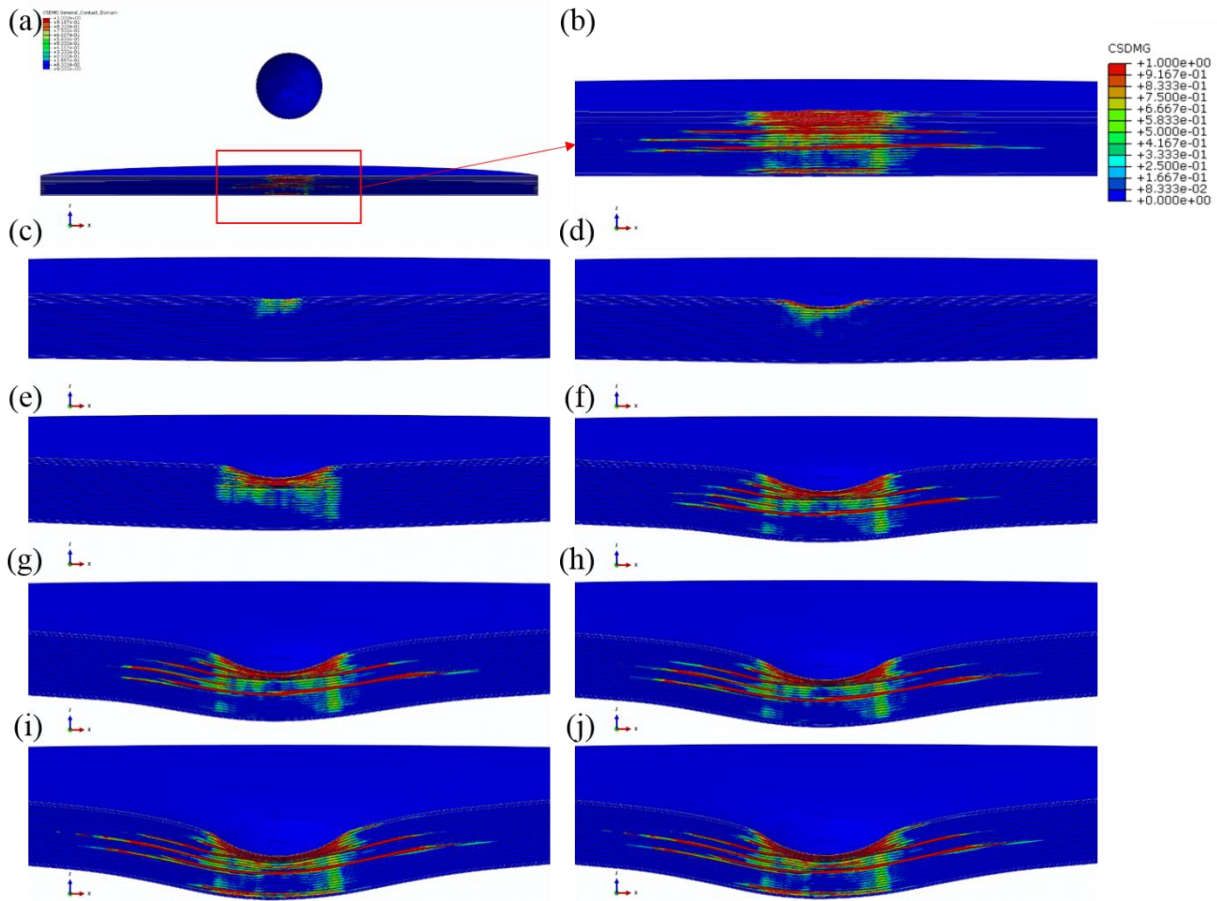


Figure 5.13. Contours of delamination process of H15sym under 40J LVI with 6mm thickness (a) The cross-section of H15sym at final state of LVI simulation (b) Zoom-in contour of delamination distribution through the thickness of H15sym at final state of LVI simulation (c)-(i) Zoom-in contours of delamination process through the thickness of H15sym (j) Zoom-in contour of delamination distribution through the thickness of H15sym at peak dent depth before rebounding

Figure 5.13(a)-(j) show the process of delamination at cross-section in $x - z$ plane, where $CSDMG$ is the failure factor to present the level of delamination. As introduced in section 5.4.2, when $CSDMG > 0$, it represents that the two nodes at one point of interface start to damage, in the propagation of damage. $CSDMG = 1$ represents for the case that two nodes at one point of interface are totally separate, denoted as delamination. As shown in Figure 5.14(a)-(d), the laminate can provide peak load and peak dent depth under 40J and 150J LVI loading. Once the force reaches the maximum load, it rebounds to the original point of force and displacement curve. No plasticity and viscosity are added to the laminate.

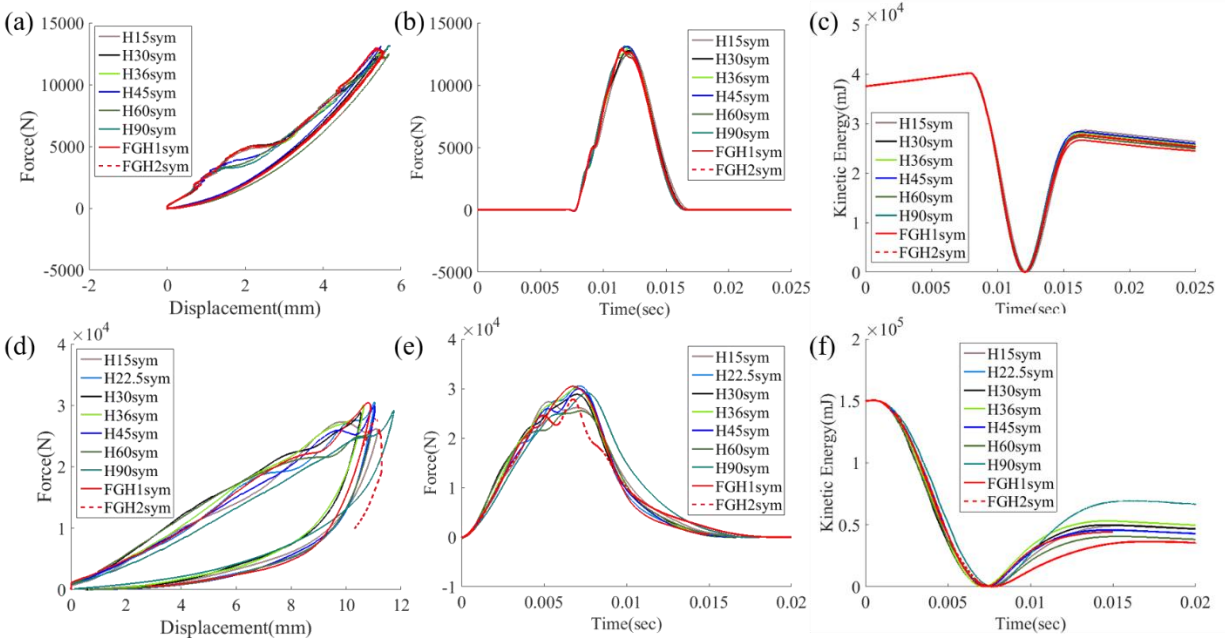


Figure 5.14. (a) Plot of force and displacement in LVI tests with total thickness 6mm (b) Force and time plot of LVI tests with total thickness 6mm (c) Plot of kinetic energy as a function of time with total thickness 6mm (d) Plot of force and displacement in LVI tests with total thickness 24mm (e) Force and time plot of LVI tests with total thickness 24mm (f) Plot of kinetic energy as a function of time with total thickness 24mm

From Figure 5.14(c), before impactor touches the surface of the laminate, the input energy is 40J. After rebounding, the energy of the whole model, including laminate and impactor, decreases to different values, which is dependent on the θ_h of the laminates, since the only parameter we changed during the analyses is θ_h . Besides, Figure 5.14(d) to (f) exhibit the force and displacement plot, force as a function of time plot and kinetic energy as a function of time plot of 24mm thick plate under 150J LVI. With increasing thickness of the plate, the difference among models with distinct pitch angles are augmenting as well.

Target outputs of LVI tests are absorbed energy (KE), Peak load (P), delamination area (A_d) and projected delamination area (A_{pd}), combing with the energy from intralaminar damage ($ALLDMD$). Most significant outputs, representing for the general mechanical behaviors of the materials, are KE and P . KE is the key factor to represent for the ability of dissipating energy, while P is the factor to show the maximum load before rebounding. A_d can provide the information about the contribution of absorbed energy from interlaminar, whereas $ALLDMD$

provides the information of intralaminar damage energy. A_{pd} convey the extent of delamination area in $x - y$ plane.

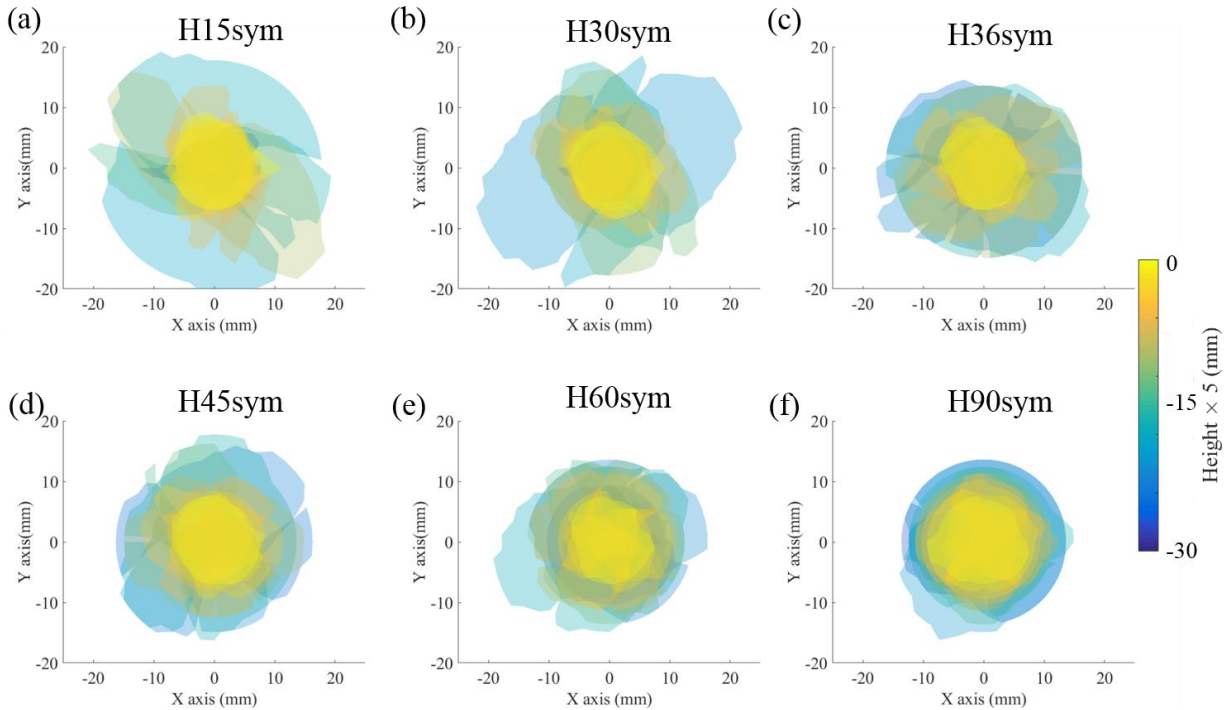


Figure 5.15. Projected delamination area A_{pd} of (a) H15sym, (b) H30sym, (c) H36sym, (d) H45sym, (e) H60sym and (f) H90sym with thickness 6mm

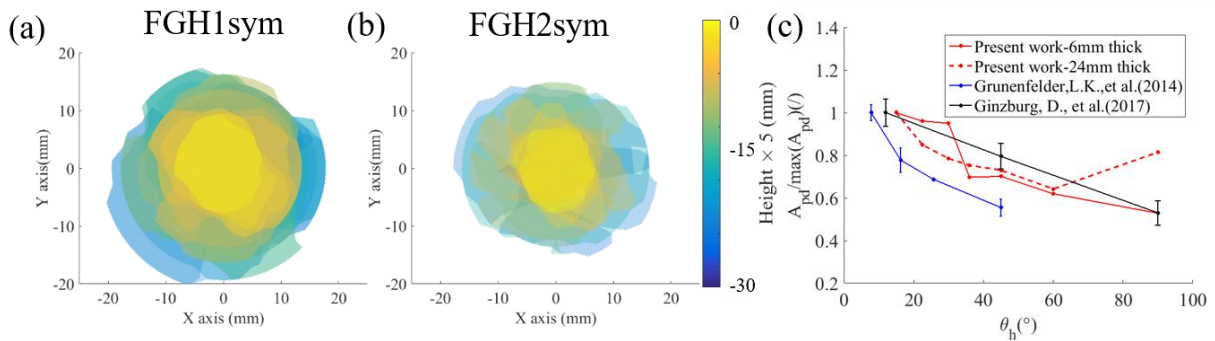


Figure 5.16. Projected delamination area A_{pd} of (a) FGH1sym, (b) FGH2sym with thickness 6mm (c) Normalized projected delamination area as a function of pitch angle (normalized by the maximum value of each set of data)

From Figure 5.15(a)-(f), the A_{pd} through the thickness of laminates with different θ_h is presented. Light yellow represents for the delamination area close to top surface, whereas the dark blue denotes the delamination close to the bottom of the laminates. Here height is multiplied by

five in order to show the delamination through thickness clearly, which is shown in appendix D3. It is observed that the laminate with less θ_h shows larger extent of in-plane delamination area (A_{pd}), up to 47.2% difference between H15sym and H90sym, also shown in Figure 5.17(c), which is the same as the observation from (Ginzburg et al., 2017; Grunenfelder et al., 2014b), see Figure 5.16(c). Projected delamination, A_{pd} , of smaller pitch angle is larger than others is because laminates with smaller pitch angle include more material principal directions in $x - y$ plane than the laminates with larger pitch angle and delamination propagates along the fiber direction (the direction with higher strain energy) of both layers close to the interface (Jiang et al., 2019; Long et al., 2015). The interesting observation is that FGH1sym shows generally larger A_{pd} compared with H36sym, H45sym and H60sym, while FGH2sym shows balanced value of A_{pd} , larger than H90sym but less than H30sym. However, the summation of delamination area through the thickness A_d of both FGH1sym and FGH2sym is larger than helicoid laminates with constant θ_h , as shown in Figure 5.17 (d). It also exhibits laminates with larger θ_h can provide higher value of A_d , but lower value of A_{pd} . The projected delamination area (A_{pd}) of models with 24 mm thickness is illustrated in appendix D4, which reveals the similar distribution on A_{pd} as 6mm thick plate does, also shown in Figure 5.18(c).

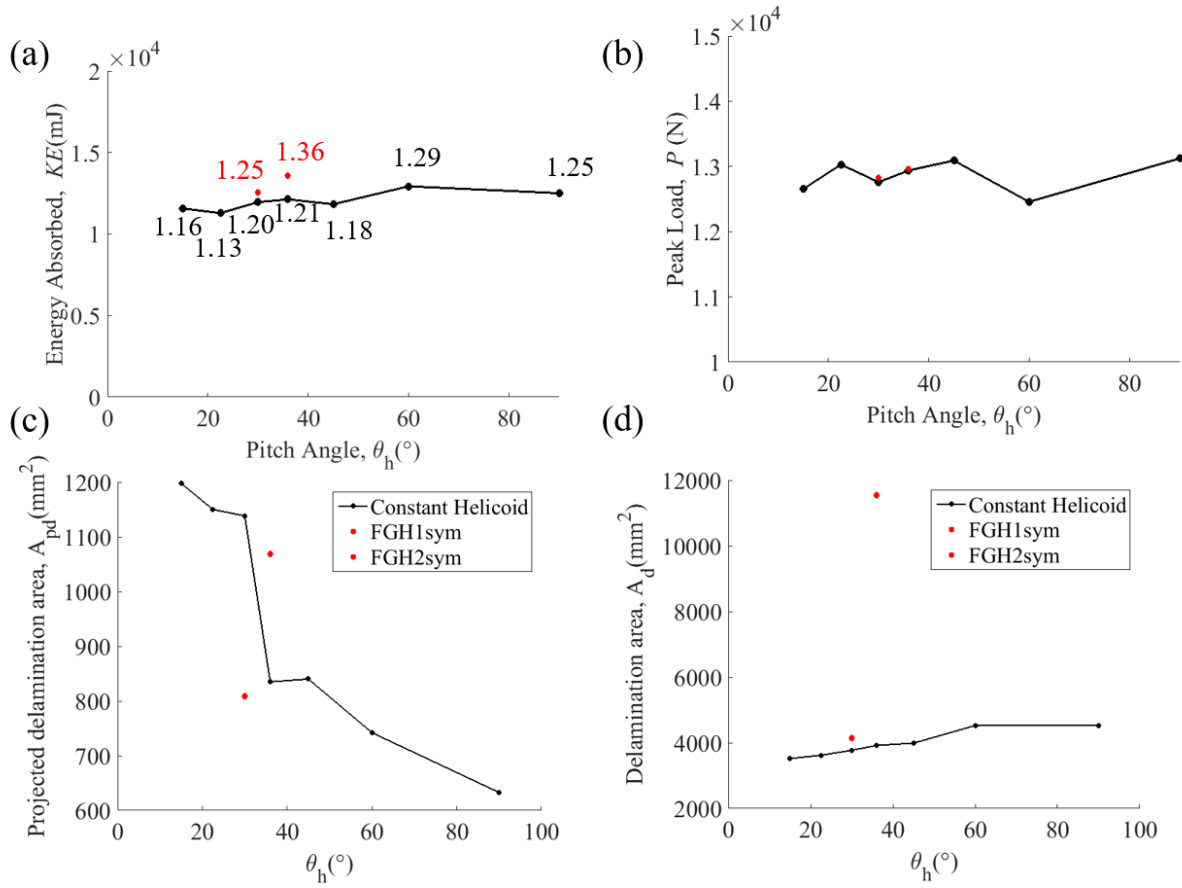


Figure 5.17. (a) Absorbed kinetic energy (KE) as a function of pitch angle (θ_h) with plate thickness 6mm (b) Peak load (P) as a function of θ_h with plate thickness 6mm (c) Projected delamination area (A_{pd}) as a function of θ_h with plate thickness 6mm (d) Delamination area in all through the thickness (A_d) as a function of θ_h with plate thickness 6mm

Figure 5.17(a) exhibits that functionally gradient helicoids can provide up to 15.3% higher absorbed kinetic energy (KE) than its associated θ_h of helicoid laminates. The relation between helicoids with different θ_h and absorb higher values of KE are not monotonically increasing or decreasing. The difference on P among laminates with different θ_h is minor, less than 5%. The values of P of FGHs do not overcome its laminates with associated θ_h , but maintain the P of θ_h close to top surface.

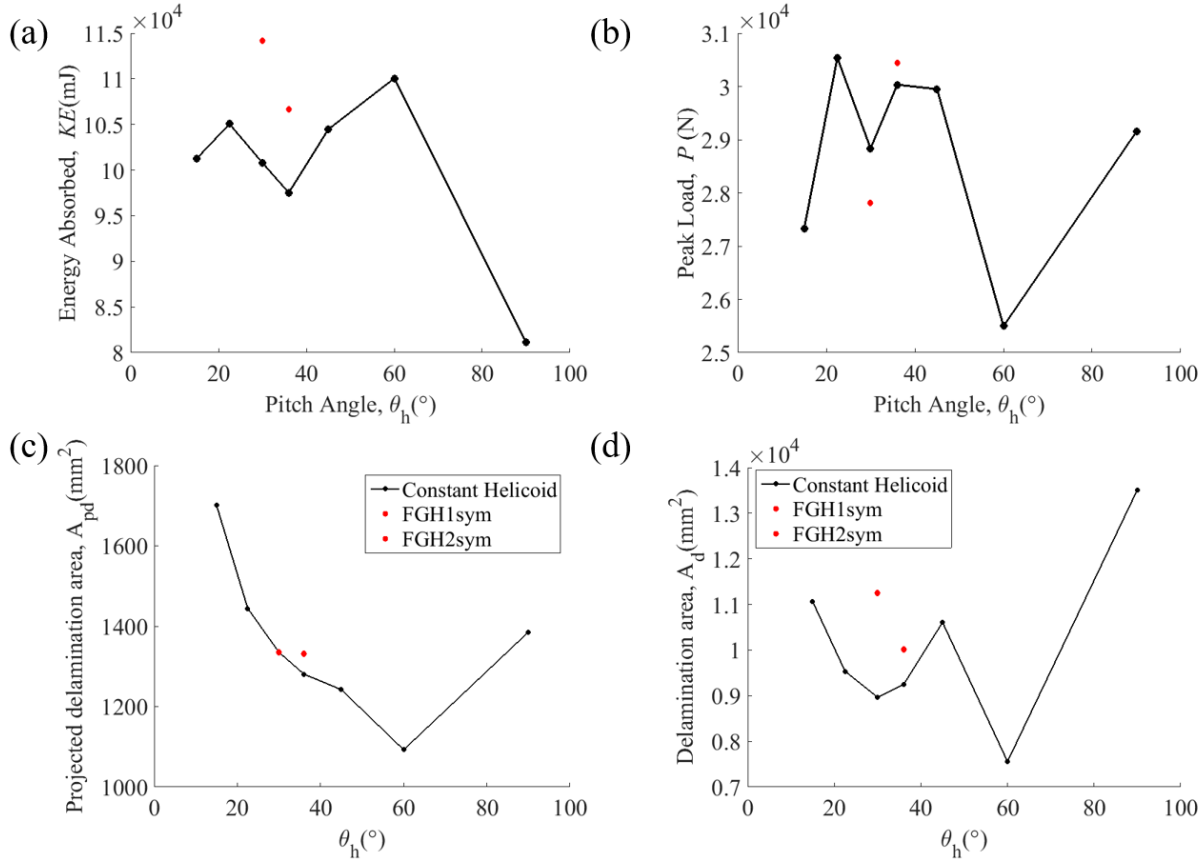


Figure 5.18. (a) Absorbed kinetic energy (KE) as a function of pitch angle (θ_h) with plate thickness 24mm (b) Peak load (P) as a function of θ_h with plate thickness 24mm (c) Projected delamination area (A_{pd}) as a function of θ_h with plate thickness 24mm (d) Delamination area in all through the thickness (A_d) as a function of θ_h with plate thickness 24mm

Similar as architectures with 6mm thickness in FEA, architectures with 24mm thickness also show that helicoid architectures with gradient pitch angle are featured with up to 40.8% higher values of absorbed energy than H90sym and 13.3% higher values of absorbed energy than H30sym, which are the associated architectures in FGH2sym, shown in Figure 5.18(a). Peak load, P , of FGHs does not show generally superior benefits over their associated architectures, see Figure 5.18(b), which needs further comparison and analysis in Ashby plots considering energy absorbed and peak load simultaneously. In Figure 5.18(c), it is revealed that in thicker plate the projected delamination area, A_{pd} , is increasing once the pitch angle, θ_h , is decreasing, except H90sym, which is much closer to cross-ply, instead of helicoid architecture. This result is similar as what we achieved in thinner plate under 40J impact, shown in Figure 5.17(c). FGHs show

maximum 32.5% larger values on summation of delamination area, A_d , than their associated architectures, shown in Figure 5.18(d).

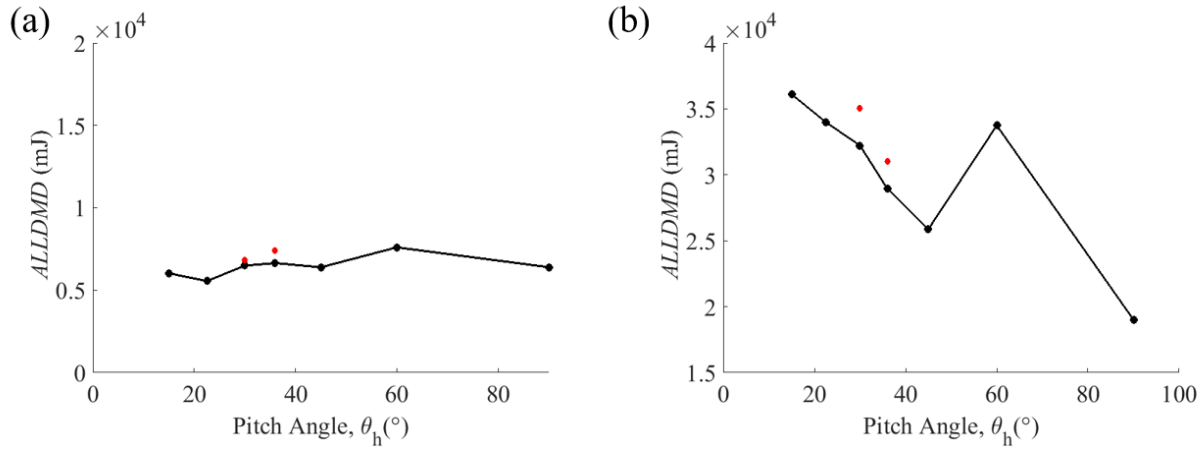


Figure 5.19. (a) Energy dissipated from intralaminar failure as a function of θ_h featured with thickness 6mm (b) Energy dissipated from intralaminar failure as a function of θ_h featured with thickness 24mm

Laminates also employed intralaminar damage to dissipate energy, such as fiber and matrix damage, which is represented by Hashin criteria in the present work. Energy dissipated by intralaminar damage ($ALLDMD$) of helicoid architectures with thickness 6mm and 24mm is summarized in Figure 5.19(a) and Figure 5.19(b). The difference on $ALLDMD$ among different θ_h featured with 6mm thickness is minor, less than 36.9%, while the difference on $ALLDMD$ among different θ_h featured with 24mm thickness is up to 90.0%. Except H60sym, architectures with smaller θ_h exhibit higher values of energy dissipated by intralaminar damage in 24mm thick laminate, whereas architectures with 6mm thickness do not show obvious trend on $ALLDMD$ as a function of θ_h . The value of $ALLDMD$ of FGH2sym with 6mm thickness is close to the values of their associated laminates, and the difference is less than 6.7%. FGH1sym with 6mm thickness provides higher values of $ALLDMD$ than H36sym and H45sym, up to 15.7%, but 2.7% lower value of $ALLDMD$ than H60sym, Architectures with $\theta_h = 60^\circ$ reveal outstanding energy dissipated by intralaminar damage both in 6mm and 24mm thickness among other pitch angles. If we assume the kinetic energy is majorly contributed by intralaminar damage ($ALLDMD$) and interlaminar damage (A_d) since the energy dissipated by friction and artificial work is minor, it is observed that $ALLDMD$ plays a more significant role compared with A_d , see Figure 5.18(a), (d) and Figure 5.19(b). For example, H60sym dissipates higher values of kinetic energy by $ALLDMD$, whereas

its A_d is the smallest among other architectures. H90sym is featured with lowest value of kinetic energy dissipated and lowest value of $ALLDMD$, but highest value of A_d among other helicoid architectures. According to these results, it is clear that $ALLDMD$ occupies more weights contributing to kinetic energy absorption, compared with interlaminar damage(delamination).

From Figure 5.17(a) and (d), combined with Figure 5.19(a), it is observed that the benefits on KE of FGHs over their associated laminates are derived from both the energy dissipated by intralaminar damage ($ALLDMD$) and interlaminar failure (A_d). However, the weight of dissipated energy by interlaminar failure contributed to KE is much smaller than the weight of intralaminar damage, especially fiber damage. FGHs sacrifice less intralaminar damage, but larger value of interlaminar failure to achieve higher value of KE , compared with their associated laminates.

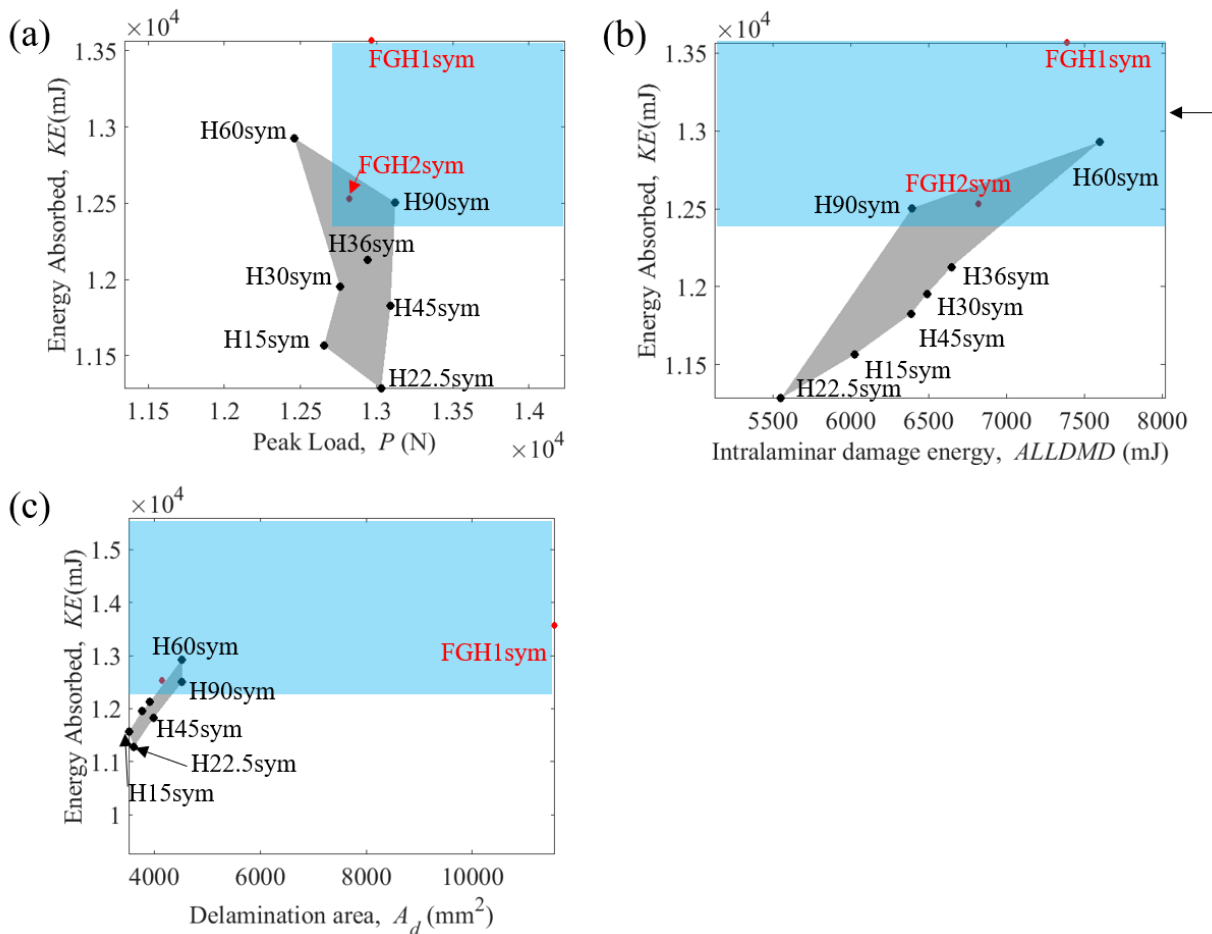


Figure 5.20. (a) Ashby plot of absorbed energy KE and Peak load P of models with thickness 6mm (b) Ashby plot of energy dissipated by intralaminar damage and absorbed energy KE of models with thickness 6mm (c) Ashby plot of delamination area A_d and absorbed energy KE of models with thickness 6mm

Similar as three-point bending tests, Ashby plots of key parameters outputted from LVI tests with thickness 6mm are illustrated to analyze the optimum θ_h and the functions of gradient in pitch angle, see Figure 5.20. In the range of smaller and middle θ_h , such as H15sym, H22.5sym, H30sym and H36sym, the energy absorbed, KE , are relatively smaller than the KE of larger θ_h , as shown in Figure 5.20(a). Meanwhile, laminates with larger θ_h either show higher P but less KE , or larger KE but lower values of P . For instance, H60sym exhibits highest value of KE , whereas it provides lower P among helicoids. Same with the results of three-point bending tests, FGHs occupy the optimum area of Ashby plot, which is the upper right corner with higher values of KE and P at the same time. As shown in Figure 5.20(b) and Figure 5.20(c), the highest values of KE of H60sym is contributed by larger amount of intralaminar damage, compared with other helicoid laminates. FGH1sym can absorb higher values of KE , up to 13.2% over its associated laminates, is largely dependent on superior delamination area. Additionally, H90sym also behaves superior to other helicoid laminates under LVI with 40J, locating in the optimum corner of Ashby plot with higher values of P and KE .

FGHs also exhibit superior properties on P and KE simultaneously in the architectures with thicker plate, 24mm thick, shown Figure 5.21(a) to (c). Similar as architectures with 6mm thickness, H60sym with 24mm thickness can provide highest value of KE in the helicoid architectures with constant pitch angle. Although more helicoid architectures are involved in the optimum corner of Ashby plot with P and KE under 150J impact with 24mm thickness plate, such as H22.5sym, H45sym and H30sym, FGHs are still located in the optimum corner of Ashby plot with higher values of P and KE at the same time.

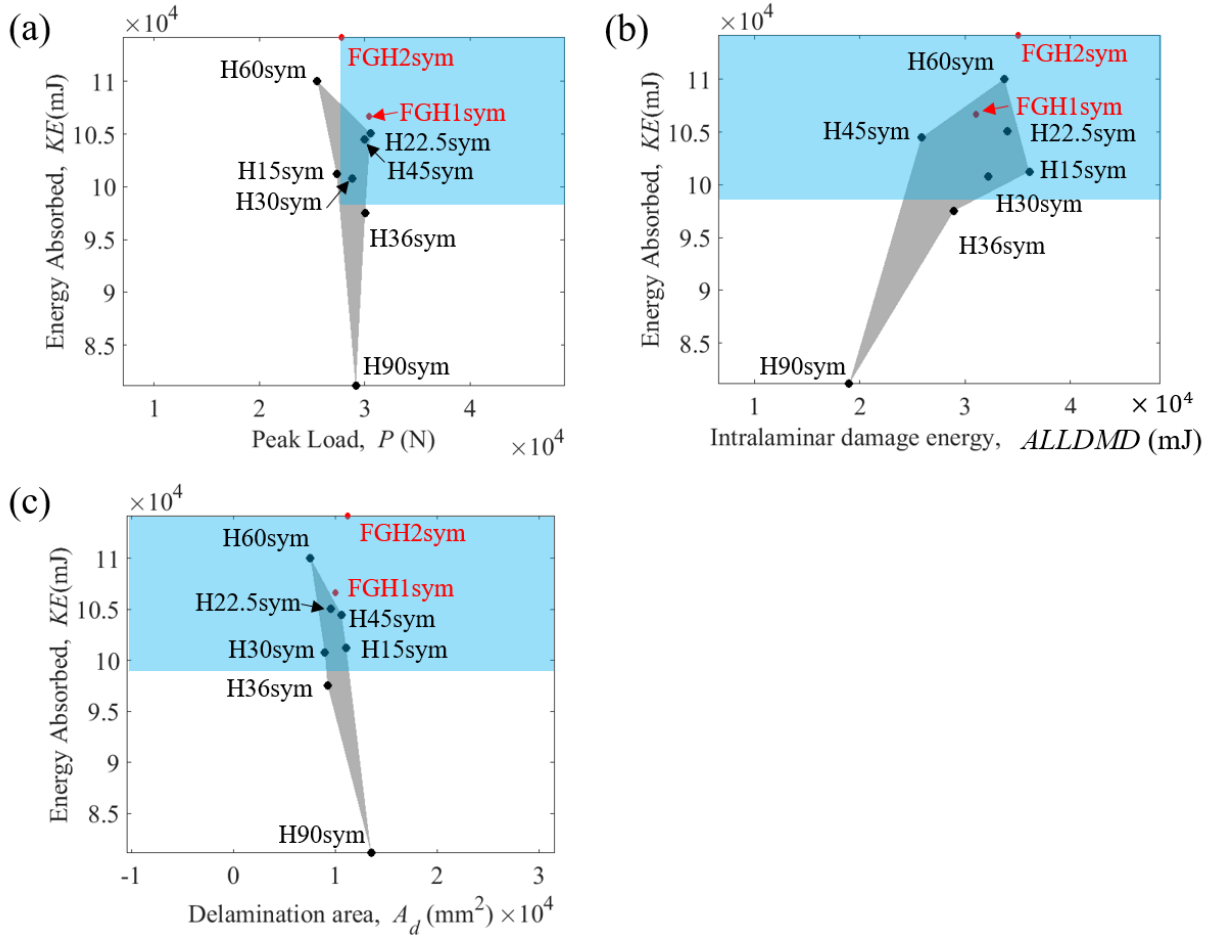


Figure 5.21. (a) Ashby plot of absorbed energy KE and Peak load P of models with thickness 24mm (b) Ashby plot of energy dissipated by intralaminar damage and absorbed energy KE of models with thickness 24mm (c) Ashby plot of delamination area A_d and absorbed energy KE of models with thickness 24mm

5.4.3 Explanation

Transverse shear stresses distribution through the thickness

a. Analytical prediction

It is necessary to show how the transverse shear stresses distributed in FGHs, and thus we can see the difference or benefits of FGHs over other helicoids. In this section, extended CLPT was employed to calculate the transverse shear stress S_{xz} in the laminated beam under three-point bending loading condition. The detailed calculation process is described in Appendix D5.

The boundary condition is shown in Figure 5.22.(a) and the S_{xz} distribution of H30sym in x - z plane is illustrated in Figure 5.22.(b), where maximum value of S_{xz} is achieved in the middle

plane of the laminate, which is also shown in Figure 5.22(c). Figure 5.22.(d) shows the difference of S_{xz} distribution along the thickness between laminate H15sym and H45sym. Smaller pitch angle $\theta_h = 15^\circ$ can provide smoother stress distribution from surface to interior, while larger pitch angle $\theta_h = 45^\circ$ exhibits step-wise manner, with big jumps occurring in the specific locations that one pitch ends. It is interesting to know that the maximum values of S_{xz} shown in the middle of the beam, of helicoids with different constant pitch angles respectively are very close, except H90sym. The reason that inducing this higher value of S_{xz} in H90sym is because S_{xz} is related to S_{xx} due to stress equilibrium equations, and then S_{xx} is influenced by the shear modulus E_{xx} when the applied strain is the same. The E_{xx} of H90sym is larger than all other helicoids and thus its value of S_{xz} is higher than other helicoid composites.

It is deserved to be noted that FGH1sym exhibits similar distribution of S_{xz} as H36sym does, which is the helicoid architecture close to surface and occupies majority number of layers in the whole laminate, shown in Figure 5.22.(f). Same behavior is observed between FGH2sym and H30sym as well, shown in Figure 5.22.(g). However, FGHs can also balance the S_{xz} distribution among its associated laminates. For example, pitch of $\theta_h = 90^\circ$ in FGH2sym can provide less S_{xz} than H90sym, up to 14.7% difference. Accordingly, it is not a surprise that FGHs can provide balanced peak load, P , among helicoid laminates with larger and smaller pitch angles separately. However, the maximum S_{xz} value of FGH1sym is very close to the maximum S_{xz} of H36sym, shown in zoom-in figure of Figure 5.22(b) and thus the peak load of FGHs is not only dependent on the maximum value of S_{xz} , but also dependent on other factors, which will be discussed in the following section.

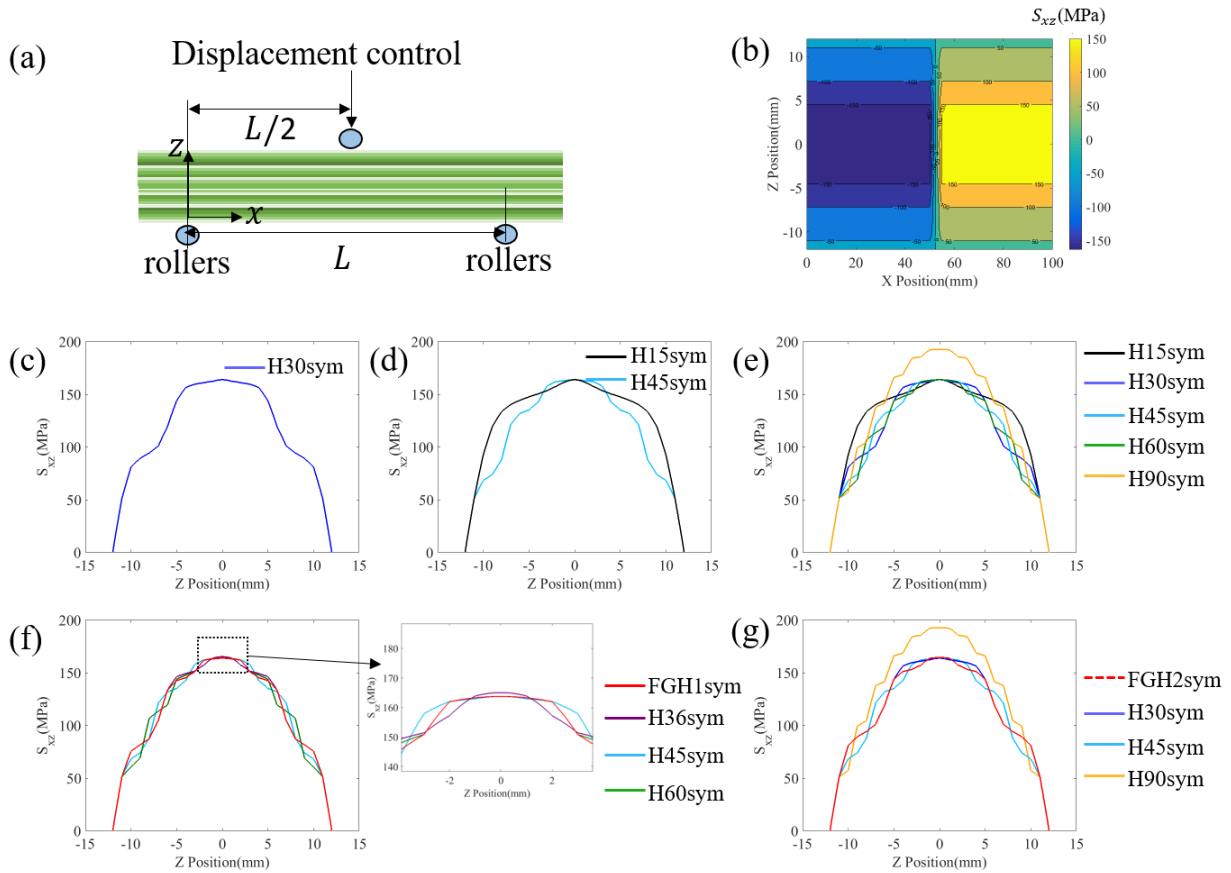


Figure 5.22. (a) Boundary conditions of quasi-static three-point bending test (b) Transverse shear stress S_{xz} distribution in $x - z$ plane predicted by extended CLPT (c) S_{xz} distribution along the thickness of the laminate H30sym when $x_1 = L$ (d) Comparison on S_{13} between H15sym and H45sym (e) Comparison on S_{xz} among helicoid laminates with different pitch angles separately (f) Comparison on S_{xz} among FGH1sym and its associated laminates (g) Comparison on S_{xz} among FGH2sym and its associated laminates.

b. FEA using solid model with two C3D20R elements per lamina

In FEA, the transverse shear stresses of smaller pitch angle, such as $\theta_h = 15^\circ$, continuously distributed along the thickness of the whole laminate, while laminates with larger pitch angles exhibit discrete transverse shear stresses, as shown in Figure 5.23 and Figure 5.24, which is the same as predicted by extended CLPT.

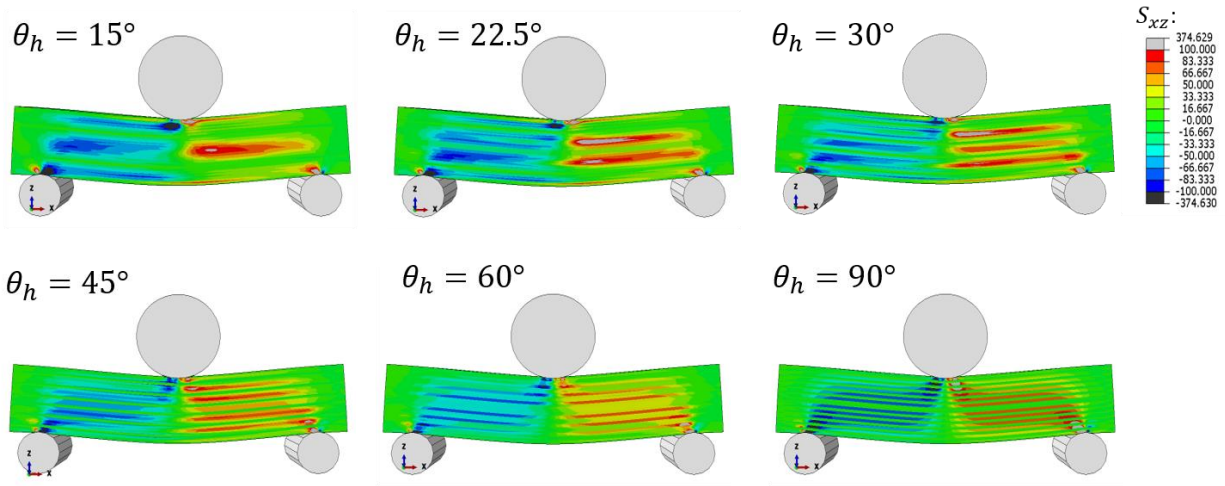


Figure 5.23. Transverse shear stress S_{xz} distribution along the thickness of the laminates with different constant pitch angles separately

Laminates with smooth transverse shear stresses can provide less localized delamination failure compared with the laminates with discrete distribution of transverse shear stresses, which exhibit high values of transverse shear stresses with high frequency in the $x - z$ cross-section when the thickness is fixed, shown in Figure 5.23 and Figure 5.24. This difference on transverse shear stresses distribution also influence the maximum peak load, P , and the toughness, T_c .

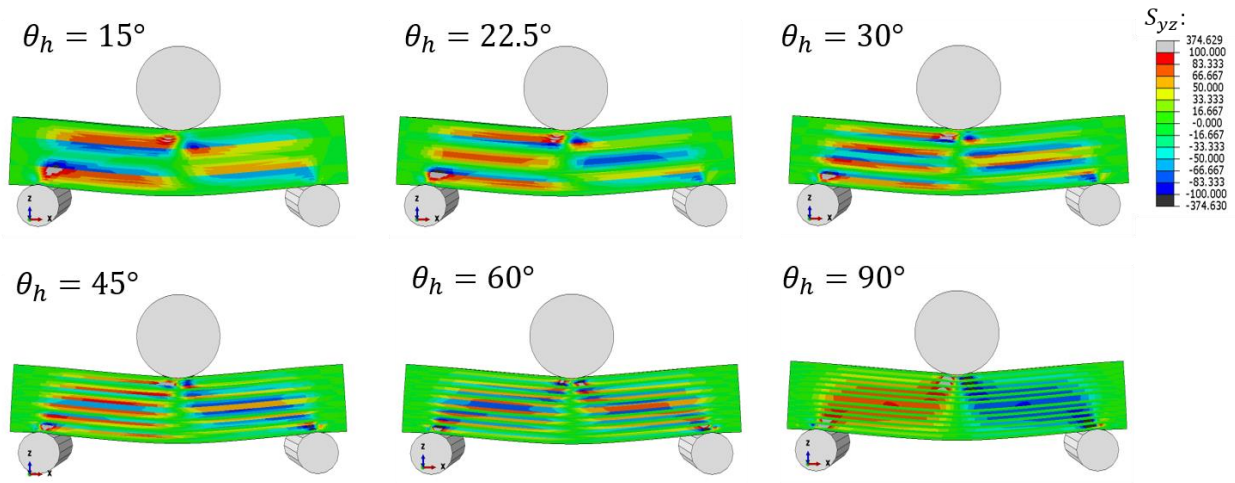


Figure 5.24. Transverse shear stress S_{yz} distribution along the thickness of the laminates with different constant pitch angles separately

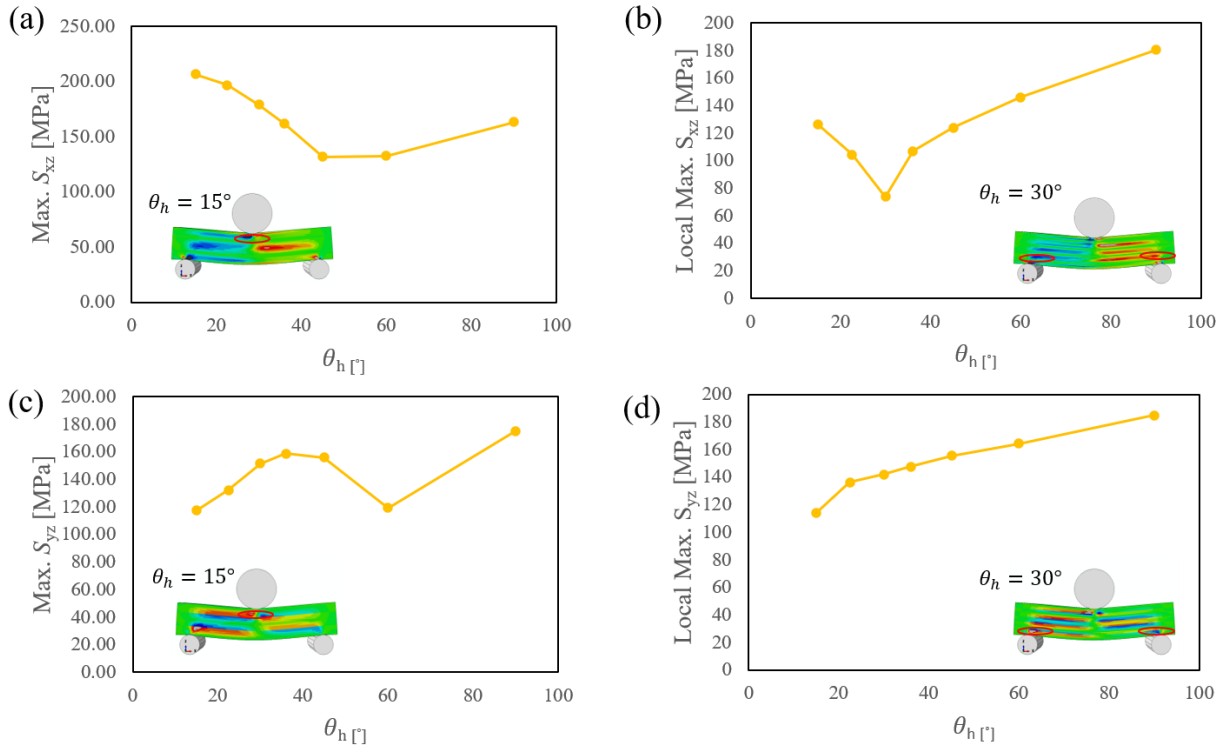


Figure 5.25. (a) Maximum S_{xz} at free-edge (close to top indenter) of the laminated beam of helicoid laminates with symmetry lay-up to the middle plane and the laminates without symmetry lay-up to the middle plane (b) Maximum S_{xz} at free-edge (close to bottom rollers) of the laminated beam of helicoid laminates with symmetry lay-up to the middle plane (c) Maximum S_{yz} at free-edge (close to top indenter) of the laminated beam of helicoid laminates with symmetry lay-up to the middle plane and the laminates without symmetry lay-up to the middle plane (d) Maximum S_{yz} at free-edge (close to bottom rollers) of the laminated beam of helicoid laminates with symmetry lay-up to the middle plane separately

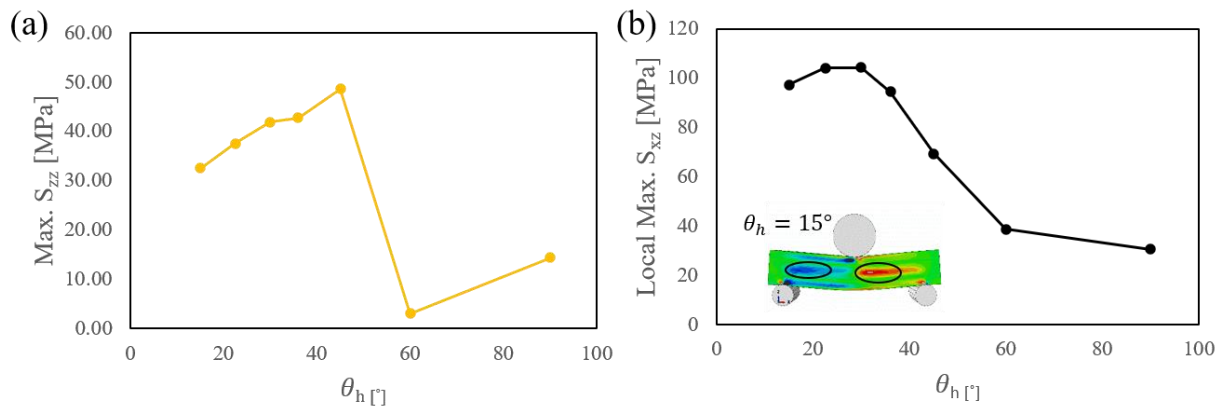


Figure 5.26. (a) Maximum S_{zz} at free-edge (close to the indenter) of the laminated beam of helicoid laminates (b) Local maximum S_{xz} at free-edge (close to the half thickness) of the laminated beam of helicoid laminates

As shown in Figure 5.25 (a) and (c), combined with Figure 5.26, S_{xz} is dominant in three-point short beam bending, compared with S_{yz} and S_{zz} , which is agreed on the prediction of beam theory. Unlike long beam bending, the values of S_{xz} here do not have absolute benefits over the values of S_{yz} . As the θ_h is decreasing, the values of maximum S_{xz} close to indenter is increasing and thus P of laminates with smaller θ_h is dependent on the local maximum S_{xz} close to indenter, while P of laminates with larger θ_h is not related to the local maximum S_{xz} close to indenter. FEA considering intralaminar and interlaminar failure can provide further confirmation on this conclusion. The P of laminates with $\theta_h = 15^\circ$ and $\theta_h = 22.5^\circ$ is characterized by local delamination close to indenter, shown in Figure D1(a), while P of laminates with larger θ_h , changing from 30° to 60° , is determined by the large extent of interlaminar failure close to bottom rollers or intralaminar failure close to top surface, shown in Figure 5.7(a), Figure 5.8(a), Figure 5.9(a) and Figure D2(a). Figure 5.25(b) and (d) show the maximum transverse shear stresses close to bottom rollers and $\theta_h = 30^\circ$ exhibits the minimum values on both of them, which explain the optimum P that $\theta_h = 30^\circ$ achieves shown in Figure 5.10(a).

θ_h smaller than 30° can provide smoother distribution of transverse shear stresses through the thickness, which limit the number of stress concentration under fixed thickness and restrict the local crack propagation at interface close to bottom rollers. This behavior also plays a significant role on bending resistance before total failure, value of T_c . For example, after first large drop on displacement and force curve, $\theta_h = 15^\circ$ does not show large extent of delamination failure, shown in Figure D1, and thus before total failure occurs, $\theta_h = 15^\circ$ can provide more interfaces to separate, indicating storage more energy before losing total resistance.

From Figure 5.25 and Figure 5.26, the difference on maximum transverse stresses found in localization due to the influence of contact from rollers among laminates with distinct pitch angle are shown. The maximum transverse stresses found in the middle of the laminates with different pitch angles also reveal the difference, shown in Figure 5.26(b). This result is different from what we predicted by extend CLPT, which ignores the transverse shear strains in the laminate and shows the consistent maximum transverse shear stresses in the middle of the laminate. However, in our FEA models considering delamination and in-plane damage, the Mindlin-Reissner plate theory is adopted for each lamina stacked in the laminate, which considers constant transverse shear strain/stress for each lamina, and the interface is connected by cohesive interaction based on surface. This method effectively shows the difference on transverse stresses/strain of

laminates with different pitch angle, which is validated in section 5.4.4. Accordingly, the corresponding components in the strain energy, which is related to the delamination initiation and evolution, of laminates with different pitch angle can be distinguished.

Laminates with θ_h equal to and larger than 45° exhibit competitive T_c , induced by slower propagation between each delamination failure, including intralaminar matrix damage, which is induced by the number of 0° lamina. Larger pitch angle featured with a greater number of 0° lamina, which shows the maximum strength and energy release rate in the longitudinal direction (align with the longitudinal direction of the beam in the global coordinates), can provide more deformation resistance under bending along the longitudinal direction of the beam. For example, the available applied displacement between first and second large extent of delamination and in-plane damage in $\theta_h = 36^\circ$ is 0.721mm, while $\theta_h = 45^\circ$ can apply 2.482mm deflection between these two large extent of delamination failures, which is 3.44 times over the value of $\theta_h = 36^\circ$.

Accordingly, FGHs with increasing pitch angles from surface to interior can provide specific transverse shear stress distribution at specific location along the thickness and thus optimize the peak load and toughness of the whole beam under bending. Also, the component layers, off-axis angle close to 0° , of helicoid laminate with different pitch angles can influence the intralaminar damage under bending.

For example, laminae close to top and bottom surfaces can be influenced by concentrated contact force and larger tensile and compression deformation. Laminates with smaller (such as $\theta_h = 15^\circ$ and $\theta_h = 22.5^\circ$) pitch angle although have larger transverse shear stress at free-edge, their distribution of transverse shear stress along the thickness is smoother and thus they can lead to lower peak load, but higher toughness, since the location of delamination occurs less than laminates with larger pitch angle when the thickness is fixed. Laminates with middle (such as $\theta_h = 30^\circ$ and $\theta_h = 36^\circ$) pitch angle can provide higher peak load, but less toughness. Larger pitch angle (such as $\theta_h = 45^\circ$, $\theta_h = 60^\circ$ and $\theta_h = 90^\circ$) can provide less peak load, but higher toughness, which is influenced by the larger quantity of 0° lamina. Accordingly, for our FGHs, encompassing $\theta_h = 30^\circ$ or $\theta_h = 36^\circ$ close to bottom and top surfaces can provide higher peak load, but in the middle of the beam along thickness is composed of $\theta_h = 45^\circ$, $\theta_h = 60^\circ$ or $\theta_h = 90^\circ$, which can provide more bending resistance because of larger number of 0° laminae. The continuous increasing pitch angle from surface to interior can provide a much smoother stress distribution

along the thickness and it can provide benefits on fracture resistance, which is also discussed in Chapter 4.

Laminate FGH1 disorder which is composed of disorder pitches of the components of FGH1sym shows that its peak load value and toughness value are lower than its associated helicoid laminates and it cannot locate at the optimum area in the Ashby plot, which is shown in Figure 5.11(a).

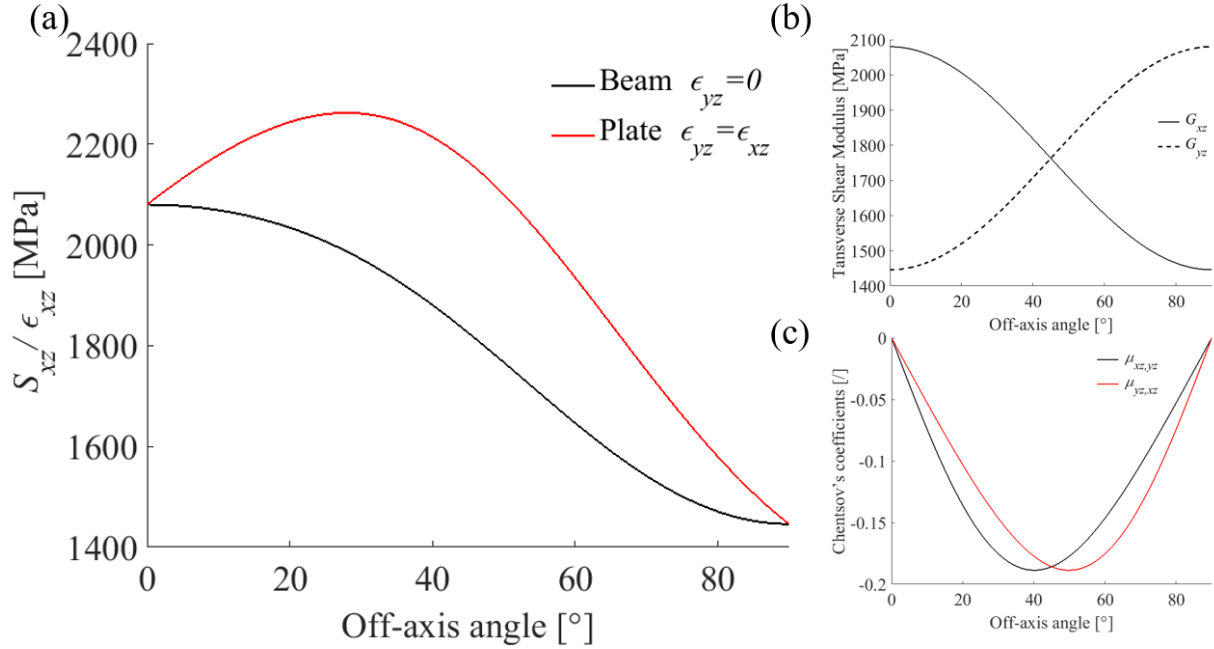


Figure 5.27 (a) S_{xz} as a function of off-axis angle, including the two cases of beam and plate (b) Transverse shear modulus as a function of off-axis angle (c) Chentsov's coefficients as a function of off-axis angle

On the other hand, the reason of laminates with smaller pitch angle can provide higher values of S_{xz} can be explained by the relation of S_{xz} and off-axis angle when their ϵ_{xz} is the same, shown in Figure 5.27, predicted by constitutive law of monoclinic material. Our FEA on short beam bending is somewhere in between the beam case ($\epsilon_{yz} = 0$) and plate case ($\epsilon_{xz} = \epsilon_{yz}$). The specific equation is shown as below. It is observed that smaller off-axis angle exhibits higher value of S_{xz} based on the constitutive relation of monoclinic material, since each lamina with off-axis angle can be considered as monoclinic material.

$$S_{xz} = (\epsilon_{xz} - \mu_{yz,xz} \epsilon_{yz}) G_{xz} \frac{1}{1 - \mu_{yz,xz} \mu_{xz,yz}} \quad (5.11)$$

5.4.4 Justification of finite element model

Continuum shell model (SC8R) is adopted to represent the lamina composite materials in the present work. It is necessary to study the accuracy of this model and to justify its feasibility to discern the difference induced by distinct pitch angles.

Continuum shell model in commercial software ABAQUS is based on first order shear deformation theory (FOSDT), which is also called Mindlin-Reissner plate theory. It is confirmed that FOSDT can provide accurate in-plane stress (Pagano, 1970; Yu, 2005) for composite materials with different lay-up sequence. However, the accuracy of prediction on transverse shear stresses needs to be studied case by case. In the present work, the distribution of transverse shear stress S_{xz} and logarithmic strain in $x - z$ direction LE_{xz} in the continuum shell model, the major part of transverse stresses/strain in short-beam bending test, is extracted at free-edge of short-beam to compare with the S_{xz} distribution of solid model, as shown in Figure 5.28 and Figure 5.29. The S_{xz} at interface from solid model due to large change in lamina orientation (from 0° to 60°), there are two values assigned to one node at the interface. Accordingly, in Figure 5.28 and Figure 5.29, the value of S_{xz} at interface is achieved by averaging the two values from two adjacent laminae. It is observed that continuum shell model can provide a good match on S_{xz} at interface between 0° and 60° or -60° plies, but it overestimates the S_{xz} value at the interface between 60° and -60° plies. Besides, the continuum shell model underestimates the S_{xz} value in the lamina with smaller off-axis angle, such as 0° and 15° , and overestimates the S_{xz} value in lamina with larger off-axis angle, such as 90° and 75° . Generally, continuum shell reduces the discrepancy on S_{xz} value among laminae with different off-axis angles, compared with the homogenized solid model. Due to the short beam structure we use here, S_{yz} and LE_{yz} are not going to be discussed.

Although the difference on S_{xz} value can not be ignored between continuum shell and solid models, as long as the continuum shell model can provide the relative difference on S_{xz} and LE_{xz} among distinct laminates with different pitch angles, the continuum shell is one of the most efficient ways to predict the delamination behavior of fiber reinforced composite materials.

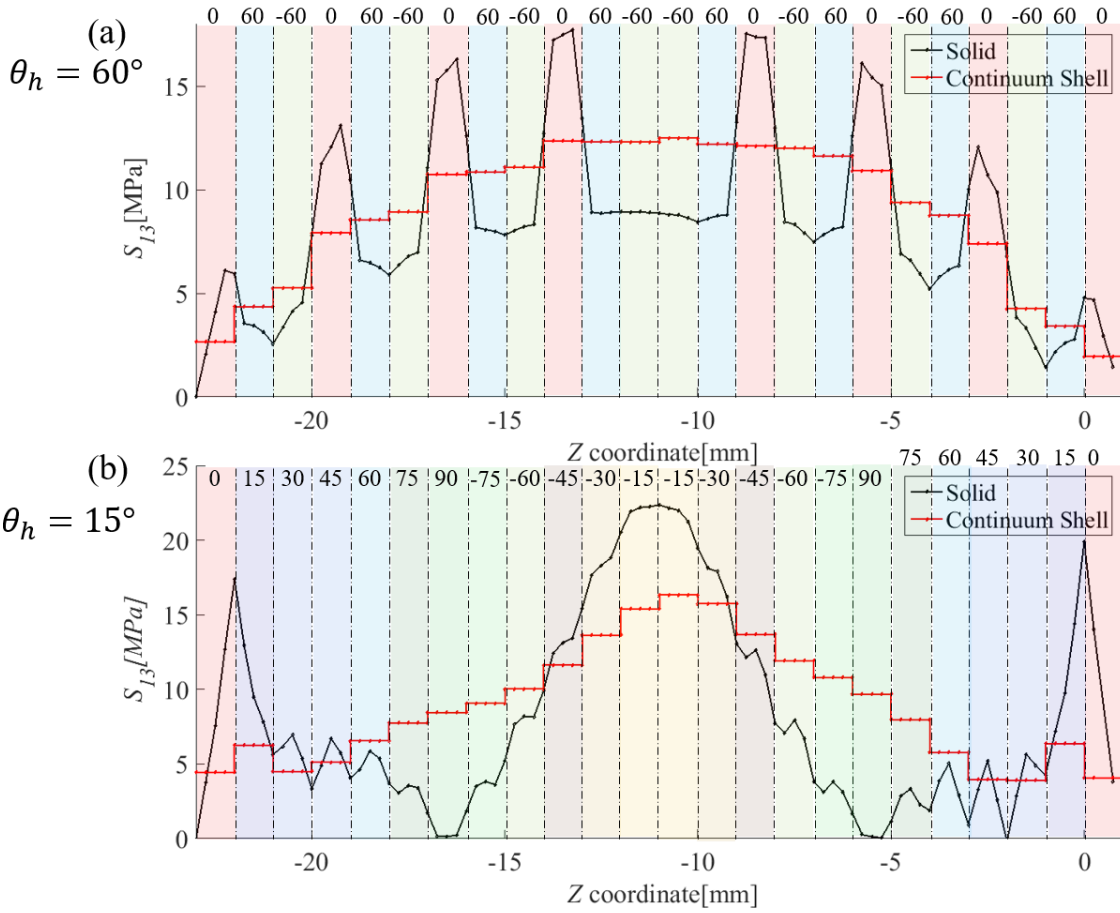


Figure 5.28. (a) S_{xz} distribution along z-direction at free-edge of short-beam H60sym (b) S_{xz} distribution along z-direction at free-edge of short-beam H15sym

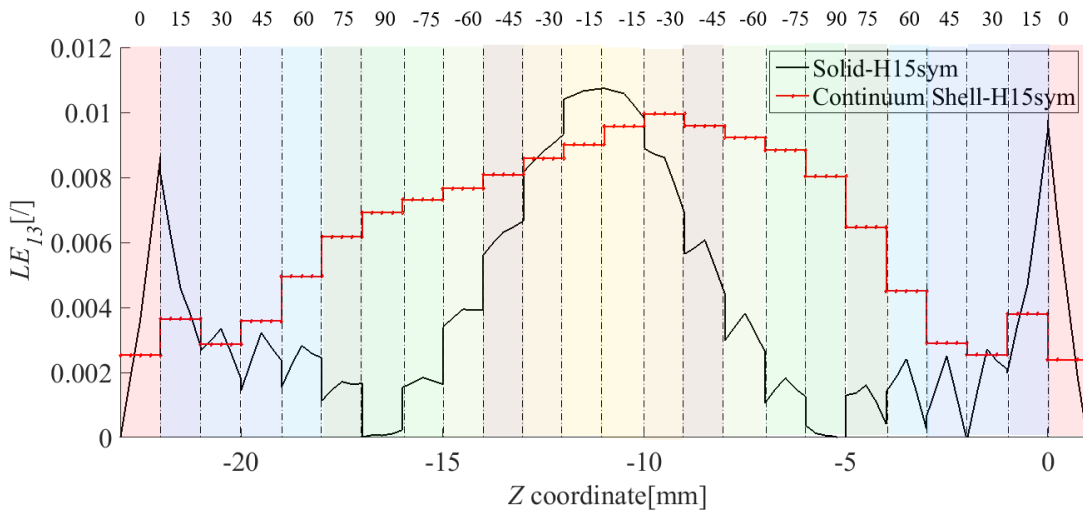


Figure 5.29. LE_{xz} distribution along z-direction at free-edge of short-beam H15sym

The relative comparison on S_{xz} distribution and U_x distribution along the thickness of the laminate at free-edge is illustrated in Figure 5.30 and Figure 5.31 respectively. It is observed that continuum shell can provide relative discrepancy on S_{xz} and U_x between laminate H15sym and laminate H60sym, compared with solid model.

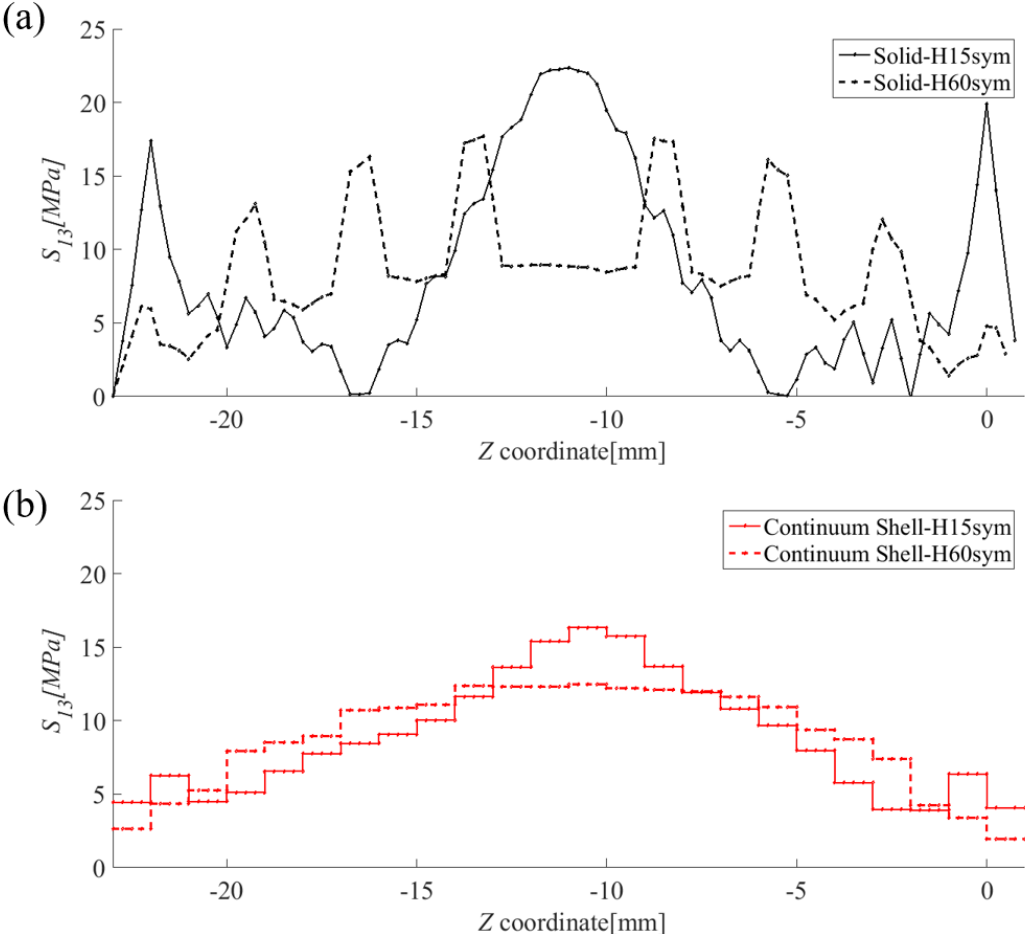


Figure 5.30. (a) S_{xz} distribution along z-axis at free-edge of short beam H15sym and H60sym both created by solid model (b) S_{xz} distribution along z-axis at free-edge of short beam H15sym and H60sym both created by continuum shell model

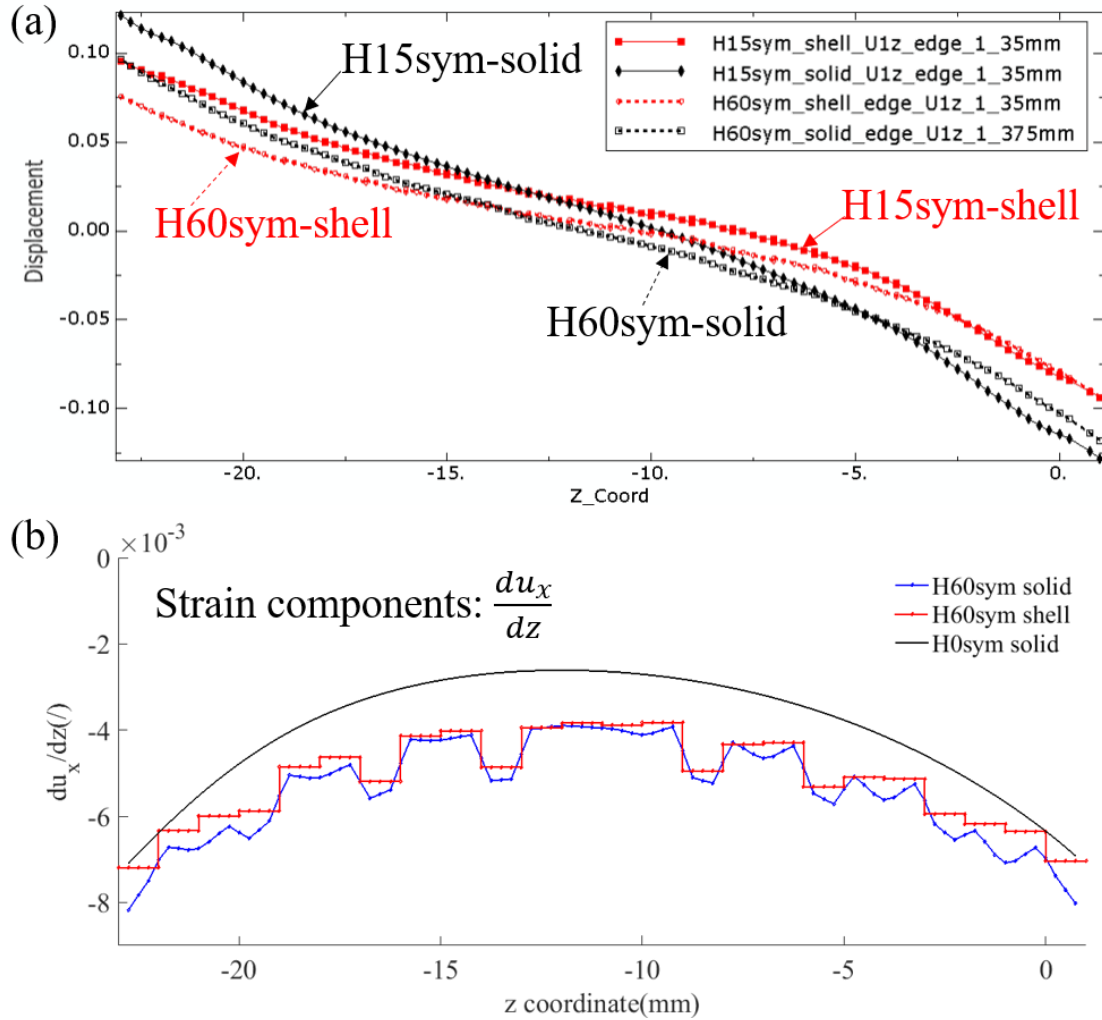


Figure 5.31. (a) u_x distribution along z-axis at free-edge of short beam H15sym and H60sym created by solid model and continuum shell models (b) du_x/dz distribution along z-axis at free-edge of short beam H15sym and H60sym created by solid model and continuum shell models

Besides, we also compare the strain energy of the whole laminate in solid and continuum shell models, shown in Figure 5.32, since it is related to energy release rate of the crack at interface. It reveals that continuum shell model underestimates the strain energy of the whole laminate. However, it accurately predicts that there is little difference on strain energy between H15sym and H60sym, which is induced by the consistent value of transverse shear modulus G_{xz} and G_{yz} between H15sym and H60sym. Additionally, the transverse shear modulus and in-plane shear modulus of all laminates with different pitch angles are tabulated in Table 5.5. Analytical predicted transverse shear modulus and in-plane shear modulus of helicoid composites and FGHs The method we used is described in the appendix of (Cheng et al., 2011).

Table 5.5. Analytical predicted transverse shear modulus and in-plane shear modulus of helicoid composites and FGHS

(MPa)	H15sym	H30sym	H45sym	H60sym	H90sym	FGH1sym	FGH2sym
G_{xz}	1.76E+03						
G_{yz}	1.76E+03						
G_{xy}	5.11E+03	5.11E+03	5.11E+03	5.11E+03	2.08E+03	5.11E+03	4.60E+03

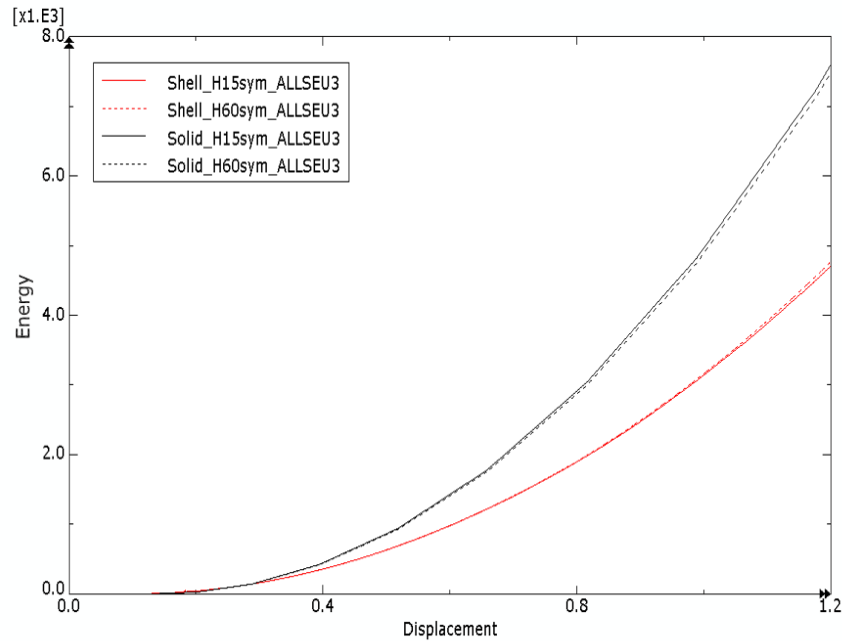


Figure 5.32. Strain energy as a function of applied displacement before any damage or failure occurs in continuum shell models

On the other hand, two C3D20R elements per lamina used for transverse shear stress/strain prediction is confirmed to be robust enough to predict the transverse shear stresses through the layers through comparing the transverse shear stress/strain at free-edge of two C3D20R elements per layer and eight C3D20R elements per layer, shown in Figure 5.33. Except the interface at free edge between laminae with dissimilar misorientation, other locations exhibit converged results on transverse shear stress/strain. The stresses at the interface close to free-edge between laminae with dissimilar misorientation has difficulty to converge due to singularity in FEA (Goodsell et al., 2013;

Goodsell and Pipes, 2016; Peng et al., 2016). However, the cohesive zone model at interface can eliminate the stress/strain singularity at interface close to free edge.

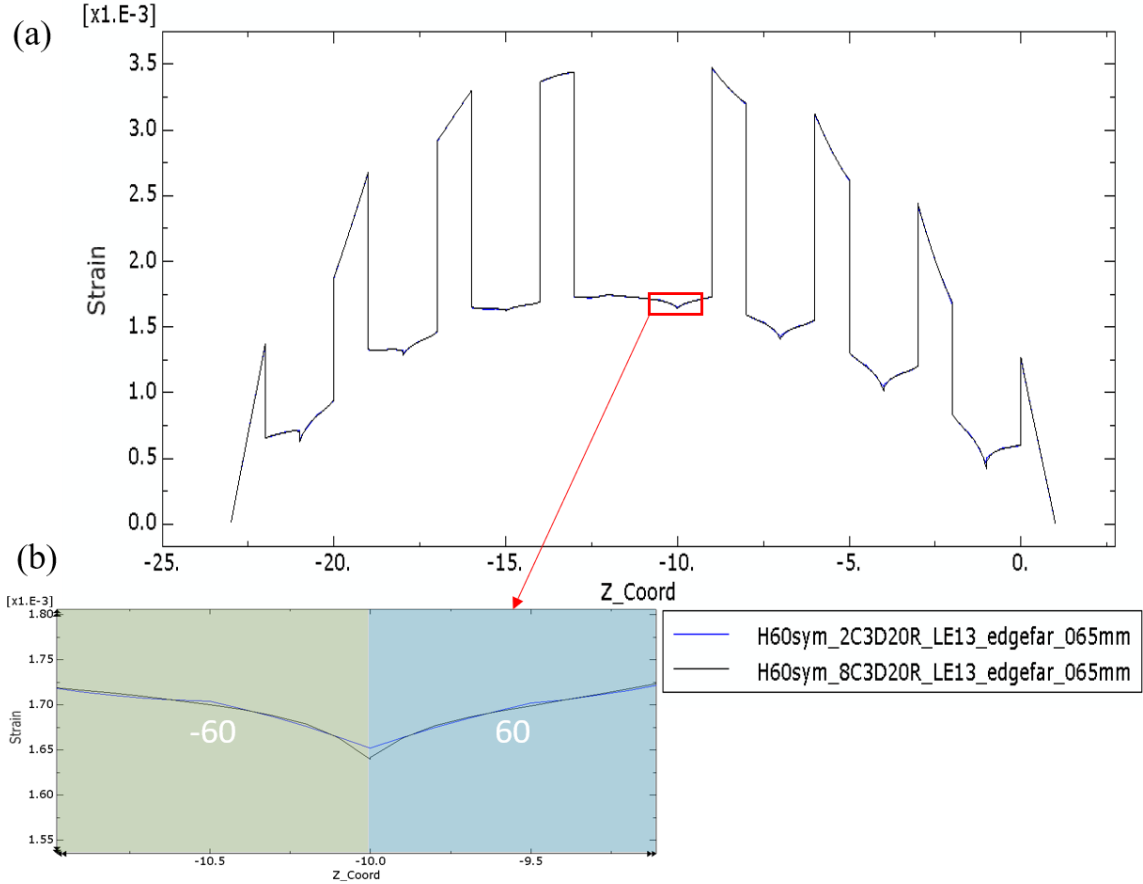


Figure 5.33. (a) Transverse shear strain LE_{xz} through the thickness at free edge of solid model with two C3D20R and with eight C3D20R per lamina (b) Zoom in plot of strain distribution at interface between -60° and 60°

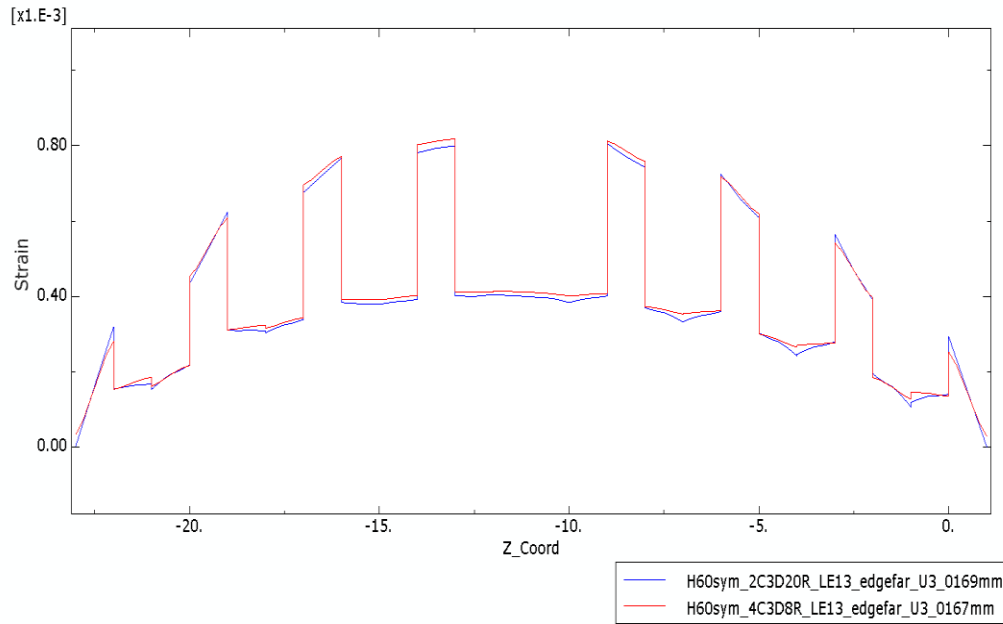


Figure 5.34. Transverse shear strain LE_{xz} through the thickness at free edge of solid model with two C3D20R and with four C3D8R per lamina

Furthermore, in order to validate the delamination initiation and propagation in our FEA model, solid model with four C3D8R elements per lamina considering delamination only is employed to compare with the continuum shell model with one SC8R per lamina considering delamination only. Due to the unavailability of C3D20R element under explicit solver in ABAQUS, model with four C3D8R elements per layer is replaced to compare with the continuum shell model. The accuracy of four C3D8R elements per layer is shown in Figure 5.34. Due to the characteristics of continuum shell model, constant transverse shear strain and stress in each lamina, our FEA based on continuum shell model has difficulty to predict the transverse shear stress and strain induced by in-plane shear stress under tension/compression at the interface between $-\theta$ lamina and θ lamina, shown in Appendix D6. Accordingly, H60sym, the worst case, and H30sym with 12 laminae in all are designed to validate our continuum shell FEA model. The ratios of length over thickness and width over thickness are consistent as the previous 24 laminae short beam. The load and displacement curves are shown in Figure 5.35(a) and Figure 5.36(a), combined with the delamination initiation and propagation in continuum shell model and solid model, shown in Figure 5.35(b-c) and Figure 5.36(b-c).

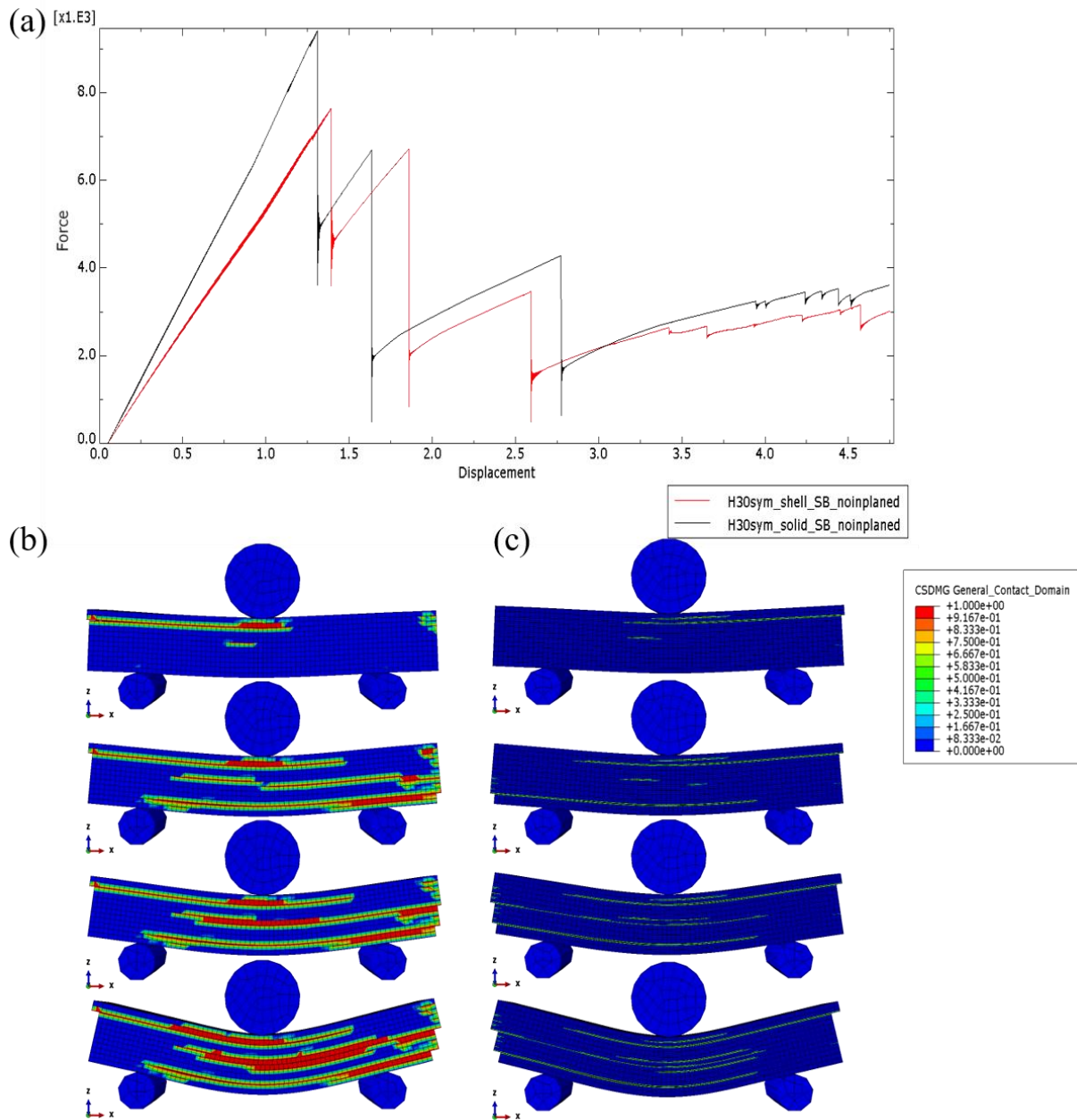


Figure 5.35. (a) Load and displacement curve of H30sym model under short beam bending with 12 laminae through the thickness. Red curve represents for continuum shell considering delamination only and black curve represents for solid model considering delamination only. (b) Delamination initiation and propagation in continuum shell model (c) Delamination initiation and propagation in solid model

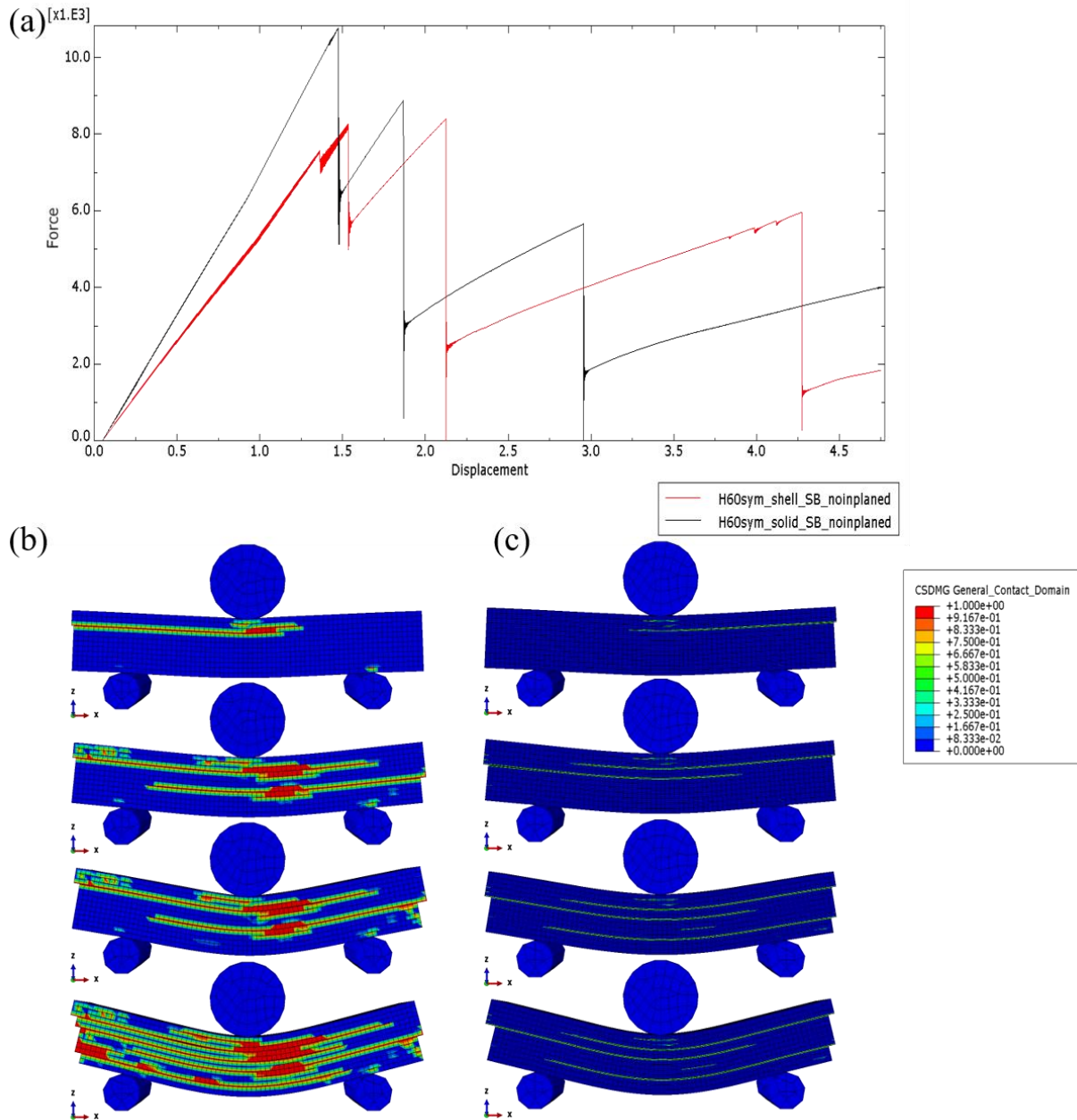


Figure 5.36. (a) Load and displacement curve of H60sym model under short beam bending with 12 laminae through the thickness. Red curve represents for continuum shell considering delamination only and black curve represents for solid model considering delamination only. (b) Delamination initiation and propagation in continuum shell model (c) Delamination initiation and propagation in solid model

It reveals that the peak load due to delamination initiation from continuum shell model is lower than the peak load, P , from solid model, up to 20.3% lower value than the solid model, shown, in Figure 5.37(a), but the critical loading displacement when P occurs from continuum shell model aligns with the critical loading displacement of solid model, shown in Figure 5.37(b).

The toughness, T_c , extracted from the continuum shell model can be up to 11.55% lower than the T_c of solid model shown in Figure 5.37(b). Besides, the location and order of delamination initiation and propagation from the continuum shell model highly matches the location and order of delamination propagation from the solid model, shown in Figure 5.36(b-c) and Figure 5.38(a-b). It reveals that in the worst case, H60sym, the delamination area, A_d , after P occurs in continuum shell model aligns with the results of solid model, shown in Figure 5.38(c). However, the A_d at the last increment of 4.75mm displacement loading in z-direction of the continuum shell model is 56.8% higher than the A_d of the solid model, shown in Figure 5.38(d). Another difference is that the continuum shell model can provide slower delamination propagation after delamination initiates under same displacement loading, compared with the solid model. In general, the continuum shell model combined with cohesive interaction underestimates the P and T_c of the short beam compared with the solid model considering delamination only. However, the accuracy of relative relationship on P and T_c among different pitch angles can be guaranteed, except the T_c of H60sym dependent on delamination only, which needs further improvement in the future.

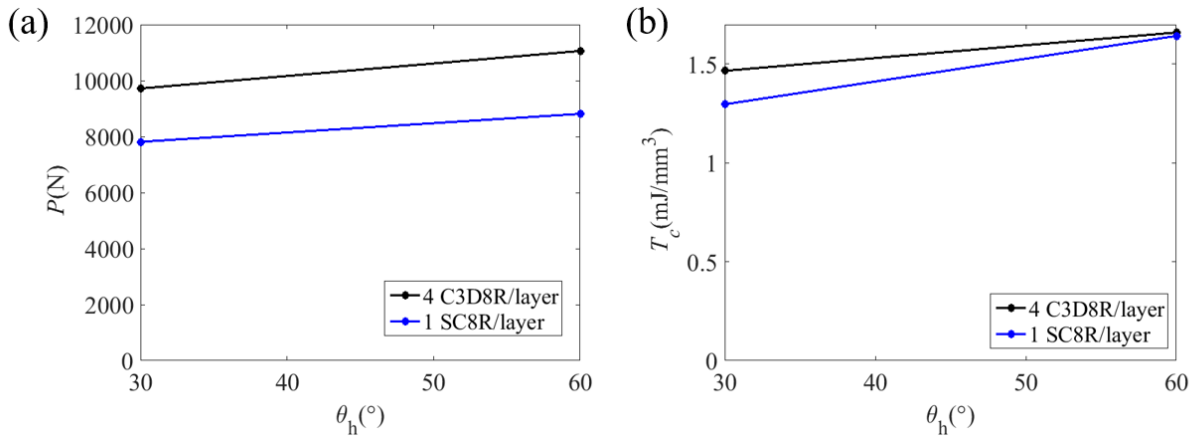


Figure 5.37. (a) Comparison on peak load, P , between solid and shell models in H30sym and H60sym (b) Comparison on toughness, T_c , between solid and shell models in H30sym and H60sym

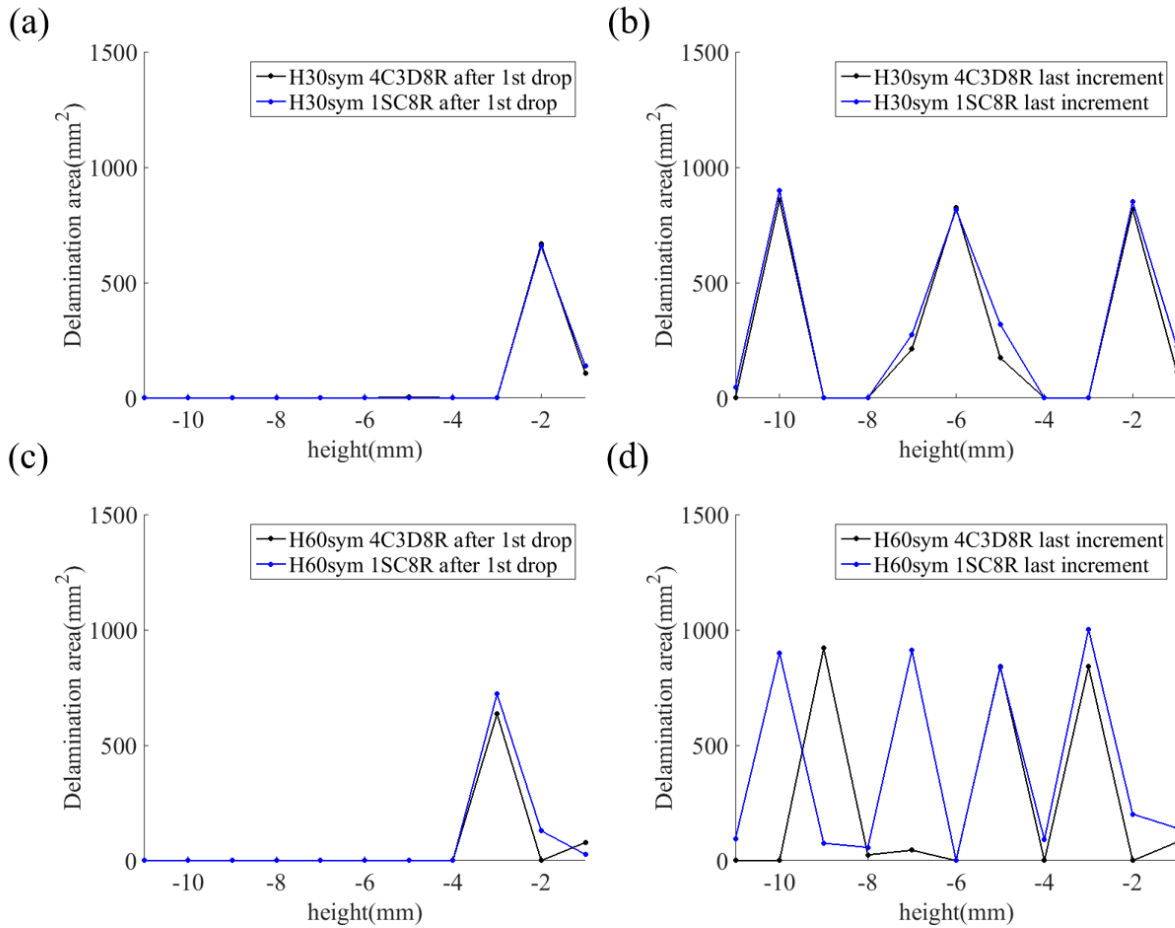


Figure 5.38.(a) Delamination area distribution along the thickness of the 12 layer short beam of H30sym after first peak load occurs (b) Delamination area distribution along the thickness of the 12 layer short beam of H30sym at the last increment under 4.75mm loading displacement in z direction (c) Delamination area distribution along the thickness of the 12 layer short beam of H60sym after first peak load occurs (d) Delamination area distribution along the thickness of the 12 layer short beam of H60sym at the last increment under 4.75mm loading displacement in z direction

Additionally, we suppose that due to continuity of transverse shear stresses (S_{xz} and S_{yz}) at interface and the influence of different pitch angles(θ_h) on S_{xz} and S_{yz} , the maximum value of S_{xz} and S_{yz} in specific pitch of functionally graded helicoids(FGHs) can be smaller or larger than the corresponding value shown in the same position of associated helicoid composites with constant θ_h , which is denoted “sympathetic behavior”, discussed in section 5.4.3.a. However, through extracting the maximum S_{xz} in corresponding pitch of FGHs, such as $\theta_h = 36^\circ$ and $\theta_h = 60^\circ$ in FGH1sym, and maximum S_{xz} at the same location in H36sym and H60sym, it is observed that the difference on maximum S_{xz} at these locations is less than 2% in the solid models(less than

3.5% in the solid models of FGH2sym and its associated helicoid composites). The continuum shell model with cohesive contact at interface can also predict this “sympathetic behavior” by introducing up to 2.5% difference on maximum S_{xz} at same location of FGHs and its associated helicoid composites. Accordingly, due to the minor difference on transverse shear stresses from same location but with different lay-up sequence, the influence of “sympathetic behavior” can be ignored under 3-point short beam bending.

According to the justification shown above, the continuum shell model is a relatively robust and efficient method to predict the difference on transverse shear stresses induced by distinct pitch angles in helicoid composites and the delamination initiation and propagation.

5.5 Conclusions

In the short-beam bending tests, $\theta_h = 30^\circ$ is the optimum pitch angle for peak load, P , and $\theta_h = 45^\circ$ is the optimum pitch angle for toughness, T_c . In the comparison analysis of P and T_c , helicoid with constant θ_h is observed without higher P and T_c at the same time, while FGHs occupy the optimum area of Ashby plot with higher P and T_c simultaneously. This is because first the maximum transverse shear stress is observed at the interfaces close to top indenter and two bottom rollers, although maximum transverse shear stresses is achieved in the middle of the laminate along the thickness in the $x - z$ plane except for the paths going through the thickness close to rollers and indenter, shown in Figure 5.23 and Figure 5.24. Secondly, except for the laminates with smaller pitch angle, which laminate’s peak load is dependent on the delamination close to top indenter, showing the higher transverse shear stress S_{xz} among other helicoids, shown in Figure 5.25(a), other helicoids reveals that their peak load is dependent on the maximum S_{xz} close to the bottom surface. H30sym shows the minimum value of S_{xz} at the interfaces close to bottom rollers at the same applied displacement and thus it can behave as a coating material, delaying the occurrence of delamination, and then provide the maximum peak load. Accordingly, $\theta_h = 30^\circ$ and $\theta_h = 36^\circ$ arranged close to the top and bottom surfaces of FGHs respectively can achieve the maximum peak load. Besides, H45sym and H60sym reveal benefits on toughness over other helicoids, since their damage evolution is slower than other helicoids due to a greater number of 0° laminae, which is the toughest lamina under bending. H90sym should be tougher as well since it encompasses larger number of 0° lamina, but its weak peak load reduces the energy

absorbed under 6mm deflection, compared with others. FGHs composed of $\theta_h = 45^\circ$ and $\theta_h = 60^\circ$ close to the middle of their whole laminate along the thickness highly increases the energy storage under damage and delamination evolution, since the delamination and damage propagates slowly due to larger number of 0° laminae.

Laminate FGH1symdisorder, which is composed of the same component pitches of FGH1sym but with different order of arrangement along the thickness from surface to interior, exhibits lower toughness and peak load compared with its associated helicoid laminates. The detailed comparison on delamination propagation between FGH1symdisorder and FGH1sym is shown in Figure D5. $\theta_h = 45^\circ$ is not beneficial for delaying delamination due to concentrated stresses induced by contact, as discussed before, which has been assigned close to bottom and top surfaces of FGH1symdisorder. In the meantime, $\theta_h = 36^\circ$ assigned close to the middle of FGH1symdisorder cannot provide enough in-plane deformation resistance after delamination initiation close to the bottom surface. Accordingly, it seems that the arrangement order of different pitch angles along the thickness is related to the delamination and in-plane damage resistance.

Furthermore, the distribution of transverse shear stresses in the short beam bending test is predicted by FEA and analytical calculation. It is shown that, due to the smooth transition of the transverse shear stress and less number of stress concentration at interfaces along the thickness in the architectures with smaller pitch angles at a given applied load/displacement, they can endure more bending deformation before large extent of delamination occurs at the bottom of the beam. However, laminates with smaller pitch angle, less than 22.5° , show lower value of P due to local maximum transverse shear stress concentration close to the indenter.

In the LVI tests, FGHs exhibit superior values of KE and P at the same time over their associated helicoid laminates with constant pitch angle as well. 24mm thick laminate due to smaller span over thickness ratio, the global deformation is dominant by transverse shear stresses, while 6mm thick laminate due to larger span over thickness ratio deforms under flexure. This is also the reason why H90sym in 24mm thick laminate exhibits less toughness but shows higher value of toughness in 6mm thick laminate. $\theta_h = 60^\circ$ is with the highest values of absorbed energy KE both in the plate with 6mm and 24mm thickness, which is largely contributed by intralaminar damage. $\theta_h = 90^\circ$ shows the maximum peak load P in the plate with 6mm thickness and $\theta_h = 22.5^\circ$ reveals the maximum peak load P while the thickness of plate is 24mm ($\theta_h = 90^\circ$ also shows competitive value of P in the plate with 24mm thickness). The FEA has shown that

FGH1sym with 6mm thickness can provide up to 2.95 times larger values of delamination area A_d over its associated helicoid laminates with constant θ_h and then it can contribute to superior energy absorption. The A_d is increasing with increasing values of θ_h in helicoid laminates with 6mm thickness. However, when the plate thickness increases to 24mm, with increasing of the pitch angle, the values of A_d decrease from $\theta_h = 15^\circ$ to $\theta_h = 30^\circ$ and then increase from $\theta_h = 45^\circ$ to $\theta_h = 90^\circ$.. The projected delamination area A_{pd} shows that smaller θ_h has larger extent of delamination area both in 6mm thick and 24mm thick plates, which aligns with the results of other publications (Ginzburg et al., 2017; Grunenfelder et al., 2014a). That projected delamination area for laminates with smaller pitch angle is larger than laminates with larger pitch angles because laminates with smaller pitch angle include more fiber directions in $x - y$ plane than the laminates with larger pitch angle and delamination propagates along the fiber direction (the direction with higher strain energy) of both layers close to the interface. This results also support the explanation that the discrepancy of energy release rate and strength of laminates with different pitch angles are related to the different transverse stresses/strains distribution.

Comparing the results of 3-point short beam bending and low-velocity impact tests, we can observe that both tests can achieve superior values of energy storage or energy absorption, up to 60% and 15% higher values than other helicoid laminates with constant pitch angle, when $\theta_h = 60^\circ$ and $\theta_h = 45^\circ$. On the other hand, both tests show that when $\theta_h = 22.5^\circ$ and $\theta_h = 36^\circ$, they can achieve benefits on peak load over other helicoids with constant pitch angles.

The relative relationship on transverse stress/strain of laminates with different pitch angles along the thickness in the continuum shell model aligns with the solid model, although the discrepancy between different lamina misorientations in the laminate is smaller than the solid model. Higher component value of transverse shear strain energy in $x-z$ direction is observed in the laminae with smaller misorientation, which is the same as solid model. Besides the delamination initiation and propagation of continuum shell is validated through comparing the delamination propagation from solid model considering delamination only.

In general, FGHs show superior mechanical behaviors at the same time over their associated laminates with constant θ_h both in static and dynamic analyses according to the characteristics on transverse stresses/strain of distinct pitch angles and their specific arrangement through the thickness.

6. CONCLUSIONS

From my thesis work, it is exhibited that bio-inspired stiff fibers, tablets or prisms reinforced composite materials can provide multi-functional behaviors through varying structural parameters, such as pitch angle θ_h of helicoid architectures, effective shear area or effective tension area of fibers/tablets reinforced composite materials, orientation of prisms in nacreous architectures and pitch distance of helicoid architectures.

Fiber reorientation behaviors due to deformation of the laminates with different θ_h and laminates with distinct lay-up sequences, combined with its contribution to the strain stiffening are analyzed in Chapter 2.

Among the dominant geometrical features, we can mention pitch angle, θ_h . Constitutive properties, such as the fiber to matrix stiffness ratio, as well as the matrix nonlinear behavior, are relevant as they relate to strain stiffening and overall failure. To deconvolve the various effects, we examined various architectures, namely DFH/DMB/DSL, to gain insights into the contribution of deformation to fiber reorientation, $\Delta\theta_c$, as it relates to lamina misorientation with respect to the loading direction and lay-up sequence. We found that the DFH architecture exhibits less in-plane shear deformation and less transverse contraction leading to smaller values of fiber reorientation, $\Delta\theta_c$, compared with the DMB and DSL architectures. We compared and quantified $\Delta\theta_c$ in individual laminae from different architectures. For instance, we found that the individual lamina θ_{30} of the DFH $\theta_h = 30^\circ$ exhibits up to 29.5% lower $\Delta\theta_c$ that found in the DSL $\theta_s = 30^\circ$ upon 15% ϵ . On the other hand, the θ_{45} lamina in the DMB architecture exhibits 28.6% higher value of $\Delta\theta_c$ than the θ_{45} lamina in the DFH with $\theta_h = 45^\circ$. In fact, the DFH architecture, due to its overall balanced lay-up sequence, exhibits smaller in-plane shear deformation than the DSL architecture and less contraction in the transverse direction than the DMB architecture. The DMB $\theta_b = 30^\circ$ exhibits a 93.4% higher ν_{xy} than the DSL architecture with $\theta_s = 30^\circ$. This is due to its compatible mechanical properties among balanced laminae.

The analysis reported in this study revealed that the DFH architecture, with a linear elastic or elasto-plastic matrix with small plastic hardening, shows negligible strain stiffening, compared with the DMB architecture, under uniaxial tensile loading, whereas the DMB architecture, show superior strain stiffening compared with DFH architecture (up to 16% under 4% local ϵ_t and 33.6%

under 10% local ϵ_t). Furthermore, evidence that no strain stiffening shown in the FEA with linear elastic matrix and negligible strain stiffening predicted by the plate theory revealed that the strain stiffening observed in 3D printed samples is primarily due to the hyperelastic constitutive response of the matrix.

Although the DFH architecture and the disorder laminates show the same elastic modulus before deformation, their fiber reorientation and strain stiffening values are slightly different after the same tensile strain (4% local ϵ_t). This observation confirms that lay-up sequence influences the deformation in each lamina through the thickness and thus, has an impact on the fiber reorientation behavior.

In Chapter 3 we provided a detailed comparative analysis that looks at the three-dimensional geometries of the rod-like and tablet-like architectures. Their mechanical behaviors, such as stiffness, strength and toughness, under uniaxial tensile in two orthogonal directions are analyzed to investigate why nature chooses two different geometries in three-dimension for the living organisms, though their two-dimensional structures are the same.

We set up the comparison between 3D tablet-like nacre architectures and rod-like chiton architectures based on dimensionless groups of mechanical properties and geometry parameters. Rigorous analytical, experimental and numerical analyses are exploited to compare and analyze the properties of two architectures from different associated factors.

Compared to 3D tablet-like nacre architectures, rod-like chiton architectures are more efficient on mechanical properties in longitudinal direction when both featured with the same volume fraction V_f and aspect ratios L/M . However, 3D tablet-like nacre architectures are more beneficial in biaxial loading. This also answers our initial question that why nature chooses rod-like chiton structures to endure axial loading in their longitudinal direction and chooses tablet-like structures to be the structured components of the nacre shell. This phenomenon can be explained by the different effective shear and tension area of the architectures, which are the hidden confounder for general geometry parameters, V_f and L/M , and mechanical properties, such as stiffness, strength and toughness. Accordingly, in three-dimension, besides V_f and L/M , the effective shear and tension area are another two key parameters needed to be considered to calculate mechanical properties, encompassing elastic modulus, critical load and toughness.

From Chapter 4, it is introduced that the functionally graded modulus distribution through the thickness of *Pinctada* shell can provide superior fracture resistance than other modulus

distributions, such as constant modulus, layered modulus and inversed functionally graded modulus. It is interesting to see that the functionally graded modulus due to varying orientations of prisms in the outer layer of the Pinctada shell can overcome other patterns of modulus distribution. Accordingly, extending from this analysis, we focus on the study of helicoid architectures with stiff fibers reinforced laminates again, which are found with functionally graded pitch distance through the thickness of dactyl clubs of mantis shrimp.

Quasi-static tests and low-velocity impact tests are designed to analyze the mechanical behaviors of helicoid architectures with different θ_h and the functionally graded helicoids (FGHs). In Chapter 5, two types of FGHs are designed with linearly decreasing pitch distance from surface to interior, which is found in the dactyl clubs of mantis shrimp and the fish scale of coelacanth. Although the minimum θ_h can only reach to 15° , which is not as small as the one occurring in the biological architectures found in dactyl clubs of mantis shrimp, these θ_h can still represent the architectures in fish scales.

In the short-beam bending tests, $\theta_h = 30^\circ$ is the optimum pitch angle for peak load, P , and $\theta_h = 45^\circ$ is the optimum pitch angle for toughness, T_c . In the comparison analysis of P and T_c , helicoid with constant θ_h is observed without higher P and T_c at the same time, while FGHs occupy the optimum area of Ashby plot with higher P and T_c simultaneously. This is because first the maximum transverse shear stress is observed at the interfaces close to top indenter and two bottom rollers, although maximum transverse shear stresses is achieved in the middle of the laminate along the thickness in the $x - z$ plane except for the paths going through the thickness close to rollers and indenter, shown in Figure 5.23 and Figure 5.24. Secondly, except for the laminates with smaller pitch angle, which laminate's peak load is dependent on the delamination close to top indenter, showing the higher transverse shear stress S_{xz} among other helicoids, shown in Figure 5.25(a), other helicoids reveals that their peak load is dependent on the maximum S_{xz} close to the bottom surface. H30sym shows the minimum value of S_{xz} at the interfaces close to bottom rollers at the same applied displacement and thus it can behave as a coating material, delaying the occurrence of delamination, and then provide the maximum peak load. Accordingly, $\theta_h = 30^\circ$ and $\theta_h = 36^\circ$ arranged close to the top and bottom surfaces of FGHs respectively can achieve the maximum peak load. Besides, H45sym and H60sym reveal benefits on toughness over other helicoids, since their damage evolution is slower than other helicoids due to a greater number of 0° laminae, which is the toughest lamina under bending. H90sym should be tougher as well

since it encompasses larger number of 0° lamina, but its weak peak load reduces the energy absorbed under 6mm deflection, compared with others. FGHs composed of $\theta_h = 45^\circ$ and $\theta_h = 60^\circ$ close to the middle of their whole laminate along the thickness highly increases the energy storage under damage and delamination evolution, since the delamination and damage propagates slowly due to larger number of 0° laminae.

Laminate FGH1symdisorder, which is composed of the same component pitches of FGH1sym but with different order of arrangement along the thickness from surface to interior, exhibits lower toughness and peak load compared with its associated helicoid laminates. The detailed comparison on delamination propagation between FGH1symdisorder and FGH1sym is shown in Figure D5. $\theta_h = 45^\circ$ is not beneficial for delaying delamination due to concentrated stresses induced by contact, as discussed before, which has been assigned close to bottom and top surfaces of FGH1symdisorder. In the meantime, $\theta_h = 36^\circ$ assigned close to the middle of FGH1symdisorder cannot provide enough in-plane deformation resistance after delamination initiation close to the bottom surface. Accordingly, it seems that the arrangement order of different pitch angles along the thickness is related to the delamination and in-plane damage resistance.

Furthermore, the distribution of transverse shear stresses in the short beam bending test is predicted by FEA and analytical calculation. It is shown that, due to the smooth transition of the transverse shear stress and less number of stress concentration at interfaces along the thickness in the architectures with smaller pitch angles at a given applied load/displacement, they can endure more bending deformation before large extent of delamination occurs at the bottom of the beam. However, laminates with smaller pitch angle, less than 22.5° , show lower value of P due to local maximum transverse shear stress concentration close to the indenter.

In the LVI tests, FGHs exhibit superior values of KE and P at the same time over their associated helicoid laminates with constant pitch angle as well. 24mm thick laminate due to smaller span over thickness ratio, the global deformation is dominant by transverse shear stresses, while 6mm thick laminate due to larger span over thickness ratio deforms under flexure. This is also the reason why H90sym in 24mm thick laminate exhibits less toughness but shows higher value of toughness in 6mm thick laminate. $\theta_h = 60^\circ$ is with the highest values of absorbed energy KE both in the plate with 6mm and 24mm thickness, which is largely contributed by intralaminar damage. $\theta_h = 90^\circ$ shows the maximum peak load P in the plate with 6mm thickness and $\theta_h = 22.5^\circ$ reveals the maximum peak load P while the thickness of plate is 24mm ($\theta_h = 90^\circ$ also

shows competitive value of P in the plate with 24mm thickness). The FEA has shown that FGH1sym with 6mm thickness can provide up to 2.95 times larger values of delamination area A_d over its associated helicoid laminates with constant θ_h and then it can contribute to superior energy absorption. The A_d is increasing with increasing values of θ_h in helicoid laminates with 6mm thickness. However, when the plate thickness increases to 24mm, with increasing of the pitch angle, the values of A_d decrease from $\theta_h = 15^\circ$ to $\theta_h = 30^\circ$ and then increase from $\theta_h = 45^\circ$ to $\theta_h = 90^\circ$.. The projected delamination area A_{pd} shows that smaller θ_h has larger extent of delamination area both in 6mm thick and 24mm thick plates, which aligns with the results of other publications (Ginzburg et al., 2017; Grunenfelder et al., 2014a). That projected delamination area for laminates with smaller pitch angle is larger than laminates with larger pitch angles because laminates with smaller pitch angle include more fiber directions in $x - y$ plane than the laminates with larger pitch angle and delamination propagates along the fiber direction (the direction with higher strain energy) of both layers close to the interface. This results also support the explanation that the discrepancy of energy release rate and strength of laminates with different pitch angles are related to the different transverse stresses/strains distribution.

Comparing the results of 3-point short beam bending and low-velocity impact tests, we can observe that both tests can achieve superior values of energy storage or energy absorption, up to 60% and 15% higher values than other helicoid laminates with constant pitch angle, when $\theta_h = 60^\circ$ and $\theta_h = 45^\circ$. On the other hand, both tests show that when $\theta_h = 22.5^\circ$ and $\theta_h = 36^\circ$, they can achieve benefits on peak load over other helicoids with constant pitch angles.

The relative relationship on transverse stress/strain of laminates with different pitch angles along the thickness in the continuum shell model aligns with the solid model, although the discrepancy between different lamina misorientations in the laminate is smaller than the solid model. Higher component value of transverse shear strain energy in $x-z$ direction is observed in the laminae with smaller misorientation, which is the same as solid model. Besides the delamination initiation and propagation of continuum shell is validated through comparing the delamination propagation from solid model considering delamination only.

In general, FGHs show superior mechanical behaviors at the same time over their associated laminates with constant θ_h both in static and dynamic analyses according to the characteristics on transverse stresses/strain of distinct pitch angles and their specific arrangement through the thickness.

In closing, we have provided rigorous analytical, experimental, and computational analyses on studying the mechanical behaviors of bio-inspired composite materials, including elastic and elasto-plastic behaviors under large deformation, damage and fracture resistance behaviors under static and dynamic loading conditions. The impact of functionally varying structural parameters and geometrical parameters on these composite materials are quantified and analyzed, which should be valuable to those designing composite materials in which tailoring of constitutive behavior is inspired by motifs found in nature.

APPENDIX A. SUPPLEMENTAL MATERIAL FOR CHAPTER 2

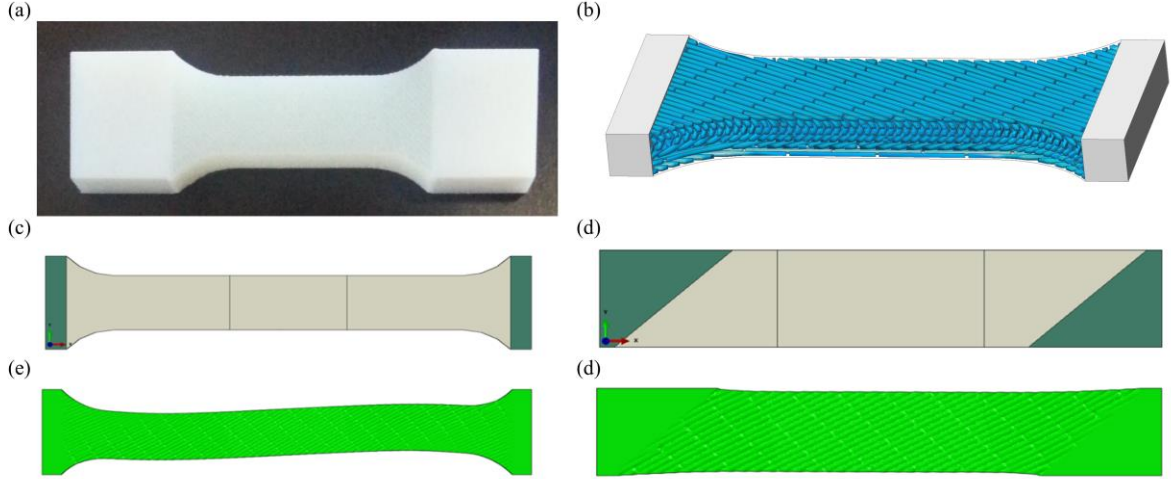


Figure A1. (a) 3D-printed sample with $L/W = 2$, and (b) FEA model with $L/W = 2$ (c) and (e) undeformed and deformed dog-bone samples of DSL $\theta_s = 30^\circ$ with $L/W = 6$ (d) and (f) undeformed and deformed oblique tab samples of DSL $\theta_s = 30^\circ$ with $L/W = 4$

A1 Material curve fitting

The energy potential of incompressible hyperelastic material with model of polynomial $N = 2$ model is shown in s(1), where \bar{I}_1 and \bar{I}_2 are the 1st and 2nd deviatoric strain invariants.

$$U = C_{10}(\bar{I}_1 - 3) + C_{01}(\bar{I}_2 - 3) + C_{20}(\bar{I}_1 - 3)^2 + C_{11}(\bar{I}_1 - 3)(\bar{I}_2 - 3) + C_{02}(\bar{I}_2 - 3)^2 \quad \text{A(1)}$$

For uniaxial mode, the relationship between traction T_U and stretch λ_U is,

$$T_U = 2(1 - \lambda_U^{-3})[C_{10}\lambda_U + C_{01} + 2C_{20}\lambda_U(\bar{I}_1 - 3) + C_{11}(\bar{I}_1 - 3 + \lambda_U(\bar{I}_2 - 3)) + 2C_{02}\lambda_U(\bar{I}_2 - 3)] \quad \text{A(2)}$$

For simple shear mode, the relationship between traction T_S and stretch γ is,

$$T_S = 2(C_{01} + C_{10})\gamma + 4(C_{20} + C_{11} + C_{02})\gamma^3 \quad \text{A(3)}$$

Based on the constitutive law of isotropic material, the initial slope of stress and strain curve extracted in the simple shear test is the shear modulus (G) of the material. It must satisfy the equation of $G = \frac{E}{2(1 + \nu)}$, where E is the elastic modulus and ν is the Poisson's ratio. Nonetheless, G calculated according to the simple shear test of 3D printed matrix material does

not satisfy the constitutive law of isotropic material, showing higher value on G than the isotropic material characterized from uniaxial tensile loading. Accordingly, we simplified the matrix material to isotropic hyperelastic model in FEA by employing least squares fit approach to represent the stress and strain behavior in uniaxial tensile and simple shear deformation, as shown in equation A(4). Specific results and coefficients are illustrated in Figure A2.

$$E_{error} = w_1 \sum_{i=1}^n \left(\frac{T^\tau - T^i}{T^\tau} \right)^2 + w_2 \sum_{i=1}^n \left(\frac{T^\sigma - T^i}{T^\sigma} \right)^2 \quad A(4)$$

Where E_{error} is the permitted error between the fitting curve and the test results. w_1 is the weight for simple shear test and w_2 is the weight for uniaxial tensile test. T^τ is the stress value from the simple shear test data and T^σ is the stress value from the uniaxial tensile test. T^i comes from equations s(2) and s(3). n is the number of data points.

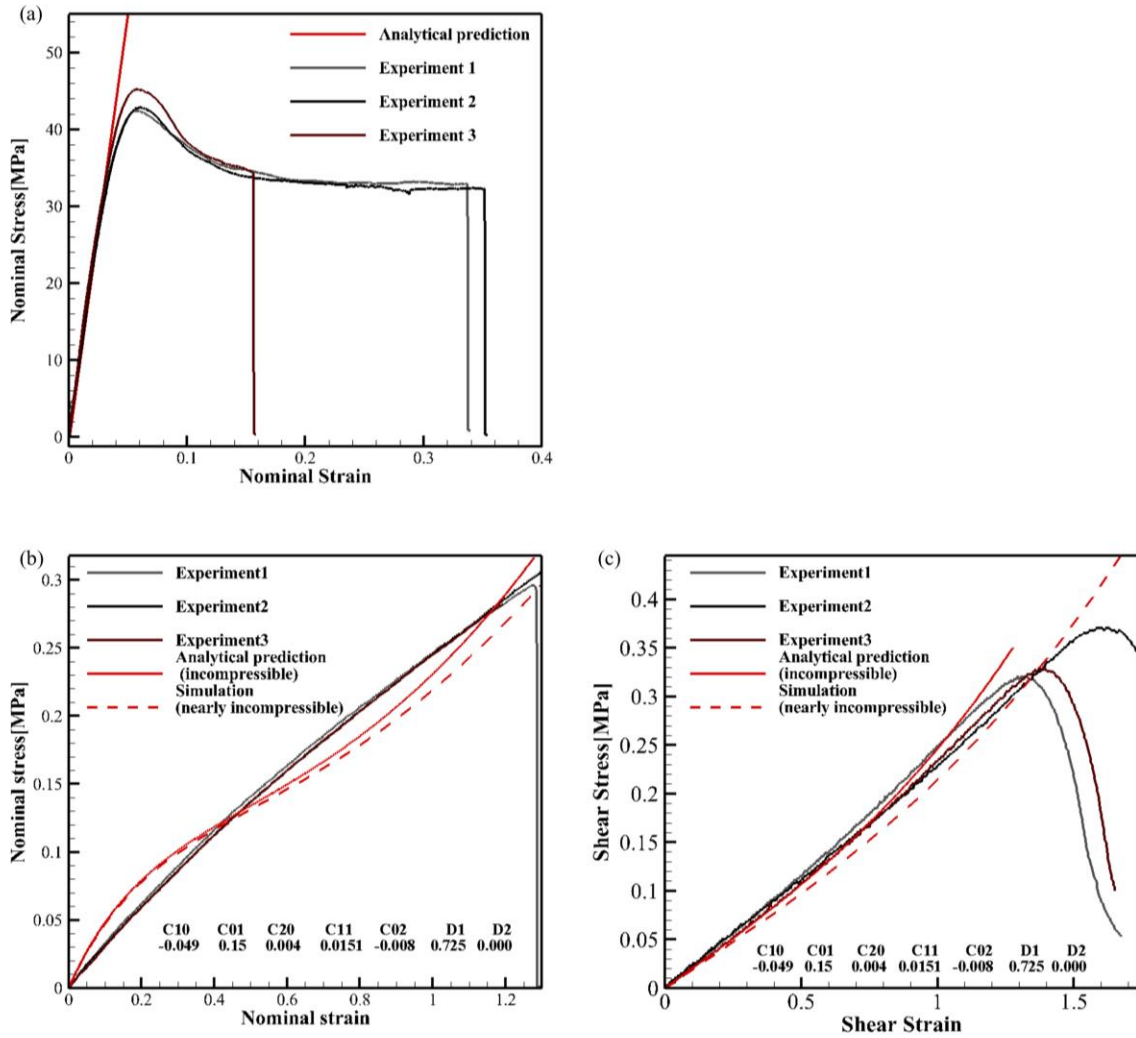


Figure A2. Stress strain curves of (a) VeroWhite fiber material under uniaxial tensile loading, and (b) TangoPlus matrix material under uniaxial tensile loading and (c) under simple shear loading

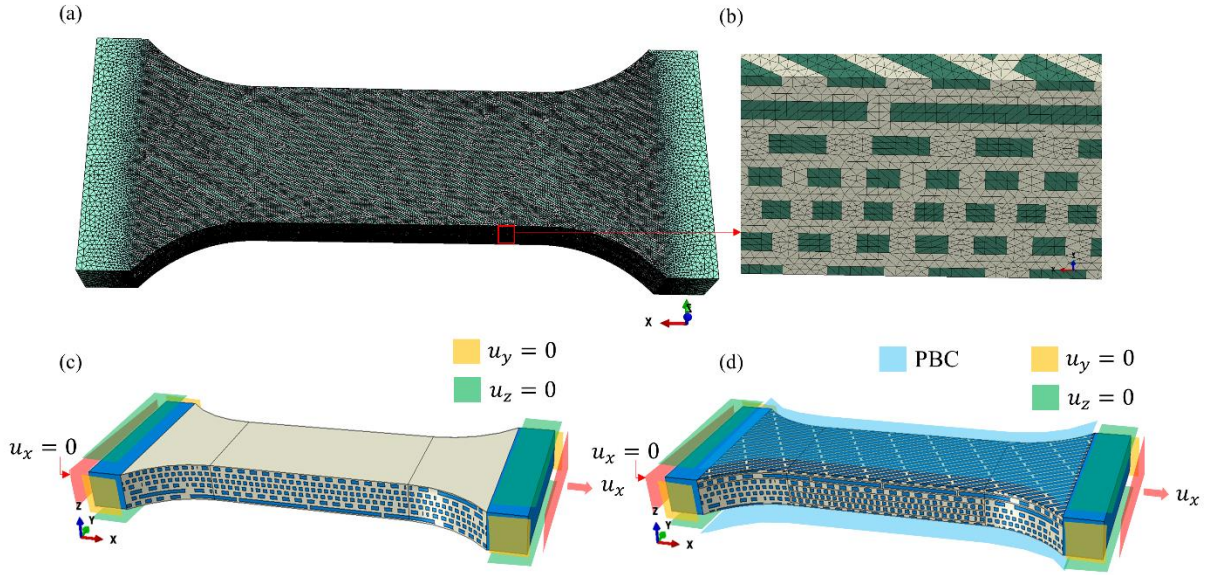


Figure A3 (a) Finite element implementation of the helicoid geometry ($\theta_h = 30^\circ$), with (b) Close up showing mesh refinement across fiber and surrounding matrix (c) Illustration of free-free boundary condition (d) Illustration of free-periodic boundary condition

A2 Mesh condition and mesh convergence study

The mesh size 0.2mm is selected such that there are approximately 2 to 3 elements across the width of the fibers and 2 to 4 elements across the matrix region between fibers, Figure A3(a) and (b). Nodes at top and bottom surfaces of gauge satisfy equations $u_i^{top} - u_i^{bottom} = 0$, where $i = x, y$ and z , which is the periodic boundary condition, shown in Figure A3(d).

Mesh convergence study is conducted on DSL $\theta_s = 90^\circ$, which is shown as an example here. Mesh sizes 0.2mm, 0.24mm, 0.3mm and 0.4mm are used in the FEA. As it can be seen in Figure A4, convergence can be attained as the number of elements increases. However, calculations with higher number of elements (beyond 6.5×10^5) becomes a limiting factor in terms of memory requirements and CPU time, and thus a mesh size with element size of 0.2mm (total of 638,901 elements) is robust enough for all the FEA simulations reported in this paper(e.g., Figure A3(a) and (b)).

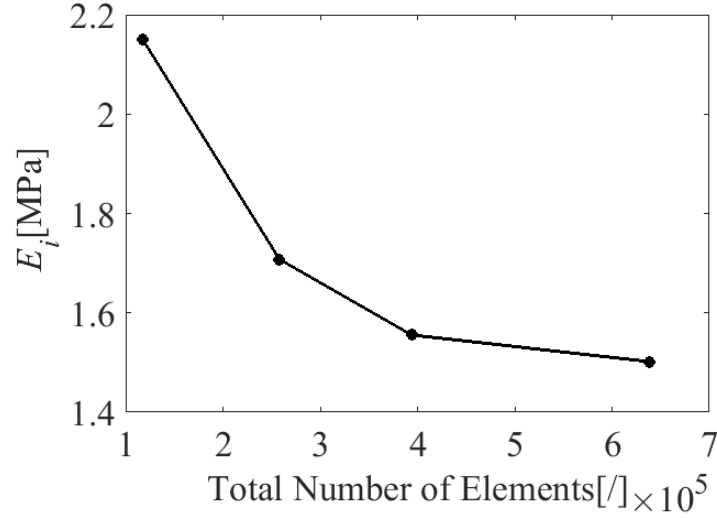


Figure A4. Initial elastic modulus, E_i , in FEA as a function of total number of elements

A3 Warping effects in DSL and its solution

Most specimens were waisted (“dog-bone”) specimens with normal tabs, as shown in Figure A1(b). However, in DSL architectures, the anisotropic in-plane behavior results in an ‘S’ shape in the deformed geometry, shown in Figure A5(b). This in-plane warping behavior influences the measurement of the fiber reorientation due to stretch only. To mitigate this effect, oblique tabs are introduced for DSL specimens (Sun and Chung, 1990) to reduce warping effects. The details are introduced in the following and the comparison between waisted and oblique tab samples is illustrated in Figure A1(e) and (f).

Based on constitutive law of uniaxial stress condition ($\sigma_{xx} = \sigma_0$), we have relationship,

$$\begin{Bmatrix} \varepsilon_{xx} \\ \varepsilon_{yy} \\ \gamma_{xy} \end{Bmatrix} = \begin{bmatrix} \overline{S_{11}} & \overline{S_{12}} & \overline{S_{16}} \\ \overline{S_{12}} & \overline{S_{22}} & \overline{S_{26}} \\ \overline{S_{16}} & \overline{S_{26}} & \overline{S_{66}} \end{bmatrix} \begin{Bmatrix} \sigma_{xx} \\ \sigma_{yy} \\ \sigma_{xy} \end{Bmatrix} \quad \text{A(5)}$$

$$\varepsilon_{xx} = \overline{S_{11}}\sigma_0; \varepsilon_{yy} = \overline{S_{12}}\sigma_0; \gamma_{xy} = \overline{S_{16}}\sigma_0 \quad \text{A(6)}$$

The displacement field should be linear in x and y directions,

$$u_x = \varepsilon_{xx}x + C_1y + C_3; u_y = \varepsilon_{yy}x + C_2x + C_4 \quad \text{A(7)}$$

In order to avoid rigid body translation and rotation, we set up

$$C_3 = C_4 = 0; C_1 = \overline{S_{16}}\sigma_0 \quad \text{A(8)}$$

Which means that the edges of specimen parallel to the loading direction before deformation keep parallel after deformation. In order to satisfy this requirement and have uniform tensile deformation along the longitudinal direction of the specimen, the edges should be oblique as

$$y = \frac{u_x}{S_{16}\sigma_0} - \frac{\overline{S_{11}}}{S_{16}}x; \tan \varphi = -\frac{\overline{S_{11}}}{S_{16}} \quad A(9)$$

where, φ is the angle between the oblique edge and the horizontal tab edge.

The relationship between misaligned angle θ_s and its corresponding oblique tab angle φ under the specific homogenized material property in the present work is illustrated in Figure A5(a),

Based on the displacement field, it is clear that this boundary condition includes rotation of the homogenized materials, which is shown in A(10)

$$w_{12} = \frac{1}{2}\overline{S_{16}}\sigma_0 \quad A(10)$$

In order to exclude the rotation in the gauge region of the laminate, the polar decomposition method is going to be introduced and discussed in *section A4*. The deflection of sample with dog-bone shape is relatively uniform in the gauge zone, as shown in Figure A5(b), and thus the homogenized rotation matrix can be excluded by using polar decomposition method. It is observed that the difference on fiber reorientation values due to stretch only, $\Delta\theta_c$, between dog-bone sample and the sample with oblique tab is small, shown in Figure A5(c). Further confirmation can be observed in Figure A5(d), which is the comparison among the $\Delta\theta_c$ measured from FEA results, calculated by using global displacement map and volume averaged deformation gradient from each element in FEA. Details are described at the end of *section A4*. Thus $\Delta\theta_c$ can be independent on the boundary conditions and the warping induced by fixed ends of the sample. Subsequently, oblique tab, which is with less rotation of the whole laminate compared with dog-bone sample, chosen to be the major approach applied in DSL.

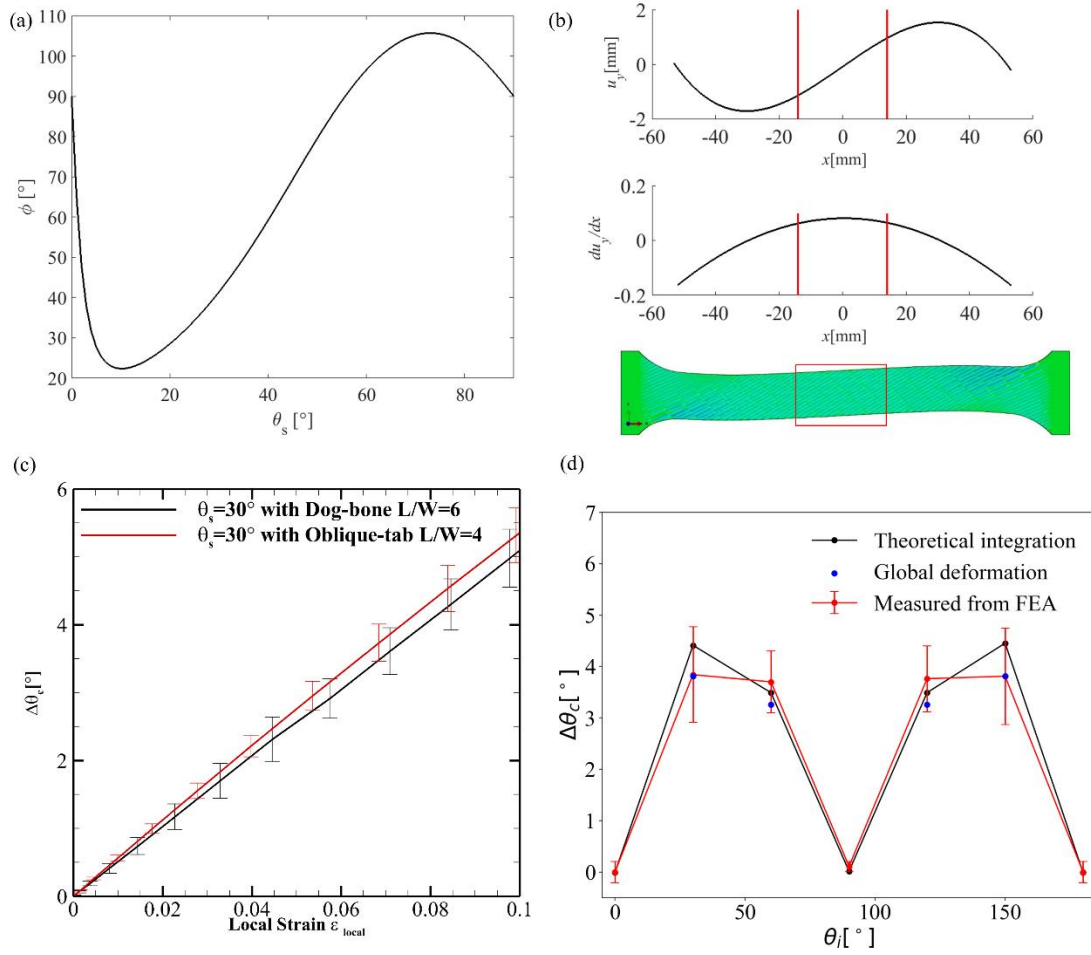


Figure A5 (a) Oblique tab angle, ϕ , as a function of laminae misorientation, θ_s , corresponding to the loading axis; (b) Theoretical deflection and rigid body rotation of dog-bone sample along longitudinal axis in uniaxial tensile; (c) Fiber reorientation of DSL with oblique tab and normal dog-bone tab. (d) $\Delta\theta_c$ measured and calculated by three different methods as a function of misorientation θ_i in DFH $\theta_h = 30^\circ$ with free-periodic boundary condition

A4 The method to exclude rigid body rotation

Before doing polar decomposition, the middle gauge region of the specimen with $L/W = 2$ is the target part to be analyzed and homogenized. Deformation gradient(\mathbf{F}) from FEA is achieved from the Gauss point of each element in the matrix and from the rotation matrix(\mathbf{R}) of the fiber, considered as a rigid body. The deformation gradient is volume averaged by the deformed volume of each element, as shown in equation A(11).

$$\mathbf{F} = [\sum_{i=1}^n (V_{fi} \mathbf{F}_{fi}) + \sum_{i=1}^N (V_{mi} \mathbf{F}_{mi})] / (V_f + V_m) \quad \text{A(11)}$$

Where N is the number of matrix elements, n is the number of fibers, V_f is the volume of all fibers in the target gauge region, V_m is the whole volume of deformed matrix in the gauge region, V_{mi} is the volume of each deformed matrix element, V_{fi} is the volume of each fiber, \mathbf{F}_{mi} is the deformation gradient of each matrix element and \mathbf{F}_{fi} is the corresponding deformation gradient representing for each fiber.

Then, the volume averaged deformation gradient can be decomposed to the product of orthogonal rotation tensor, \mathbf{R} , and right stretch tensor, \mathbf{U} . After calculation, \mathbf{R} tensor of the homogenized laminate is available, as shown in equation s(12). Then based on the uniform warping deformation in the gauge part, we can conduct the calculation on all the fibers in gauge region to exclude the rotation effect from the homogenized laminate.

Once finish the calculation on fibers reorientation, the model with oblique tab and the dog-bone shape with normal tab should have the same values of fiber reorientation, $\Delta\theta_c$, which is induced by deformation, \mathbf{U} tensor, only. The results calculated from two methods are illustrated in Figure A5(c).

$$\mathbf{F} = \mathbf{R} \cdot \mathbf{U} \quad \text{A(12)}$$

Further confirmation is established by comparing the $\Delta\theta_c$ extracted from the displacement field in FEA, theoretical-homogenized \mathbf{F} tensor, and the values measured directly from FEA, as shown in Figure A5(d). The first method assumes that homogeneous deformation is distributed in each individual lamina. Based on the deformed and undeformed coordinates at four vertices of the gauge region, the deformation map can be achieved, and then polar decomposition method is implemented again to extract right stretch tensor \mathbf{U} . In the next step, the deformed vector is calculated as $\bar{\mathbf{v}} = \mathbf{U}\bar{\mathbf{v}}_0$, where $\bar{\mathbf{v}}_0$ is the initial unit vector before deformation, such as $(\cos 30^\circ, \sin 30^\circ)$. The angle between $\bar{\mathbf{v}}$ and $\bar{\mathbf{v}}_0$ is $\arccos\left(\frac{\bar{\mathbf{v}} \cdot \bar{\mathbf{v}}_0}{|\bar{\mathbf{v}}||\bar{\mathbf{v}}_0|}\right)$. The 2nd method (theoretical-homogenized \mathbf{F} tensor) is introduced in section 2.3.3 of the main text and the 3rd method is introduced in this section. The \mathbf{F} tensor from 2nd and 3rd method both are based on the volume averaged deformation gradient components from matrix and fibers.

The fiber reorientation due to stretch only, $\Delta\theta_c$, and fiber reorientation considering in-plane warping effects, $\Delta\theta$, as a function of applied strain, ϵ , from DFH, DMB and DSL architectures are illustrated in Figure A6.

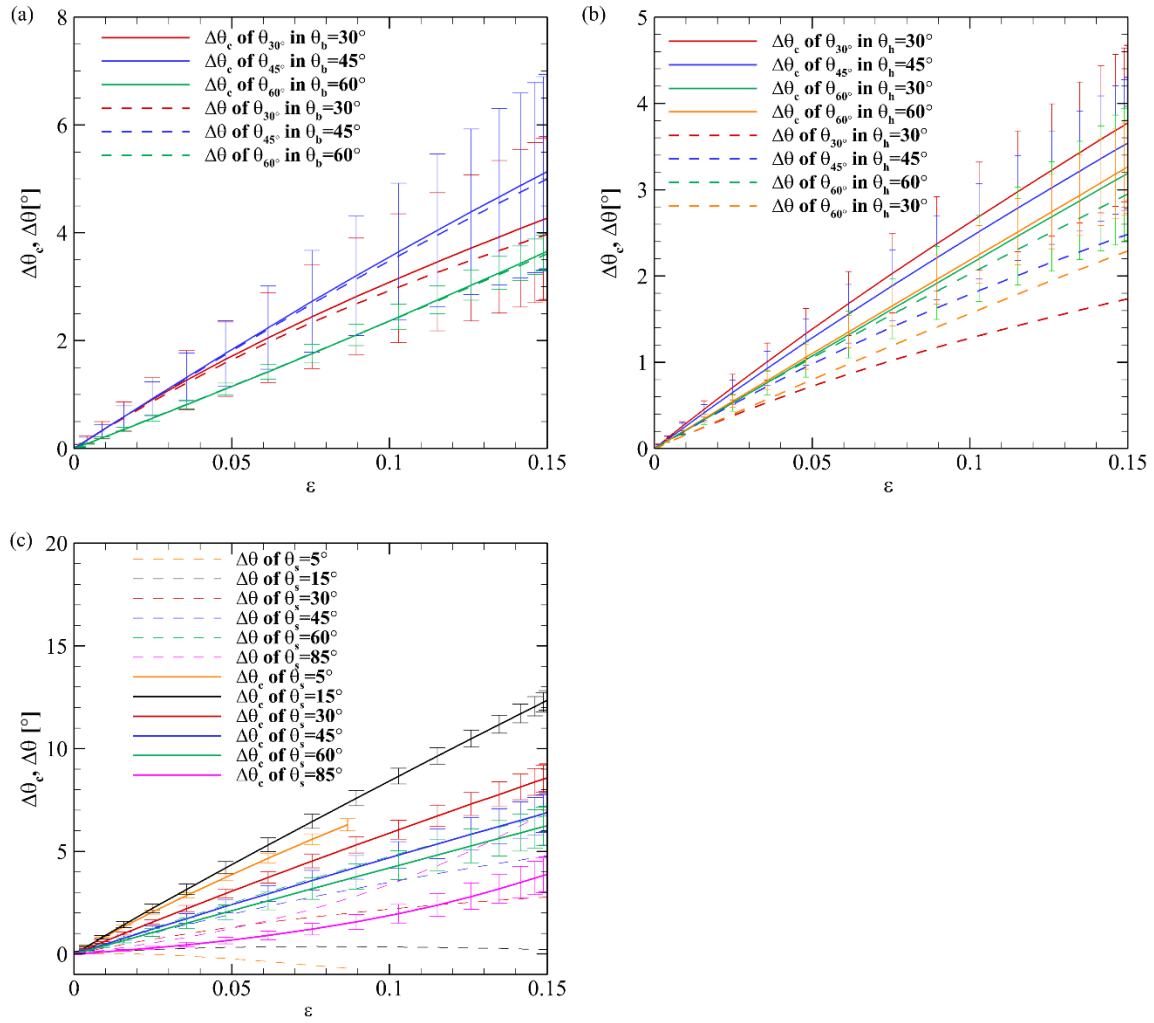


Figure A6 (a)-(b) Fiber reorientation values due to stretch, $\Delta\theta_c$, and fiber reorientation considering in-plane warping effects, $\Delta\theta$, of DFH, DMB and DSL architectures.

Table A1 Components of stretch tensor polar decomposed from deformation gradient extracted from FEA

		U_{xx}	U_{yy}	U_{xy}	U_{yx}
θ_{30} in $\theta_h = 30^\circ$	θ_{h30}	1.1104	0.9455	-0.0196	-0.0196
θ_{60} in $\theta_h = 30^\circ$	θ_{h60}	1.1059	0.9606	-0.0047	-0.0047
θ_{30} in $\theta_b = 30^\circ$	θ_{b30}	1.1099	0.9018	-0.0097	-0.0097
$\theta_s = 30^\circ$	θ_{s30}	1.1121	0.9432	-0.0791	-0.0791

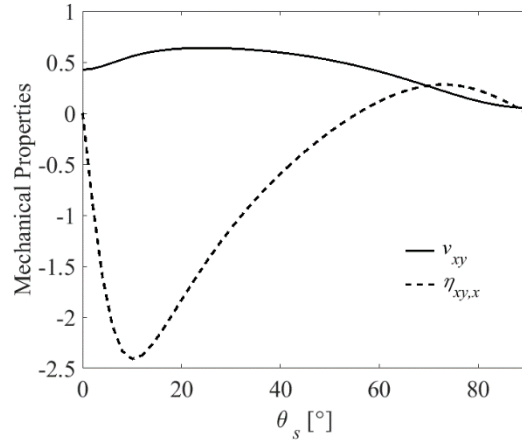


Figure A7. Poisson's ratio v_{xy} and extensional-shear coupling coefficients $\eta_{xy,x}$ as a function of misorientation θ_s .

A5 Stress and strain plots

Stress and strain curves in region II of DFHs in FEA, compared with experimental results are summarized in Figure A8. Hyperelastic model is used in this part with 15% of ϵ . Similarly, stress and strain curves of DSLs with hyperelastic matrix in FEA are plotted in Figure A10(a).

Stress and strain curves of DFH, DMB and DSL architectures with linear elastic matrix under 4% of ϵ_t are illustrated in Figure A10(b)-(d).

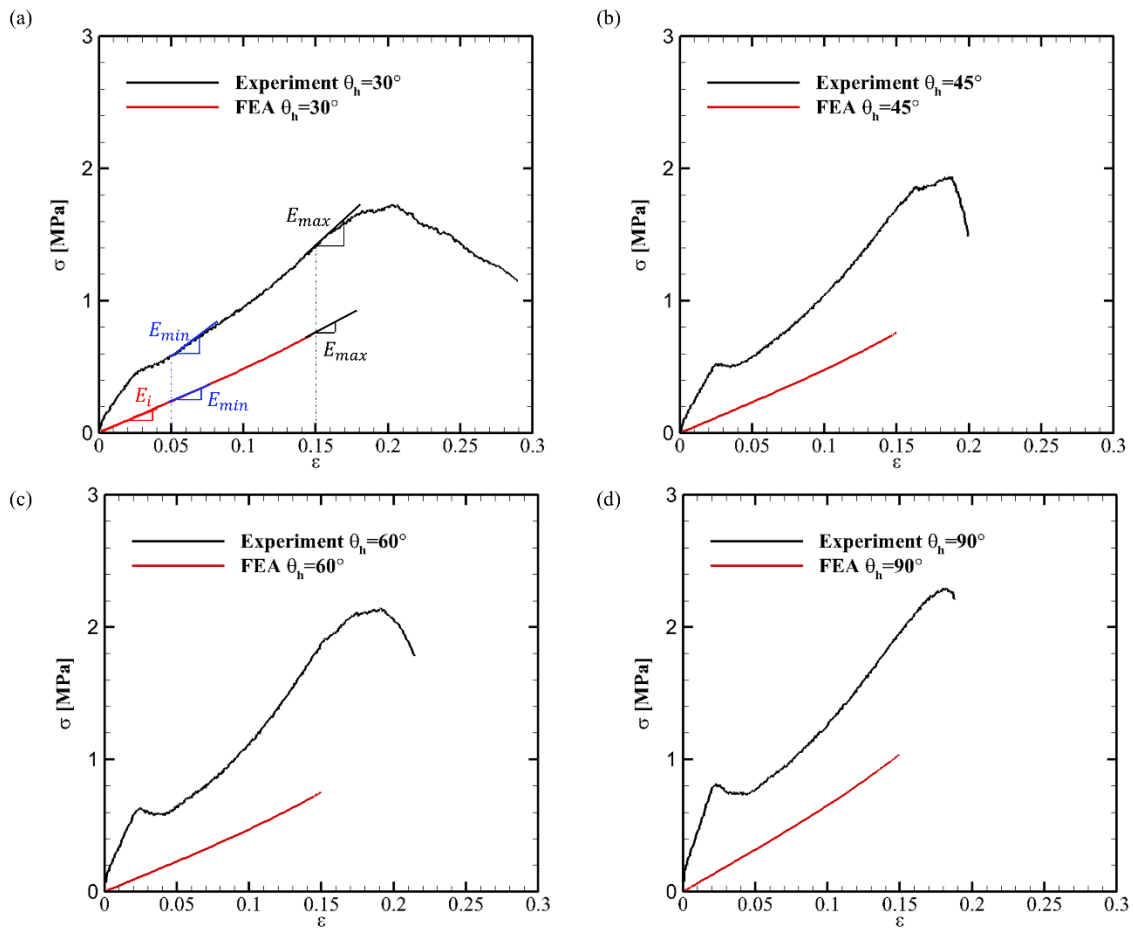


Figure A8. Stress and strain curves in experiments ($L/W=2$) and FEA of DFHs (a) $\theta_h = 30^\circ$, (b) $\theta_h = 45^\circ$, (c) $\theta_h = 60^\circ$, (d) $\theta_h = 90^\circ$.

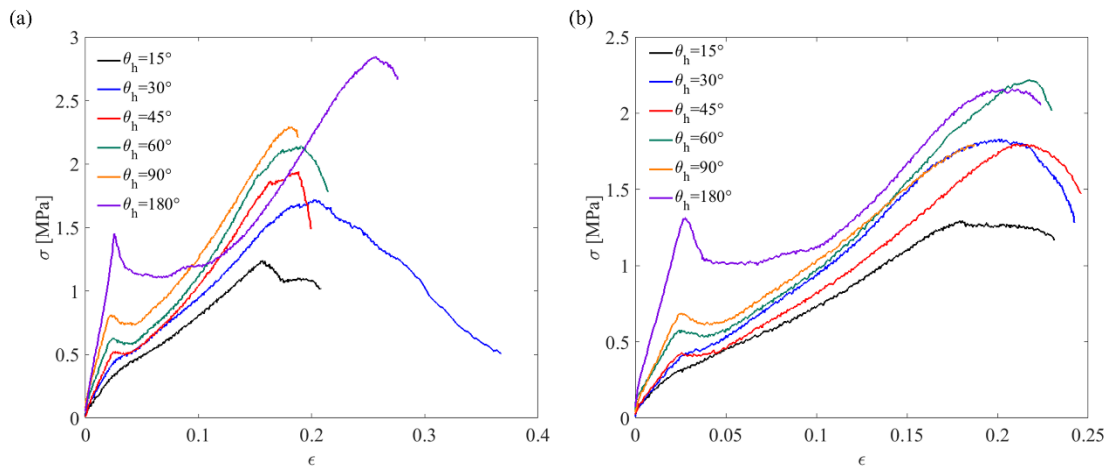


Figure A9. Stress and strain curves in experiments with (a) $L/W=2$ and (b) $L/W=4$

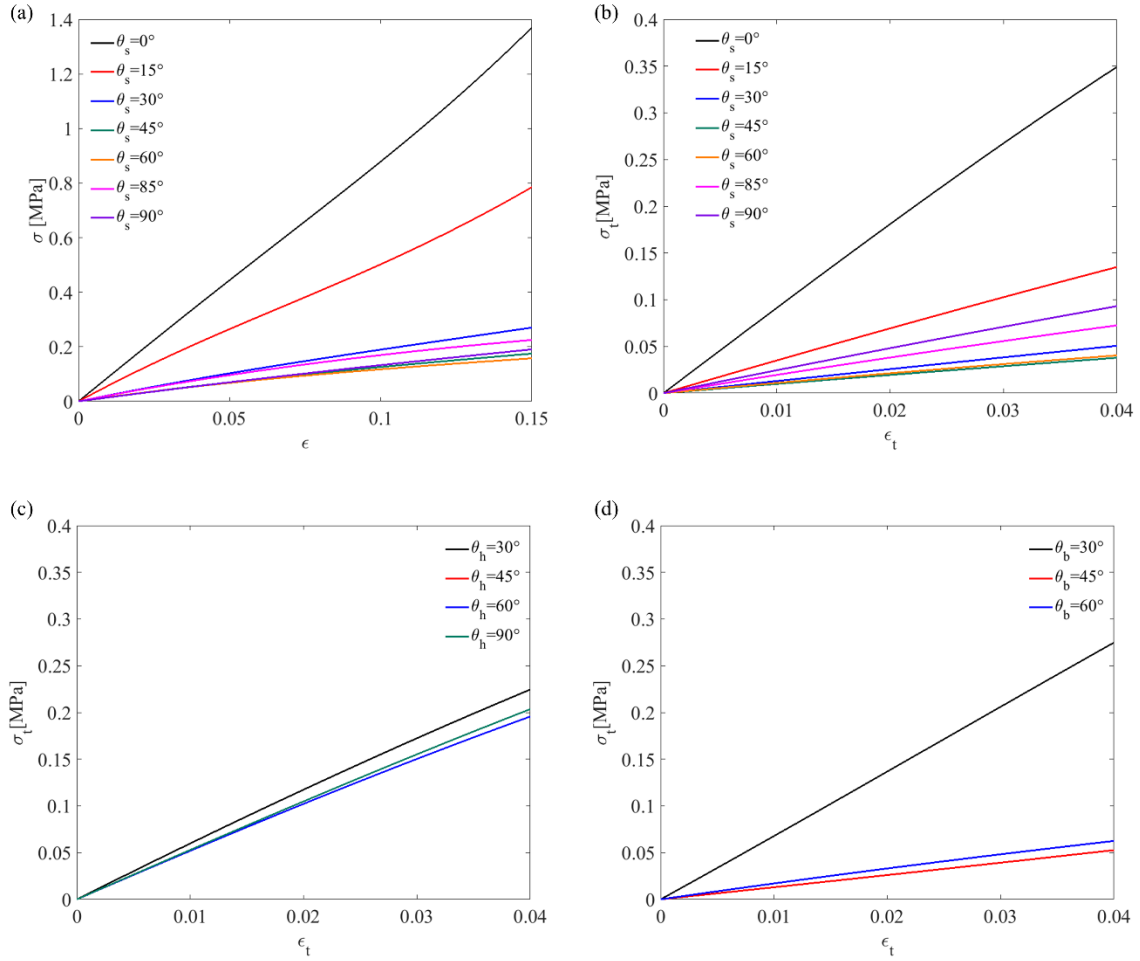


Figure A10. (a) Stress and strain curves in FEA of DSL architectures with hyperelastic matrix (b-d) True stress and strain curves in FEA of DSL architectures, DFH and DMB architectures with linear elastic matrix material.

A6 The stiffening parameter Γ and Γ_{iof}

The stiffening parameter Γ is defined as $\frac{E_{max}}{E_{min}}$ in region II of the stress and strain curve. E_{min} is calculated by fitting a linear model within the interval from $\epsilon = 5\%$ to 6% , where ϵ represents for the applied strain, in the stress and strain curve for all the experimental results. E_{max} is calculated by fitting a linear model within the interval from $\epsilon = 14\%$ to 15% , see Figure A8(a). Γ value of architecture $\theta_h = 0^\circ$ was not shown in Figure 2.2(e), since fiber reorientation in unidirectional laminate due to uniaxial tensile is not our focus. Besides, due to long plateau of

stress and strain curve induced by propagation of local failures at fiber ends after 1st peak stress of $\theta_h = 0^\circ$, shown in Figure A9, the value of E_{min} is close to zero.

The approach to calculate Γ in FEA is similar. In order to match the same deformation that the sample from experiments undergo, E_{min} and E_{max} are defined by fitting linear models based on 5% to 6% and 14% to 15% of ϵ separately from the stress and strain curves in region II(discontinuous matrix), as shown in Figure A8(a).

Γ_{iof} is the stiffening parameter in the specific case that it represents for the E_{max} over the initial modulus, E_i (the interval between 0% to 1% of ϵ in FEA). This is implemented in the calculation of semi-analytical prediction, as shown in Figure 2.4(e) and the stiffness variation of models with linear matrix, shown in Figure 2.6(c) and (d). Γ_{iof} in Figure 2.4(e) is not based on stress and strain curve of FEA, yet it is based on the fiber orientation after 15% of ϵ , while $\Gamma_{iof(4\%)}$ in Figure 2.6(c-d) is based on local true strain, ϵ_t , and true stress curve.

A7 Inclusion of discontinuities to represent early failure

The modulus mismatch between fiber and matrix results in a severe stress concentration at the fiber ends. This has the consequence of an early failure at relatively low ϵ (~3%) at these positions in the experiments. Since a fracture criterion is not implemented in FEA, a separate simulation is conducted to capture the resultant impact of these fractures on the macroscopic stress-strain response. Here, discontinuities are placed within the matrix structure at the fiber ends to represent the local failures, Figure A11.

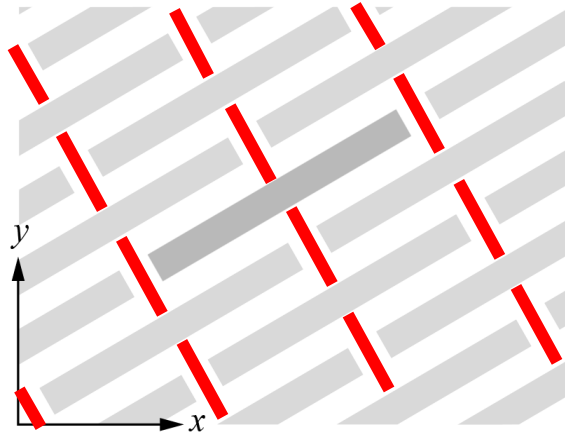


Figure A11. Discontinuities in the matrix between two fibers to mimic the local failures at the beginning of region II

A8 Study on ratio of elastic modulus of fibers (E_{fiber}) over elastic modulus of matrix (E_{matrix})

In the present paper, E_{fiber}/E_{matrix} is approximately 3288. In this section, E_{fiber}/E_{matrix} is extended to 0.01, 0.1, 1, 10, 100 and 1000. From Figure A12(a) and (b), it is observed that once the ratio of E_{fiber}/E_{matrix} is increasing, the $\Delta\theta_c$ value and the strain stiffening Γ_{iof} is going to be converged. In Figure A12(a), with the deceasing of E_{fiber}/E_{matrix} , the material property incompatibility is eliminated. Thereby, minor fiber reorientation is observed.

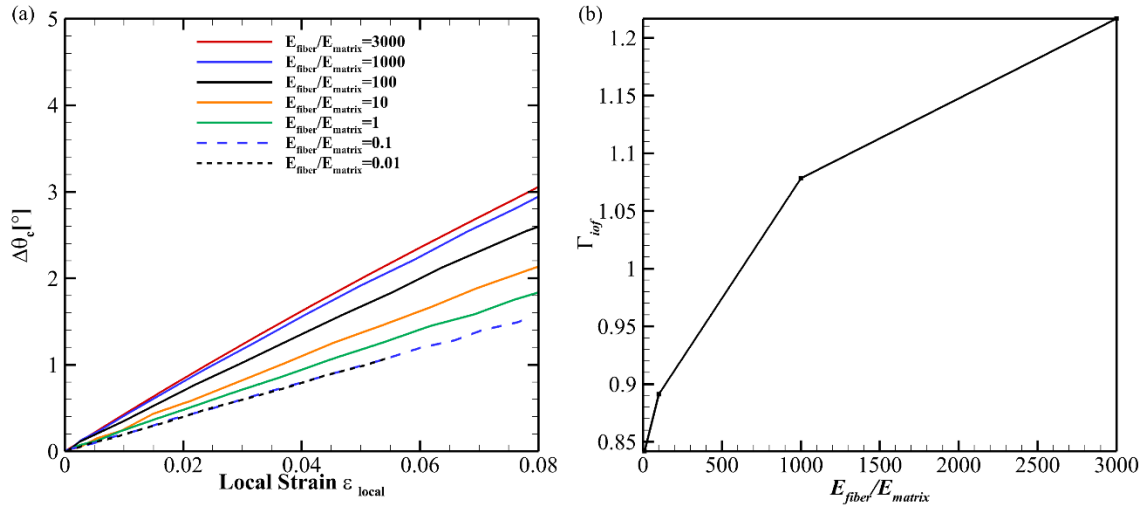


Figure A12. (a) $\Delta\theta_c$ of $\theta_h = 30^\circ$ with different ratios of E_{fiber}/E_{matrix} as a function of local strain. (b) Strain stiffening of $\theta_h = 30^\circ$ as a function of E_{fiber}/E_{matrix} .

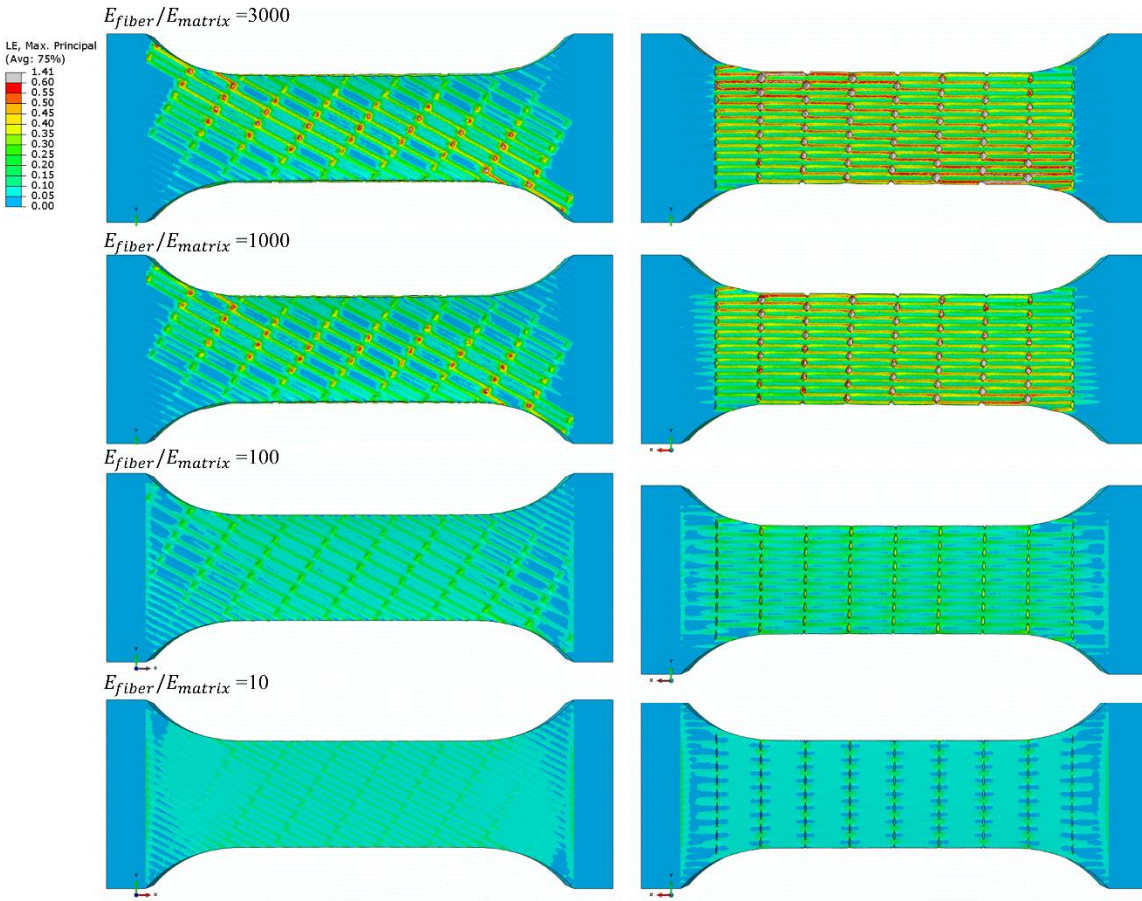


Figure A13. Maximum logarithmic strain, ϵ_{ln} distribution of $\theta_h = 30^\circ$ with different E_{fiber}/E_{matrix}

A9 Shear strain distribution at lamina interface of DMB $\theta_b = 30^\circ$ and DFH $\theta_h = 30^\circ$

The in-plane shear deformation and contraction due to uniaxial tensile of single lamina is dependent on misaligned angle θ_i , shown in Figure A7. However, in a laminate, the adjacent laminae and lay-up sequence can change the deformation of lamina with θ_i , as discussed in section 3.3.1. In this section, we focus on the local in-plane shear deformation of laminates with distinct lay-up sequences.

Based on the in-plan shear strain distribution map at each interface of DFH $\theta_h = 30^\circ$ and DMB $\theta_b = 30^\circ$ under same uniaxial tensile, as shown in Figure A14, large amount of shear deformation is observed at the interface between individual layer θ_0 and $\theta_{30}(\theta_{150})$ of $\theta_h = 30^\circ$. Unignorable shear deformation is also found in the matrix gap between two aligned fibers at the

interface between laminae θ_{30} and θ_{60} , compared with the shear deformation at all interfaces of DMB $\theta_b = 30^\circ$

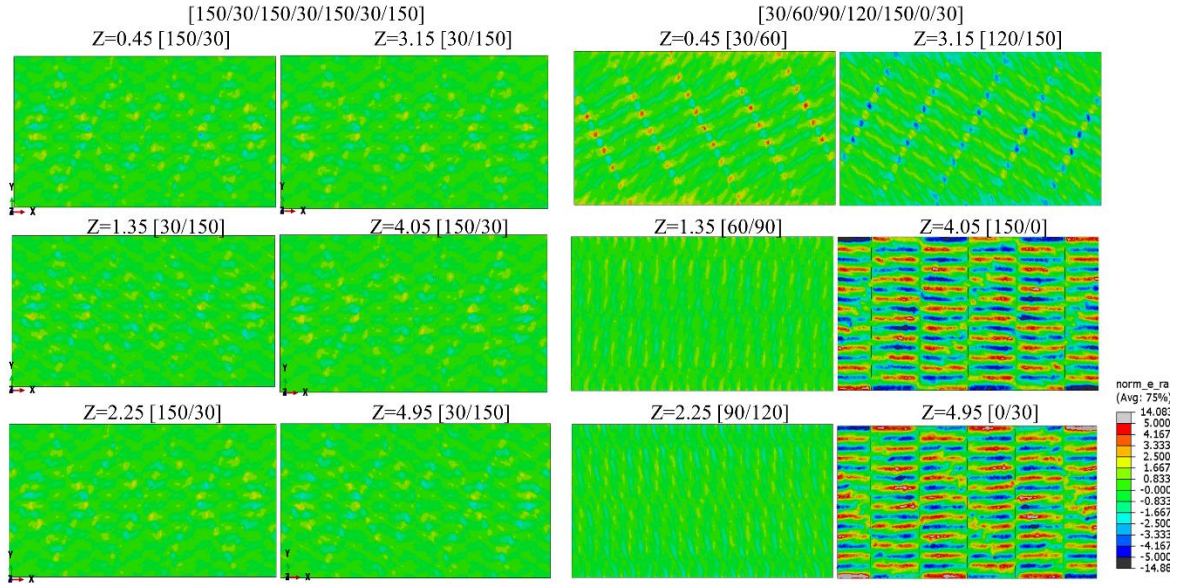


Figure A14. In-plane shear strain, LE_{12} , distribution at the interface of DMB $\theta_b = 30^\circ$ (left) and DFH $\theta_h = 30^\circ$ (right)

After seeing the strain distribution in plane, the shear strain distribution through the thickness is also deserved to be noted. Figure A15 shows the shear strain distribution through the thickness along two distinct paths. These paths go through the matrix part between two parallel fibers, shown in Figure A15.

The in-plane logarithmic shear strain, LE_{12} , of DMB is diminished to 0 or close to 0 at the interface between laminae, whereas DFH is with more shear strain distribution, shown in Figure A15(e) and (f). The paths we chose to show is representative since the shear strain distribution is periodical in-plane, Figure A14.

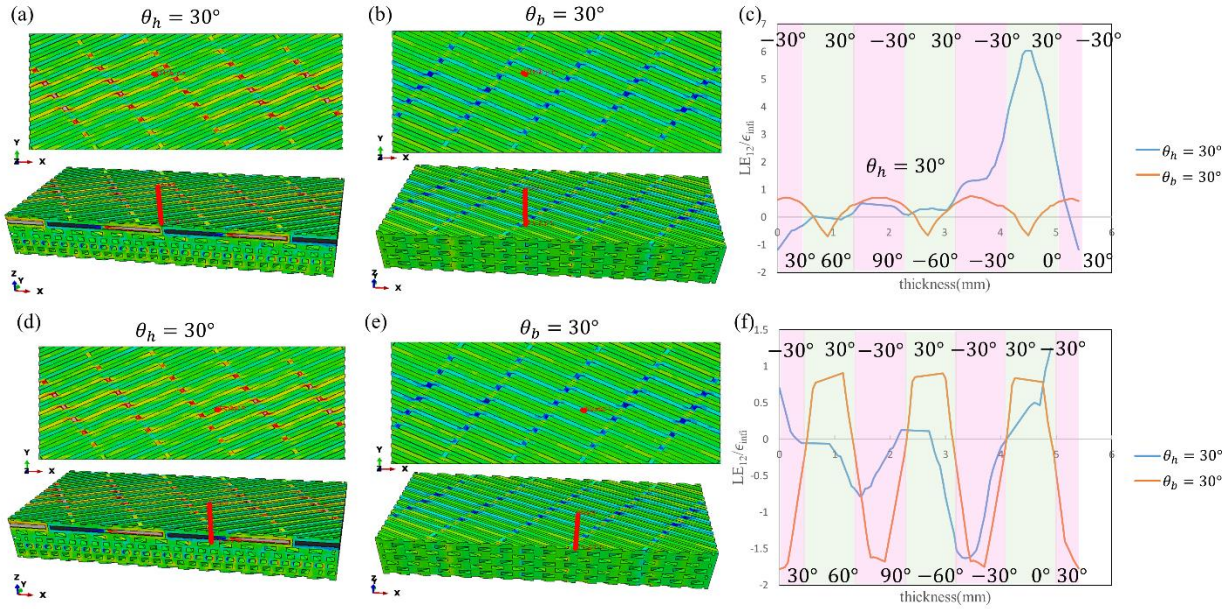


Figure A15. Shear strain distribution, LE_{12} , through the thickness of different two paths of DFH $\theta_h = 30^\circ$ and DMB $\theta_b = 30^\circ$

A10 Comparison on $\Delta\theta$ between models with hyperelastic and linear elastic matrix.

Fiber reorientation values, $\Delta\theta$, are illustrated as a function of loading displacement, which is shown in Figure A16. $\Delta\theta$ is the fiber reorientation values without excluding rotation tensor \mathbf{R} of the homogenized lamina using polar decomposition method. It is observed that $\Delta\theta$ of DFH $\theta_h = 30^\circ$ and DMB $\theta_b = 30^\circ$ with hyperelastic matrix is consistent with the results of DFH $\theta_h = 30^\circ$ and DMB $\theta_b = 30^\circ$ with linear elastic matrix.

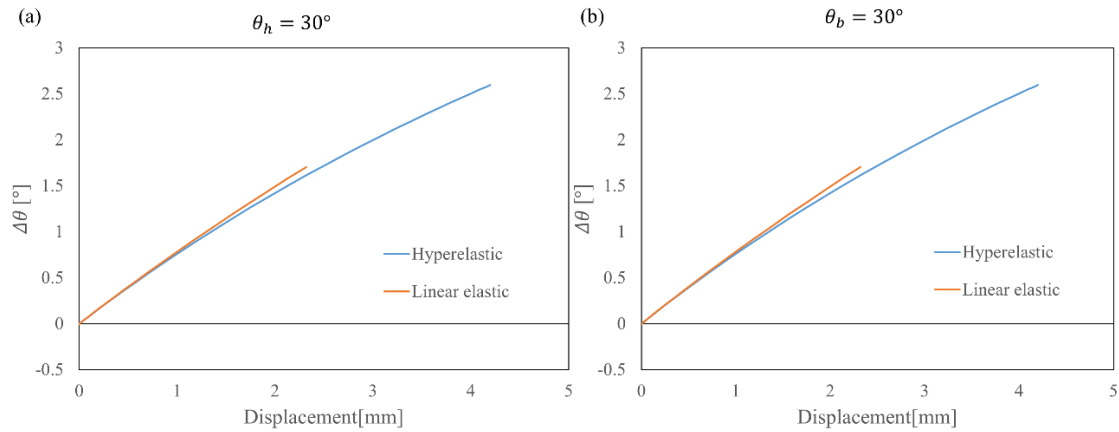


Figure A16. Fiber reorientation, $\Delta\theta$, as a function of applied displacement in (a) DFH $\theta_h = 30^\circ$ and (b) DMB $\theta_b = 30^\circ$ with hyperelastic and linear elastic matrix.

A11 Fiber reorientation in models with free-periodic boundary condition

$\Delta\theta_c$ values in DFH with free-periodic boundary condition totally exclude the size effect in z direction. $\Delta\theta_c$ values in DFH show the symmetry results corresponding to vertical axis θ_{90} , shown in Figure A17. However, due to discontinuous lay-up sequence, the $\Delta\theta_c$ values of disorder laminate $\theta_r=[30/150/60/120/0/90/30]$ are not symmetry to the vertical axis θ_{90} . $\Delta\theta_c$ of individual lamina θ_{60} in θ_r is 15.5% higher than the individual lamina θ_{60} of $\theta_h = 30^\circ$, due to larger in-plane shear deformation of adjacent lamina θ_{150} in θ_r and more contraction in transverse direction due to “balanced” effect of adjacent lamina θ_{120} in θ_r .

The E_{ini} of disorder laminates with the same lamina misorientations of DFH $\theta_h = 30^\circ$, but with different lay-up sequence is tabulated in Table A2. All these results are calculated by CLPT and there are 120 N repeated in z direction to represent infinite case in the material.

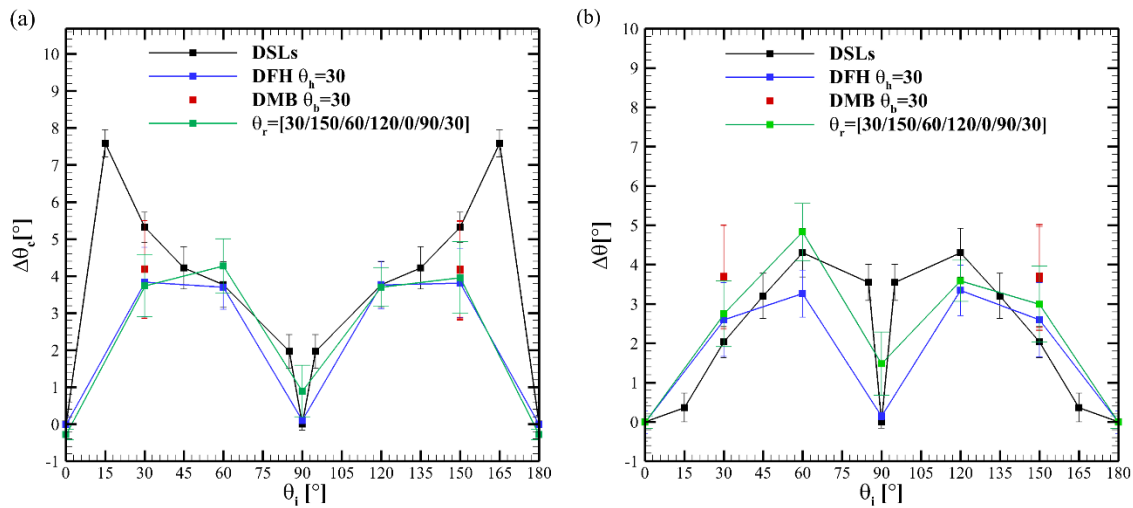


Figure A17. Fiber reorientation (a) after and (b) before excluding rotation tensor \mathbf{R} as a function of initial misorientation of laminae

Table A2 E_{ini} of alternative disorder lay-up sequence predicted by CLPT with 120 N (pitches)

	[30/150/60/120/0/90]	[90/60/150/0/30/120]	[30/60/0/150/90/120]
E_{ini} [MPa]	2.4423	2.4423	2.4423
	[150/90/60/30/120/0]	[0/30/60/90/120/150]	[60/0/150/30/90/120]
	2.4423	2.4423	2.4423

A12 Matrix with elasto-plastic model

To remedy the limited deformation of model with linear elastic matrix, elasto-plastic matrix is used in FEA. The yielding stress and hardening slope are $\sigma_y = 0.014$ (MPa) and $E_{plastic} = 0.03$ (MPa) respectively.

The true stress and strain curve and the elastic modulus as a function of local true strain, ϵ_t , is illustrated in Figure A18. It is observed that even with elasto-plastic matrix and large deformation, the DFH $\theta_h = 30^\circ$ does not show any strain stiffening.

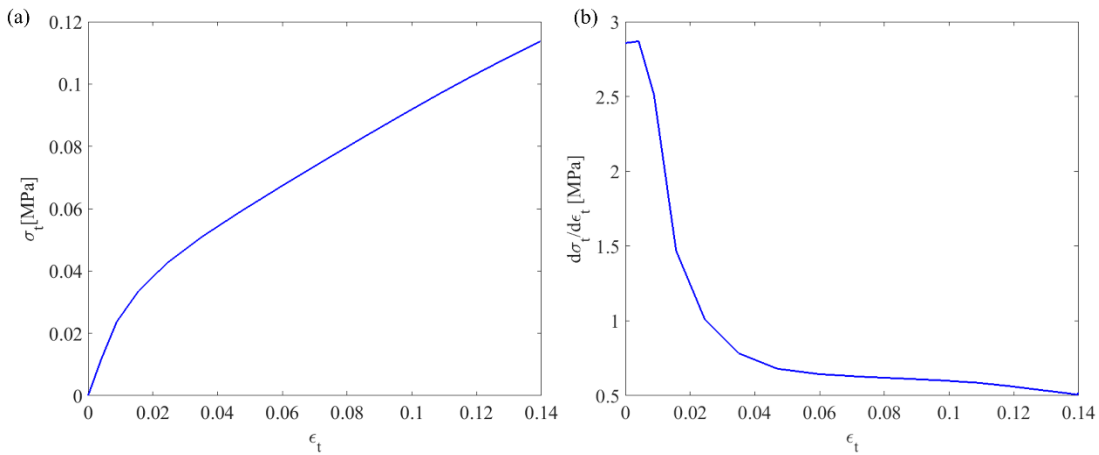


Figure A18. (a) True stress and strain curve of DFH $\theta_h = 30^\circ$. (b) Elastic modulus as a function of local true strain.

A13 Rotation distribution in matrix

In Figure A19(a) to (j), the values of rotation are illustrated by the integration points in the matrix elements from three categories of laminates: DMB, DSL and DFH. The rotation in the matrix around one single fiber exhibits diagonal pattern, shown in Figure A19(e), which means the rotation values in upper right and lower left (main diagonal zone) or upper left and lower right area (minor diagonal zone) encircling one fiber are respectively the same in these three types of laminates. The main and minor diagonal zones in a DSL are with positive counter-clockwise rotation, but their values are different as a result of in-plane shear deformation, as shown in Figure A19(a) and (d). In DFH and DMB, the rotation values surrounding fibers in main diagonal zone are positive, whereas in the minor zones the rotation values are found to be negative (clockwise). The difference on absolute rotation values of diagonal zones in individual lamina of DFH is larger

than the absolute values of DMB since there is less in-plane shear deformation in the DMB, shown in Figure A19(b)-(c) and (d)-(e).

Meanwhile non-negligible shear deformation exists in the individual lamina θ_{30} of $\theta_h = 30^\circ$. However, the in-plane shear deformation in individual layer of helicoidal laminate is less than the shear deformation of corresponding single lamina due to interlayer restriction. The green field values, in Figure A19(b) and (c), from DFH and DMB represent the rotation value of interlayer matrix. The dark blue zones, as shown in Figure A19(d), of DSL exhibit the rotation values of interlayer matrix. These two rotation values from interlayer matrix above/below fibers are the same as the rotation values of fibers that we measured from simulation by setting up vectors from two ends of fibers.

The rotation distribution maps along Y direction are illustrated in Figure A19(h-j) and there is less size effect on rotation in DSL. Due to less in-plane shear deformation of DFH and DMB, size effect on rotation distribution in the matrix is larger than DSL.

Fiber reorientation after correction as a function of applied strain is illustrated in Figure A6(a)-(c). One point deserved to be mentioned is that the maximum reorientation of $\theta_s = 5^\circ$ for a given applied strain, is larger than the original orientation $\theta_s = 5^\circ$. This is due to the procedure that fibers rotate toward the loading direction and then rotate away from the loading axis (X-axis) once fiber longitudinal axis coincides the loading direction.

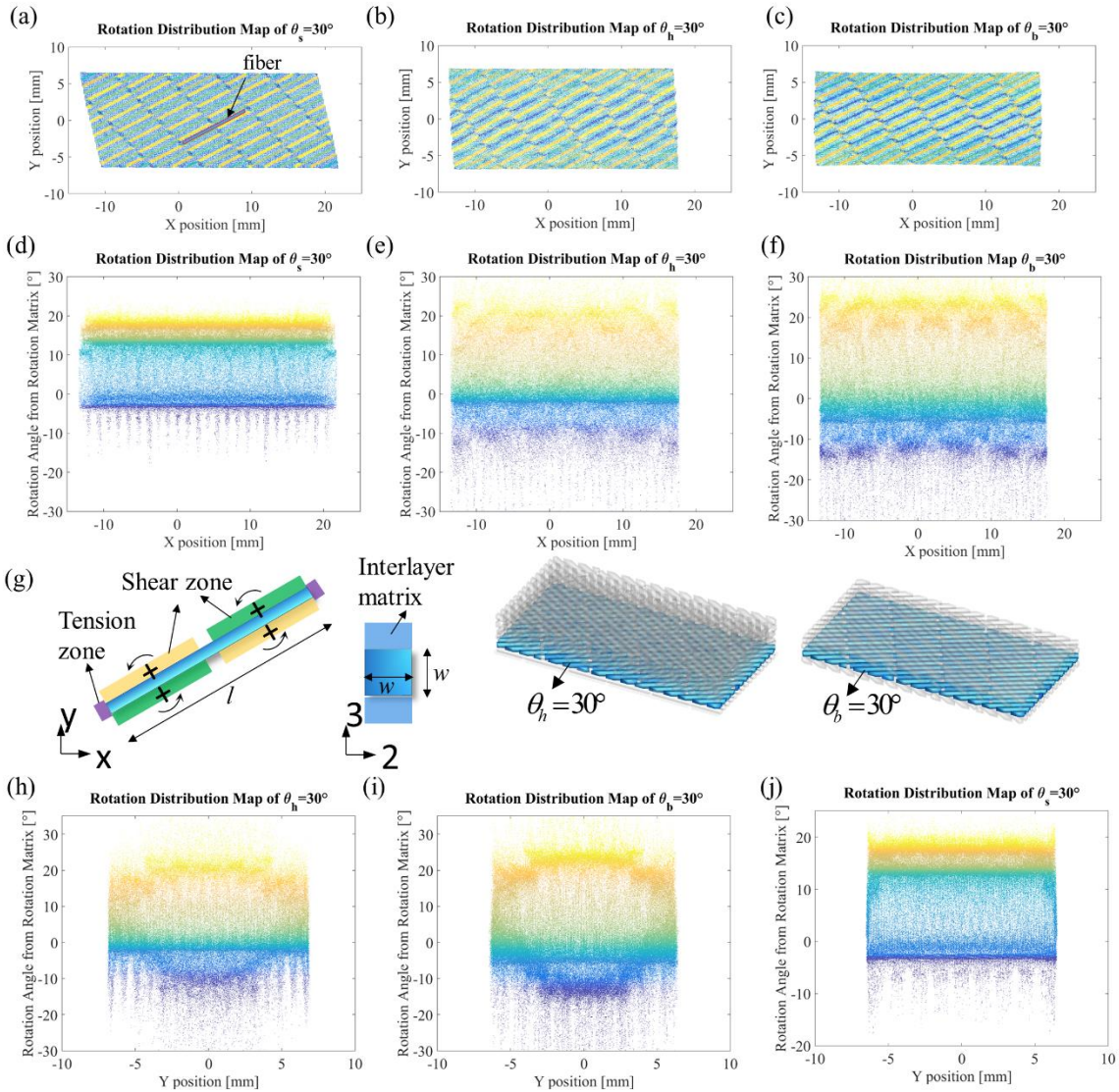


Figure A19. (b) rotation map of matrix of $\theta_s = 30^\circ$ from two different of views; (c) rotation map of matrix of θ_{30} of $\theta_h = 30^\circ$ from two different of views; (d) rotation map of matrix of θ_{30} of $\theta_b = 30^\circ$; from two different of views; (e) rotation distribution in matrix surrounding fiber and shear\ tension zone illustration; (f) Rotation values along Y direction of lamina θ_{30} in DFH $\theta_h = 30^\circ$; (g) Rotation values along Y direction of lamina θ_{30} of DMB $\theta_b = 30^\circ$; (h) Rotation values along Y direction of DSL $\theta_s = 30^\circ$.

A14 In-plane shear and transverse strain at the middle of θ_{30} laminae from DFH, DSL and DMB

Figure A20(a) to (d) illustrated the strain distribution of logarithmic transverse strain (LE22) and logarithmic shear strain (LE12) in the matrix of lamina θ_{30} of DSL $\theta_s = 30^\circ$ and DFH $\theta_h = 30^\circ$. The directions of LE22 and LE12 are all negative around fibers in DSL $\theta_s = 30^\circ$, whereas the

directions of strain around fibers of DFH $\theta_h = 30^\circ$ are staggered (“positive” and “negative”). However, this kind of deformation is not obvious in $\theta_h = 60^\circ$, shown in Figure A20(g), (h), (k) and (j). This specific staggered directions of deformation around fibers could be one of the reasons of limited fiber rotation and relatively isotropic in-plane property of each laminae in DFH.

It is exhibited that the transverse deformation LE22 of DFH $\theta_h = 30^\circ$ is larger than SL $\theta_s = 30^\circ$, however smaller than MBL $\theta_b = 30^\circ$. Compared to other two, transverse squeezing deformation of DMB contributes more to the fiber reorientation. Same behavior is found in $\theta_b = 60^\circ$, shown in Figure A19(i) and (l). The shear strain in the matrix of $\theta_b = 60^\circ$ is close to zero during the global deformation.

At the same time, DSL $\theta_s = 30$ is with the maximum in-plane shear deformation, shown in Figure A20(c) and (f). However, turn to DSL $\theta_s = 60$, illustrated in Figure A20(i) and (l), the benefits of shear are not solid compared with transverse strain. Stimulation of fiber reorientation in DSL probably mainly comes from in-plane shear deformation when off-axis angle is small. Nevertheless, once turn to larger off-axis angle, transverse squeezing plays more roles in fiber reorientation.

DFH $\theta_h = 30$ does not perform outstanding either in LE22 or in LE12 with the same axial elongation of DMB and DSL.

It is worthy to be noticed that there is less shear, greater transverse strain with larger θ_h , for a fixed θ_i , such as θ_{60} laminae in $\theta_h = 30$ and $\theta_h = 60$ laminates. For a fixed θ_h , there is less shear and transverse strain with larger off-axis angle, such as θ_{30} and θ_{60} in $\theta_h = 30$ laminate.

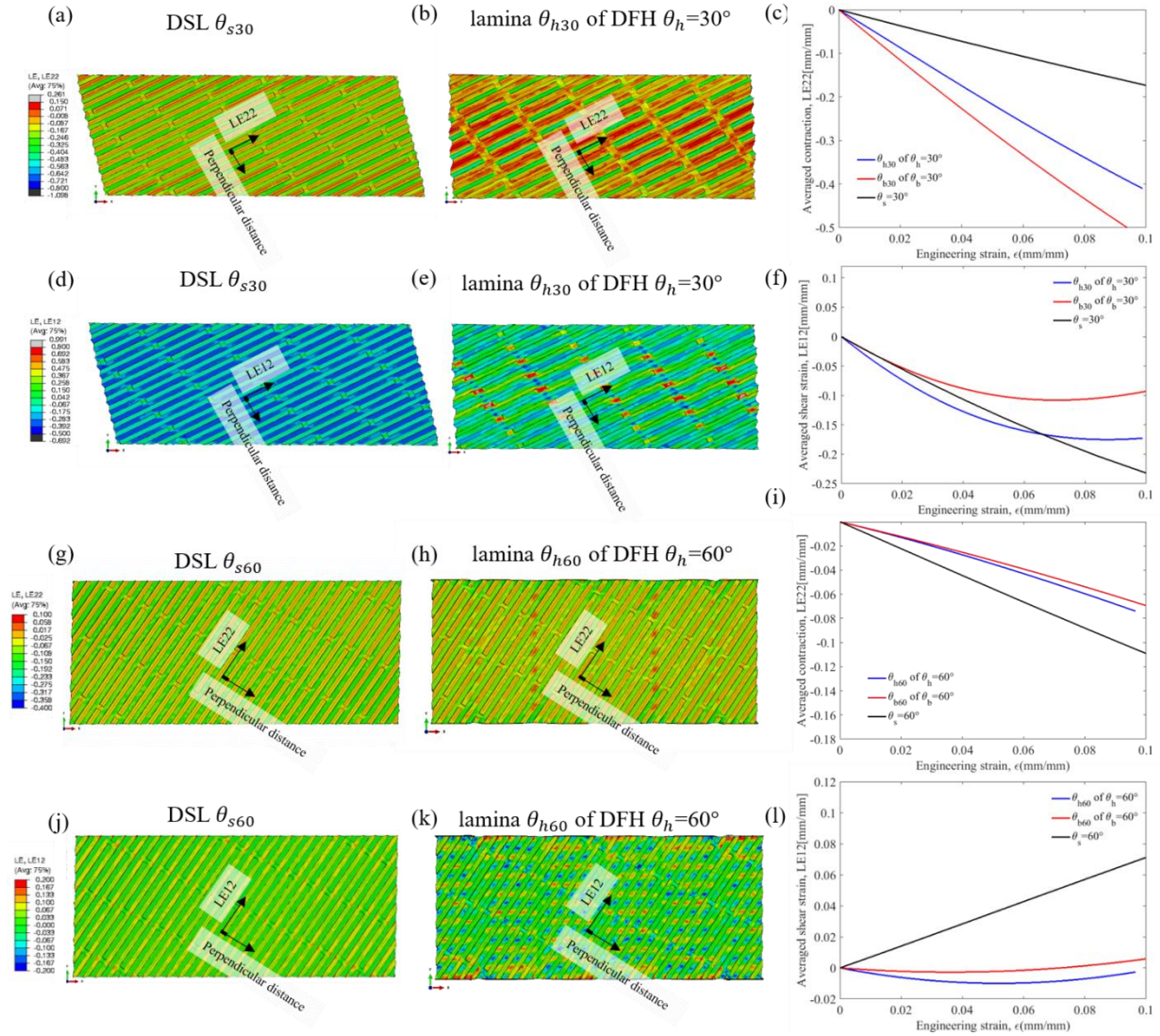


Figure A20. (a) Logarithmic strain in Y direction of SL30 and (b) individual lamina 30 of DFH30 with PBC. (c) Distribution of Logarithmic strain in Y direction along the perpendicular distance. (d) In-plane shear logarithmic strain of SL30 and (e) individual lamina 30 of DFH30. (f) Distribution of In-plane shear logarithmic strain along the perpendicular distance. (g) Logarithmic strain in Y direction of SL60 and (h) individual lamina 60 of DFH60 with PBC. (i) Distribution of Logarithmic strain in Y direction along the perpendicular distance. (j) In-plane shear logarithmic strain of SL60 and (k) individual lamina 60 of DFH60. (l) Distribution of In-plane shear logarithmic strain along the perpendicular distance.

A15 Definite values of E_{ini}

Due to high Poisson's ratio 0.48, the hydrostatic resistance in the zone between two aligned fibers is considerably high. However, CLPT does not consider this contribution. Thus, the difference between E_{ini} , Elastic modulus of $\theta_s = 0^\circ$, of CLPT and FEA is high, illustrated in

Figure A21(a). Once we use E_{ini} from $\theta_s = 0^\circ$ without local failures to normalize other values from FEA, other off-axis angle laminae would be with lower normalized elastic modulus than prediction from CLPT, shown in Figure 2.2(b). Specifically, the definite value of Elastic modulus of $\theta_s = 0^\circ$ from FEA without local failures is 14.59MPa, when the Poisson's ratio of matrix is 0.48. However once the Poisson's ratio of matrix changes to 0.3, the Elastic modulus turns to 9.75MPa. At the same time, the elastic modulus of $\theta_s = 0^\circ$ with local failures are 5.69MPa and 5.94 MPa separately of models with 0.48 and 0.3 matrix Poisson's ratio.

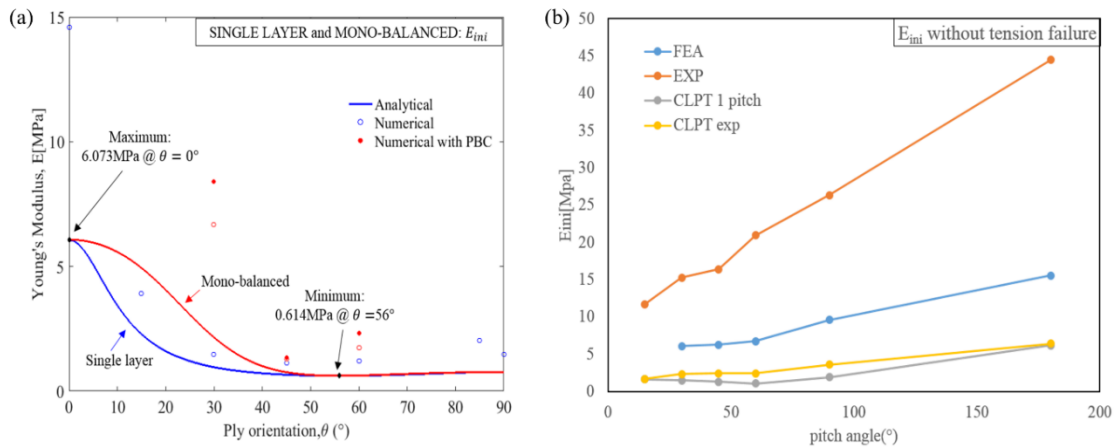


Figure A21. (a) Definite value of E_{ini} of DSL and DMB (b) Definite value of E_{ini} of DFH

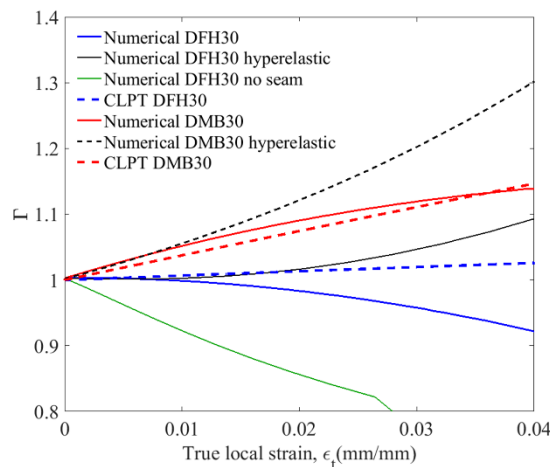


Figure A22. Strain stiffening as a function of local true strain of numerical and analytical prediction with linear elastic matrix

APPENDIX B. SUPPLEMENTAL MATERIALS FOR CHAPTER 3

B1 Effective shear and tension volume of 3D models

The effective shear/tension area over volume of unit cell of nacre structure $\frac{A_s}{V_{cell}}$ and $\frac{A_t}{V_{cell}}$ are calculated by equation B(1) and B(2).

$$\frac{A_s}{V_{cell}} = \frac{2 \times (A_{hex} - 3A_{tension})}{L \times W \times \left(\frac{H}{2}\right)} = \frac{2 \left(\frac{3\sqrt{3}}{2} w_n^2 - 3 \left(w_n t - \frac{\sqrt{3}}{6} t^2 \right) \right)}{(3w_n + \sqrt{3}t)(\sqrt{3}w_n + t)(h+t)} \quad B(1)$$

$$\frac{A_t}{V_{cell}} = \frac{8 \times \left(w_n + \frac{t}{2\sqrt{3}} \right) \left(\frac{h}{2} + t \right) \cos(30^\circ)}{L \times W \times \frac{H}{2}} \quad B(2)$$

$$\text{Where volume fraction } V_f = \frac{4 \cdot \frac{h}{2} \left(\frac{3\sqrt{3}}{2} w_n^2 \right)}{LWH \cdot 0.5} = \frac{\frac{3\sqrt{3}}{2} w_n^2 h}{\frac{3\sqrt{3}}{2} \left(w_n + \frac{t}{\sqrt{3}} \right)^2 (h+t)}$$

The effective shear/tension area over volume of unit cell of chiton structure $\frac{A_s}{V_{cell}}$ and $\frac{A_t}{V_{cell}}$ are calculated as following.

$$\frac{A_s}{V_{cell}} = \frac{\frac{(h-t)}{2} w_c}{\frac{L}{2} \times \frac{W}{4} \times H/2} = \frac{\frac{(h-t)}{2} w_c}{\frac{(3w + \sqrt{3}t)2(\sqrt{3}w + t)(h+t)}{2 \cdot 4 \cdot 2}} = \frac{4(h-t)w_c}{(3w_c + \sqrt{3}t)(\sqrt{3}w_c + t)(h+t)} \quad B(3)$$

$$\frac{A_t}{V_{cell}} = \frac{2 \left(\frac{L}{2} \times \frac{W}{4} - \frac{A_{hex}}{4} \right)}{\frac{L}{2} \times \frac{W}{4} \times H/2} = \frac{2 \left(\frac{L}{2} \times \frac{W}{4} - \frac{A_{hex}}{4} \right)}{\frac{(3w_c + \sqrt{3}t)2(\sqrt{3}w_c + t)(h+t)}{2 \cdot 4 \cdot 2}} = \frac{2(3w_c + \sqrt{3}t)(\sqrt{3}w_c + t) - 4A_{hex}}{(3w_c + \sqrt{3}t)(\sqrt{3}w_c + t)(h+t)} \quad B(4)$$

$$\text{Where volume fraction } V_f = \frac{\frac{1}{2} \left(\frac{3\sqrt{3}}{2} w_c^2 \right) \frac{h}{2}}{\frac{L}{2} \times \frac{W}{4} \times H/2} = \frac{\frac{3\sqrt{3}}{2} w_c^2 h}{\frac{3\sqrt{3}}{2} \left(w_c + \frac{t}{\sqrt{3}} \right)^2 (h+t)}$$

B2 Analytical prediction of 3D nacre structure

The displacements of 3D nacre structure solve by equilibrium equations are in B(5) to B(8).

$$\begin{aligned} u_l(x) = & \frac{1}{3} \sigma_f \sqrt{3} \left(-k\sqrt{2} x \cosh \left(\frac{k\sqrt{2}(l_v - l_w)}{w_n} \right) + k\sqrt{2} x \cosh \left(\frac{k\sqrt{2}(l_v + l_w)}{w_n} \right) + \right. \\ & 4Mx \sinh \left(\frac{k\sqrt{2}l_w}{w_n} \right) + 4Mx \sinh \left(\frac{k\sqrt{2}l_v}{w_n} \right) + 4Mx \sinh \left(\frac{k\sqrt{2}(l_v + l_w)}{w_n} \right) - w_n \sinh \left(\frac{k\sqrt{2}(l_v - l_w + x)}{w_n} \right) + \\ & \left. w_n \sinh \left(\frac{k\sqrt{2}(l_v + l_w + x)}{w_n} \right) + w_n \sinh \left(\frac{k\sqrt{2}(l_w - x)}{w_n} \right) + w_n \sinh \left(\frac{k\sqrt{2}(l_w + x)}{w_n} \right) - 2 \sinh \left(\frac{k\sqrt{2}(l_w)}{w_n} \right) w_n + \right. \end{aligned}$$

$$w_n \sinh\left(\frac{k\sqrt{2}(l_v-l_w)}{w_n}\right) - w_n \sinh\left(\frac{k\sqrt{2}(l_v+l_w)}{w_n}\right) / E_f \left(-k\sqrt{2} \cosh\left(\frac{k\sqrt{2}(l_v-l_w)}{w_n}\right) + k\sqrt{2} \cosh\left(\frac{k\sqrt{2}(l_v+l_w)}{w_n}\right) + 2M \sinh\left(\frac{k\sqrt{2}l_w}{w_n}\right) + 2M \sinh\left(\frac{k\sqrt{2}l_v}{w_n}\right) + 2M \sinh\left(\frac{k\sqrt{2}(l_v+l_w)}{w_n}\right)\right) \quad \text{B(5)}$$

$$u_r(x) = \frac{1}{3} \sigma_f \sqrt{3} \left(-k\sqrt{2} x \cosh\left(\frac{k\sqrt{2}(l_v-l_w)}{w_n}\right) + k\sqrt{2} x \cosh\left(\frac{k\sqrt{2}(l_v+l_w)}{w_n}\right) + 4Mx \sinh\left(\frac{k\sqrt{2}l_w}{w_n}\right) + 4Mx \sinh\left(\frac{k\sqrt{2}l_v}{w_n}\right) + 4Mx \sinh\left(\frac{k\sqrt{2}(l_v+l_w)}{w_n}\right) - w_n \sinh\left(\frac{k\sqrt{2}(l_v+l_w-x)}{w_n}\right) - w_n \sinh\left(\frac{k\sqrt{2}(l_v+x)}{w_n}\right) - w_n \sinh\left(\frac{k\sqrt{2}(l_v-x)}{w_n}\right) - w_n \sinh\left(\frac{k\sqrt{2}(l_v-l_w+x)}{w_n}\right) + 2 \sinh\left(\frac{k\sqrt{2}(l_v)}{w_n}\right) w_n + w_n \sinh\left(\frac{k\sqrt{2}(l_v-l_w)}{w_n}\right) + w_n \sinh\left(\frac{k\sqrt{2}(l_v+l_w)}{w_n}\right) / E_f \left(-k\sqrt{2} \cosh\left(\frac{k\sqrt{2}(l_v-l_w)}{w_n}\right) + k\sqrt{2} \cosh\left(\frac{k\sqrt{2}(l_v+l_w)}{w_n}\right) + 2M \sinh\left(\frac{k\sqrt{2}l_w}{w_n}\right) + 2M \sinh\left(\frac{k\sqrt{2}l_v}{w_n}\right) + 2M \sinh\left(\frac{k\sqrt{2}(l_v+l_w)}{w_n}\right)\right) \quad \text{B(6)}$$

$$v(x) = \frac{1}{3} \sigma_f \sqrt{3} \left(-k\sqrt{2} x \cosh\left(\frac{k\sqrt{2}(l_v-l_w)}{w_n}\right) + k\sqrt{2} x \cosh\left(\frac{k\sqrt{2}(l_v+l_w)}{w_n}\right) + 4Mx \sinh\left(\frac{k\sqrt{2}l_w}{w_n}\right) + 4Mx \sinh\left(\frac{k\sqrt{2}l_v}{w_n}\right) + 4Mx \sinh\left(\frac{k\sqrt{2}(l_v+l_w)}{w_n}\right) + w_n \sinh\left(\frac{k\sqrt{2}(l_v-l_w+x)}{w_n}\right) - w_n \sinh\left(\frac{k\sqrt{2}(l_v+l_w+x)}{w_n}\right) - w_n \sinh\left(\frac{k\sqrt{2}(l_w-x)}{w_n}\right) - w_n \sinh\left(\frac{k\sqrt{2}(l_w+x)}{w_n}\right) - 2 \sinh\left(\frac{k\sqrt{2}(l_w)}{w_n}\right) w_n + w_n \sinh\left(\frac{k\sqrt{2}(l_v-l_w)}{w_n}\right) - w_n \sinh\left(\frac{k\sqrt{2}(l_v+l_w)}{w_n}\right) / E_f \left(-k\sqrt{2} \cosh\left(\frac{k\sqrt{2}(l_v-l_w)}{w_n}\right) + k\sqrt{2} \cosh\left(\frac{k\sqrt{2}(l_v+l_w)}{w_n}\right) + 2M \sinh\left(\frac{k\sqrt{2}l_w}{w_n}\right) + 2M \sinh\left(\frac{k\sqrt{2}l_v}{w_n}\right) + 2M \sinh\left(\frac{k\sqrt{2}(l_v+l_w)}{w_n}\right)\right) \quad \text{B(7)}$$

$$w(x) = \frac{1}{3} \sigma_f \sqrt{3} \left(-k\sqrt{2} x \cosh\left(\frac{k\sqrt{2}(l_v-l_w)}{w_n}\right) + k\sqrt{2} x \cosh\left(\frac{k\sqrt{2}(l_v+l_w)}{w_n}\right) + 4Mx \sinh\left(\frac{k\sqrt{2}l_w}{w_n}\right) + 4Mx \sinh\left(\frac{k\sqrt{2}l_v}{w_n}\right) + 4Mx \sinh\left(\frac{k\sqrt{2}(l_v+l_w)}{w_n}\right) + w_n \sinh\left(\frac{k\sqrt{2}(l_v+l_w-x)}{w_n}\right) + w_n \sinh\left(\frac{k\sqrt{2}(l_v+x)}{w_n}\right) + w_n \sinh\left(\frac{k\sqrt{2}(l_v-x)}{w_n}\right) + w_n \sinh\left(\frac{k\sqrt{2}(l_v-l_w+x)}{w_n}\right) + 2 \sinh\left(\frac{k\sqrt{2}(l_v)}{w_n}\right) w_n + w_n \sinh\left(\frac{k\sqrt{2}(l_v-l_w)}{w_n}\right) + w_n \sinh\left(\frac{k\sqrt{2}(l_v+l_w)}{w_n}\right) / E_f \left(-k\sqrt{2} \cosh\left(\frac{k\sqrt{2}(l_v-l_w)}{w_n}\right) + k\sqrt{2} \cosh\left(\frac{k\sqrt{2}(l_v+l_w)}{w_n}\right) + 2M \sinh\left(\frac{k\sqrt{2}l_w}{w_n}\right) + 2M \sinh\left(\frac{k\sqrt{2}l_v}{w_n}\right) + 2M \sinh\left(\frac{k\sqrt{2}(l_v+l_w)}{w_n}\right)\right) \quad \text{B(8)}$$

Where $k = \sqrt{\frac{2w_n^2 G_m}{E_f h t}}$, $M = \frac{C_m w_n}{E_f t}$ and the displacement distribution under unit loading ($\sigma_f = 1$) is illustrated in Figure B1.

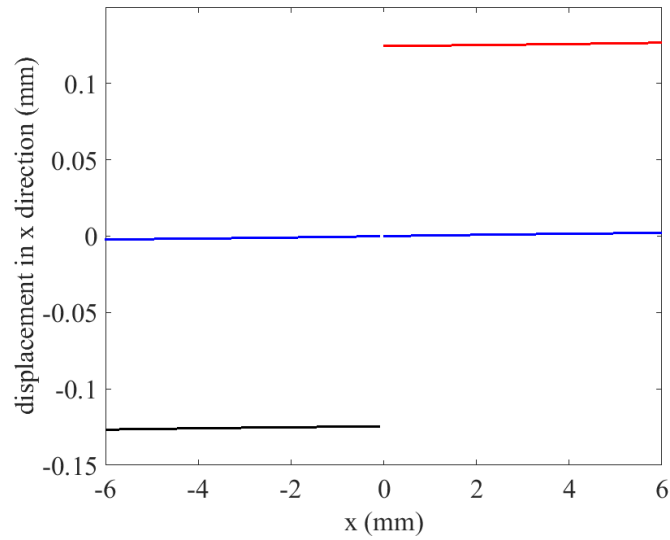


Figure B1. Displacement distribution of the analytical prediction on 3D nacre model

B3 Material characterization of matrix and fiber

Simple shear and uniaxial tension tests are prepared to conduct material characterization under different thickness. Vertically and horizontally printed samples are shown in Figure B2. The elastic modulus of compliant matrix material is shown in Figure B3(1) and the maximum shear stress τ_c of matrix material is in Figure B3(2). The elastic modulus E and maximum shear stress τ_c could be achieved as 0.437MPa (horizontally printed value) and 1.256MPa.

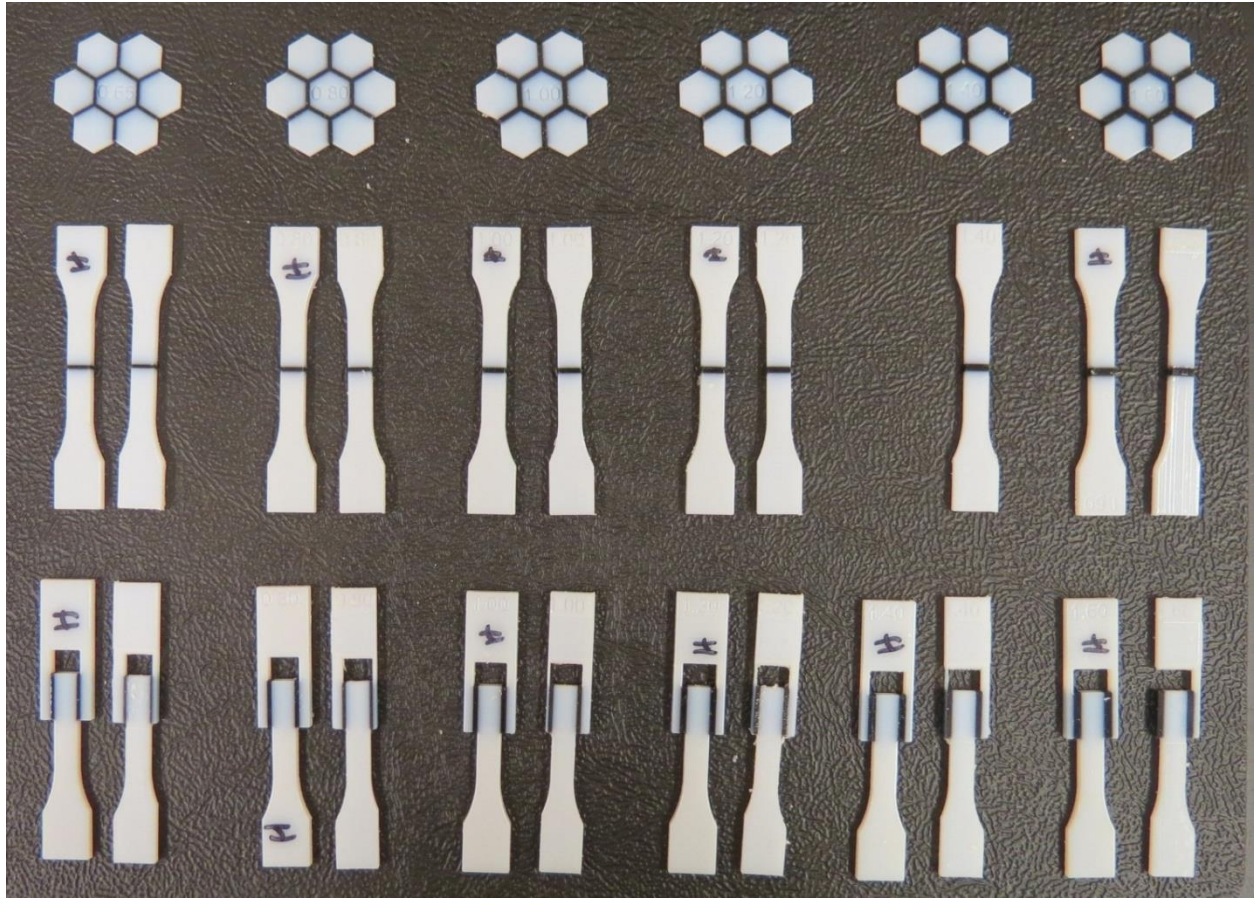


Figure B2. 3D printed (vertically and horizontally) material characterization samples for simple shear (2nd row) and uniaxial tension (1st row) tests with different thickness of matrix material (prepared by Chan Hue Jeong).

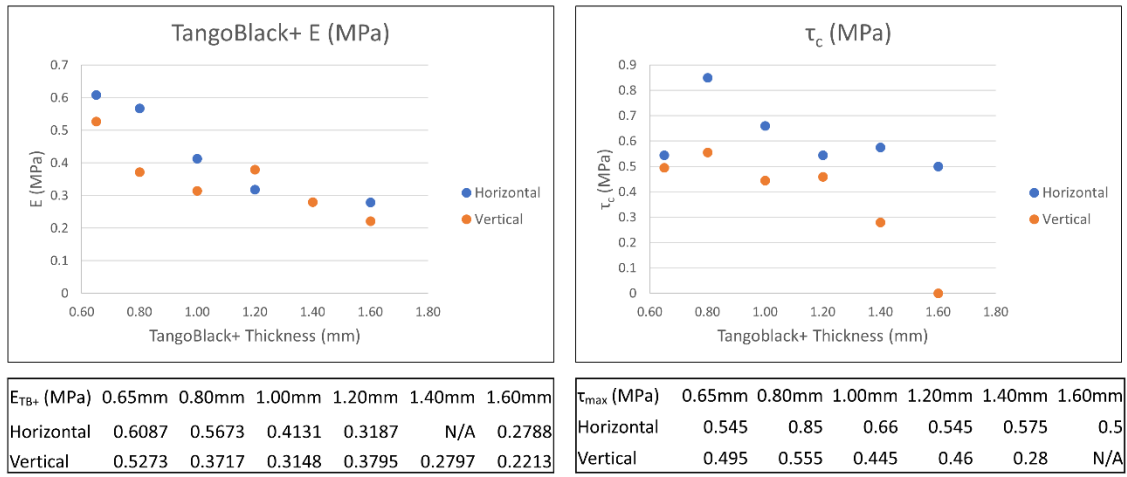


Figure B3. (1) Elastic modulus E and (2) maximum shear stress τ_c of matrix material with different thickness.

B4 Periodic boundary condition

Periodic boundary condition is implemented on 3D nacre and chiton Representative Volume Element (RVE) to avoid size effect. The detailed description is introduced in (Al Kassem and Weichert, 2009). Three pairs of surfaces are correlated by equation s(9), where dummy represents for dummy node, a node out of the model itself.

$$u_i^{k+} - u_i^{k-} + u_i^{dummy} = 0 \quad \text{B(9)}$$

Where indices ‘ $k +$ ’ and ‘ $k -$ ’ represent for the k th pair of opposite parallel surfaces of one RVE. Index ‘ i ’ identify the dimension, such as 1, 2 and 3.

B5 $\pi_3 = A_s l_s^2 / V_{cell} t$

The shear-lag model is illustrated in Figure B4 and we assume fibers are infinitely stiff. Another assumption is there is no sliding between fiber and matrix, which means the interface between fiber and matrix is perfect boundary. Concentrated load P is applied at the right edge of the top fiber, which induces shear deformation in the compliant matrix. Thus the shear stress in the matrix could be represented by equation s(10).

$$\frac{P}{A_s} = G \frac{\Delta}{t} \quad \text{B(10)}$$

Also equation s(10) could be transferred to s(11), where A_{ef} is the effective cross-section area of the shear-lag model and L_{eff} is the effective length of shear-lag model.

$$\frac{P}{A_{ef}} = G \frac{A_s \Delta}{t A_{ef} L_{eff}} L_{eff} \quad \text{B(11)}$$

$\frac{P}{A_{ef}}$ could be considered as normal stress applied on the shear-lag model and $\frac{\Delta}{L_{eff}}$ is the engineering strain. Thus equation s(11) could be transferred to equation s(12) and s(13).

$$\sigma = G \frac{A_s L_{eff}}{t A_{ef}} \varepsilon \quad \text{B(12)}$$

$$\sigma = G \frac{A_s L_{eff}^2}{t V_{cell}} \varepsilon \quad \text{B(13)}$$

It is observed that $\frac{A_s L_{eff}^2}{t V_{cell}}$ is the dimensionless geometry parameter influencing the stiffness of the shear-lag model.

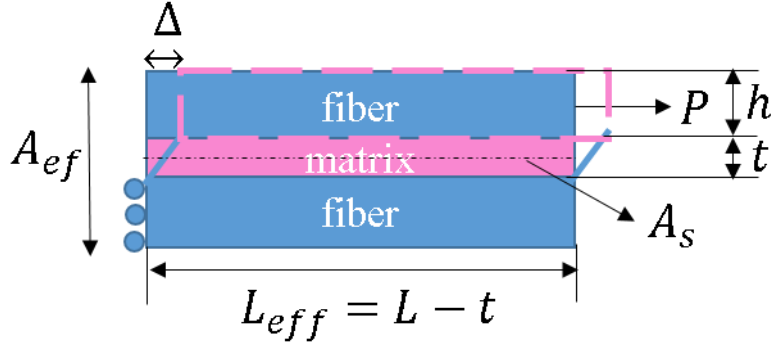


Figure B4. 2D shear-lag model

B6 critical shear stress in matrix

As discussed in section 3.2.1, maximum shear stress is located at both ends of the tablet, shown in Figure B5. Replacing $x = -l_v$ could achieve the maximum shear stress and we define τ_c as the maximum shear stress of matrix material. Then the yield strength σ_c of 3D nacre could be achieved by equation s(14).

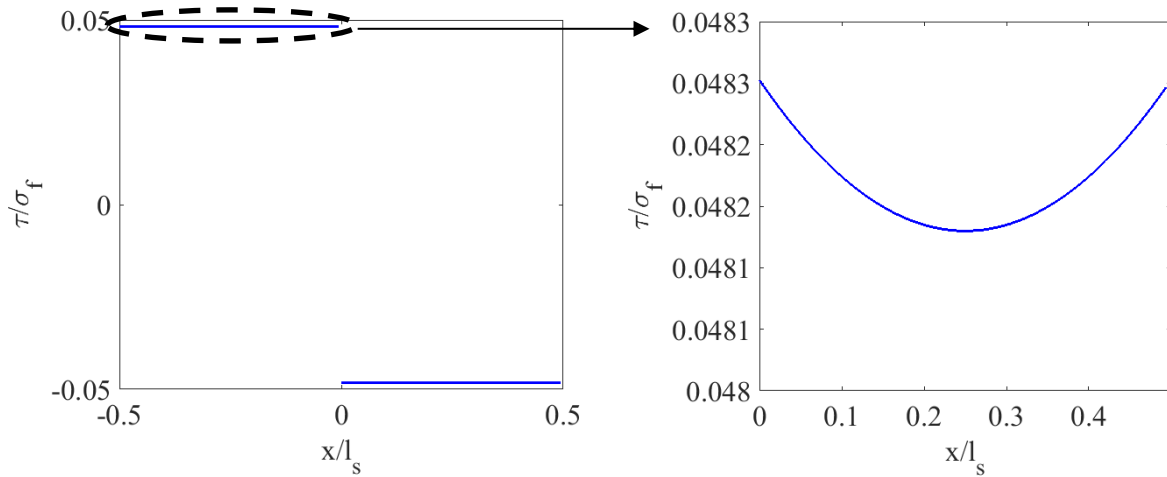


Figure B5. (a) normalized shear stress in matrix and (b) normalized shear stress in prism 2, which is a zoom in figure.

$$\sigma_c = \frac{-\frac{\sqrt{3}}{2} \tau_c t E_f \left(-\sqrt{2} k \cosh\left(\frac{k\sqrt{2}(l_v - l_w)}{w_n}\right) + \sqrt{2} k \cosh\left(\frac{k\sqrt{2}(l_v + l_w)}{w_n}\right) + 2M_{cof} \sinh\left(\frac{k\sqrt{2}(l_w)}{w_n}\right) + 2M_{cof} \sinh\left(\frac{k\sqrt{2}(l_v)}{w_n}\right) + 2M_{cof} \sinh\left(\frac{k\sqrt{2}(l_v + l_w)}{w_n}\right) \right)}{G_m w_n \left(\sinh\left(\frac{k\sqrt{2}(l_v - l_w + x)}{w_n}\right) - \sinh\left(\frac{k\sqrt{2}(l_v + l_w + x)}{w_n}\right) - \sinh\left(\frac{k\sqrt{2}(l_w - x)}{w_n}\right) - \sinh\left(\frac{k\sqrt{2}(l_w + x)}{w_n}\right) \right)} A_s \frac{M}{2}}{V_{cell}} \quad \text{B(14)}$$

APPENDIX C. SUPPLEMENTAL MATERIAL FOR CHAPTER 4

C1 mesh condition, J-integral comparison and stress distribution

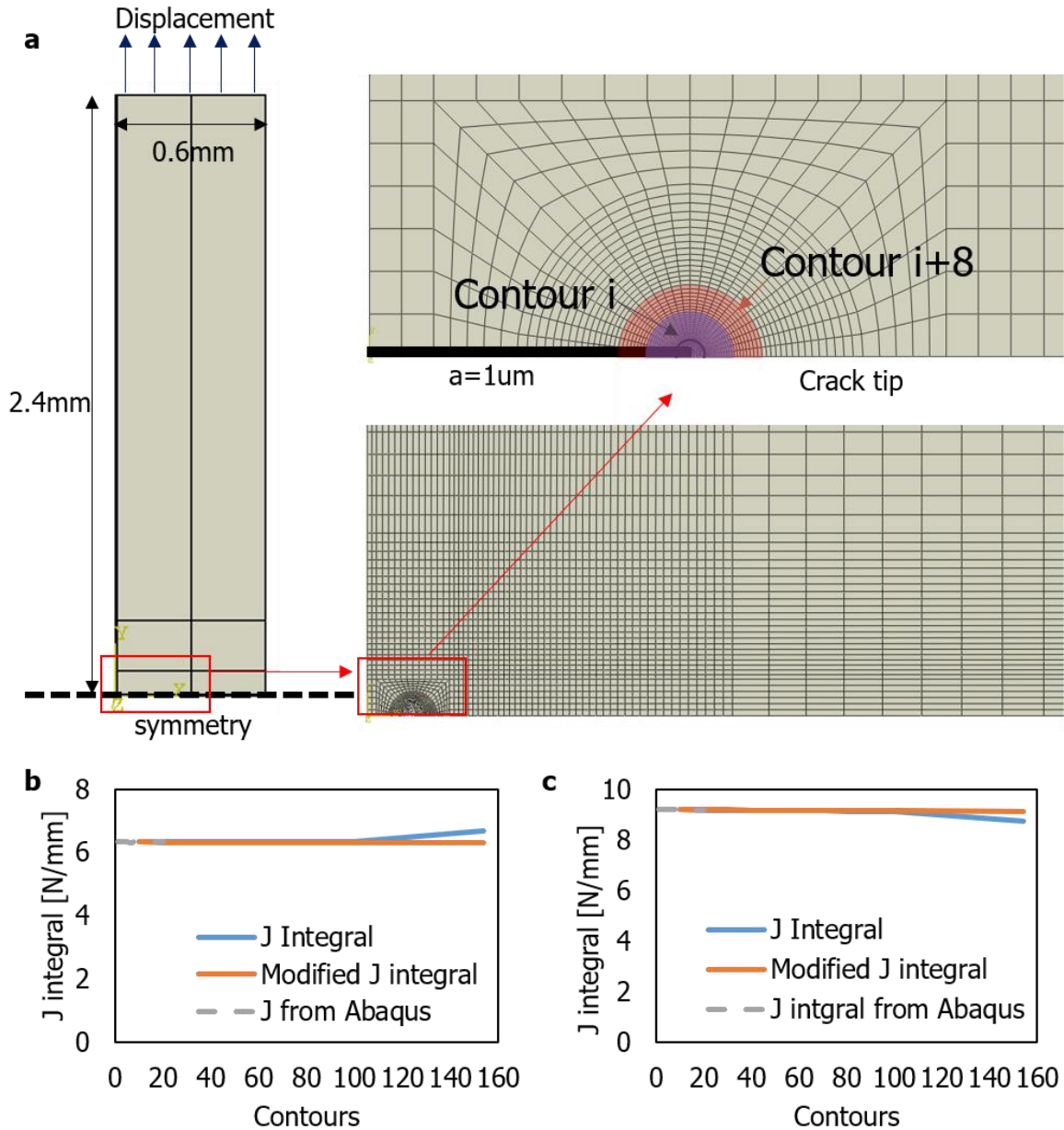


Figure C1. (a) Boundary condition and mesh condition of mode I crack; (b) Comparison of J-integral calculation for isotropic material and Graded, coupled with the prediction of ABAQUS; (c) Comparison of J-integral calculation for isotropic material and Inverse graded, coupled with the prediction of ABAQUS.

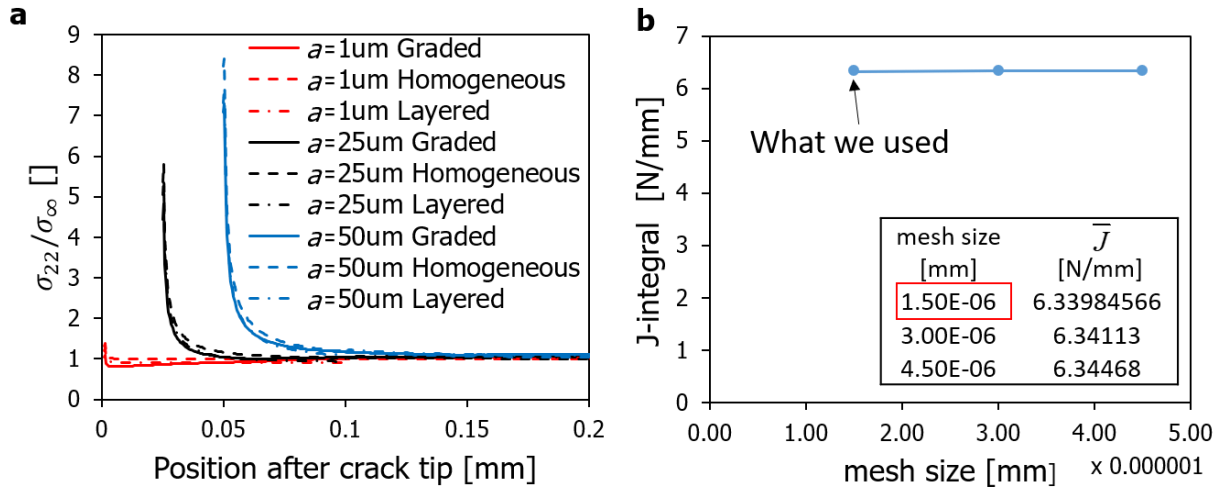


Figure C2. (a) Normalized opening stress distribution close to crack tip for three different sizes of crack model (b) Mesh convergence study on model with crack size $a=50\mu\text{m}$.

APPENDIX D. SUPPLEMENTAL MATERIAL FOR CHAPTER 5

D1. Delamination procedure of FGH2sym and its associated laminates

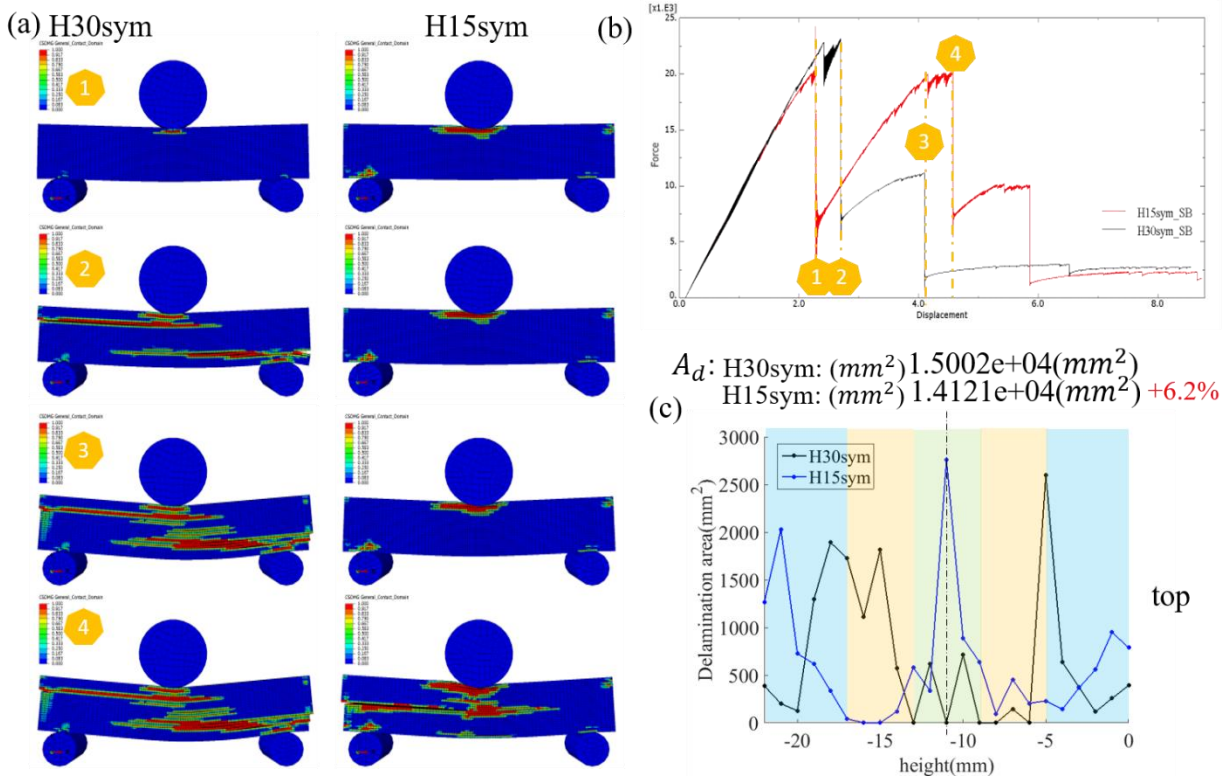
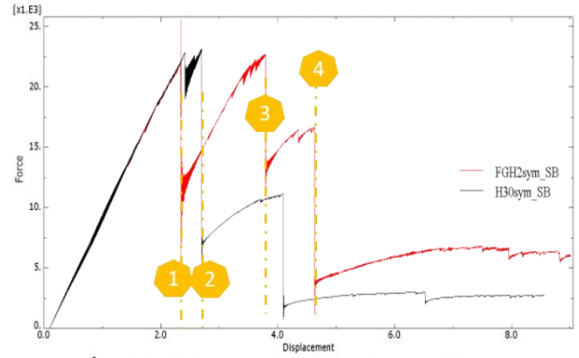
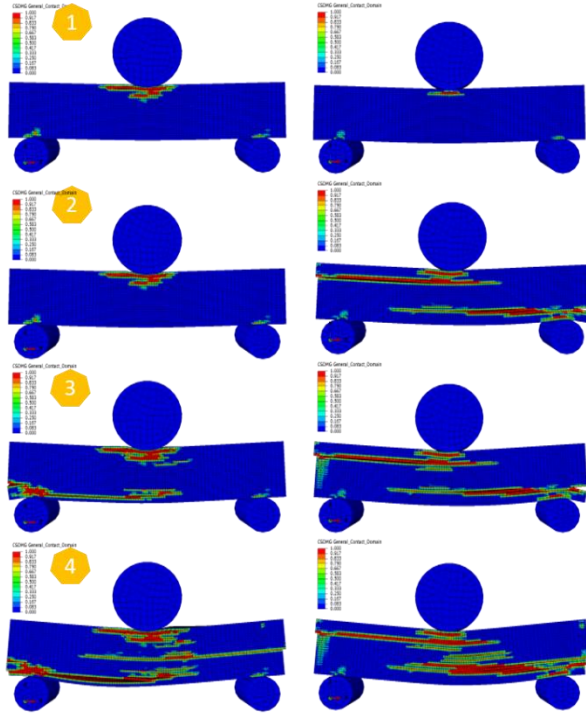


Figure D1. (a) Delamination failure distribution through the thickness of short beams H30sym and H15sym (b) Load and displacement curves of H15sym (red) and H30sym (black) (c) Delamination area distribution layer by layer. Different shaded color represents for different pitch of FGH1sym

(a) FGH2sym(30-45-90)

H30sym

(b)



A_d : FGH2sym: $1.2328e+04(mm^2)$
H30sym: $1.5002e+04(mm^2)$ -17.8%

(c)

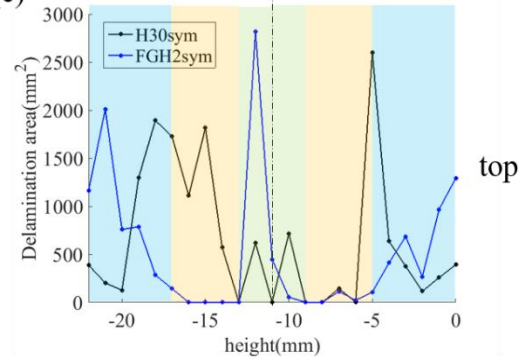
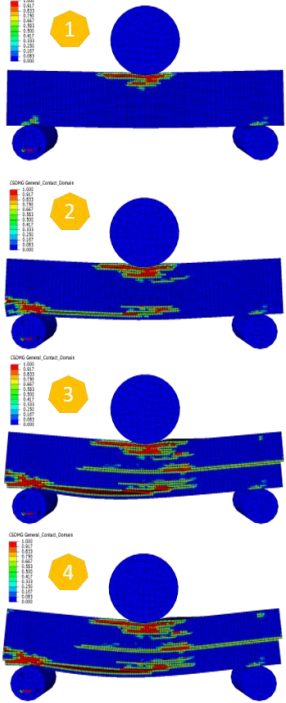
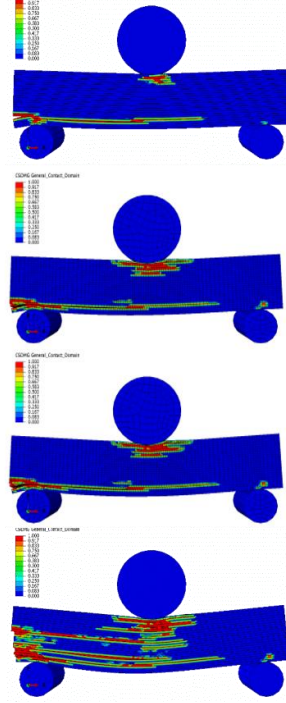


Figure D2. (a) Delamination failure distribution through the thickness of short beams FGH2sym and H30sym (b) Load and displacement curves of FGH2sym(red) and H30sym(black) (c) Delamination area distribution layer by layer. Different shaded color represents for different pitches of FGH2sym

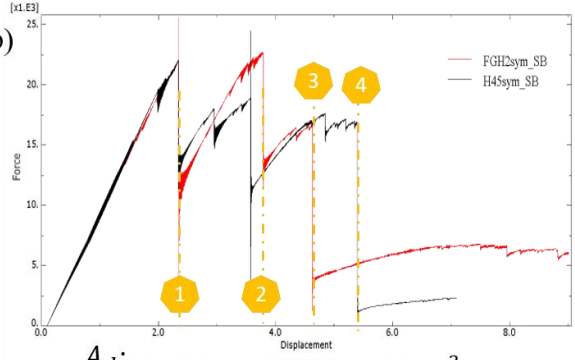
(a) FGH2sym(30-45-90)



H45sym



(b)



A_d : FGH2sym: $1.2328e+04(mm^2)$

H45sym: $1.6115e+04(mm^2)$ -23.5%

(c)

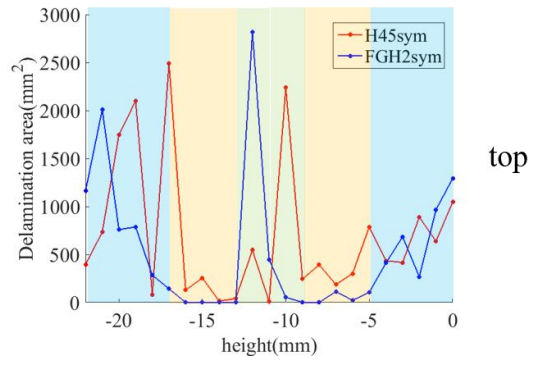


Figure D3. (a) Delamination failure distribution through the thickness of short beams FGH2sym and H45sym (b) Load and displacement curves of FGH2sym(red) and H45sym(black) (c) Delamination area distribution layer by layer. Different shaded color represents for different pitches of FGH2sym

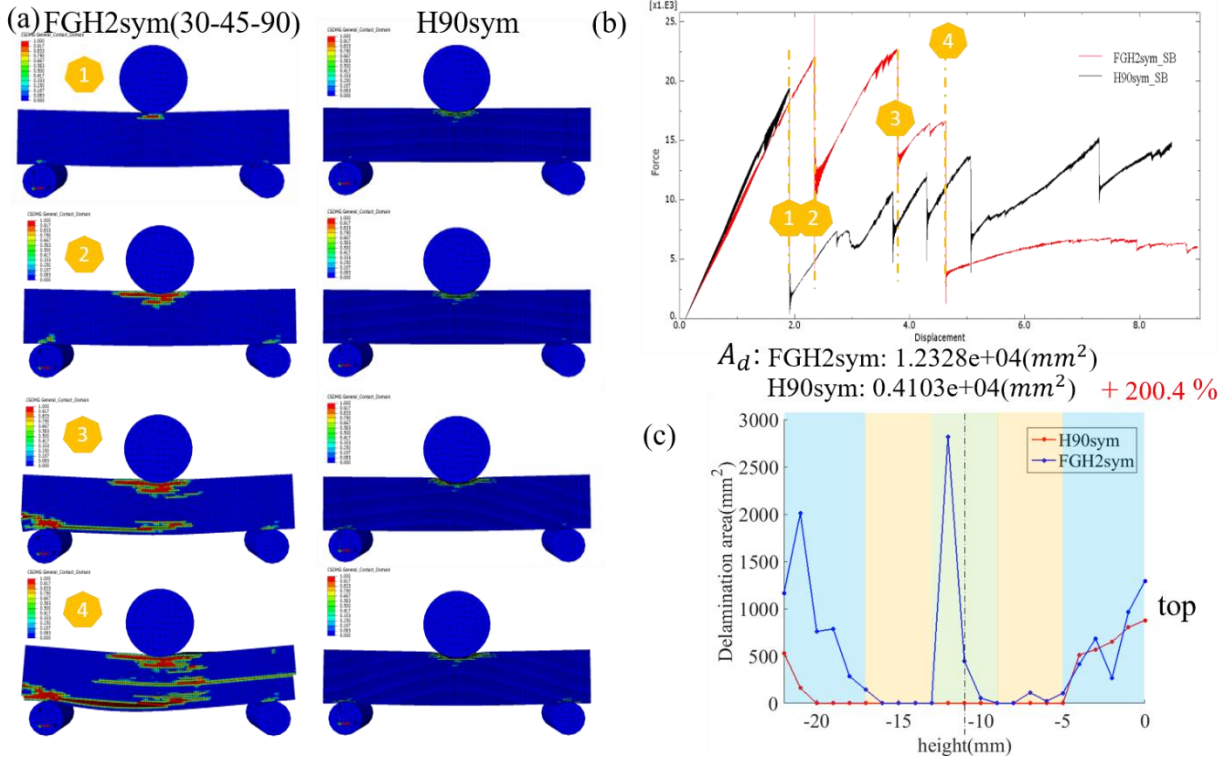


Figure D4. (a) Delamination failure distribution through the thickness of short beams FG2sym and H90sym (b) Load and displacement curves of FG2sym(red) and H90sym(black) (c) Delamination area distribution layer by layer. Different shaded color represents for different pitches of FG2sym

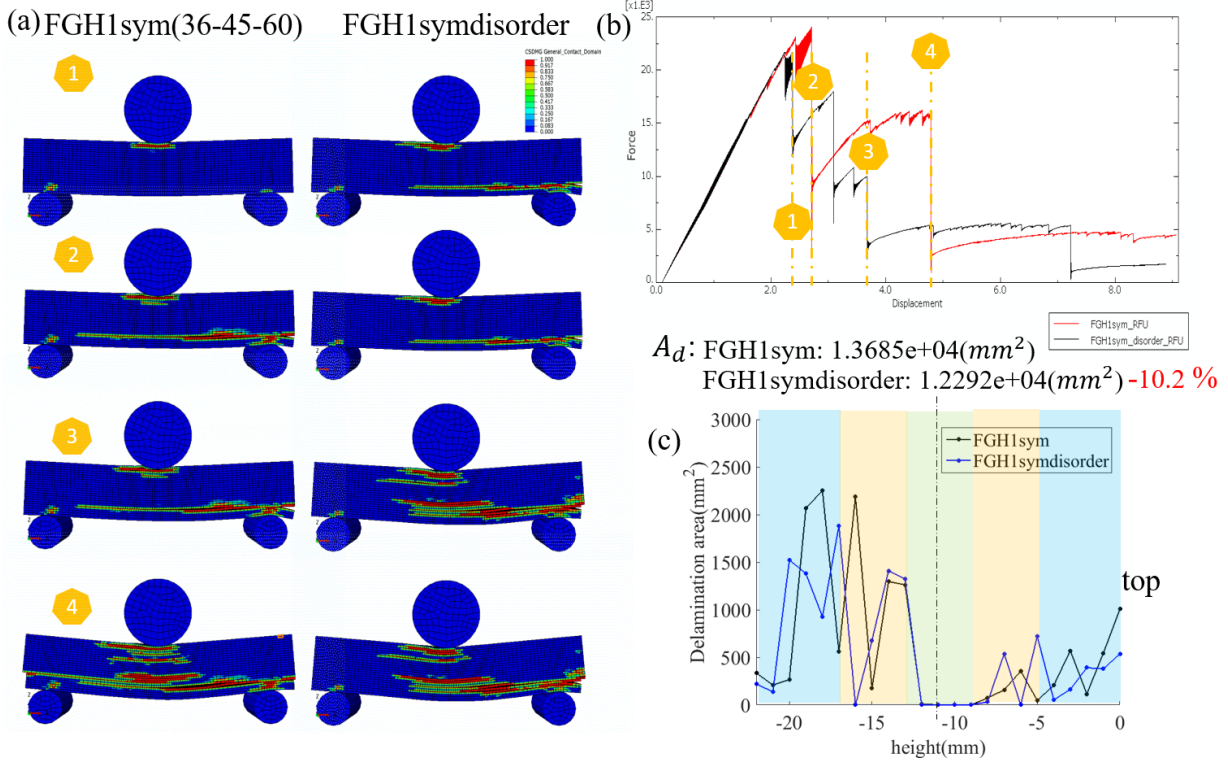


Figure D5. (a) Delamination failure distribution through the thickness of short beams FGH1sym and FGH1symdisorder (b) Load and displacement curves of FGH1sym (red) and FGH1symdisorder (black) (c) Delamination area distribution layer by layer. Different shaded color represents for different pitches of FGH1sym

D2. 1st drop on force and displacement plot

There are minor drops (stiffness is close to 0) on the stiffness in force and displacement plot due to delamination initiation when short beam is under 3-point bending. These drops on stiffness do not show severe drop (stiffness is much less than 0) on the force and displacement plot, which means no catastrophic failure observed in the beam.

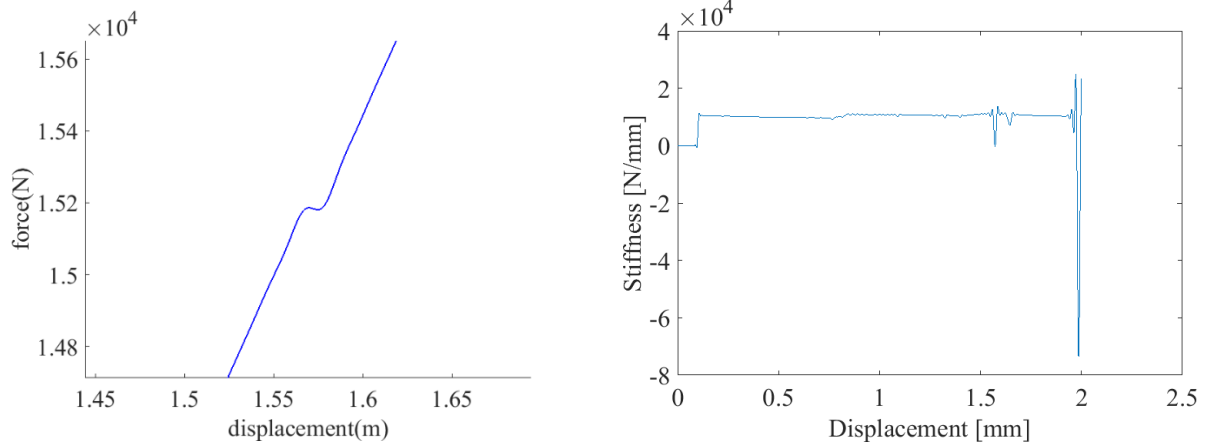


Figure D6. Force and displacement plot of H45sym under 3-point bending test(left) and stiffness as a function of displacement plot of H45sym under 3-point bending plot

D3. Delamination area distribution in 3D

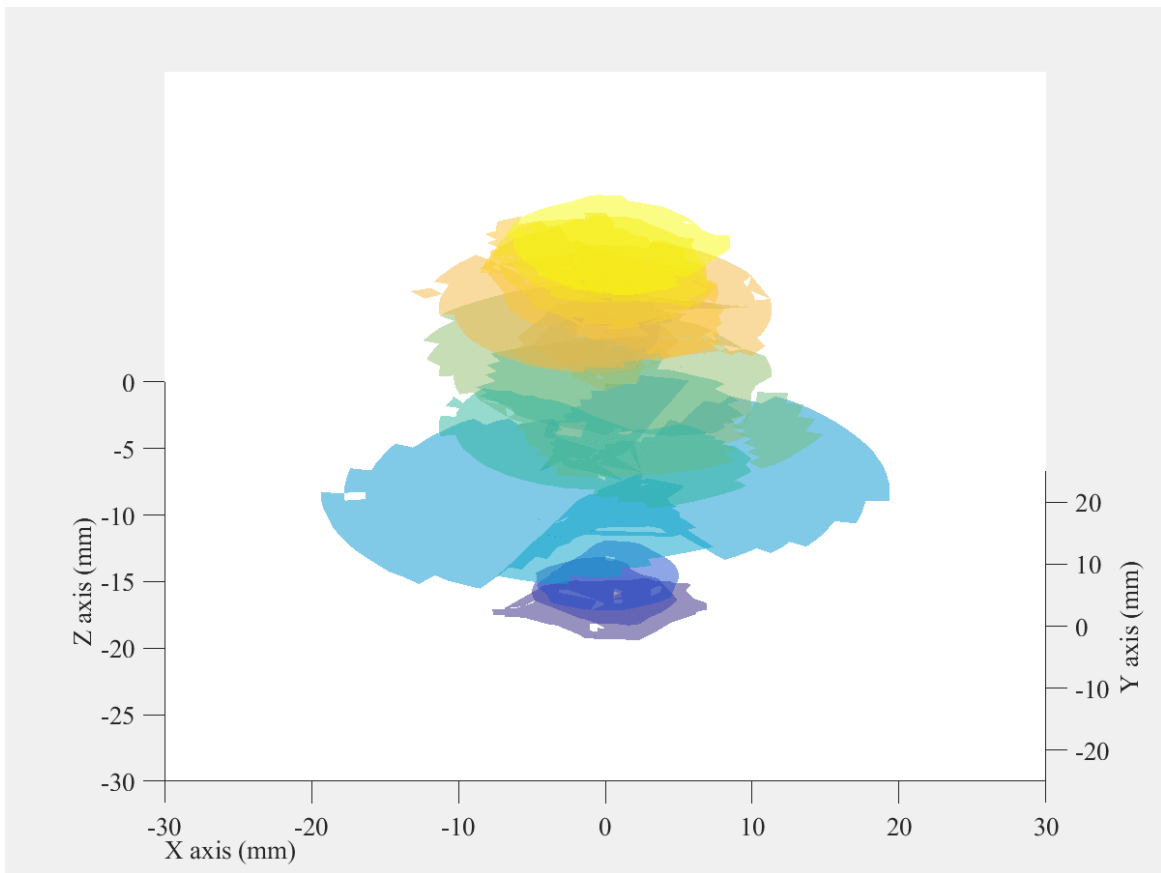


Figure D7. Delamination distribution in 3D of H30sym

D4. Projected delamination area of models with 24 mm thickness under LVI

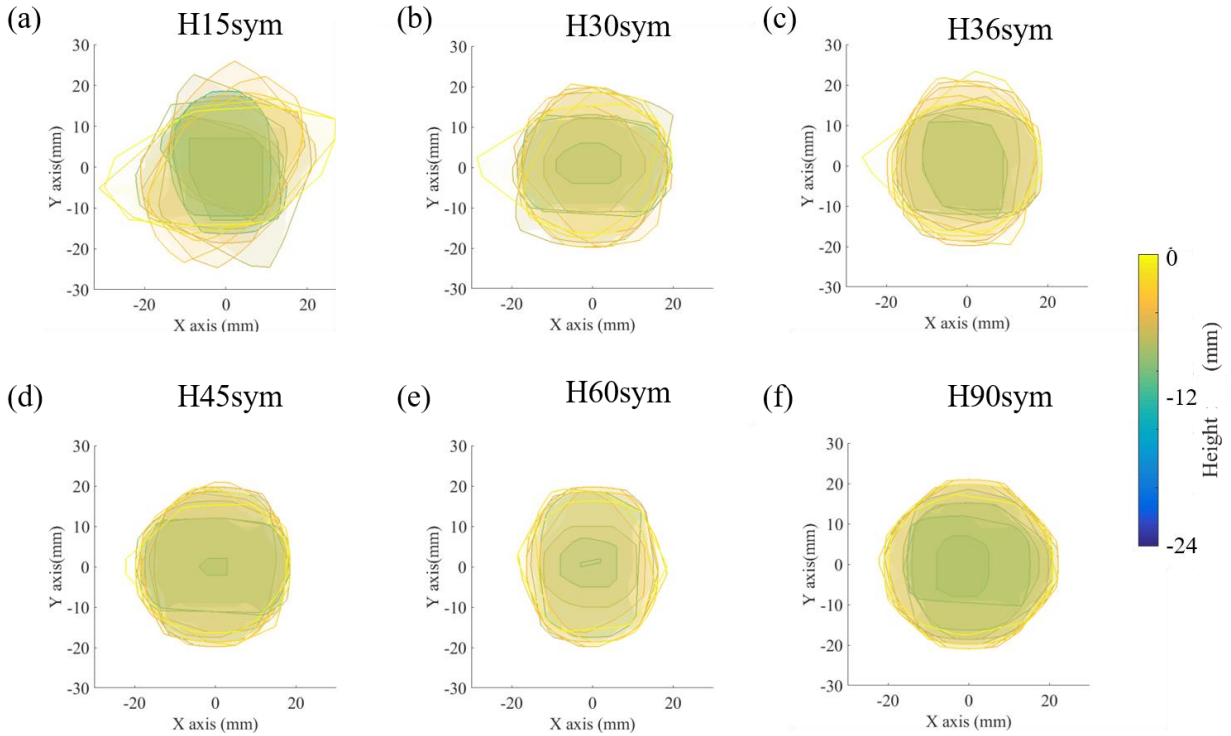


Figure D8. Projected delamination area A_{pd} of (a) H15sym, (b) H30sym, (c) H36sym, (d) H45sym, (e) H60sym and (f) H90sym with thickness 24mm

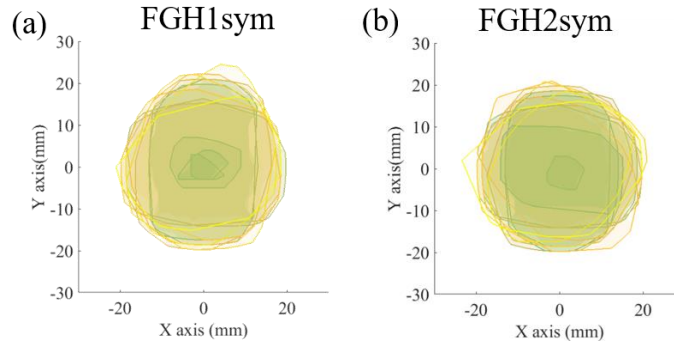


Figure D9. Projected delamination area A_{pd} of (a) FGH1sym, (b) FGH2sym with thickness 24mm

D5. Analytical prediction on transverse shear stress of 3-point bending test

According to the classical laminate plate theory, resultant forces and strain at middle plane has following relationship (Reddy, 2004; Yu, 2016).

$$\begin{bmatrix} N \\ M \end{bmatrix} = \begin{bmatrix} A & B \\ B & D \end{bmatrix} \begin{bmatrix} \varepsilon^0 \\ \kappa^0 \end{bmatrix} \quad \text{D(1)}$$

In our case, the laminate is symmetry to middle plane, and thus $B = 0$. We have

$$N_{11} = A_{11}u_{1,1} + A_{16}(u_{1,2} + u_{2,1}) \quad \text{D(2)}$$

$$N_{22} = A_{12}u_{1,1} + A_{26}(u_{1,2} + u_{2,1}) \quad \text{D(3)}$$

$$N_{12} = A_{16}u_{1,1} - B_{16}u_{3,11} + A_{66}u_{2,1} \quad \text{D(4)}$$

$$M_{11} = B_{11}u_{1,1} + B_{16}u_{2,1} - D_{11}u_{3,11} \quad \text{D(5)}$$

$$M_{22} = B_{12}u_{1,1} + B_{26}u_{2,1} - D_{12}u_{3,11} \quad \text{D(6)}$$

$$M_{12} = B_{16}u_{1,11} + B_{66}u_{2,1} - D_{16}u_{3,11} \quad \text{D(7)}$$

Due to resultant force equilibrium of uniform stress element in the plate (Yu, 2016), which is

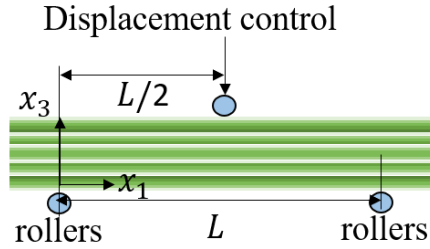


Figure D10 loading condition of short beam 3-point bending test

$$\frac{\partial N_{11}}{\partial x_1} + \frac{\partial N_{12}}{\partial x_2} + p_1 = 0 \quad \text{D(8)}$$

$$\frac{\partial N_{21}}{\partial x_1} + \frac{\partial N_{22}}{\partial x_2} + p_2 = 0 \quad \text{D(9)}$$

$$\frac{\partial^2 M_{11}}{\partial x_1^2} + \frac{\partial^2 M_{22}}{\partial x_2^2} + 2 \frac{\partial^2 M_{12}}{\partial x_1 \partial x_2} + \frac{\partial q_2}{\partial x_1} - \frac{\partial q_1}{\partial x_2} + p_2 = 0 \quad \text{D(10)}$$

Where q_2 and q_1 are moments and p_i is distributed force.

We have

$$A_{11}u_{1,11} + A_{16}u_{2,11} = 0 \quad \text{D(11)}$$

$$A_{16}u_{1,11} + A_{66}u_{2,11} = 0 \quad \text{D(12)}$$

$$-D_{11}u_{3,1111} = 0 \quad \text{D(13)}$$

Accordingly, from $x_1 = 0$ to $x_1 = L/2$

$$u_3^- = \frac{C_1}{6}x_1^3 + C_2x_1^2 + C_3x_1 + C_4 \quad \text{D(14)}$$

$$u_1^- = C_5x_1 + C_6 \quad \text{D(15)}$$

$$u_2^- = C_7 x_1 + C_8 \quad \text{D(16)}$$

and from $x_1 = L/2$ to $x_1 = L$

$$u_3^+ = \frac{C_1^+}{6} x_1^3 + C_2^+ x_1^2 + C_3^+ x_1 + C_4^+ \quad \text{D(17)}$$

$$u_1^+ = C_5^+ x_1 + C_6^+ \quad \text{D(18)}$$

$$u_2^+ = C_7^+ x_1 + C_8^+ \quad \text{D(19)}$$

According to boundary conditions as following for the left part of the beam,

$$u_3^-(0) = 0 \quad \text{D(20)}$$

$$u_3^-(L/2) = Z \quad \text{D(21)}$$

$$u_{3,11}^-(0) = 0 \quad \text{D(22)}$$

We have $C_4 = 0, \frac{C_1 L^3}{48} + \frac{C_3 L}{2} = Z, C_2 = 0$

According to boundary conditions as following for the right part of the beam,

$$u_3^+(L) = 0 \quad \text{D(23)}$$

$$u_3^+(L/2) = Z \quad \text{D(24)}$$

$$u_{3,11}^+(L) = 0 \quad \text{D(25)}$$

We have $C_4 = 0, \frac{C_1 L^3}{48} + \frac{C_3 L}{2} = Z, C_2 = 0$

$$\frac{C_1^+}{6} L^3 + \frac{C_2^+}{2} L^2 + C_3^+ L + C_4^+ = 0 \quad \text{D(26)}$$

$$C_1^+ L + C_2^+ = 0 \quad \text{D(27)}$$

$$\frac{C_1^+}{6} \frac{L^3}{8} + \frac{C_2^+}{2} \frac{L^2}{4} + C_3^+ \frac{L}{2} + C_4^+ = Z \quad \text{D(28)}$$

Furthermore, considering the continuity at the middle of the beam, we have

$$u_{3,1}^-(L/2) = -u_{3,1}^+(L/2) \quad \text{D(29)}$$

$$u_{3,11}^-(L/2) = u_{3,11}^+(L/2) \quad \text{D(30)}$$

Solve the equilibrium equations combined with boundary conditions, we can achieve

$$u_3^- = \frac{3Zx_1}{L} - \frac{4Z}{L^3} x_1^3 \quad \text{D(31)}$$

$$u_3^+ = -Z + \frac{9Zx_1}{L} - \frac{12Z}{L^2} x_1^2 + \frac{4Z}{L^3} x_1^3 \quad \text{D(32)}$$

Strain for individual layer is

$$\varepsilon_{11} = \varepsilon_{11}^0 + x_3 \kappa^0 = u_{1,1} - x_3 u_{3,11} \quad \text{D(33)}$$

From $x_1 = 0$ to $x_1 = L/2$

$$\varepsilon_{11}^- = \frac{24Z}{L^3} x_1 x_3 \quad \text{D(34)}$$

from $x_1 = L/2$ to $x_1 = L$

$$\varepsilon_{11}^+ = \frac{-24Z}{L^3} x_1 x_3 + \frac{24Z}{L^2} x_3 \quad \text{D(35)}$$

For each individual layer, the relationship between stress and strain is

$$\begin{bmatrix} \sigma_{11} \\ \sigma_{22} \\ \tau_{12} \end{bmatrix} = \begin{bmatrix} Q_{11} & Q_{12} & Q_{13} \\ Q_{21} & Q_{22} & Q_{23} \\ Q_{31} & Q_{32} & Q_{33} \end{bmatrix} \begin{bmatrix} \varepsilon_{11} \\ \varepsilon_{22} \\ \gamma_{12} \end{bmatrix} \quad \text{D(36)}$$

$$\sigma_{11} = Q_{11} \begin{cases} \frac{24Z}{L^3} x_1 x_3, & x_1 \in [0, \frac{L}{2}] \\ \frac{-24Z}{L^3} x_1 x_3 + \frac{24Z}{L^2} x_3, & x_1 \in [L/2, L] \end{cases} \quad \text{D(37)}$$

Thus, according to $div\sigma + b = 0$, we can achieve

$$\sigma_{13} = - \int \frac{\partial \sigma_{11}}{\partial x_1} dx_3 + C \quad \text{D(38)}$$

Combined with the boundary condition that $\sigma_{13} = 0$ at bottom and top surface and σ_{13} is continuous at interface, we can solve the σ_{13} distribution map as Figure 5.22(b).

D6. Transverse shear strain induced by in-plane shear stress in mono-balanced laminate

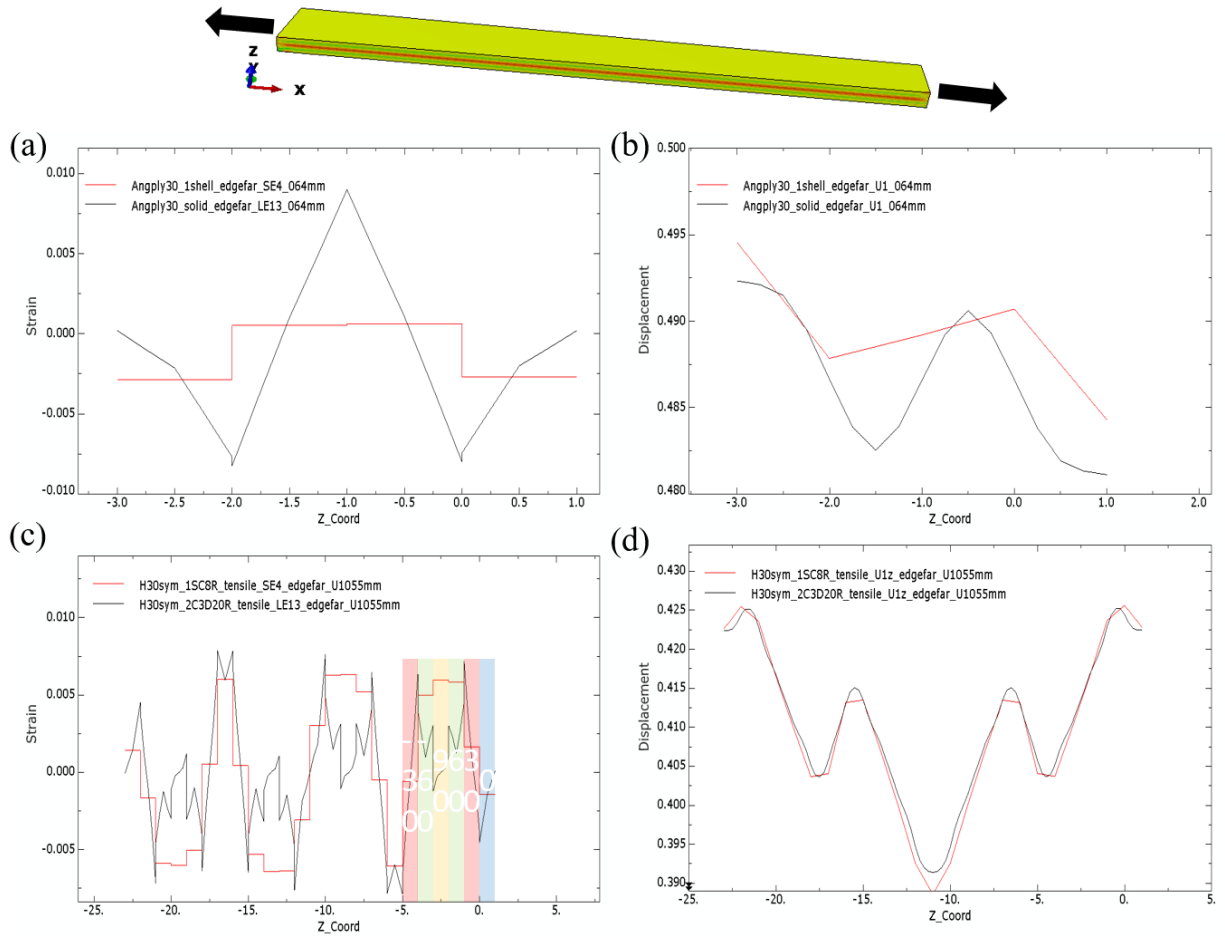


Figure D11. (a) Transverse shear strain (LE_{xz}) distribution of [-30/30/-30/30] along the thickness at free edge of mono-balanced laminate under uniaxial tensile (b) Displacement in x direction of [-30/30/-30/30] along the thickness at free edge of mono-balanced laminate under uniaxial tensile. (c) Transverse shear strain (LE_{xz}) distribution of H30sym along the thickness at free edge of mono-balanced laminate under uniaxial tensile. (d) Displacement in x direction of [-30/30/-30/30] along the thickness at free edge of mono-balanced laminate under uniaxial tensile.

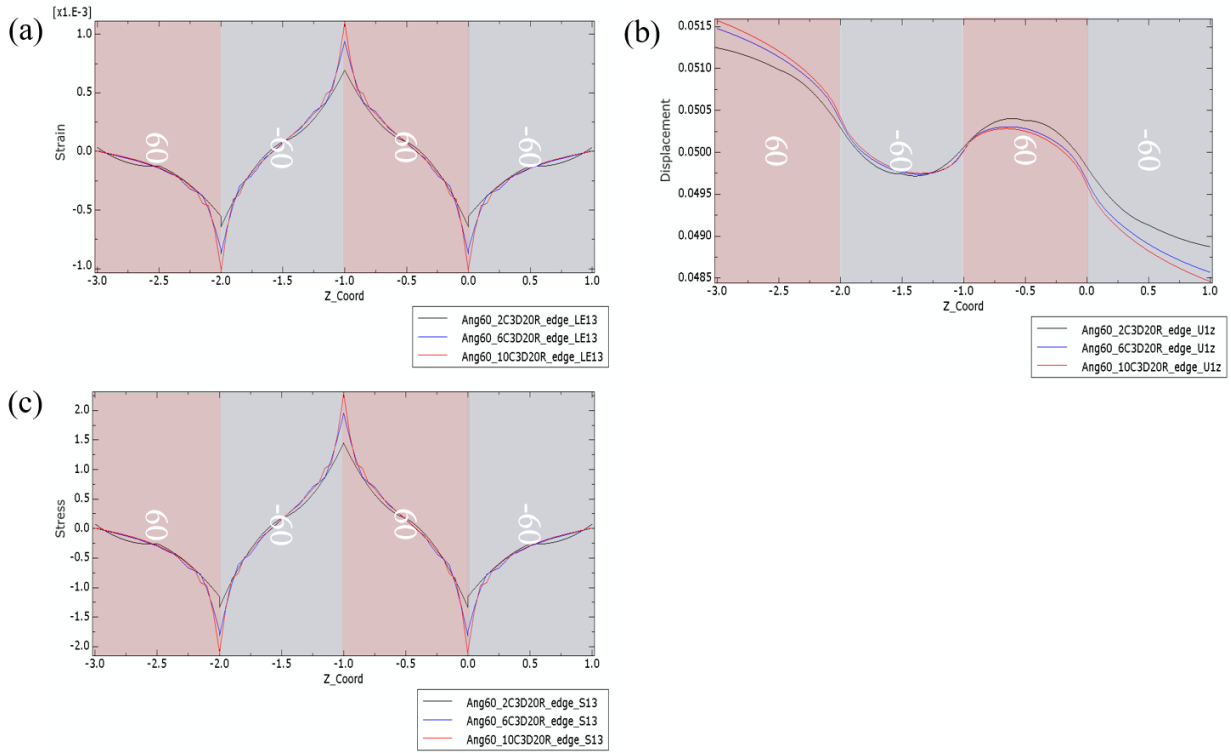


Figure D12. (a) Transverse shear strain (LE_{xz}) distribution of [-60/60/-60/60] along the thickness at free edge of mono-balanced laminate under uniaxial tensile (b) Displacement in x direction of [-60/60/-60/60] along the thickness at free edge of mono-balanced laminate under uniaxial tensile. (c) Transverse shear stress (S_{xz}) distribution of [-60/60/-60/60] along the thickness at free edge of mono-balanced laminate under uniaxial tensile.

REFERENCES

- Aizenberg, J., Weaver, J.C., Thanawala, M.S., Sundar, V.C., Morse, D.E., Fratzl, P., 2005. Skeleton of *Euplectella* sp.: Structural Hierarchy from the Nanoscale to the Macroscale 10.1126/science.1112255. *Science* (80-.). <https://doi.org/10.1126/science.1112255>
- Al Kassem, G., Weichert, D., 2009. Micromechanical material models for polymer composites through advanced numerical simulation techniques. *PAMM*. <https://doi.org/10.1002/pamm.200910180>
- Anlas, G., Santare, M.H., Lambros, J., 2000. Numerical calculation of stress intensity factors in functionally graded materials. *Int. J. Fract.* <https://doi.org/10.1023/A:1007652711735>
- Aslan, Z., Şahin, M., 2009. Buckling behavior and compressive failure of composite laminates containing multiple large delaminations. *Compos. Struct.* <https://doi.org/10.1016/j.compstruct.2008.08.011>
- Barthelat, F., Tang, H., Zavattieri, P.D., Li, C.M., Espinosa, H.D., 2007. On the mechanics of mother-of-pearl: A key feature in the material hierarchical structure. *J. Mech. Phys. Solids*. <https://doi.org/10.1016/j.jmps.2006.07.007>
- Barthelat, F., Yin, Z., Buehler, M.J., 2016. Structure and mechanics of interfaces in biological materials. *Nat. Rev. Mater.* <https://doi.org/10.1038/natrevmats.2016.7>
- Benzeggagh, M.L., Kenane, M., 1996. Measurement of mixed-mode delamination fracture toughness of unidirectional glass/epoxy composites with mixed-mode bending apparatus. *Compos. Sci. Technol.* [https://doi.org/10.1016/0266-3538\(96\)00005-X](https://doi.org/10.1016/0266-3538(96)00005-X)
- Bigi, A., Burghammer, M., Falconi, R., Koch, M.H.J., Panzavolta, S., Riekkel, C., 2001. Twisted plywood pattern of collagen fibrils in teleost scales: An X-ray diffraction investigation. *J. Struct. Biol.* 136, 137–143. <https://doi.org/10.1006/jsbi.2001.4426>
- Bouligand, Y., 1972. Twisted fibrous arrangements in biological materials and cholesteric mesophases. *Tissue Cell* 4, 189–217. [https://doi.org/10.1016/S0040-8166\(72\)80042-9](https://doi.org/10.1016/S0040-8166(72)80042-9)
- Bruet, B.J.F., Song, J., Boyce, M.C., Ortiz, C., 2008. Materials design principles of ancient fisharmour. *Nat. Mater.* 7, 748–756. <https://doi.org/10.1038/nmat2231>
- Camanho, P., Davila, C.G., 2002. Mixed-Mode Decohesion Finite Elements in for the Simulation Composite of Delamination Materials. *Nasa*. <https://doi.org/10.1177/002199803034505>

- Carlsson, L.A., Adams, D.F., Pipes, R.B., 2014. Experimental Characterization of Advanced Composite Materials, *Experimental Characterization of Advanced Composite Materials*. <https://doi.org/10.1201/b16618>
- Chen, P.Y., McKittrick, J., Meyers, M.A., 2012. Biological materials: Functional adaptations and bioinspired designs. *Prog. Mater. Sci.* <https://doi.org/10.1016/j.pmatsci.2012.03.001>
- Cheng, L., Thomas, A., Glancey, J.L., Karlsson, A.M., 2011. Mechanical behavior of bio-inspired laminated composites. *Compos. Part A Appl. Sci. Manuf.* 42, 211–220. <https://doi.org/10.1016/j.compositesa.2010.11.009>
- Cheng, L., Wang, L., Karlsson, A.M., 2008a. Image analyses of two crustacean exoskeletons and implications of the exoskeletal microstructure on the mechanical behavior. *J. Mater. Res.* 23, 2854–2872. <https://doi.org/10.1557/JMR.2008.0375>
- Cheng, L., Wang, L., Karlsson, A.M., 2008b. Image analyses of two crustacean exoskeletons and implications of the exoskeletal microstructure on the mechanical behavior. *J. Mater. Res.* <https://doi.org/10.1557/JMR.2008.0375>
- Chintapalli, R.K., Breton, S., Dastjerdi, A.K., Barthelat, F., 2014. Strain rate hardening: A hidden but critical mechanism for biological composites? *Acta Biomater.* <https://doi.org/10.1016/j.actbio.2014.08.027>
- Chung, W.J., Oh, J.W., Kwak, K., Lee, B.Y., Meyer, J., Wang, E., Hexemer, A., Lee, S.W., 2011. Biomimetic self-templating supramolecular structures. *Nature* 478, 364–368. <https://doi.org/10.1038/nature10513>
- de Obaldia, E.E., Jeong, C., Grunenfelder, L.K., Kisailus, D., Zavattieri, P., 2015. Analysis of the mechanical response of biomimetic materials with highly oriented microstructures through 3D printing, mechanical testing and modeling. *J. Mech. Behav. Biomed. Mater.* 48, 70–85. <https://doi.org/10.1016/j.jmbbm.2015.03.026>
- Eder, M., Jungnikl, K., Burgert, I., 2009. A close-up view of wood structure and properties across a growth ring of Norway spruce (*Picea abies* [L] Karst.). *Trees - Struct. Funct.* <https://doi.org/10.1007/s00468-008-0256-1>
- Escobar de Obaldia, E., Herrera, S., Grunenfelder, L.K., Kisailus, D., Zavattieri, P., 2016. Competing mechanisms in the wear resistance behavior of biomineralized rod-like microstructures. *J. Mech. Phys. Solids.* <https://doi.org/10.1016/j.jmps.2016.08.001>

- Fang, Z., Wang, Y., Feng, Q., Kienzle, A., Müller, W.E.G., 2014. Hierarchical structure and cytocompatibility of fish scales from *Carassius auratus*. *Mater. Sci. Eng. C* 43, 145–152. <https://doi.org/10.1016/j.msec.2014.07.015>
- Gao, H., 2006. Application of fracture mechanics concepts to hierarchical biomechanics of bone and bone-like materials. *Int. J. Fract.* 138, 101–137. <https://doi.org/10.1007/s10704-006-7156-4>
- Garg, A.C., 1988. Delamination—a damage mode in composite structures. *Eng. Fract. Mech.* [https://doi.org/10.1016/0013-7944\(88\)90181-6](https://doi.org/10.1016/0013-7944(88)90181-6)
- Gibson, L.J., 2012. The hierarchical structure and mechanics of plant materials. *J. R. Soc. Interface.* <https://doi.org/10.1098/rsif.2012.0341>
- Gil-Duran, S., Arola, D., Ossa, E.A., 2016. Effect of chemical composition and microstructure on the mechanical behavior of fish scales from *Megalops Atlanticus*. *J. Mech. Behav. Biomed. Mater.* 56, 134–145. <https://doi.org/10.1016/j.jmbbm.2015.11.028>
- Gilbert, P.U.P.A., Metzler, R.A., Zhou, D., Scholl, A., Doran, A., Young, A., Kunz, M., Tamura, N., Coppersmith, S.N., 2008. Gradual ordering in red abalone nacre. *J. Am. Chem. Soc.* <https://doi.org/10.1021/ja8065495>
- Ginzburg, D., Pinto, F., Iervolino, O., Meo, M., 2017. Damage tolerance of bio-inspired helicoidal composites under low velocity impact. *Compos. Struct.* 161, 187–203. <https://doi.org/10.1016/j.compstruct.2016.10.097>
- Goodsell, J., Pagano, N.J., Kravchenko, O., Pipes, R.B., 2013. Interlaminar stresses in composite laminates subjected to anticlastic bending deformation. *J. Appl. Mech. Trans. ASME.* <https://doi.org/10.1115/1.4007969>
- Goodsell, J., Pipes, R.B., 2016. Free-Edge Interlaminar Stresses in Angle-Ply Laminates: A Family of Analytic Solutions. *J. Appl. Mech. Trans. ASME.* <https://doi.org/10.1115/1.4032766>
- Grunenfelder, L.K., Suksangpanya, N., Salinas, C., Milliron, G., Yaraghi, N., Herrera, S., Evans-Lutterodt, K., Nutt, S.R., Zavattieri, P., Kisailus, D., 2014a. Bio-inspired impact-resistant composites. *Acta Biomater.* 10, 3997–4008. <https://doi.org/10.1016/j.actbio.2014.03.022>
- Grunenfelder, L.K., Suksangpanya, N., Salinas, C., Milliron, G., Yaraghi, N., Herrera, S., Evans-Lutterodt, K., Nutt, S.R., Zavattieri, P., Kisailus, D., 2014b. Bio-inspired impact-resistant composites, in: *Acta Biomaterialia*. <https://doi.org/10.1016/j.actbio.2014.03.022>

- Gu, P., Dao, M., Asaro, R.J., 1999. A simplified method for calculating the crack-tip field of functionally graded materials using the domain integral. *J. Appl. Mech. Trans. ASME*. <https://doi.org/10.1115/1.2789135>
- Guarín-Zapata, N., Gomez, J., Yaraghi, N., Kisailus, D., Zavattieri, P.D., 2015. Shear wave filtering in naturally-occurring Bouligand structures. *Acta Biomater.* 23, 11–20. <https://doi.org/10.1016/j.actbio.2015.04.039>
- Halpin, J.C., 1969. Stiffness and Expansion Estimates for Oriented Short Fiber Composites. *J. Compos. Mater.* 3, 732–734. <https://doi.org/10.1177/002199836900300419>
- Hashin, Z., 1980. Failure criteria for unidirectional fiber composites. *J. Appl. Mech. Trans. ASME*. <https://doi.org/10.1115/1.3153664>
- Hashin, Z., Rotem, A., 1973. A Fatigue Failure Criterion for Fiber Reinforced Materials. *J. Compos. Mater.* <https://doi.org/10.1177/002199837300700404>
- Hibbit, H.D., Karlsson, B.I., Sorensen, E.P., 2012. ABAQUS user manual, version 6.12. Simulia. <https://doi.org/10.1577/T09-122.1>
- Ho, S.P., Marshall, S.J., Ryder, M.I., Marshall, G.W., 2007. The tooth attachment mechanism defined by structure, chemical composition and mechanical properties of collagen fibers in the periodontium. *Biomaterials*. <https://doi.org/10.1016/j.biomaterials.2007.08.031>
- Ho, S.P., Yu, B., Yun, W., Marshall, G.W., Ryder, M.I., Marshall, S.J., 2009. Structure, chemical composition and mechanical properties of human and rat cementum and its interface with root dentin. *Acta Biomater.* <https://doi.org/10.1016/j.actbio.2008.08.013>
- Hofer, A.K., Walton, R., Ševeček, O., Messing, G.L., Bermejo, R., 2020. Design of damage tolerant and crack-free layered ceramics with textured microstructure. *J. Eur. Ceram. Soc.* <https://doi.org/10.1016/j.jeurceramsoc.2019.09.004>
- Hovden, R., Wolf, S.E., Holtz, M.E., Marin, F., Muller, D.A., Estroff, L.A., 2015. Nanoscale assembly processes revealed in the nacroprismatic transition zone of *Pinna nobilis* mollusc shells. *Nat. Commun.* <https://doi.org/10.1038/ncomms10097>
- Ikoma, T., Kobayashi, H., Tanaka, J., Walsh, D., Mann, S., 2003. Microstructure, mechanical, and biomimetic properties of fish scales from *Pagrus major*. *J. Struct. Biol.* 142, 327–333. [https://doi.org/10.1016/S1047-8477\(03\)00053-4](https://doi.org/10.1016/S1047-8477(03)00053-4)
- Isaac M Daniel, Ori Ishai, 1994. *Engineering Mechanics of Composite Materials*. New York Oxford Univ. Press. Vol.3, pp.256-256.

- Ji, B., Gao, H., 2004. Mechanical properties of nanostructure of biological materials. *J. Mech. Phys. Solids* 52, 1963–1990. <https://doi.org/10.1016/j.jmps.2004.03.006>
- Jiang, H., Ren, Y., Liu, Z., Zhang, S., Lin, Z., 2019. Low-velocity impact resistance behaviors of bio-inspired helicoidal composite laminates with non-linear rotation angle based layups. *Compos. Struct.* <https://doi.org/10.1016/j.compstruct.2019.02.034>
- Kokkinis, D., Bouville, F., Studart, A.R., 2018. 3D Printing of Materials with Tunable Failure via Bioinspired Mechanical Gradients. *Adv. Mater.* <https://doi.org/10.1002/adma.201705808>
- Kose, O., Tran, A., Lewis, L., Hamad, W.Y., MacLachlan, M.J., 2019. Unwinding a spiral of cellulose nanocrystals for stimuli-responsive stretchable optics. *Nat. Commun.* 10. <https://doi.org/10.1038/s41467-019-08351-6>
- Lawn, B.R., Lee, J.J.-W., Chai, H., 2010. Teeth: Among Nature’s Most Durable Biocomposites. *Annu. Rev. Mater. Res.* <https://doi.org/10.1146/annurev-matsci-070909-104537>
- Li, F.Z., Shih, C.F., Needleman, A., 1985. A comparison of methods for calculating energy release rates. *Eng. Fract. Mech.* [https://doi.org/10.1016/0013-7944\(85\)90029-3](https://doi.org/10.1016/0013-7944(85)90029-3)
- Li, X., Hallett, S.R., Wisnom, M.R., 2008. Predicting the effect of through-thickness compressive stress on delamination using interface elements. *Compos. Part A Appl. Sci. Manuf.* <https://doi.org/10.1016/j.compositesa.2007.11.005>
- Lin, Y.S., Wei, C.T., Olevsky, E.A., Meyers, M.A., 2011. Mechanical properties and the laminate structure of *Arapaima gigas* scales. *J. Mech. Behav. Biomed. Mater.* 4, 1145–1156. <https://doi.org/10.1016/j.jmbbm.2011.03.024>
- Liu, J.L., Lee, H.P., Lai, K.S., Tan, V.B.C., 2020. Bio-Inspired Laminates of Different Material Systems. *J. Appl. Mech.* 87, 1–7. <https://doi.org/10.1115/1.4045280>
- Liu, J.L., Lee, H.P., Tan, V.B.C., 2018a. Effects of inter-ply angles on the failure mechanisms in bioinspired helicoidal laminates. *Compos. Sci. Technol.* <https://doi.org/10.1016/j.compscitech.2018.07.017>
- Liu, J.L., Lee, H.P., Tan, V.B.C., 2018b. Failure mechanisms in bioinspired helicoidal laminates. *Compos. Sci. Technol.* <https://doi.org/10.1016/j.compscitech.2018.01.033>
- Liu, Z., Meyers, M.A., Zhang, Z., Ritchie, R.O., 2017. Functional gradients and heterogeneities in biological materials: Design principles, functions, and bioinspired applications. *Prog. Mater. Sci.* <https://doi.org/10.1016/j.pmatsci.2017.04.013>

- Long, S., Yao, X., Zhang, X., 2015. Delamination prediction in composite laminates under low-velocity impact. *Compos. Struct.* <https://doi.org/10.1016/j.compstruct.2015.05.037>
- Matzenmiller, A., Lubliner, J., Taylor, R.L., 1995. A constitutive model for anisotropic damage in fiber-composites. *Mech. Mater.* [https://doi.org/10.1016/0167-6636\(94\)00053-0](https://doi.org/10.1016/0167-6636(94)00053-0)
- Mencattelli, L., Pinho, S.T., 2019. Realising bio-inspired impact damage-tolerant thin-ply CFRP Bouligand structures via promoting diffused sub-critical helicoidal damage. *Compos. Sci. Technol.* 182, 107684. <https://doi.org/10.1016/j.compscitech.2019.107684>
- Menig, R., Meyers, M.H., Meyers, M.A., Vecchio, K.S., 2000. Quasi-static and dynamic mechanical response of *Haliotis rufescens* (abalone) shells. *Acta Mater.* 48, 2383–2398. [https://doi.org/10.1016/S1359-6454\(99\)00443-7](https://doi.org/10.1016/S1359-6454(99)00443-7)
- Meyers, M.A., Chen, P.-Y., Lin, A.Y.-M., Seki, Y., 2008. Biological materials: Structure and mechanical properties. *Prog. Mater. Sci.* 53, 1–206. <https://doi.org/10.1016/j.pmatsci.2007.05.002>
- Meyers, M.A., Lin, Y.S., Olevsky, E.A., Chen, P.Y., 2012. Battle in the Amazon: Arapaima versus piranha. *Adv. Eng. Mater.* 14, 279–288. <https://doi.org/10.1002/adem.201180027>
- Miserez, A., Weaver, J.C., Thurner, P.J., Aizenberg, J., Dauphin, Y., Fratzl, P., Morse, D.E., Zok, F.W., 2008. Effects of laminate architecture on fracture resistance of sponge biosilica: Lessons from nature. *Adv. Funct. Mater.* <https://doi.org/10.1002/adfm.200701135>
- Murcia, S., Lavoie, E., Linley, T., Devaraj, A., Ossa, E.A., Arola, D., 2017a. The natural armors of fish: A comparison of the lamination pattern and structure of scales. *J. Mech. Behav. Biomed. Mater.* 73, 17–27. <https://doi.org/10.1016/j.jmbbm.2016.09.025>
- Murcia, S., Lavoie, E., Linley, T., Devaraj, A., Ossa, E.A., Arola, D., 2017b. The natural armors of fish: A comparison of the lamination pattern and structure of scales. *J. Mech. Behav. Biomed. Mater.* <https://doi.org/10.1016/j.jmbbm.2016.09.025>
- Pagano, N.J., 1970. Influence of Shear Coupling in Cylindrical Bending of Anisotropic Laminates. *J. Compos. Mater.* <https://doi.org/10.1177/002199837000400305>
- Pender, D.C., Padture, N.P., Giannakopoulos, A.E., Suresh, S., 2001. Gradients in elastic modulus for improved contact-damage resistance. Part I: The silicon nitride-oxynitride glass system. *Acta Mater.* [https://doi.org/10.1016/S1359-6454\(01\)00200-2](https://doi.org/10.1016/S1359-6454(01)00200-2)

- Peng, B., Goodsell, J., Pipes, R.B., Yu, W., 2016. Generalized Free-Edge Stress Analysis Using Mechanics of Structure Genome. *J. Appl. Mech. Trans. ASME*. <https://doi.org/10.1115/1.4034389>
- Porter, M.M., Ravikumar, N., Barthelat, F., Martini, R., 2017. 3D-printing and mechanics of bio-inspired articulated and multi-material structures. *J. Mech. Behav. Biomed. Mater.* 73, 114–126. <https://doi.org/10.1016/j.jmbbm.2016.12.016>
- Pro, J.W., Lim, R.K., Petzold, L.R., Utz, M., Begley, M.R., 2015. The impact of stochastic microstructures on the macroscopic fracture properties of brick and mortar composites. *Extrem. Mech. Lett.* <https://doi.org/10.1016/j.eml.2015.09.001>
- Quan, H., Yang, W., Schaible, E., Ritchie, R.O., Meyers, M.A., 2018. Novel Defense Mechanisms in the Armor of the Scales of the “Living Fossil” Coelacanth Fish. *Adv. Funct. Mater.* 28. <https://doi.org/10.1002/adfm.201804237>
- Raabe, D., Romano, P., Sachs, C., Al-Sawalmih, A., Brokmeier, H.G., Yi, S.B., Servos, G., Hartwig, H.G., 2005. Discovery of a honeycomb structure in the twisted plywood patterns of fibrous biological nanocomposite tissue. *J. Cryst. Growth* 283, 1–7. <https://doi.org/10.1016/j.jcrysgro.2005.05.077>
- Raju, I.S., Shivakumar, K.N., 1990. An equivalent domain integral method in the two-dimensional analysis of mixed mode crack problems. *Eng. Fract. Mech.* [https://doi.org/10.1016/0013-7944\(90\)90070-W](https://doi.org/10.1016/0013-7944(90)90070-W)
- Ramirez, G., 1999. Book Reviews: Design and Optimization of Laminated Composite Materials. *J. Struct. Eng.* 125, 1082–1082. [https://doi.org/10.1061/\(asce\)0733-9445\(1999\)125:9\(1082\)](https://doi.org/10.1061/(asce)0733-9445(1999)125:9(1082))
- Reddy, J.N., 2013. An Introduction to Continuum Mechanics, Second Edition, An Introduction to Continuum Mechanics, Second Edition. <https://doi.org/10.1017/cbo9781139178952>
- Reddy, J.N., 2004. Mechanics of Laminated Composite Plates and Shells, Mechanics of Laminated Composite Plates and Shells. <https://doi.org/10.1201/b12409>
- Rivlin, R.S., Saunders, D.W., 1951. Large Elastic Deformations of Isotropic Materials. VII. Experiments on the Deformation of Rubber. *Philos. Trans. R. Soc. A Math. Phys. Eng. Sci.* 243, 251–288. <https://doi.org/10.1098/rsta.1951.0004>
- Roland, J.C., Reis, D., Vian, B., Roy, S., 1989. The helicoidal plant cell wall as a performing cellulose-based composite. *Biol. Cell* 67, 209–220. <https://doi.org/10.1111/j.1768-322X.1989.tb00864.x>

- Sachs, C., Fabritius, H., Raabe, D., 2008. Influence of microstructure on deformation anisotropy of mineralized cuticle from the lobster *Homarus americanus*. *J. Struct. Biol.* 161, 120–132. <https://doi.org/10.1016/j.jsb.2007.09.022>
- Sakhavand, N., Shahsavari, R., 2015. Universal composition-structure-property maps for natural and biomimetic platelet-matrix composites and stacked heterostructures. *Nat. Commun.* 6. <https://doi.org/10.1038/ncomms7523>
- Salinas, C., Kisailus, D., 2013. Fracture mitigation strategies in gastropod shells. *Jom* 65, 473–480. <https://doi.org/10.1007/s11837-013-0570-y>
- Shang, J.S., Ngern, N.H.H., Tan, V.B.C., 2016. Crustacean-inspired helicoidal laminates. *Compos. Sci. Technol.* <https://doi.org/10.1016/j.compscitech.2016.04.007>
- Shishehbor, M., Zavattieri, P.D., 2019. Effects of interface properties on the mechanical properties of bio-inspired cellulose nanocrystal (CNC)-based materials. *J. Mech. Phys. Solids* 124, 871–896. <https://doi.org/10.1016/j.jmps.2018.12.002>
- Speck, T., Burgert, I., 2011. Plant Stems: Functional Design and Mechanics. *Annu. Rev. Mater. Res.* <https://doi.org/10.1146/annurev-matsci-062910-100425>
- Stratasys Ltd., 2019. Stratasys Tango Datasheet [WWW Document]. *Strat. Tango Datasheet*. URL <https://www.stratasys.com/materials/search/tango>
- Stratasys Ltd., 2018. Stratasys Vero material data sheet [WWW Document]. URL <https://www.stratasys.com/materials/search/vero>
- Studart, A.R., 2016. Additive manufacturing of biologically-inspired materials. *Chem. Soc. Rev.* <https://doi.org/10.1039/c5cs00836k>
- Suksangpanya, N., Yaraghi, N.A., Kisailus, D., Zavattieri, P., 2017. Twisting cracks in Bouligand structures. *J. Mech. Behav. Biomed. Mater.* 76, 38–57. <https://doi.org/10.1016/j.jmbbm.2017.06.010>
- Suksangpanya, N., Yaraghi, N.A., Pipes, R.B., Kisailus, D., Zavattieri, P., 2018. Crack twisting and toughening strategies in Bouligand architectures. *Int. J. Solids Struct.* 150, 83–106. <https://doi.org/10.1016/j.ijsolstr.2018.06.004>
- Sun, C.T., Chung, I., 1990. Oblique end tab design for testing off-axis composite specimens. *Am. Soc. Mech. Eng. Aerosp. Div. AD* 19, 7–11. [https://doi.org/10.1016/0010-4361\(93\)90124-Q](https://doi.org/10.1016/0010-4361(93)90124-Q)
- Sun, J., Bhushan, B., 2012a. Hierarchical structure and mechanical properties of nacre: A review. *RSC Adv.* 2, 7617–7632. <https://doi.org/10.1039/c2ra20218b>

- Sun, J., Bhushan, B., 2012b. Hierarchical structure and mechanical properties of nacre: A review. RSC Adv. <https://doi.org/10.1039/c2ra20218b>
- Suresh, S., 2001. Graded materials for resistance to contact deformation and damage. Science (80-). <https://doi.org/10.1126/science.1059716>
- Torres, F.G., Troncoso, O.P., Nakamatsu, J., Grande, C.J., Gómez, C.M., 2008. Characterization of the nanocomposite laminate structure occurring in fish scales from Arapaima Gigas. Mater. Sci. Eng. C 28, 1276–1283. <https://doi.org/10.1016/j.msec.2007.12.001>
- Tucker, C.L., Liang, E., 1999. Stiffness predictions for unidirectional short-fiber composites: Review and evaluation. Compos. Sci. Technol. 59, 655–671. [https://doi.org/10.1016/S0266-3538\(98\)00120-1](https://doi.org/10.1016/S0266-3538(98)00120-1)
- Turon, A., Camanho, P.P., Costa, J., Dávila, C.G., 2006. A damage model for the simulation of delamination in advanced composites under variable-mode loading. Mech. Mater. <https://doi.org/10.1016/j.mechmat.2005.10.003>
- Turon, A., Dávila, C.G., Camanho, P.P., Costa, J., 2007. An engineering solution for mesh size effects in the simulation of delamination using cohesive zone models. Eng. Fract. Mech. <https://doi.org/10.1016/j.engfracmech.2006.08.025>
- Vargas, W.E., Hernández-Jiménez, M., Libby, E., Azofeifa, D.E., Barboza, C., Solis, Á., 2016. Light Reflection by Cuticles of Chrysina Jewel Scarabs: Optical Measurements, Morphology Characterization, and Theoretical Modeling. Opt. Photonics J. <https://doi.org/10.4236/opj.2016.67017>
- Weaver, J.C., Milliron, G.W., Miserez, A., Evans-Lutterodt, K., Herrera, S., Gallana, I., Mershon, W.J., Swanson, B., Zavattieri, P., DiMasi, E., Kisailus, D., 2012. The stomatopod dactyl club: A formidable damage-tolerant biological hammer. Science (80-). 336, 1275–1280. <https://doi.org/10.1126/science.1218764>
- Wei, X., Naraghi, M., Espinosa, H.D., 2012. Optimal length scales emerging from shear load transfer in natural materials: Application to carbon-based nanocomposite design. ACS Nano 6, 2333–2344. <https://doi.org/10.1021/nn204506d>
- Yang, R., Zaheri, A., Gao, W., Hayashi, C., Espinosa, H.D., 2017. AFM Identification of Beetle Exocuticle: Bouligand Structure and Nanofiber Anisotropic Elastic Properties. Adv. Funct. Mater. 27. <https://doi.org/10.1002/adfm.201603993>

- Yang, W., Liu, Q., Yue, Z., Li, X., Xu, B., 2017. Rotation of hard particles in a soft matrix. *J. Mech. Phys. Solids* 101, 285–310. <https://doi.org/10.1016/j.jmps.2017.01.008>
- Yang, W., Quan, H., Meyers, M.A., Ritchie, R.O., 2019. Arapaima Fish Scale: One of the Toughest Flexible Biological Materials. *SSRN Electron. J.* 1–10. <https://doi.org/10.2139/ssrn.3401845>
- Yang, W., Sherman, V.R., Gludovatz, B., Mackey, M., Zimmermann, E.A., Chang, E.H., Schaible, E., Qin, Z., Buehler, M.J., Ritchie, R.O., Meyers, M.A., 2014. Protective role of Arapaima gigas fish scales: Structure and mechanical behavior. *Acta Biomater.* 10, 3599–3614. <https://doi.org/10.1016/j.actbio.2014.04.009>
- Yao, H., Zheng, G., Li, W., McDowell, M.T., Seh, Z., Liu, N., Lu, Z., Cui, Y., 2013. Crab shells as sustainable templates from nature for nanostructured battery electrodes. *Nano Lett.* 13, 3385–3390. <https://doi.org/10.1021/nl401729r>
- Yaraghi, N.A., Kisailus, D., 2018. Biomimetic Structural Materials: Inspiration from Design and Assembly. *Annu. Rev. Phys. Chem.* <https://doi.org/10.1146/annurev-physchem-040215-112621>
- Yin, S., Yang, W., Kwon, J., Wat, A., Meyers, M.A., Ritchie, R.O., 2019. Hyperelastic phase-field fracture mechanics modeling of the toughening induced by Bouligand structures in natural materials. *J. Mech. Phys. Solids* 131, 204–220. <https://doi.org/10.1016/j.jmps.2019.07.001>
- Yu, W., 2016. Chapter 6. Laminated plate theories, in: *Multiscale Structural Mechanics*. pp. 279–333.
- Yu, W., 2005. Mathematical construction of a Reissner-Mindlin plate theory for composite laminates. *Int. J. Solids Struct.* 42, 6680–6699. <https://doi.org/10.1016/j.ijsolstr.2005.02.049>
- Zaheri, A., Fenner, J.S., Russell, B.P., Restrepo, D., Daly, M., Wang, D., Hayashi, C., Meyers, M.A., Zavattieri, P.D., Espinosa, H.D., 2018. Revealing the Mechanics of Helicoidal Composites through Additive Manufacturing and Beetle Developmental Stage Analysis. *Adv. Funct. Mater.* 28. <https://doi.org/10.1002/adfm.201803073>
- Zelazny, B., Neville, A.C., 1972. Quantitative studies on fibril orientation in beetle endocuticle. *J. Insect Physiol.* 18. [https://doi.org/10.1016/0022-1910\(72\)90243-0](https://doi.org/10.1016/0022-1910(72)90243-0)
- Zhang, C., Mcadams, D.A., Grunlan, J.C., 2016. Nano/Micro-Manufacturing of Bioinspired Materials: a Review of Methods to Mimic Natural Structures. *Adv. Mater.* <https://doi.org/10.1002/adma.201505555>

- Zhang, J., Zhang, X., 2015. Simulating low-velocity impact induced delamination in composites by a quasi-static load model with surface-based cohesive contact. *Compos. Struct.* <https://doi.org/10.1016/j.compstruct.2015.01.050>
- Zhang, P., Heyne, M.A., To, A.C., 2015. Biomimetic staggered composites with highly enhanced energy dissipation: Modeling, 3D printing, and testing. *J. Mech. Phys. Solids* 83, 285–300. <https://doi.org/10.1016/j.jmps.2015.06.015>
- Zhang, Z.Q., Liu, B., Huang, Y., Hwang, K.C., Gao, H., 2010a. Mechanical properties of unidirectional nanocomposites with non-uniformly or randomly staggered platelet distribution. *J. Mech. Phys. Solids* 58, 1646–1660. <https://doi.org/10.1016/j.jmps.2010.07.004>
- Zhang, Z.Q., Liu, B., Huang, Y., Hwang, K.C., Gao, H., 2010b. Mechanical properties of unidirectional nanocomposites with non-uniformly or randomly staggered platelet distribution. *J. Mech. Phys. Solids*. <https://doi.org/10.1016/j.jmps.2010.07.004>
- Zhu, D., Ortega, C.F., Motamedi, R., Szewciw, L., Vernerey, F., Barthelat, F., 2012. Structure and mechanical performance of a “modern” fish scale. *Adv. Eng. Mater.* 14, 185–194. <https://doi.org/10.1002/adem.201180057>
- Zimmermann, E.A., Gludovatz, B., Schaible, E., Dave, N.K.N., Yang, W., Meyers, M.A., Ritchie, R.O., 2013. Mechanical adaptability of the Bouligand-type structure in natural dermal armour. *Nat. Commun.* 4, 1–7. <https://doi.org/10.1038/ncomms3634>

PUBLICATIONS

Wang, D., Zaheri, A., Russell, B., Espinosa, H. D., Zavattieri, P. D., “Fiber Reorientation in Hybrid Helicoidal Composites”. *Journal of the Mechanical Behavior of Biomedical Material*(2020)

Revisions being processed

Wang, D., Chan, H.J., Restrepo, D., Zavattieri, P., “On the 3D Architecture of Naturally-occurring Lamellar Structures. A Comparative Analysis”. *Additive Manufacturing of Designer Biomedical and Bioinspired Materials* (2020) Finished writing

Zaheri, A., Fenner, J., Russell, B., Restrepo, D., Daly, M., **Wang, D.**, Hayashi, C., Meryers, M.A., Zavattieri, P.D., Espinosa, H.D., “Revealing the Mechanics of Helicoidal Composites through Additive Manufacturing and Beetle Developmental Stage Analysis”. *Advanced Functional Materials* (2018): 1803073.

Wallis, D., Harris, J., Bohm, C. F., **Wang, D.**, Zavattieri, D., Feldner, P., Merle, B., Hansen, L. N., Marin, F. and Wolf, S.E., “Functional gradients by crystallographic gradation toughens calcareous bivalves”. *Advanced Functional Materials* (2020). Finished writing